



university of
groningen

Non-thermal emission and magnetic fields in nearby galaxies

A low-frequency radio continuum perspective

PhD thesis

to obtain the degree of PhD at the
University of Groningen
on the authority of the
Rector Magnificus Prof. E. Sterken
and in accordance with
the decision by the College of Deans.

This thesis will be defended in public on

Monday 29 October 2018 at 12.45 hours

by

Sarrvesh Seethapuram Sridhar

born on 15 September 1989
in Chennai, Tamil Nadu, India

Supervisor

Prof. J. M. van der Hulst

Co-supervisor

Dr. George H. Heald

Assessment Committee

Prof. A. Scaife

Prof. J. A. Irwin

Prof. P. Barthel

*To N. B.
who wanted to be here,
but couldn't make it.*

Cover – Front: A typical LOFAR High Band Antenna (HBA) image processed using the facet-based direction-dependent calibration scheme. Back cover: Image of LOFAR Low Band Antenna (LBA) dipoles by Hans Hordijk.

Research included in this thesis was performed at the following scientific institutions:

Kapteyn Astronomical Institute, University of Groningen, PO Box 800, 9700AV, Groningen, the Netherlands.

ASTRON, the Netherlands Institute for Radio Astronomy, Postbus 2, 7990AA, Dwingeloo, the Netherlands.

CSIRO Astronomy and Space Science (CASS), 26 Dick Perry Ave, Kensington, WA 6101, Australia

This research was supported by funding from ASTRON, Nederlandse Onderzoekschool Voor Astronomie (NOVA), and the Kapteyn Institute. Multiple trips to conferences and work visits were also funded by the Leids Kerkhoven Bosscha Fonds (LKBF). Additional travel funding to Perth, Australia was provided by CSIRO Astronomy and Space Science.

Thesis printed by: GVO drukkers & vormgevers B.V.

ISBN: 978–94–034–1148–4

ISBN: 978–94–034–1147–7 (electronic version)

Contents

1	Prologue	1
1.1	Historical overview	2
1.2	Radio continuum emission from galaxies	2
1.2.1	Thermal radio emission	3
1.2.2	Non-thermal radio emission	4
1.2.3	Synchrotron emission, Faraday rotation and magnetic fields	5
1.2.4	Nearby galaxies at low radio frequencies	8
1.3	Radio telescopes used in this thesis	8
1.3.1	Westerbork Synthesis Radio Telescope	10
1.3.2	The International LOFAR Telescope	13
1.3.3	Challenges of observing at low radio frequencies	16
1.4	Outline of this thesis	17
2	The curious case of NGC 4258: a new low-frequency radio-continuum perspective	21
2.1	Introduction	22
2.2	LOFAR Observation and data reduction	24
2.2.1	Observational setup	24
2.2.2	Pre-processing	25
2.2.3	Calibration	26
2.2.4	Ionospheric RM correction	27
2.2.5	Self-calibration and imaging	28
2.2.6	Flux and astrometry uncertainties	28
2.3	Westerbork observations and data reduction	30
2.4	Results	32
2.4.1	Total intensity maps	32
2.4.2	Other nearby galaxies in the LOFAR field of view	34
2.4.3	Spectral properties of NGC 4258	34
2.4.4	Thermal fraction and non-thermal spectral index	37
2.4.5	Magnetic field strength	40
2.4.6	Relation with the H i disk	42
2.5	Search for polarized emission	42
2.5.1	Polarized emission at 1.4 GHz	42
2.5.2	Polarized emission at 141.8 MHz	44

2.5.3	Stacking polarized emission in the galactic disk	46
2.6	Where are the anomalous arms located?	48
2.7	Summary and conclusions	52
3	Multifrequency radio continuum observations of the Pinwheel galaxy (M 101)	55
3.1	Introduction	56
3.2	WSRT observations and data reduction	59
3.3	LOFAR observation and data reduction	60
3.4	Radio continuum morphology of M 101	64
3.5	The H _I disk and the high-velocity gas complex	65
3.6	Integrated flux densities and radio spectrum	69
3.7	Estimating the thermal contribution	71
3.8	Non-thermal spectral index	74
3.8.1	Radial scale length	78
3.9	Equipartition magnetic field strength	80
3.10	Summary and conclusions	83
4	Resolved low-frequency radio images of nearby dwarf galaxies	85
4.1	Introduction	86
4.2	LOFAR observations and data reduction	87
4.2.1	Observational setup and preprocessing	87
4.2.2	Calibration	89
4.2.3	Final imaging	93
4.3	Total intensity maps	95
4.3.1	NGC 1569	95
4.3.2	NGC 4214	99
4.3.3	NGC 2366	102
4.3.4	DDO 50	106
4.4	Estimating thermal fraction	107
4.5	Non-thermal spectral index maps	110
4.6	Equipartition magnetic field strength	110
4.7	Search for polarized emission	112
4.7.1	Polarized Galactic foreground	114
4.7.2	Polarized emission from a giant radio galaxy	114
4.8	Discussion	116
4.9	Summary and conclusions	119
5	cuFFS: A GPU-accelerated Rotation Measure Synthesis Code	121
5.1	Introduction	122
5.2	Background	123
5.2.1	RM synthesis: Theory	123
5.2.2	RM synthesis: In practice	125
5.2.3	RM synthesis: Computational costs	126
5.3	GPU implementation of RM Synthesis	128
5.3.1	FITS, HDF5, and HDFITS	131
5.3.2	Science verification and benchmarks	135

5.4	Conclusion and future outlook	139
6	Conclusions	141
6.1	Summary of key results	141
6.2	Avenues for future research	143
6.2.1	Broadband polarimetry as a probe of anomalous arms in NGC 4258	143
6.2.2	Mapping the halos of nearby dwarf galaxies	144
	Appendices	147
	A Calibrating LOFAR HBA Data	149
A.1	Need for direction-dependent calibration	150
A.2	LOFAR Facet Calibration	153
A.2.1	Direction-independent steps	153
A.2.2	Direction-dependent steps	158
	Samenvatting	165
	Acknowledgements	170
	Bibliography	175

Chapter 1

Prologue

1.1 Historical overview

Though magnetism has been known to mankind for more than two and a half millennia, the role of magnetism in the astrophysical context was recognised only in the twentieth century. In 1908, George Hale discovered magnetic fields in the Sun using Zeeman splitting thereby providing the first observational evidence for the existence of extraterrestrial magnetic fields (Hale 1908a,b). Following the discovery of radio waves from the Milky Way in 1933 (Jansky 1933), the subsequent survey of the sky by Grote Reber in 1938 (Reber 1940), and the discovery of the first discrete radio source towards Cyg A by Hey et al. (1946), Fermi (1949) came up with the idea that the entire galaxy could be filled with cosmic ray electrons and the observed radio waves could be linked to their acceleration in the large-scale galactic magnetic fields thus leading to the idea that the observed radiation is non-thermal.

The first conclusive evidence for the existence of interstellar magnetic field came with the discovery of linearly polarized starlight that arises due to the Davis-Greenstein mechanism¹ (Hiltner 1949; Davis & Greenstein 1951). Although it was widely believed that the radio waves coming from the galactic foreground are largely due to synchrotron emission, this was only confirmed in the 1960's with the detection of linearly polarized radio emission from the Galaxy (Westerhout et al. 1962; Wielebinski & Shakeshaft 1962). Faraday rotation measurements of the galactic foreground towards polarized extragalactic background point sources (Morris & Berge 1964; Berge & Seielstad 1967) and of pulsars within the Galaxy (Manchester 1972, 1974) led to the first measurement of ordered magnetic field ($\sim 2 - 3 \mu\text{G}$) in the Galaxy. The first detection of linearly polarized synchrotron emission from an external spiral galaxy was made by Mathewson et al. (1972) towards the nearby spiral galaxy M 51.

Since the discovery of linear polarization towards M 51 in 1972², numerous surveys and detailed studies of individual galaxies have been carried out to understand the origin and evolution of magnetic fields in spiral galaxies. A large number of nearby spiral galaxies have been mapped in radio polarization using a combined observational effort with single dish telescopes like Effelsberg and Parkes and interferometers like the Westerbork Synthesis Radio Telescope (WSRT) and the Very Large Array (VLA).

1.2 Radio continuum emission from galaxies

Broadband emission from galaxies at radio wavelengths is dominated by radiation due to two physical processes: non-thermal synchrotron emission from relativistic electrons accelerating in galactic magnetic fields, and thermal free-free emission from sites of star formation (Condon 1992). While the physical mechanisms that

¹Davies-Greenstein mechanism is a physical process by which starlight can be polarized when they are absorbed and scattered by interstellar dust grains which can align themselves with the local magnetic field.

²Wielebinski (2012) has an excellent compilation of the history of radio polarimetric detections of various astrophysical sources.

give rise to the thermal and the non-thermal radio emission are different, they are both related to the underlying population of massive stars in normal galaxies.

1.2.1 Thermal radio emission

In this picture, ionising ultra-violet (UV) photons from massive stars produce a sea of free electrons which get accelerated in the proton electric field resulting in thermal free-free emission. The velocities of the free electrons follow the Maxwellian distribution governed by the temperature of the electron gas. Taking the optical depth of the electron gas into account, the intensity of a source emitting thermal (or free-free) emission follows the blackbody spectrum (B_ν) at electron gas temperature T_e as

$$I(\nu) = B_\nu(T_e) \cdot (1 - e^{-\tau_\nu}) \quad (1.1)$$

where τ_ν is the optical depth at frequency ν . In the radio part of the electromagnetic spectrum, the Rayleigh-Jeans approximation holds and hence the above relation simplifies to

$$I_\nu \approx \frac{2h\nu^2}{c^2} \cdot kT_e \cdot (1 - e^{-\tau_\nu}) \quad (1.2)$$

where k , h , and c are the Boltzmann constant, the Planck constant, and the speed of light respectively. Optical depth (τ_ν) is related to emission measure (EM) and the electron temperature (T_e) through the relation

$$\tau_\nu = \frac{8.2 \times 10^{-2} \nu^{2.1} EM}{T_e^{1.35}} \quad (1.3)$$

where emission measure is related to the number density of electrons in the ionised medium along the path length l as

$$EM = \int_0^l n_e^2 ds. \quad (1.4)$$

Note, in equation 1.2, that the spectral index of the thermal emission depends on whether the source is optically thick/thin at a given frequency. In the case of an optically thick source ($\tau_\nu \gg 1$), the emission has a positive spectral index with $I_\nu \propto \nu^{-2}$. In the case of an optically thin source, the thermal emission has an almost flat spectral index with $I_\nu \propto \nu^{0.1}$.

In addition to producing thermal emission, a cloud of electron gas can also absorb radio emission. Depending on where the absorbing medium is located along the line of sight (colocated with the source or in the foreground), the observed radio flux (I) can be different from the total intrinsic radio flux (I_0) as (Longair 2010)

$$I(\nu) = \begin{cases} I_0 \left(\frac{\nu}{\nu_0} \right)^{-\alpha} e^{-\tau(\nu)} & ; \text{foreground absorbing screen} \\ I_0 \left(\frac{\nu}{\nu_0} \right)^{-2} (1 - e^{-\tau(\nu)}) & ; \text{intrinsic to the source.} \end{cases} \quad (1.5)$$

where α is the observed spectral index.

1.2.2 Non-thermal radio emission

On the other hand, the massive stars that produce the thermal emission discussed above explode as supernovae resulting in shock waves in the interstellar medium. The shock waves produced collectively by supernova explosions act as the site of (re)acceleration for cosmic ray electrons, which in turn accelerate in the galactic magnetic field lines producing linearly polarized synchrotron emission³ (Kiepenheuer 1950; Shklovskii 1960). The spectrum $I(\nu)$ of the emitted synchrotron emission depends on the energy spectrum of the ensemble of cosmic ray electrons in the interstellar medium as

$$I(\nu) = \frac{1}{4\pi} \int_0^{s_0} \int_0^{\infty} P(\nu) N(E) dE ds \quad (1.6)$$

where $P(\nu)$ is the power radiated by the cosmic ray electrons and s is the path length between the telescope and the synchrotron emitting region. Assuming that the energy spectrum of the ensemble of cosmic ray electrons is the same as the cosmic ray electrons measured in Earth's atmosphere ($N(E)dE = A \cdot E^{-2.4}dE$), the observed intensity of the synchrotron radiation is

$$\frac{I(\nu)}{\text{erg s}^{-1}\text{cm}^{-2}\text{Hz}^{-1}\text{sr}^{-1}} = 2.4 \times 10^{-10} \left(\frac{s_0}{\text{cm}} \right) \left(\frac{A}{\text{erg}^{1.4}\text{cm}^{-3}} \right) \left(\frac{B_{\perp}}{\text{G}} \right)^{1.7} \left(\frac{\nu}{\text{Hz}} \right)^{-0.7} \quad (1.7)$$

where A is a constant near Earth and is equal to 8.2×10^{-17} erg^{1.4}cm⁻³. It is worth noting in the above equation that, for a given source and observing frequency, the observed synchrotron intensity is directly proportional to the strength of the magnetic field (B_{\perp}) projected in the plane perpendicular to the line of sight.

If α_{nth} is the spectral index of the non-thermal emission, the maximum fractional polarization (p_{\max}) of the synchrotron emission is given as

$$p_{\max} = \frac{\alpha_{\text{nth}} + 1}{\alpha_{\text{nth}} + 5/3}. \quad (1.8)$$

For a typical spectral index of $\alpha_{\text{nth}} = 0.7$, the maximum fractional polarization, $p_{\max} \approx 72\%$. Note, however, that the observed polarization fraction from normal spiral galaxies is always less than p_{\max} due to a number of astrophysical and instrumental effects that cause depolarization. Details of the various depolarization mechanisms are beyond the scope of this thesis. For a detailed discussion on this topic, I refer the reader to Gardner & Whiteoak (1966) and references therein.

Another relation that is relevant for the discussion on synchrotron emission is the lifetime of the cosmic ray electron that gives rise to the synchrotron emission.

³Relativistic electrons in the interstellar medium can also lose energy through other physical mechanisms like the inverse Compton loss and ionization loss. However, these mechanisms are not dominant in the radio domain. For a detailed discussion on these loss mechanisms, see for example Longair (2010).

As the relativistic electron accelerates along the interstellar magnetic field lines, it loses energy and the half-lifetime ($t_{1/2}$) is given as

$$\frac{t_{1/2}}{\text{year}} = 8.35 \times 10^9 \cdot \left(\frac{B}{\mu\text{G}} \right)^{-2} \cdot \left(\frac{E_0}{\text{GeV}} \right)^{-1}. \quad (1.9)$$

Notice in the above equation that the half-lifetime of the cosmic ray electrons is inversely proportional to the interstellar magnetic field strength (B) and the initial energy of the electron (E_0). For a constant magnetic field strength, the above equation implies that lower energy cosmic ray electrons which contribute to synchrotron emission at low radio frequencies have a longer half-lifetime than their higher energy counterparts and hence can travel farther from their sites of (re)acceleration.

1.2.3 Synchrotron emission, Faraday rotation and magnetic fields

As discussed earlier, synchrotron radiation emitted by relativistic electrons accelerating in magnetic field lines is linearly polarized, and the observed (electric) polarization angle is perpendicular to the orientation of the magnetic field projected in the sky plane. The degree of linear polarization (p) – or fractional polarization – and the polarization angle of the electric field vector (ψ) is related to the Stokes parameters produced by modern radio interferometers⁴ as

$$p = \sqrt{\frac{Q^2 + U^2}{I^2}} \quad (1.10)$$

$$\psi = \frac{1}{2} \tan^{-1} \frac{U}{Q} \quad (1.11)$$

where I is a Stokes parameter that contains information about the total intensity of the electromagnetic wave. The state of linear polarization of the electromagnetic wave is contained in the Stokes parameters Q and U . Thus, by measuring three Stokes parameters (I , Q , and U) across a galaxy, one can estimate the orientation of the large-scale magnetic field lines in that galaxy. In practice, this is not so straightforward due to the effect of Faraday rotation.

In almost all astrophysical scenarios, the line of sight between the synchrotron emitting region and the telescope has at least one magneto-ionic medium (for example the ionosphere and/or the Galactic foreground). As the electromagnetic wave travels through the magneto-ionic medium, due to birefringence, the polarization angle of the electromagnetic vector rotates as a function of frequency. This phenomenon is called Faraday rotation, and the amount of rotation is wavelength-dependent as

$$\psi - \psi_0 = \Delta\psi = \phi \cdot \lambda^2 \quad (1.12)$$

⁴See Hamaker et al. (1996) for a detailed explanation on Stokes parameters in radio polarimetry.

where ψ_0 is the intrinsic polarization angle and ψ is the observed angle of polarization measured at wavelength λ . The parameter ϕ is called Faraday depth and it is defined as

$$\frac{\phi}{\text{rad/m}^2} = 0.81 \int_{\text{source}}^{\text{observer}} \left(\frac{n_e}{\text{cm}^{-3}} \right) \left(\frac{B_{||}}{\mu\text{G}} \right) \left(\frac{dl}{\text{pc}} \right) \quad (1.13)$$

where n_e is the number density of thermal electrons along the line of sight, $B_{||}$ is the component of magnetic field parallel to the line of sight, and l is the pathlength between the telescope and the radio source. Notice from equation 1.12 that the difference between the intrinsic and observed polarization angle depends strongly on wavelength. This wavelength dependent nature of $\Delta\psi$ implies that telescopes with coarse frequency resolution will tend to average polarized signal with variable polarization angle (within the broad channel) resulting in bandwidth depolarization. The only way to avoid bandwidth polarization is to observe with finer frequency resolution and to compensate for the consequently lower signal-to-noise in each channel, is to employ a technique called rotation measure synthesis ([Brentjens & de Bruyn 2005](#)). A detailed description of the Faraday rotation measure synthesis technique and its relevance to this thesis are described in subsequent chapters.

Based on the discussion presented above, it is easy to note that

- the Faraday depth (ϕ) is related to the component of the magnetic field parallel to the line of sight,
- the intrinsic polarization angle (ψ_0) is related to the orientation of the magnetic field line projected on the sky plane (B_{\perp}), and
- the total intensity radio continuum emission (after correcting for the thermal contribution) is a direct measure of the total magnetic field strength.

Thus, by measuring these quantities, one can attempt to estimate the strength and the morphology of magnetic field lines in any astrophysical source. A number of studies carried out in the last four decades have exploited this to produce a detailed map of the distribution of magnetic field lines in numerous nearby galaxies. Typical examples of the distribution of magnetic field lines in the disk and in the halos of normal galaxies are shown in Figures 1.1 and 1.2. The orientation of the polarization vectors – which trace the magnetic field lines – show that the magnetic field lines in the face-on case have a morphology that is akin to the morphology of material spiral arms. In the edge-on case, the field lines tend to take an x-shaped morphology.

While significant progress has been made in the last four decades in understanding magnetic fields in spiral galaxies, numerous questions still remain to be resolved. One such question that still remains to be answered is the extent of magnetic field lines in galaxies. While the resolved radio continuum observations of nearby galaxies in the literature have been used to construct various phenomenological models of the three dimensional structure of the

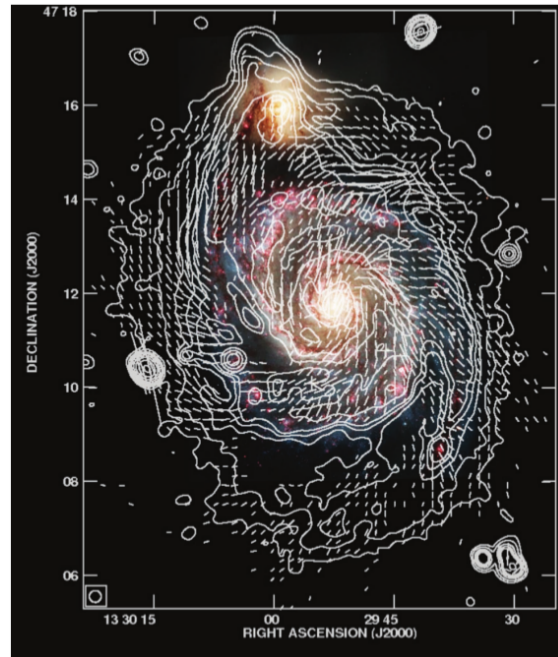


Figure 1.1 – Distribution of magnetic field lines and total intensity radio emission (contours) in the nearby spiral galaxy M 51 at 3 cm overlaid on an optical image. Image credit: [Fletcher et al. \(2011\)](#).

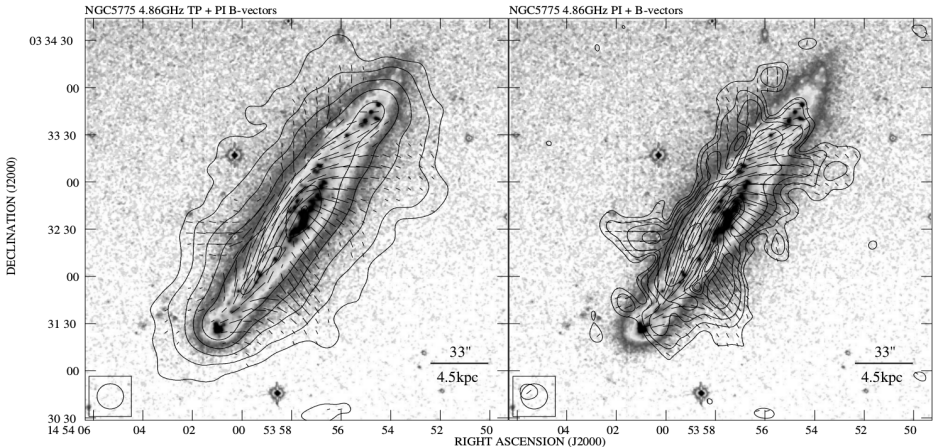


Figure 1.2 – Magnetic field vectors overlaid on a H α map of the nearby, highly-inclined galaxy NGC 5775. Contours on the left represent total intensity emission at ~ 5 GHz while the ones on the right represent polarized emission at the same frequency. Image credit: [Tüllmann et al. \(2000\)](#).

magnetic field lines in spiral galaxies (see for example [Braun et al. 2010](#); [Ferrière & Terral 2014](#); [Nixon et al. 2018](#)), existing radio images are insufficient to figure out to what distance (in both the radial and vertical directions) these field lines exist and how strong they are at such large galactic radii.

1.2.4 Nearby galaxies at low radio frequencies

Since synchrotron emission at low radio frequencies originates from old, low-energy cosmic ray electrons that have propagated far from their sites of origin/reacceleration due to their longer half-lifetimes, sensitive low radio frequency observations of galaxies are an excellent probe for studying weak magnetic fields located at large galactic radii. Figures 1.3 and 1.4 show a 151 MHz total intensity image of M 51 from the Low Frequency Array (LOFAR) and an image of NGC 253 obtained using the Murchison Widefield Array (MWA). In both galaxies, one seen nearly face-on and the other seen edge-on, the low frequency radio images show extended diffuse emission originating at large galactic radii and height.

In addition to tracing extended diffuse emission, low frequency radio emission is dominated by synchrotron emission and the low contamination by thermal emission makes low frequency radio images of nearby galaxies an excellent tracer to study galactic magnetic fields.

However, past efforts to map the resolved low frequency radio continuum emission from a large sample of nearby galaxies have largely been limited by low sensitivity and low angular resolution achieved by telescopes traditionally operating in this frequency regime. For example, [Israel & Mahoney \(1990\)](#) observed a sample of nearby galaxies at 57.5 MHz using the Clarke Lake Telescope but they hardly resolved any of the observed 133 galaxies. This picture is further complicated by technical challenges associated with carrying out observations at low radio frequencies (see section 1.3.3). To date, M 51 ([Mulcahy et al. 2014](#)), IC 10 ([Heesen et al. 2018](#)) and NGC 253 ([Kapińska et al. 2017](#)) are the only nearby galaxies for which resolved radio continuum maps exist in the literature at frequencies below about 300 MHz.

This is about to change with the advent of new low frequency radio telescopes like LOFAR that provide improved sensitivity and sub-arcsecond angular resolution. The on-going LOFAR Two-metre Sky Survey (LoTSS; [Shimwell et al. 2017](#)) aims to image the entire northern sky at 120 – 168 MHz with a sensitivity of 0.1 mJy/beam at about 6'' angular resolution. To prepare for large datasets from low frequency radio surveys like LoTSS, in this thesis, I have studied a sample of nearby galaxies including normal spiral galaxies to (post-) starburst dwarf galaxies searching for and characterising diffuse radio continuum emission from the outer regions of galaxies.

1.3 Radio telescopes used in this thesis

Chapters 3, 2, 4 presented in this thesis rely predominantly on radio continuum observations of nearby galaxies at 150 MHz and 1.4 GHz which were carried out using the LOw Frequency Array (LOFAR) and the Westerbork Synthesis Radio

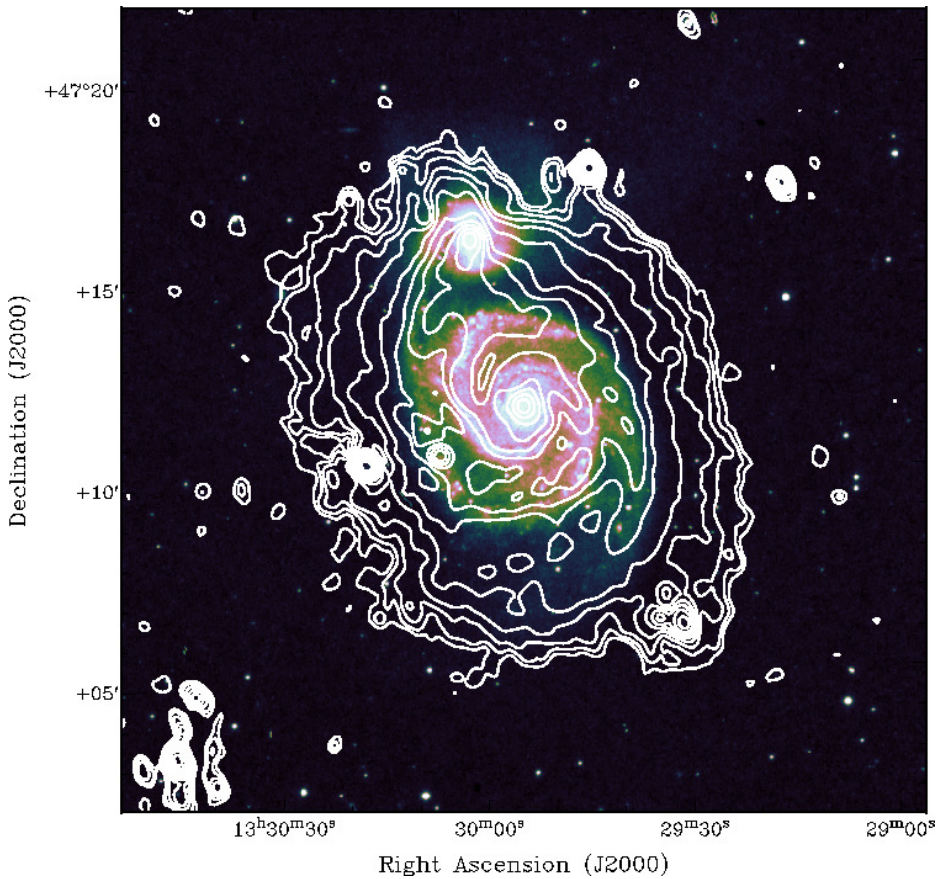


Figure 1.3 – LOFAR 151 MHz total intensity contours overlaid on optical DSS image of M 51 ([Mulcahy et al. 2014](#)).

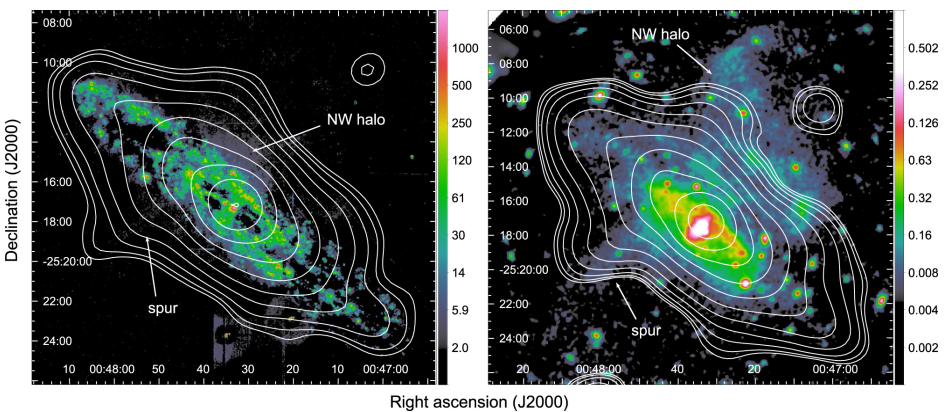


Figure 1.4 – MWA radio continuum contours overlaid on H α (left) and X-ray (right) images of NGC 253 ([Kapińska et al. 2017](#)).

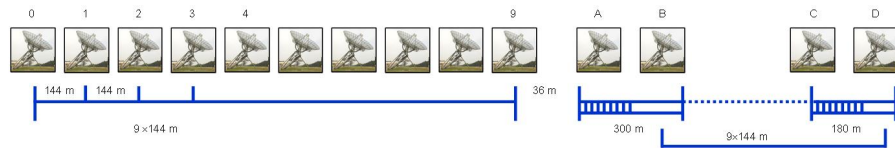


Figure 1.5 – Array configuration of the Westerbork Synthesis Radio Telescopes. Image credit: ASTRON.

Telescope (WSRT) respectively. In the following sub-sections, I present a brief overview of these two radio telescopes.

1.3.1 Westerbork Synthesis Radio Telescope

The Westerbork Synthesis Radio Telescope (WSRT) is a radio interferometric array located in the north-east of The Netherlands. Completed in 1970⁵ (with further hardware upgrades in the 80s and 90s), the current WSRT consists of 14 parabolic dishes arranged along the east-west direction. The layout of the telescope array is shown in Figure 1.5. Ten of the 14 telescopes (labelled 0-9 in Figure 1.5) are on a fixed pad with a separation of 144 m between adjacent antennas. The remaining four telescopes (labelled A-D) are on rail tracks and can be moved to achieve different baseline configurations depending on the science needs. The WSRT offers a minimum unprojected baseline length of 36m between antennas ‘9’ and ‘A’ and a maximum baseline length of 2.7 km between antennas ‘0’ and ‘D’.

As mentioned above, the exact configuration of the array depends on the science objective of the observing project and the amount of observing time available. The WSRT data presented in chapters 3 and 2 were observed with the telescope array in the “maxi-short” configuration which is well suited for imaging extended sources. In this configuration, the moveable antennas are arranged such that the 9A, 9B, 9C, and 9D baselines have a baseline length of 36, 90, 1332, and 1404 m respectively so that the four shortest spacings (36m, 54m, 72m, and 90m) are covered in one 12 hour observation, thus providing good sensitivity to extended structures.

Each parabolic dish in the array is 25m in diameter and has an equatorial mount. The equatorial mount of the telescopes implies that the parabolic dishes rotate with the sky as they track astrophysical sources over a long period of time and hence the calibration procedure does not have to account for a parallactic angle correction⁶. An aerial view of the array and a close-up of a single WSRT parabolic dish on its equatorial mount are shown in Figures 1.6 and 1.7.

When the data used in this thesis were obtained, WSRT was equipped with both cooled and uncooled receivers sensitive to a wide range of wavelengths

⁵For more information on the original Westerbork array, see Baars & Hooghoudt (1974), Casse & Muller (1974), and Högbom & Brouw (1974)

⁶Radio telescopes like the Very Large Array in New Mexico have alt-az mounts which cause the parabolic dishes to rotate with respect to the sky.



Figure 1.6 – An aerial view of the Westerbork Synthesis Radio Telescope. Image credit: ASTRON



Figure 1.7 – A 25m WSRT parabolic dish on an equatorial mount. Image credit: ASTRON.

from 4 m to 3.6 cm. The cooled Multi-Frequency Front Ends (MFFE) could observe at 3.6, 6, 13, 18, and 21 cm while the uncooled receivers could observe at 92 cm, 46 cm and 2 m. However, at the time of writing, the above-mentioned receivers are no longer available on WSRT due to the APERTIF telescope upgrade. APERTIF, or APERture Tile In Focus, is an on-going upgrade where the “single pixel” radio receivers on WSRT are replaced with L-band phased array feeds. This upgrade increases the field of view of the telescope significantly, making WSRT an efficient survey machine. For more information on the ongoing APERTIF upgrade, see for example Oosterloo et al. (2009) or the APERTIF website⁷.

1.3.2 The International LOFAR Telescope

A brief overview of the LOFAR telescope and its interferometric observing mode relevant to the chapters in this thesis are presented here. For a detailed overview of the full functionality of the telescope and its various observing modes, the reader is referred to van Haarlem et al. (2013)⁸.

LOFAR, the LOw-Frequency ARray, is a radio interferometric array that operates in the 10 - 240 MHz frequency range. Operated by ASTRON⁹ in the Netherlands, the 51 individual telescopes¹⁰ – or stations – that constitute the telescope array are distributed across six countries in Europe. Of the 51 LOFAR stations, 24 stations are co-located within a 2 km radius forming the LOFAR core stations (CS) providing excellent *uv* coverage on short baselines. The remaining 14 stations in the Netherlands are distributed within a radius of 90 km from the LOFAR core and are usually referred to as the remote stations (RS). The remaining 12 international stations are located in Germany, Sweden, France, Poland, and the United Kingdom. The geographical locations of the individual LOFAR stations are shown in figure 1.8.

The basic function of a LOFAR station is akin to the conventional radio telescope wherein both setups provide the collecting area to measure the incoming electromagnetic wave along with necessary pointing and tracking mechanisms. However, unlike most traditional radio telescopes, LOFAR stations have no moving components. Instead, LOFAR uses a fixed set of dipoles per station whose signals are combined electronically to mimic the pointing and tracking of a traditional steerable dish.

Each LOFAR station hosts two types of antennas: the Low Band Antenna (LBA) which operates from 10 - 90 MHz and the High Band Antenna (HBA) which operates in the 110 - 240 MHz frequency range. Both the LBA and the HBA use an inverted vee antenna to detect the incoming electromagnetic radiation (as shown in Figure 1.10). The normalised bandpass of the LOFAR dipoles at different frequency bands is shown in figure 1.9.

While all LOFAR stations use identical dipoles and station electronics, the exact layout of the LOFAR stations varies depending on the geographical

⁷www.apertif.nl

⁸Up to date information about the telescope is available online at www.astron.nl/

⁹www.astron.nl

¹⁰as of January 2018

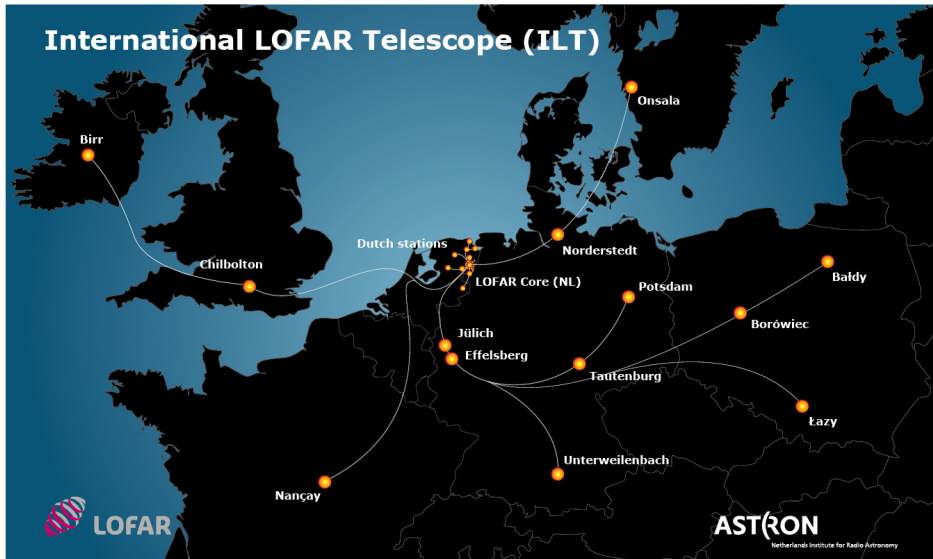


Figure 1.8 – Geographical layout of the International LOFAR Telescope array (as of January 2018). Note that an additional planned station in Latvia is not shown on this map. Image credit: ASTRON.

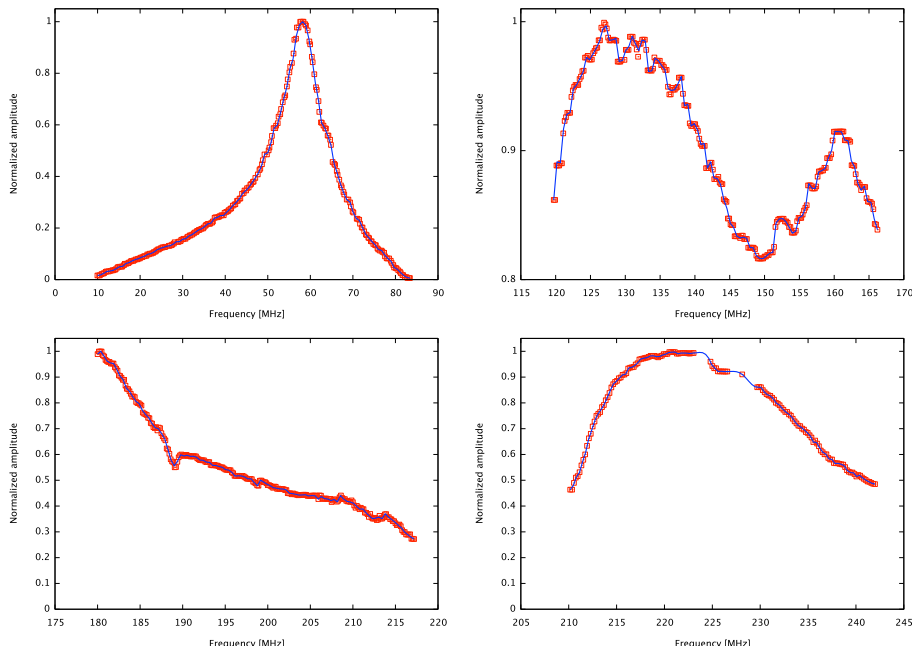


Figure 1.9 – Bandpass response of the LOFAR dipoles for different frequency bands. Image credit: [van Haarlem et al. \(2013\)](#).



Figure 1.10 – Dipoles in the Low (left) and the High (right) Band Antenna. Image credits: Nelles et al. (2015) and I-LOFAR.

location. Figure 1.11 shows the different station layout for core, remote and international stations. The primary difference between the core, remote, and the international stations is the number of dipoles in the LBA and the HBA station (and hence a different station size). The need and the scientific justification for different station sizes are beyond the scope of this thesis, and we refer the reader to van Haarlem et al. (2013). The point of interest to this thesis is that different station sizes will cause each station to have different fields of view. In order to achieve the same field of view between all stations, all observations presented in this thesis have been carried out under the HBA_Dual_Inner configuration¹¹. In HBA_Dual_Inner configuration, the effective station size of the remote stations is matched to that of the core stations by deactivating the outermost HBA tiles resulting in a similar field of view between the core and the remote stations.

Since LOFAR is a telescope that relies on electronic signal processing for beamforming, pointing and tracking, each LOFAR station has local computing resources, in addition to the LBA dipoles and HBA tiles, required for station-level preprocessing and digital beamforming. The station electronics are housed inside an RF-shielded cabinet to prevent electronic signal interference. The cabinet that houses the station electronics along with the LBA and the HBA dipoles is shown in figure 1.12.

The analogue signals from the LBA dipoles or from the HBA tiles (after analogue beamforming) are brought to the station electronics cabinet using coaxial cables for digitisation and preprocessing. In the electronics cabinet, the analogue signals are first digitised using a 12-bit analogue-to-digital converter and then split into individual subbands using a poly-phase filter. All subsequent processing is carried out on individual subbands independent of each other. In addition to preprocessing and digital beamforming, a real-time gain correction is also applied to the data to correct for variations caused by environmental changes (Wijnholds & van der Veen 2009, 2010). Note that the GPS-corrected

¹¹For a full list of allowed observing configurations, see <https://www.astron.nl/radio-observatory/astronomers/users/technical-information/lofar-stations/lofar-stations-description->

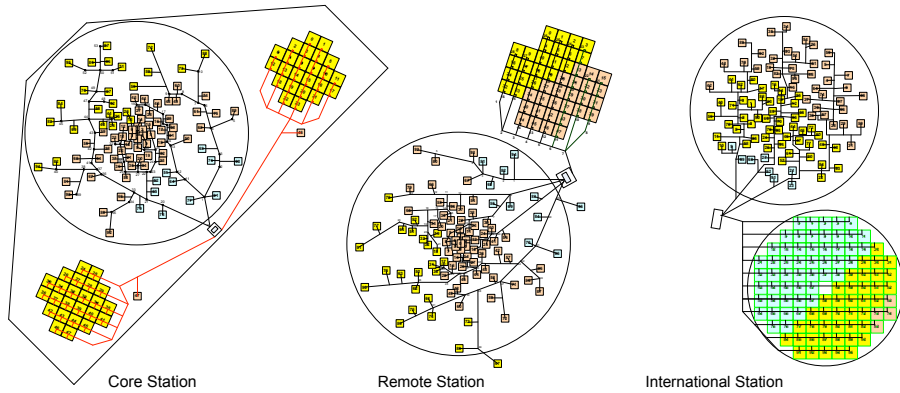


Figure 1.11 – Layout of dipoles in the core, remote and international stations. Image credit: van Haarlem et al. (2013).

Rubidium clocks connected to the remote and the international stations can drift up to 20 ns per 20 minutes and this clock drift is not corrected at the station level. Correction for the clock drifts is applied during calibration, and this will be addressed in detail in section A.2.1.

After digital beamforming at each station, the resulting data stream is brought to the Central Processing facility at the University of Groningen in the Netherlands over a dedicated optical fibre network for correlation and long-term archiving.

1.3.3 Challenges of observing at low radio frequencies

Interferometric observations at low radio frequencies ($\nu < 300$ MHz) can be challenging due to a number of physical effects that increase the background rms noise and create artefacts in the image. Some common physical effects include

- significant contribution to the system temperature by the bright Galactic foreground,
- poor knowledge of the time-dependent antenna beam response,
- imaging issues due to wide field of view,
- increased RFI, and
- ionospheric propagation effects.

The combined effect of all the above-mentioned physical effects implies that the rms noise in the image can rise faster than the flux density of steep spectrum sources. Different techniques have been developed in the literature to remove or suppress some of the issues mentioned above are described later in this thesis where relevant.

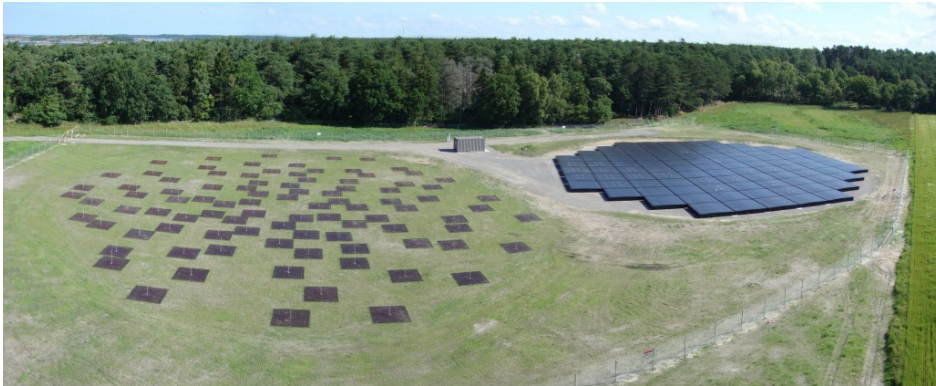


Figure 1.12 – Layout of the Swedish LOFAR station in Onsala. The electronic station cabinet can be seen at the top of the image in-between the LBA dipoles (left) and the HBA tiles (right). Image credit: LOFAR Sweden.

An additional problem while observing at low radio frequencies is caused by the large field of view. While the large field of view can be an advantage for carrying out surveys of the entire sky, the presence of strong radio sources (some with flux densities ranging up to a few thousand Jy) in the main or distant sidelobes of the primary beam can significantly affect the quality of the final images. Removing the effects of such bright off-axis sources from the data involves advanced calibration and imaging procedures like “peeling” ([Noordam 2004](#)) and “demixed peeling” ([van der Tol et al. 2007](#)) which are computationally expensive. An example of such a scenario was encountered in one of our LOFAR observation and is discussed in chapter [3](#).

To be able to deal with several of these above-mentioned technical challenges, new calibration and imaging algorithms have been developed within the LOFAR community. For example, direction-dependent calibration effects caused by the ionosphere and poor knowledge of the antenna beam response are in part corrected using new Factor calibration scheme ([van Weeren et al. 2016](#)). New imagers like AWImager ([Tasse et al. 2013](#)) and WSClean ([Offringa et al. 2014](#)) have also been developed to make use of Graphical Processing Units (GPUs) to speed up computationally expensive parts of W-projection ([Cornwell et al. 2008](#)) that is needed to account for imaging issues related to wide field of view and non-coplanar baselines. There is also an on-going effort at ASTRON to better characterise the antenna beam response using drone measurements.

1.4 Outline of this thesis

As discussed above, resolved low-frequency radio continuum observations of nearby galaxies are excellent tracers of magnetic fields in the outer regions of these galaxies. In this thesis, we have studied a sample of nearby spiral and (post-)starburst dwarf galaxies at low radio frequencies using the LOFAR and the WSRT radio telescopes. Some of the images presented in this thesis are the

most sensitive radio continuum images of those galaxies. This thesis is organised as follows:

In [Chapter 2](#), we present new LOFAR and WSRT observations of the nearby spiral galaxy NGC 4258 that is known to host anomalous spiral arms. Using the new sensitive LOFAR and WSRT data, we study for the first time the radio continuum emitting star-forming disk in NGC 4258. These new sensitive radio observations reveal, for the first time, total intensity radio continuum emission from the star-forming disk of NGC 4258. In addition to studying the radio emission from the star-forming disk, using radio polarimetry data at 1.4 GHz, we provide new insight into the orientation of the anomalous arms in NGC 4258.

In [Chapter 3](#), we present multi-frequency radio continuum observations of the nearby spiral galaxy M 101 obtained using the LOFAR and the WSRT radio telescopes. Using the sensitive, high resolution radio images, we show that the integrated spectra of M 101 shows evidence for spectral flattening towards low radio frequencies. The radio images presented in this chapter are the most sensitive radio maps of this galaxy.

Inspired by the results presented in Chapters [2](#) and [3](#) in which we detect extended radio emission from galaxies compared to archival observations at wavelengths shorter than 20 cm, we planned and carried out pilot observations with LOFAR to detect and study weak, diffuse radio emission from the halos of nearby (post-) starburst dwarf galaxies. The results of this pilot study are presented in [Chapter 4](#).

The LOFAR data presented in Chapters [2](#), [3](#), and [4](#) were calibrated and imaged using a common data reduction procedure. A detailed overview of the Facet calibration scheme used to calibrate and image LOFAR data is presented in [Appendix A](#). Only those details that are specific to the individual observations are presented in each chapter.

Over the last four years, while analysing multiple LOFAR HBA datasets, it became apparent to us that a significant fraction of my time will be spent on number-crunching to image and carry out post-processing on large datasets. Furthermore, thinking beyond this thesis, it is becoming obvious now that almost all current and upcoming radio telescope facilities will generate data in the tera- and petabyte regimes. Thus, in addition to extracting scientific insights from the radio data, radio astronomers will now also have to think about computational resources that need to be put in place to analyse future radio data. A number of image-processing algorithms used in radio astronomy like moments analysis can easily be parallelised. As a first step in combating large datasets, we developed a GPU-accelerated software package to perform a commonly used radio polarimetry technique called Faraday Rotation Measure Synthesis. The software package is presented in [chapter 5](#). While developing the software package, we realised that efficient processing could sometimes be achieved simply by changing the way the input data is structured. In addition to the GPU-accelerated code, chapter [5](#) also presents further discussion on the need for a better astronomical data format than the current FITS standard for storing multi-dimensional data sets like spectral line and Faraday depth cubes.

Finally, in **Chapter 6**, we summarise the key results from this thesis and discuss future prospects.

Chapter 2

The curious case of NGC 4258: a new low-frequency radio-continuum perspective

Sridhar, S. S., Heald, G., et al., To be submitted to
Astronomy & Astrophysics

2.1 Introduction

NGC 4258 is a nearby ($D = 7.6$ Mpc; [Humphreys et al. 2013](#)) spiral galaxy that is well known for its anomalous arms. Figure 2.1 shows a multicolour (X-rays, optical, and radio) image of NGC 4258 revealing X-rays and radio emission from the anomalous arms, and optical emission from the star-forming disk. The anomalous arms were first detected in the $\text{H}\alpha$ images of [Courtes & Cruellier \(1961\)](#) who found that apart from the previously known optical spiral arms, the galaxy also exhibits two additional arms. Further $\text{H}\alpha$ observations revealed that the anomalous arms have similar rotational velocity as the optical spiral arms apart from large deviations from circular motion in the inner parts of the galaxy ([Burbidge et al. 1963](#); [Chincarini & Walker 1967](#); [van der Kruit 1974](#)).

The first radio continuum image of NGC 4258 was produced by [van der Kruit et al. \(1972\)](#) using the Westerbork Synthesis Radio Telescope (WSRT). They found radio continuum counterparts to the anomalous arms detected in $\text{H}\alpha$. While the radio continuum emission from the anomalous arms appears smooth and continuous, the normal spiral arms appear mottled due to dominant radio emission from the HII regions. Despite this difference, [van der Kruit et al. \(1972\)](#) pointed out two similarities between the normal and the anomalous arms: (i) the arms are wound along the same direction, and (ii) both sets of arms appear to end at a similar distance from the nucleus. A high resolution radio continuum observation with the Very Large Array (VLA) showed that the anomalous arms bifurcate into smaller arms in the outer regions of the galaxy ($r \geq 5$ kpc) and the western arm brightens considerably just before bifurcating ([van Albada & van der Hulst 1982](#)). Furthermore, spectral index maps from combining the WSRT and the VLA data showed that the radio emission in the anomalous arms is non-thermal and that the leading edges are the youngest ([de Bruyn 1977](#); [Hummel et al. 1989](#)).

The first neutral hydrogen (H I) spectral line observations of NGC 4258 were carried out by [van Albada & Shane \(1975\)](#). They reported that although the inner disk of the galaxy is kinematically disturbed, the outer regions of the H I disk are reminiscent of normal spiral galaxies. Noticing that the radio continuum emission from the anomalous arms ended abruptly at the edge of the H I disk, [de Bruyn \(1977\)](#) suggested that the anomalous arms are embedded in the galactic disk.

Since the discovery of the anomalous arms, numerous models have been proposed to explain the three-dimensional structure of the galaxy ([van der Kruit et al. 1972](#); [Icke 1979](#); [van Albada 1978](#); [Sofue 1980](#); [Sanders 1982](#)). All the proposed anomalous arm models fall into two categories: *in-disk* models and *out-of-disk* models. Both models are based on the assumption that the anomalous arms are produced by the interaction of matter ejected from the nucleus with either the gas in the disk (in-disk model) or with coronal gas (out-of-disk model; for example see [Sofue 1980](#); [Sanders 1982](#)). For a detailed summary of all the models and how they fare against the observational evidence, we refer to reader to [van Albada & van der Hulst \(1982\)](#); [Wilson et al. \(2001\)](#). For the sake of completeness, we provide a brief overview of the two different scenarios.



Figure 2.1 – A multicolour image of NGC 4258. The emission from the anomalous arms aligned east-west is visible in X-rays (blue) and in radio continuum (purple). Emission from the star-forming disk is composed of optical (yellow) and infrared (red) data. Image credit: X-ray: NASA/CXC/Caltech/[Ogle et al. \(2014\)](#); Optical: NASA/STScI; IR: NASA/JPL-Caltech; Radio: NSF/NRAO/VLA

The *in-disk* model proposes that gas is ejected from the nucleus roughly parallel to the galactic disk. The initial ejecta carves out a tunnel through the galactic disk, and subsequent ejected material follows the path of least resistance through the disk while injecting mechanical energy into the surrounding interstellar medium. Optical line ratios and lack of blue stellar emission ([Courtes & Cruvellier 1961](#); [van der Kruit 1974](#)) indicate that the anomalous arms are excited by strong shock fronts. Shock fronts created when the expelled gas interacts with the galactic disk gives rise to the H α emission while compression of the galactic magnetic field lines enhances the synchrotron radio emission. Additionally, H I observations indicate that the arms extend roughly up to the edge of the H I disk. Furthermore, gaps can also be seen in the H I in regions where the anomalous arms coincide with the H I spiral arms. In the *out-of-disk* model ([Sanders 1982](#); [Sofue 1980](#)), the anomalous arms are produced by the interaction of a steady jet outflow with the galactic outflow. The arms are bent by pressure gradients and ram pressure from the rotating gaseous halo. In this scenario, the anomalous arms and the galactic disk do not interact and evolve as two separate entities.

Table 2.1 – Physical parameters of NGC 4258

Parameters	Value	Ref.
Morphology	SABbc	1
Distance	$7.60 \pm 0.17 \pm 0.15$ Mpc	2
D_{25}	$17'.1$	1
Inclination i	71°	1
PA of major axis	-30°	3
H I mass	$5.8 \times 10^9 M_\odot$	3
Star formation rate	$1.4 M_\odot \text{ yr}^{-1}$	4

Notes. The uncertainties quoted for the distance to NGC 4258 include systematic error (0.15) and a formal fitting error (0.17).

References. (1) [Tully & Fisher \(1988\)](#); (2) [Humphreys et al. \(2013\)](#); (3) [van Albada \(1980\)](#); (4) [Kennicutt et al. \(2008\)](#)

In light of all the observational evidence published in the literature, the *in-disk* model appears to be the most plausible candidate (see for example [Martin et al. 1989](#)). Though the *in-disk* model explains most observed features in the galaxy, the model does not give insight into the following questions: (i) What causes the anomalous arms to be curved against the direction of galactic rotation? (ii) Up to what distance from the nucleus do the arms lie within the disk? and (iii) What is the status of the large-scale magnetic field in the underlying star-forming disk? While a number of radio continuum observations of NGC 4258 carried out thus far have studied magnetic field structure in the anomalous arms ([Krause & Löhre 2004](#); [Krause et al. 2007](#)), not much is known about the continuum emission from the star-forming disk in the galaxy. In this paper, we present sensitive radio continuum observations with the WSRT and the LOw Frequency ARray (LOFAR; [van Haarlem et al. 2013](#)) with which we detect continuum emission from both the anomalous arms and the star-forming disk in NGC 4258.

This chapter is organised as follows. The observational setups and the data reduction procedures are outlined in sections 2.2 and 2.3. Results including the total intensity map, the spectral properties of NGC 4258, and its total magnetic field strength are discussed in section 2.4. In section 2.5, we show the results of RM synthesis and polarization stacking to probe the orientation of the magnetic field lines in the anomalous arms. We present our new model for the morphology of the anomalous arms in section 2.6. Finally, we summarise our results in section 2.7. Throughout this work, spectral index α is defined such that $S \propto \nu^{-\alpha}$.

2.2 LOFAR Observation and data reduction

2.2.1 Observational setup

The target galaxy NGC 4258 and the primary flux calibrator source 3C 295 were observed with the LOFAR High Band Antenna (HBA) on March 20, 2014, and

Table 2.2 – LOFAR HBA Observational parameters

Parameter	Value
Project ID	LC1_024
Target pointing	12h18m57.5s +47d18m14.0s
Calibrator pointing	14h11m20.5s +52d12m10.0s
Distance between calibrator and target	18°.6
Integration time	1 s
Total on-source time	15 min (3C 295) 8.75 hr (NGC 4258)
Useful bandwidth	71.48 MHz
Observation date	2014 March 20
Correlations	XX, XY, YX, YY
Frequency range	110.74 – 182.22 MHz
Subbands (SBs)	366 contiguous SBs
Bandwidth per SB	195.3125 kHz
Channels per SB	64
LOFAR Array Mode	HBA Dual Inner
Stations	60 total 23 core (each split in two) 14 remote

the relevant observational parameters are listed in Table 2.2. The observation was carried out in such a way that each 37-minute scan on NGC 4258 was followed by a one-minute scan on 3C 295 resulting in a total of 8.75 hours on the target galaxy and 16 minutes on 3C 295. Both sources were observed with identical frequency setup ranging from 110.74 MHz to 182.22 MHz providing a total bandwidth of 71.48 MHz. The entire frequency range was divided into 366 195.3125 kHz wide subbands (SBs) that were further sub-divided into 64 channels each. The full resolution visibility data were uploaded to the LOFAR Long Term Archive (LTA)¹ after correlation.

The observations were carried out with the HBA Dual Inner configuration (van Haarlem et al. 2013) where the core stations are split into two stations, and only those tiles in the inner $\sim 30.8\text{m}$ were used for remote stations. This setup was used to have a common station beam size for both core and remote stations. The resulting *uv*-coverage from this observation is shown in Figure 2.2.

2.2.2 Pre-processing

We averaged the raw visibility data to 8 channels per SB and a time resolution of 2s after removing radio frequency interference (RFI) at high time and frequency resolution. RFI flagging was done using `A0Flagger` (Offringa et al. 2010, 2012) while the averaging was carried out using the New Default Pre-Processing

¹<http://lofar.target.rug.nl/>

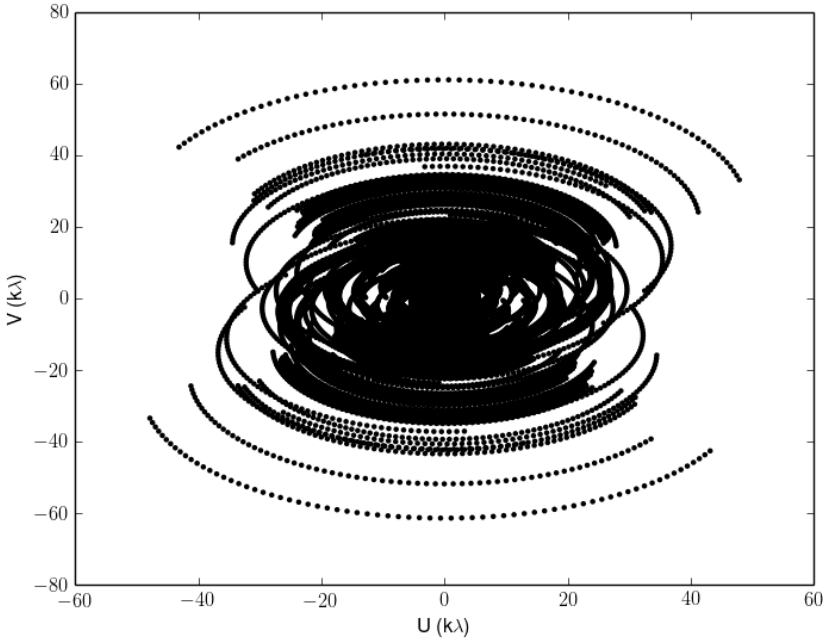


Figure 2.2 – Monochromatic LOFAR uv -coverage of a single sub band at 150 MHz. Note that the wide bandwidth of LOFAR fills the uv plane radially.

Pipeline (NDPPP; [Heald et al. 2010](#)). After averaging the visibilities, we removed the contribution from bright off-axis A-team sources (Cyg A, Cas A, Vir A, Tau A) using a procedure called A-team clipping. In this step, we predicted the contribution from these A-team sources to the MODEL_DATA column and flagged the observed visibilities with corresponding visibility amplitude in the MODEL_DATA column more than 5.0 Jy.

2.2.3 Calibration

Observations of 3C 295 were used to derive time-dependent antenna gains using the Black Board Selfcal (BBS) software ([Panedy et al. 2009](#)) assuming the flux scale defined in [Scaife & Heald \(2012\)](#). Inspecting the amplitude solutions, we noticed that subbands with frequency above 173 MHz were severely affected by RFI and hence were discarded. Using the derived gain solutions, we determined direction independent corrections for instrumental effects like amplitude corrections, a phase correction for clock delays at the station level, and an offset between XX and YY phases using the method described in [van Weeren et al. \(2016\)](#). The correction for clock delay is needed because the remote LOFAR stations have their own clocks. Since the remote station clocks are not perfectly synchronised with the clock attached with the core stations, large clock offsets of the order of 100ns can be introduced.

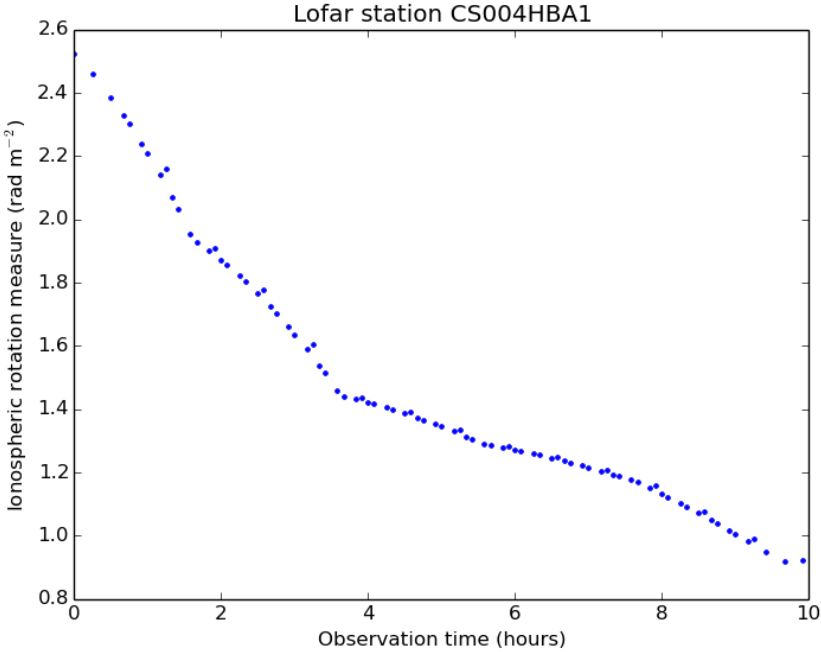


Figure 2.3 – Estimated ionospheric rotation measure as a function of observing time for the core station CS004HBA1

Corrections for amplitude, clock offset and phase offset were applied to each target measurement set using BBS and the corrected target visibilities were averaged further down to 2 channels per sub band and 6s time resolution. The averaged target visibilities were then merged into blocks of 10 subbands each with a bandwidth of 2 MHz.

Time-dependent phase calibration was performed against a skymodel extracted from the TIFR GMRT Sky Survey (TGSS) Alternate Data Release (ADR1)² image of the field (Intema et al. 2017) using the source finder pyBDSF³ (Mohan & Rafferty 2015). The source finder was used to extract all sources above a sensitivity threshold of 24 mJy/beam ($\approx 6\sigma$) from a $5^\circ \times 5^\circ$ field centered on NGC 4258. The extracted sky model contains 544 components (132 point and 412 Gaussian) and has a resolution of $25'' \times 25''$. Direction-independent phase solutions were solved for and applied to each sub band block separately with a 12s solution interval assuming no frequency dependence within the 2 MHz block.

2.2.4 Ionospheric RM correction

At the low radio frequencies at which LOFAR operates, ionospheric Faraday rotation measure corrections are important for polarimetric work since the

²tgssadr.strw.leidenuniv.nl

³previously pyBDSM; <https://github.com/lofar-astron/PyBDSF>

ionosphere interacts with the Earth’s magnetic field resulting in a time-dependent Faraday screen for any incoming electromagnetic radiation. The incremental effect of this ionospheric phase screen has to be corrected in the calibration step to avoid decoherence of the polarization signal. We used the tool `RMextract`⁴ to correct the ionospheric rotation measure. `RMextract` estimates the ionospheric Faraday rotation for each LOFAR station using measurements of ionospheric free electron content from the Total Electron Content (TEC) maps released by the Royal Observatory of Belgium (ROB)⁵ and the latest model of the Earth’s magnetic field (Finlay et al. 2010). The estimated ionospheric rotation measure as a function of observing time for a core LOFAR station is shown in Fig 2.3. A correction counteracting the estimated ionospheric RM was applied to each channel separately using the BBS software.

2.2.5 Self-calibration and imaging

Amplitude- and phase-calibrated data were averaged in time to 12 s and one channel per sub band after flagging for residual RFI using `A0Flagger`. Phase solutions applied to the target field were improved further with three iterations of self-calibration. With each self-calibration cycle, the uv range was progressively increased and imaged with lower `CLEAN` threshold thereby improving the skymodel with each iteration.

A 141.8 MHz Briggs (Briggs 1995) weighted (`robust=-0.5`) image with a bandwidth of 62.5 MHz is shown in Fig 2.4. The dirty image was deconvolved with a clean mask using the wideband multi-frequency deconvolution algorithm⁶ available in the imager `WSClean` (Offringa et al. 2014). The image has a resolution of $14''.2 \times 10''.4$ and the rms noise near NGC 4258 is 0.3 mJy/beam. Correction for the average primary beam was applied in the image plane using the time-averaged primary beam generated with `AWImager` (Tasse et al. 2013). Phase errors due to ionospheric distortions can be seen around bright point sources which can be corrected by performing direction dependent calibration. However, since these ionospheric distortions are localized and are not seen near NGC 4258, we did not apply any direction dependent corrections. Note that NGC 4258 has also been observed with the LOFAR HBA as part of the LOFAR Two-metre Sky Survey (LoTSS; Shimwell et al. 2017) and a direction-dependent calibrated image of NGC 4258 will be made available as part of the survey. However, the direction-independent calibrated dataset used here is sufficient for our scientific analysis.

2.2.6 Flux and astrometry uncertainties

To quantify the systematic flux uncertainty in our LOFAR maps, we compared the integrated source flux in our primary beam corrected and resolution-matched LOFAR maps with the catalogued sources from the 7C (Riley et al. 1999) and

⁴<https://github.com/maaijke/RMextract/> written by Maaijke Mevius at ASTRON.

⁵http://gnss.be/Atmospheric_Maps/ionospheric_maps.php

⁶<https://sourceforge.net/p/wsclean/wiki/WidebandDeconvolution>

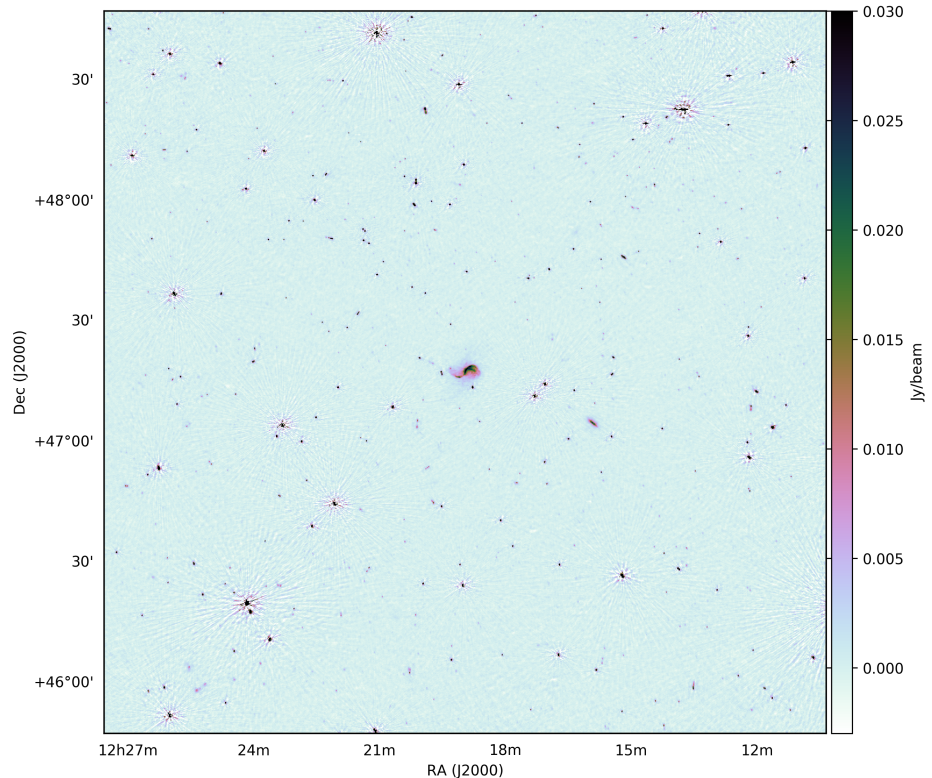


Figure 2.4 – Primary beam corrected image of a $3.0^\circ \times 3.0^\circ$ field of view around NGC 4258. The resolution of the image is $14''.2 \times 10''.4$ and the rms noise near NGC 4258 is 0.3 mJy/beam. The galaxy visible to the south-west of NGC 4258 is the nearby edge-on galaxy NGC 4217. The image is displayed using the `cubehelix` colour scheme (Green 2011).

the TGSS ([Intema et al. 2017](#)) surveys. We used a matching radius of $70''$ for the 7C catalogue and $25''$ for the TGSS catalogue. We find a median LOFAR to 7C flux ratio of 0.94 and median LOFAR to TGSS flux ratio of 1.07. Since we used a model for 3C 295 from [Scaife & Heald \(2012\)](#) which has less than 4% intrinsic flux uncertainty, and since we have not corrected for direction-dependent ionospheric phase errors, we assume a conservative 10% error on all our LOFAR flux estimates.

To assess the astrometric accuracy of our LOFAR maps, we compared our source positions with the catalogued source positions from the WENSS survey ([Rengelink et al. 1997](#)) which reports an astrometric accuracy of $1''.5$. We cross-matched the sources with a $25''$ matching radius and find a median positional offset of $4''.8$. Since the positional offset is much smaller than the resolution of the catalogues used, we do not perform any astrometric corrections on our maps.

2.3 Westerbork observations and data reduction

NGC 4258 was observed with WSRT in full polarization for 5×12 hours as part of the HALOGAS Continuum and Polarization Survey (HCAPS; Adebarh et al in prep). The available 80 MHz bandwidth was split into four 20 MHz-wide spectral windows and each spectral window was split into 64 channels. Each 12-hour track on NGC 4258 was bracketed by calibrator observations including a standard polarized and an unpolarized calibrator. The telescope array was used in the Maxi-short configuration resulting in unprojected (physical) baseline lengths ranging from 36 m to 2.7 km. This configuration was used to enhance the imaging performance for extended sources. The combined *uv*-coverage for a single channel is shown in Fig 2.5.

Standard calibration using Common Astronomical Software Application (CASA; [McMullin et al. 2007](#)) was used to calibrate the continuum datasets. However, as CASA could not then read the system temperature tables from WSRT, we applied system temperature corrections using the Astronomical Image Processing Software (AIPS; [Greisen 1998](#)) before exporting the visibilities to CASA Measurement Set (MS) format.

Before performing the calibration, we first flagged the visibilities for Radio Frequency Interference (RFI) using `A0Flagger` ([Offringa et al. 2010, 2012](#)) after applying a preliminary bandpass correction. This was needed for optimal RFI identification especially at the edges of the spectral windows where WSRT's bandpass shape is very steep. Note that these preliminary bandpass corrections were used only for RFI flagging and were discarded after RFI flagging.

Each continuum dataset corresponding to a single 12-hour track was calibrated separately. The unpolarized calibrator was used to derive the calibrator gains and polarization leakage corrections while the polarized calibrator was used to derive the polarization angle corrections. A channel-based calibration scheme was used to derive the polarization angle to reduce the 17 MHz ripple usually seen in polarized WSRT datasets ([Brentjens 2008; Adebarh et al. 2013](#)). After applying the calibrator solutions to the target data, we inspected each target dataset for solar interference and flagged the affected time slots manually. The

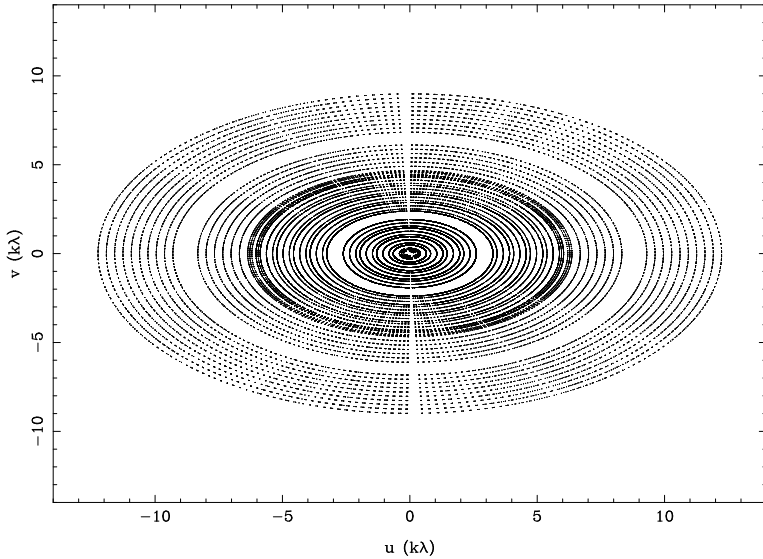


Figure 2.5 – WSRT *UV*-coverage corresponding to a single channel at 1.4 GHz. Note that the 80 MHz bandwidth fills the *uv*-plane radially.

calibrated target field data were then exported to `miriad` (Sault et al. 1995) format and concatenated into a single dataset for further self-calibration and imaging.

A few iterations of self-calibration were performed to improve the applied phase solutions to the target field by progressively improving the model of the sky. With each self-calibration iteration, the CLEAN mask was improved to better include the diffuse emission and the CLEAN threshold and the solution interval were progressively reduced. We continued performing self-calibration until all the flux in the field was included in the model. In the final iteration, a 1-minute solution interval was used (equal to the correlator integration time). During self-calibration, we noticed that a strong off-center source (NVSS J121715+471214) was limiting the dynamic range of our images. This source was removed from the visibility data using the standard “peeling” technique (Noordam 2004).

After self-calibration, the visibilities were inverted and deconvolved with a CLEAN mask using the Clark Clean algorithm. While deconvolving the dirty image, we employed the smoothness stabilized CLEAN algorithm (Cornwell 1983) to avoid badly corrugated reproduction of the diffuse emission from the galaxy. Primary beam correction was applied to the final images using the relation

$$A(r) = \cos^6(cvr) \quad (2.1)$$

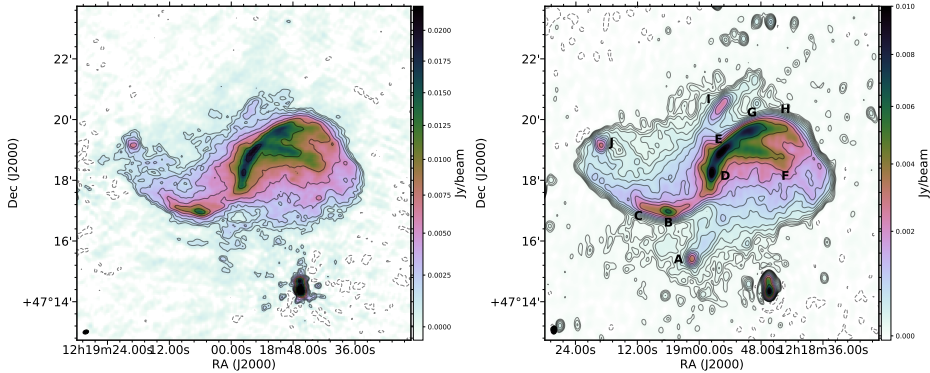


Figure 2.6 – High resolution LOFAR total intensity map of NGC 4258 at 141.8 MHz (left) and WSRT 1.38 GHz map (right). The images were produced with -0.5 robust weighting and have resolutions $11''.3 \times 7''.7$ and $16''.4 \times 11''.6$ respectively. The resolution of the radio continuum maps are indicated using a black ellipse in the lower left corner of each image. Regions of interest are labelled in the 1.4 GHz map and discussed in the text.

where ν is the observed frequency in GHz, r is the radial distance from the pointing center in radians, and c is a constant and is 68 at L-band⁷.

2.4 Results

2.4.1 Total intensity maps

Total intensity LOFAR HBA and WSRT maps of NGC 4258 are shown in Fig 2.6. The LOFAR map, with a central frequency of 141.8 MHz, is at a resolution of $11''.3 \times 7''.7$ and has an rms noise of about $290\mu\text{Jy}/\text{beam}$ near the galaxy. The WSRT 1.4 GHz is at a resolution of $16''.4 \times 11''.6$ resolution and has an rms noise of $23\mu\text{Jy}/\text{beam}$.

The observed radio continuum emission from NGC 4258 at both 141.8 MHz and 1.4 GHz is dominated by emission from the anomalous radio arms which are aligned roughly east-west. The overall morphology of the anomalous arms detected in our radio continuum maps is consistent with higher frequency radio continuum observations published in the literature. In the LOFAR map shown in Fig 2.6, radio continuum emission from the arms can be traced out to a distance of $4'$.9 from the nucleus which is consistent with the extent reported by de Bruyn (1977). Consistent with other previous observations (for example, see Hummel et al. 1989; Krause & Löhr 2004), our maps also show that the leading edges of both the arms exhibit a steep intensity gradient.

The low luminosity AGN, which is thought to be feeding the anomalous arms, is located just south of the region marked ‘D’ in Fig 2.6. The western arm, which dominates the integrated radio continuum emission from NGC 4258 and is a

⁷See section 5.7 on <https://www.astron.nl/radio-observatory/astronomers/wsrt-guide-observations/5-technical-information/5-technical-information>

factor of three brighter than the eastern arm, bifurcates at position ‘E’. The western arm brightens substantially near location E just before bifurcating into a brighter northern fragment and a weaker southern fragment. The eastern arm initially undergoes an enhancement in surface brightness near position ‘B’ and ‘C’ at a distance of about 3.6 kpc along the arm from the nucleus. Similar to the western arm, the eastern arms bifurcate into two (near position ‘C’) after undergoing brightness enhancement. Apart from the emission corresponding to the anomalous arm, low-level diffuse emission is seen on the trailing side of both the arms in the regions that have been historically labelled “plateau” in the literature ([van der Kruit et al. 1972](#)).

In addition to the dominant bifurcation at location E noted above, we see that the western arm in our image LOFAR map appears to show further bifurcations near locations G, H, and F. This is not evident in our WSRT map or in other radio continuum maps published in the literature possibly due to our improved resolution, sensitivity or a combination of both.

Regions marked ‘A’ and ‘I’ correspond to H II regions in the disk of the galaxy. The H II region marked ‘A’ is not visible in our LOFAR map while faint emission from region ‘I’ is visible. In the high resolution VLA 6cm and 20cm maps published by [Hymen et al. \(2001\)](#), region ‘I’ is resolved into four distinct H II regions.

While the radio continuum contours in the “plateau” appear to show filamentary structures running almost perpendicular to the anomalous arms, the resolution of our maps is not high enough to figure out whether these result from a superposition of multiple filamentary structures.

To pick up diffuse, low surface brightness radio continuum emission from the outer regions of the galaxy, we reimaged both the LOFAR and the WSRT visibility data by applying a 35'' Gaussian *uv* taper and a **robust** value of -0.7. The need for a more uniform visibility weighting than previous higher resolution images is discussed in detail in section 4.2.3. After deconvolving with a CLEAN mask, the images were smoothed further down to a resolution of 45''. Contours from the 45'' LOFAR and WSRT images overlayed on a *GALEX* UV map ([Gil de Paz et al. 2007](#)) are shown in Fig 2.7. In addition to the anomalous radio arms, the 45'' map also shows radio continuum emission from the underlying star-forming disk closely tracing the outer spiral arms out to a distance of $\approx 9'.6$ from the nucleus. At our adopted distance, this corresponds to 21 kpc from the nucleus. While other works have detected radio continuum emission from the inner regions of the underlying galactic disk (for example see [de Bruyn 1977](#); [Krause et al. 1984](#); [Hummel et al. 1989](#)), our LOFAR and WSRT maps detect the largest radial extent of the underlying radio continuum disk in NGC 4258. Recently, NGC 4258 has been observed again with LOFAR HBA as part of the LOFAR Tier-1 Sky Survey (LoTSS; [Shimwell et al. 2017](#)) and the extended emission detected in our map is consistent with a preliminary image from LoTSS (Hardcastle private comm.).

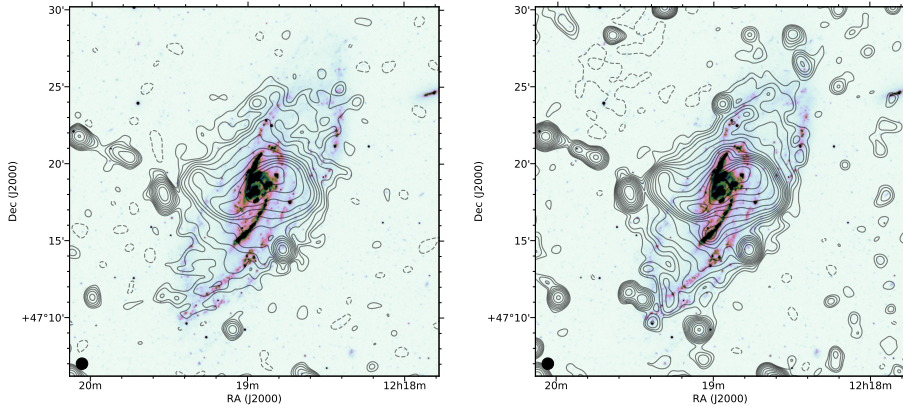


Figure 2.7 – Low resolution LOFAR (*left*) and 1.4 GHz WSRT (*right*) contour lines plotted on a GALEX NUV image of NGC 4258. The $45''$ beam is shown in the lower left corner as a filled circle in both maps. LOFAR contours are drawn at $2^n \times 3$ mJy/beam and the WSRT contours are drawn at $1.5^n \times 0.15$ mJy/beam levels where $n = 0, 1, 2, ..$. The noise floor is indicated using the broken contour lines drawn at -3.0 mJy/beam and -0.15 mJy/beam respectively.

2.4.2 Other nearby galaxies in the LOFAR field of view

NGC 4248 has been proposed to be a satellite galaxy of NGC 4258 (van Albada 1977; Spencer et al. 2014). Additionally, Spencer et al. (2014) identified 16 candidate satellite galaxies around NGC 4258 using spectroscopic observations from the Apache Point Observatory. While de Bruyn (1977) reports an upper limit on the integrated flux of 4 mJy from NGC 4248 at 610 MHz, we do not detect any radio continuum emission at either 141.8 MHz or 1.4 GHz from any of the satellite galaxies listed in Spencer et al. (2014) except NGC 4288.

In addition to NGC 4258, our LOFAR map contains a few other nearby galaxies within the primary beam. Their integrated flux densities and spectral indices computed using L-band flux densities from the literature are listed in Table 2.3.

2.4.3 Spectral properties of NGC 4258

Before estimating the integrated flux density of NGC 4258, we first masked the point sources that overlap with the diffuse radio emission. After masking the background point sources, we estimate the total radio continuum flux density of NGC 4258 at 0.14 and 1.4 GHz to be 4.82 ± 0.96 Jy and 0.82 ± 0.08 Jy respectively. The uncertainties on the reported integrated flux densities were estimated by accounting for both the rms noise in the image and the systematic uncertainty associated with amplitude/flux calibration.

We estimated the total spectral index of NGC 4258 from our flux density measurements in combination with flux density measurements reported in the literature at other radio frequencies. The integrated flux density of NGC 4258 from our radio continuum maps, along with the values published in the literature,

Table 2.3 – Integrated flux densities at 141.8 MHz of other nearby galaxies in our LOFAR map. The global spectral indices were computed using L-band flux densities reported in the literature.

Galaxy ID 1	$S_{141.8\text{MHz}}$ 2	$S_{1.4\text{GHz}}$ 3	$\alpha_{0.141-1.4}$ 4	References 5
NGC 4047	213.4 ± 42.8	31.7 ± 1.7	0.83 ± 0.09	1
NGC 4096	353.0 ± 70.6	54.9 ± 3.4	0.81 ± 0.09	1
NGC 4217	708.5 ± 141.7	122.8 ± 4.4	0.77 ± 0.09	1
NGC 4218	16.1 ± 3.6	5.3 ± 0.5	0.49 ± 0.11	1
NGC 4220	42.3 ± 8.5	3.9 ± 0.6	1.04 ± 0.11	1
NGC 4226	128.9 ± 25.8	23.5 ± 1.1	0.74 ± 0.09	1
NGC 4231/32	45.8 ± 9.2	–	–	–
NGC 4288	20.8 ± 4.3	6.6 ± 0.6	0.50 ± 0.10	2
NGC 4357	17.3 ± 3.7	3.0 ± 0.5	0.77 ± 0.12	1
NGC 4389	96.4 ± 19.4	20.8 ± 1.7	0.67 ± 0.09	1

Notes. (1) Galaxy ID; (2) Integrated flux at 141.8 MHz; (3) Integrated flux at 1.4 GHz; (4) Spectral index between 0.142 and 1.4 GHz; (5) References for 1.4 GHz flux density measurement

References. (1) [Condon et al. \(1998\)](#); (2) [Condon et al. \(2002\)](#)

Table 2.4 – Integrated flux densities of NGC 4258

ν (GHz)	I_ν (Jy)	Reference
0.142	4.820 ± 0.960	this work
0.408	1.830 ± 0.270	1
0.610	1.420 ± 0.100	2
0.750	1.230 ± 0.220	3
1.412	0.820 ± 0.040	4
1.415	0.840 ± 0.050	2
1.418	0.820 ± 0.080	this work
2.695	0.660 ± 0.060	5
4.750	0.399 ± 0.026	6
10.55	0.236 ± 0.021	7

References. (1) [Gioia & Gregorini \(1980\)](#); (2) [de Bruyn \(1977\)](#); (3) [de Jong \(1965\)](#); (4) [van Albada \(1980\)](#); (5) [Kazès et al. \(1970\)](#); (6) [Krause et al. \(1984\)](#); (7) Marita Krause (private comm.)

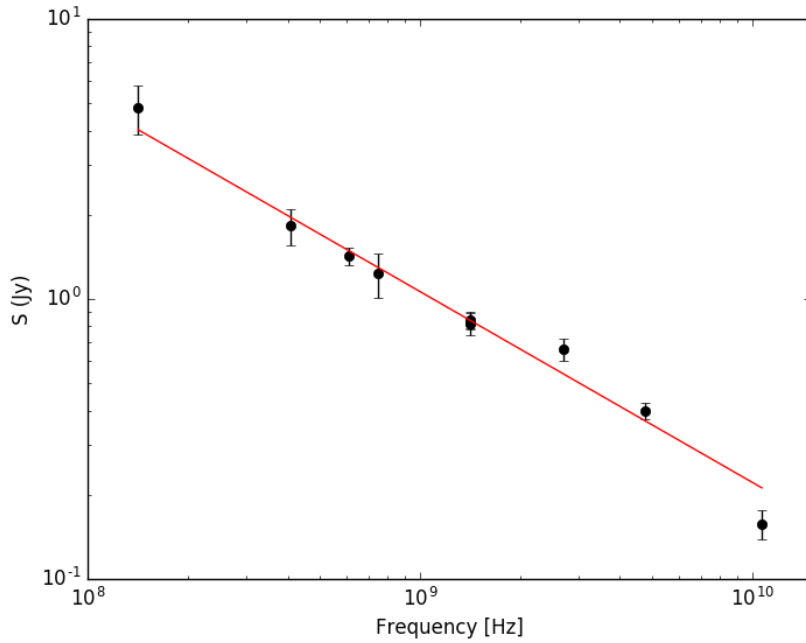


Figure 2.8 – Integrated flux density of NGC 4258 fitted with a power law spectral index $\alpha = -0.63 \pm 0.03$.

are listed in Table 3.4. The flux densities are well fit using a power law fit to the measured flux densities as shown in Fig 2.8. We do not see any indication of curvature in the spectrum.

We computed the spectral index map of NGC 4258 using the WSRT 1.4 GHz and LOFAR 141.8 MHz maps. To match the angular scales in both maps, we reimaged the two datasets using a common *uv*-cut ($0.12 - 13.3$ k λ) using a 35'' Gaussian taper. The restored images were convolved to 45'' resolution and then regridded to a common coordinate grid. The spectral index was computed on a pixel-by-pixel basis and the error on spectral index was computed using the relation

$$\alpha_{\text{err}} = \frac{1}{\log(\nu_{141.8}/\nu_{1.4})} \sqrt{\left(\frac{S_{141.8,\text{err}}}{S_{141.8}} \right)^2 + \left(\frac{S_{1.4,\text{err}}}{S_{1.4}} \right)^2} \quad (2.2)$$

where $S_{1.4}$ and $S_{141.8}$ are the pixel values in the WSRT and LOFAR maps and $S_{1.4,\text{err}}$ and $S_{141.8,\text{err}}$ are the corresponding errors on the pixel values. The spectral index and the spectral index error maps are shown in Fig 2.9, and pixels with spectral index error greater than 0.25 have been masked.

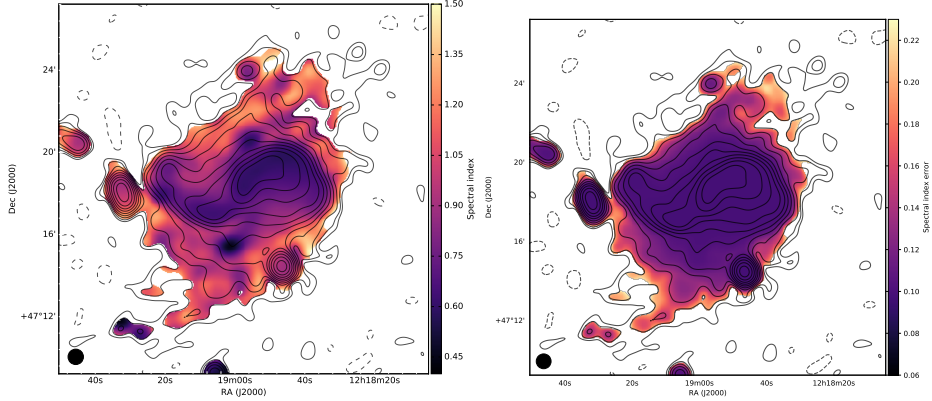


Figure 2.9 – Spectral index and spectral index error maps of NGC 4258 computed using the 141.8 MHz and 1.4 GHz radio continuum map. The LOFAR contour lines are drawn at the same level as in Figure 2.7 and the 45'' Gaussian beam is shown as a filled circle in the lower left corner.

2.4.4 Thermal fraction and non-thermal spectral index

To estimate the thermal contribution to the observed radio continuum emission at both 0.142 and 1.4 GHz, we used the H α map of NGC 4258 obtained using the KPNO 4.0-meter Mayall telescope (Maria Patterson priv. comm.). H α emission, which arises from the recombination of electrons that give rise to the free-free emission, is an excellent tracer of the thermal component.

The H α map was corrected for dust extinction from the Galactic foreground using the standard dust extinction maps from Schlegel et al. (1998). The foreground-extinction corrected H α map was then smoothed with a 45'' Gaussian to match the resolution of the radio continuum maps and regredded to a common coordinate grid. Following Hunt et al. (2004), we estimated the thermal contribution from the foreground-extinction corrected H α map using the relation:

$$\left(\frac{F_\nu}{\text{mJy}} \right) = 1.16 \left(1 + \frac{n(\text{He}^+)}{n(\text{H}^+)} \right) \left(\frac{T}{10^4 \text{ K}} \right)^{0.617} \left(\frac{\nu}{\text{GHz}} \right)^{-0.1} \times \left(\frac{F_{\text{H}\alpha}}{10^{-12} \text{erg cm}^{-2} \text{s}^{-1}} \right) \quad (2.3)$$

where F_ν is the thermal emission at radio frequency ν , T is the temperature of the emitting region, $n(\text{He}^+)/n(\text{H}^+)$ is the ratio of ionized helium to ionized hydrogen, and $F_{\text{H}\alpha}$ is the extinction-corrected H α flux. We assume that the temperature of the emitting region $T \sim 10^4 \text{K}$. Following Martin & Kennicutt (1997), we also assume that $n(\text{He}^+)/n(\text{H}^+) = 0.087$. The non-thermal synchrotron flux (F_{nth})

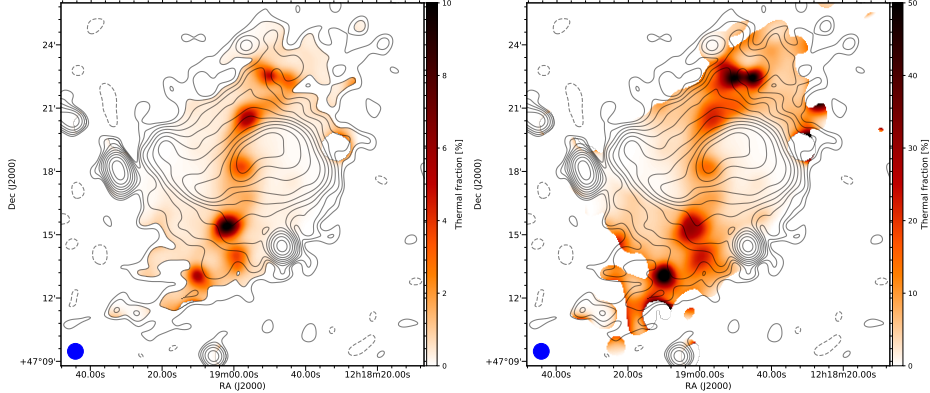


Figure 2.10 – Thermal fraction in NGC 4258 at 0.142 GHz (left) and 1.4 GHz (right) estimated using a foreground-extinction corrected H α map. The overlayed contour lines are LOFAR contours and are drawn at the same level as Fig 2.7. The size of the 45'' beam is shown in the lower left corner as a blue circle.

was then computed from the estimated thermal emission (F_{th}) and the observed total intensity maps (F_{tot}) using the relation

$$f_{\text{nth}} = f_{\text{tot}} \left(1 - \frac{f_{\text{th}}}{f_{\text{tot}}} \right) \quad (2.4)$$

The estimated thermal fractions ($F_{\text{th}}/F_{\text{tot}}$) at 141.8 MHz and 1.4 GHz at 45'' resolution are shown in Fig 2.10. At 1.4 GHz, as expected, the thermal emission is significant in regions along the inner spiral arms that contain large HII regions. The thermal fraction is as high as 50% in these regions. However, the thermal fraction in the rest of the galactic disk is $\leq 20\%$. Note that the anomalous arms themselves show very little thermal contribution ($\leq 2.0\%$). The estimated thermal fraction at 0.142 GHz is $\leq 10\%$ throughout the galaxy with the maximum thermal fraction ($\sim 10\%$) occurring in regions containing the same HII regions discussed before. In the remainder of the galactic disk, the thermal fraction is $\leq 4\%$.

Using the above-described procedure, we carried out thermal/non-thermal separation at two different spatial resolutions (7'' and 45'') to highlight features on both small and large scales. The non-thermal spectral index maps of NGC 4258 computed after subtracting the thermal contribution at 0.142 and 1.4 GHz are shown in Fig 2.11.

In the low resolution spectral index map, we find that both the eastern and the western anomalous arms show similar spectral indices of ~ 0.6 . The rest of the galaxy appears to have a steeper spectral index than the anomalous arms except for two HII regions which exhibit spectral flattening. On both sides, the spectral index distribution also steepens as one moves vertically along the declination axis from the anomalous arms to the “radio plateau”. This contrast in spectral index between the anomalous arms and the “radio plateau” is visible quite clearly in the high resolution spectral index map shown in Fig 2.11. On both anomalous

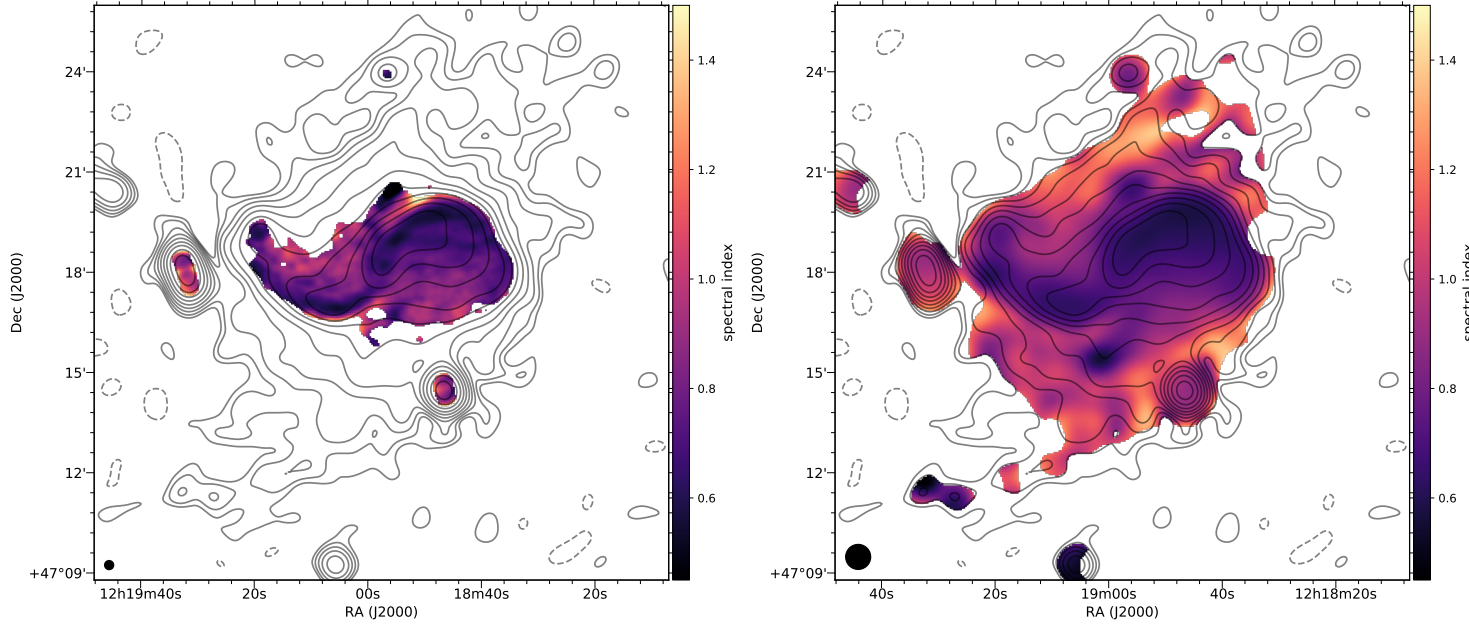


Figure 2.11 – High and low resolution non-thermal spectral index maps of NGC 4258 estimated using the 0.142 and 1.4 GHz radio continuum maps after subtracting out the thermal contribution. In both spectral index maps, all pixels with spectral index error larger than 0.1 have been blanked. The resolutions of the spectral index maps are shown in the lower left corner of each image. The overlayed LOFAR contours are drawn at the same level as in Fig 2.7.

arms, we find that the spectral index steepens from 0.54 – 0.93 as one moves from the leading edge of the anomalous arms in to the plateau. Similar spectral index steepening has been seen in radio relic in galaxy clusters (for example, see [van Weeren et al. 2010, 2012](#)) where the spectral index steepens along the direction away from the shock front.

The bifurcated western anomalous arm shows an interesting non-thermal spectral index distribution, especially between the two fragments. We find that the spectral index of the region where the western arm bifurcates is flatter than the surrounding region. After bifurcation, the northern fragment ($\alpha \sim 0.56$) of that arm has a flatter spectral index than the southern fragment ($\alpha \sim 0.66$). This observed steepening in spectral index in the southern fragment could indicate that the southern fragment is older than the northern fragment and was perhaps created by previous episodic outflow from the nucleus.

2.4.5 Magnetic field strength

Assuming energy equipartition between cosmic rays and the magnetic fields, we can estimate the total magnetic field strength in NGC 4258 using the non-thermal radio continuum maps. The equipartition magnetic field strength (B_{eq}) is related to the observed synchrotron intensity (I_{syn}) as ([Beck & Krause 2005](#))

$$B_{eq} = \left[\frac{4 \pi (2\alpha + 1) (K_0 + 1) I_{syn} E_p^{1-2\alpha} (\nu/2c_1)^\alpha}{(2\alpha - 1) c_2(\alpha) l c_4(i)} \right]^{1/(3+\alpha)} \quad (2.5)$$

where i is the inclination angle of the galaxy, l is the path length through the synchrotron emitting region, α is the spectral index, K_0 is the proton-to-electron ratio, and E_p is the rest mass-energy of the proton. The coefficients c_1 , c_3 , and c_4 are defined as

$$c_1 = 6.26428 \times 10^8 \text{ erg}^{-1} \text{ s}^{-1} \text{ G}^{-1} \quad (2.6)$$

$$c_3 = 1.86558 \times 10^{-23} \text{ erg G}^{-1} \text{ sr}^{-1} \quad (2.7)$$

$$c_4(i) = [\cos(i)]^{\alpha+1} \quad (2.8)$$

and c_2 is a constant tabulated on page 232 of [Pacholczyk \(1970\)](#). Further assumptions are needed to compute the magnetic field strength using the equipartition formula. We have assumed that the cosmic ray proton-to-electron number density $K_0 = 100$ throughout the galaxy and that the projected pathlength through the synchrotron emitting media is 1000 pc.

Using these assumptions, we computed the magnetic field strength on a pixel-by-pixel basis using the masked 45'' resolution radio continuum (Fig. 2.7) and the spectral index (Fig. 2.9) maps. The revised equipartition formula diverges for spectral index $\alpha \leq 0.5$ and thus we have masked pixels with spectral index values less than 0.5. In addition, we also masked pixels corresponding to background point sources. The computed magnetic field strength map is shown in Fig 2.12.

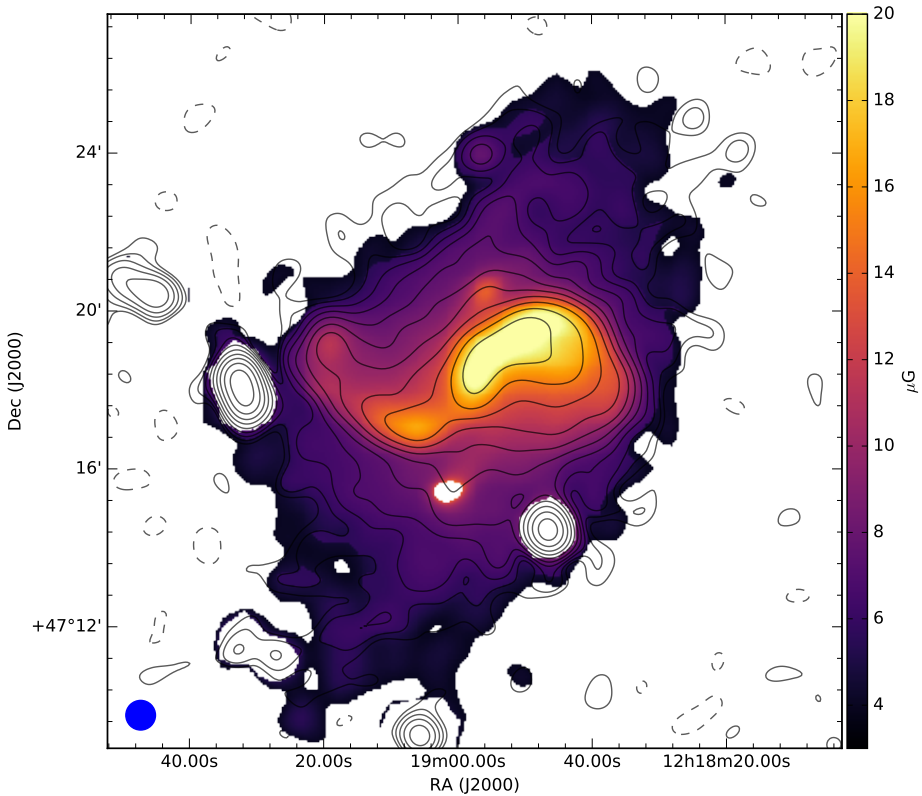


Figure 2.12 – Equipartition magnetic field map of NGC 4258. The size of the $45''$ beam is shown as a filled blue circle in the lower left corner. The contour levels are drawn at the same level as Fig 2.7. Note that pixels corresponding to background sources and to H II regions with spectral indices less than 0.5 have been masked and appear as white regions.

The equipartition magnetic field appears to be the strongest in the western anomalous arm with field strengths up to $20\mu\text{G}$ in the inner parts. Along the eastern anomalous arm, we find that the field strength is about $15\mu\text{G}$ in the inner 2.5 kpc and then gradually decreases radially outwards. Outside the anomalous arms, we find field strengths of about $5-8\mu\text{G}$ in the galactic disk which is normal for star-forming disks.

2.4.6 Relation with the H I disk

Figure 2.13 shows the LOFAR low resolution total intensity radio continuum contours overlayed on a new sensitive H I column density map of NGC 4258. The H I observations of NGC 4258 were carried out as part of the Hydrogen Accretion in LLocal GAlaxieS (HALOGAS) survey (Heald et al. 2011). The HALOGAS survey is a deep H I survey of a sample of 24 nearby galaxies where each galaxy is observed for 10×12 hours using WSRT. The survey provides a Hanning smoothed frequency resolution of 4.12 km s^{-1} reaching a typical column density sensitivity of a few times 10^{19} cm^{-2} .

NGC 4258 has been observed in the 21 cm H I line by van Albada (1977) using the Westerbork telescope with a column density sensitivity of $6 \times 10^{20} \text{ cm}^{-2}$. The H I column density maps presented in van Albada (1977) show a lack of H I emission in and around the anomalous arms compared to the rest of the H I disk. This is confirmed in our column density map which is about 20 times more sensitive than the map used by van Albada (1977). The lack of H I associated with the anomalous arms is most obvious in the western arm (indicated using an arrow in the left panel of Fig 2.13). A higher resolution zoomed-in H I map of this region is shown in the right panel of Fig 2.13. The high resolution map shows clear gaps in the H I spiral arms coincident with the two fragments of the western anomalous arm. This strongly suggests that the western arm interacts with the galactic disk and is perhaps embedded in the disk. We do not see similar gaps in H I associated with the south-eastern arm. However, a large discontinuity in H I is seen coincident with the “radio plateau” associated with the south-eastern arm.

2.5 Search for polarized emission

2.5.1 Polarized emission at 1.4 GHz

To detect polarized emission in our WSRT dataset, we first made Stokes Q and U images each with a bandwidth of 2.5 MHz, using the self-calibrated uv-data presented in section 2.3. Each image was cleaned separately using a mask derived from the total intensity 1.4 GHz image. The deconvolved Stokes Q and U channel images were restored using a $30''$ circular Gaussian beam. Faraday rotation measure synthesis (Brentjens & de Bruyn 2005) was applied to the resulting Stokes Q and U channel images.

All areas with no polarised emission in the polarised intensity (PI) cube were used to derive the polarization bias correction. We calculated the average for

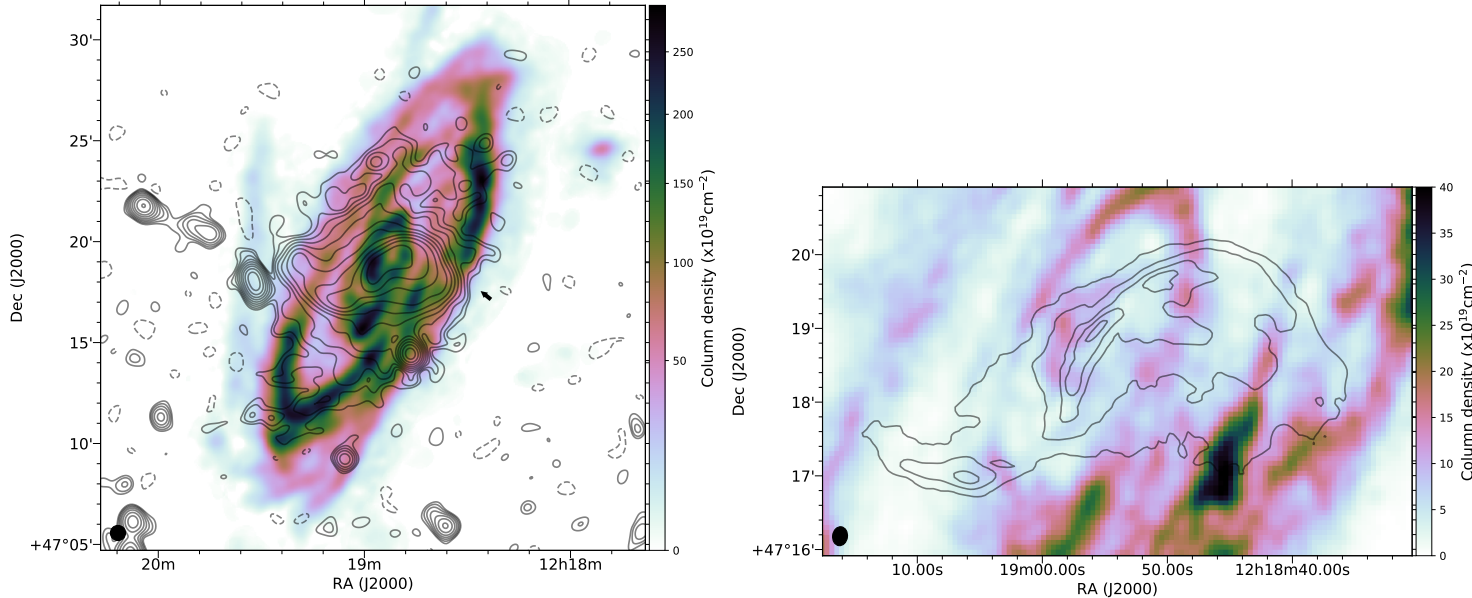


Figure 2.13 – Left: LOFAR total intensity contour lines overlaid on a 30'' H I column density map of NGC 4258. LOFAR contour levels are drawn at the same level as in Fig 2.7. The black arrow indicates the location along the outer spiral arm where we observe a lack of H I coincident with the anomalous arm. **Right:** High resolution H I column density map of the anomalous arms showing clear gaps in H I spiral arms coincident with the western anomalous radio arms. WSRT 1.4 GHz radio continuum contours are drawn at 0.0035, 0.007, 0.012, 0.016, 0.02 Jy beam $^{-1}$ and the resolution of the H I map ($15''.5 \times 12''.1$) is shown in the lower left corner of the image.

each pixel in RA and DEC along the Faraday axis. The resulting 2D image was then used to fit a point-symmetric second order polynomial with the minimum fixed at the pointing centre. This gives an offset (bias) correction, which was then subtracted from each individual plane of the Faraday PI-cube.

The Faraday rotation-corrected polarised intensity image was calculated by taking the maximum along the Faraday axis of each individual pixel in the bias-corrected cube. Rotation Measures (RM) and polarisation angles (PA) were derived from the position of this maximum pixel in the PI-cube. Intrinsic polarisation angles (PA0) were then calculated from the derived RM and PA values by calculating the PA at $\lambda = 0$ cm. In addition, fractional polarisation (FP) images were created using the PI image and the final total power image from our observations.

The WSRT polarized intensity overlayed with Faraday rotation corrected B-vectors and the Faraday depth map are shown in Fig 2.14. Note that the polarization vectors plotted in Fig 2.14 differ from the 1.4 GHz B-field vectors published in [Hummel et al. \(1989\)](#) because these authors did not apply a rotation measure correction.

The polarized intensity in the left panel of Fig 2.14 shows that most of the linearly polarized emission arises from the peripheries of the two arms with no linearly polarized emission detected in the inner kpc. Comparing the polarization fraction in the two arms, we notice that parts of the eastern arm show up to $\sim 40\%$ fractional polarization compared to about 20% fractional polarization in the western arm suggesting that the magnetic field lines are more ordered in the eastern arm. In addition to the polarized emission from the anomalous arms, we detect a weak emitting region to the south of the western arm which is coincident with an inter-arm region. However, the exact origin of this weak, diffuse polarized emission is unclear.

From the Faraday depth map shown in the right panel of Fig 2.14, we see that the synchrotron emission seen in the outer regions of the eastern arm undergo relatively small Faraday rotation (-10 to -20 rad m $^{-2}$) compared to the western arm which has a typical Faraday rotation of -25 rad m $^{-2}$ to -40 rad m $^{-2}$ extending up to ~ -100 rad m $^{-2}$ at the outer-most part. Such a large difference in Faraday rotation between the two arms indicates that the quantity $n_e B \cdot dl$ is larger along the line of sight towards the western arm. This is discussed further in section 2.6. Note that the Faraday depth values stated above have not been corrected for the Faraday rotation caused by the Galactic foreground which is about 11.8 rad m $^{-2}$ ([Taylor et al. 2009](#)) along the line of sight towards NGC 4258.

2.5.2 Polarized emission at 141.8 MHz

We applied the RM synthesis technique to search for polarized emission in the ionosphere RM corrected LOFAR data. The rotation measure synthesis procedure shifts all the instrumentally polarized emission to a Faraday depth of 0 rad m $^{-2}$. However, applying ionospheric correction smears the instrumental polarization. In our case, the applied ionospheric RM varies between 1 rad m $^{-2}$ and 2.6 rad m $^{-2}$ and RMSF width of ~ 1 rad m $^{-2}$ implying that the instrumental

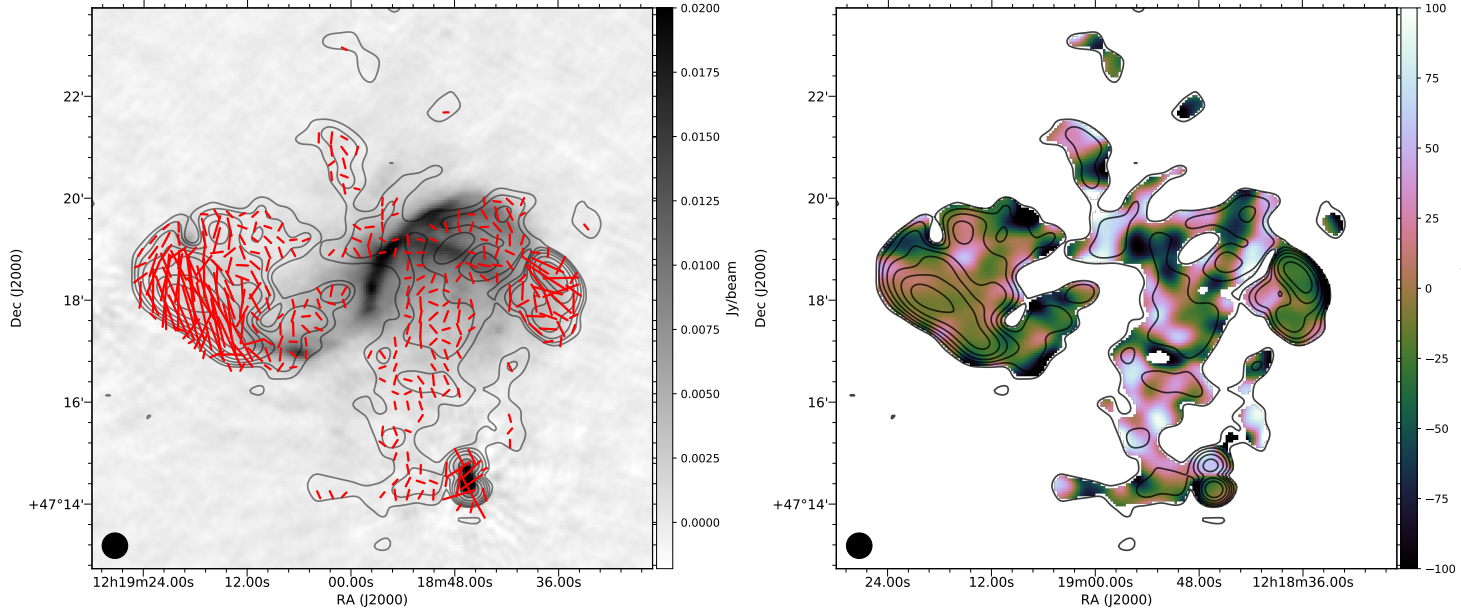


Figure 2.14 – Left: WSRT polarized intensity contours and B-vectors overlaid on LOFAR total intensity image. The length of the polarization contours are proportional to the polarization fraction. **Right:** Faraday depth map of NGC 4258 at 1.4 GHz. Faraday rotation contributed by the Galactic foreground ($\sim 11.8 \text{ rad m}^{-2}$) has not been subtracted. In both panels, polarized intensity contours are drawn at levels $74 \times 1.5^n \mu\text{Jy}/\text{beam}$ where $n = 0, 1, 2, 3, \dots$. The $30''$ resolution of the WSRT polarized intensity map is shown in the lower left corner of both panels.

polarization will be smeared between 0 rad m^{-2} and 3.6 rad m^{-2} . After applying the ionospheric RM corrections, we made Stokes I, Q, U, and V channel maps for each channel with a bandwidth of 195.3 kHz. Images were made at two different angular resolutions to search for diffuse polarized emission from the Galactic foreground and to search for polarized emission from extragalactic sources. We visually inspected each channel map and removed channels that were corrupted by residual RFI resulting in 320 Stokes I, Q, U, and V maps. We applied the RM synthesis technique (Brentjens & de Bruyn 2005) to the Stokes Q and U cubes to produce the Faraday depth cubes.

Inspecting the Faraday depth cubes produced by RM synthesis, we find no polarized emission from NGC 4258 in our LOFAR data down to a 5σ detection threshold of $350\mu\text{Jy}/\text{beam}$. Our non-detection of polarized emission at 150 MHz is consistent with previous finding of Farnes et al. (2013) and Mulcahy et al. (2014) who were unable to detect polarized emission from M51 using 610 MHz GMRT and 150 MHz LOFAR observations respectively.

2.5.3 Stacking polarized emission in the galactic disk

We carried out a stacking analysis on our WSRT and LOFAR polarized intensity maps to obtain a statistical detection of low surface brightness polarized emission from the galactic star-forming disk of NGC 4258. We did not include pixels where we detect polarized emission (as shown in Fig 2.14). In addition to these, we also masked pixels corresponding to the anomalous arms using a high resolution total intensity mask. We also masked out known background point sources. Apart from the pixels corresponding to the galactic disk, we also stacked pixels from a few “empty” regions around the galaxy to act as a control sample where we do not expect to see any polarized emission. Since the pixels corresponding to the galactic disk and the “empty” regions are sufficiently close, any contribution due to the galactic foreground should be similar in both cases and hence we should be able to attribute the difference between the two stacked signal to polarized synchrotron emission from NGC 4258. The left panel in Fig 2.15 shows the pixels that were included in our stacking analysis with the green pixels corresponding to the galactic disk and pixels shown in black corresponding to the “empty” sky.

Using the mask, we estimated the mean polarized intensity within each Faraday depth bin. The result from the stacking analysis showing the mean polarized intensity as a function of Faraday depth for the WSRT Faraday depth cubes is shown in the right panel of Fig 2.15. At 1.4 GHz, we find that the pixels corresponding to the galactic disk in NGC 4258 show a 1.5 mJy excess in polarized intensity compared to pixels from nearby “empty” regions. We do not find any excess polarization signal from the LOFAR data cubes.

The peak polarization fraction at 1.4 GHz is observed in the Faraday depth bin ranging from -4 rad m^{-2} to -100 rad m^{-2} . A mean polarized intensity of 1.5 mJy corresponds to a polarized fraction of 6.7%. Notice that a mean polarization intensity of about 6.7% is not atypical in the disks of nearby normal spiral galaxies. For example, the nearby normal spiral galaxies M 51 and NGC 6946 have a polarization fraction of about 5.7% and 8.8% at 1.4 GHz (Heald 2009).

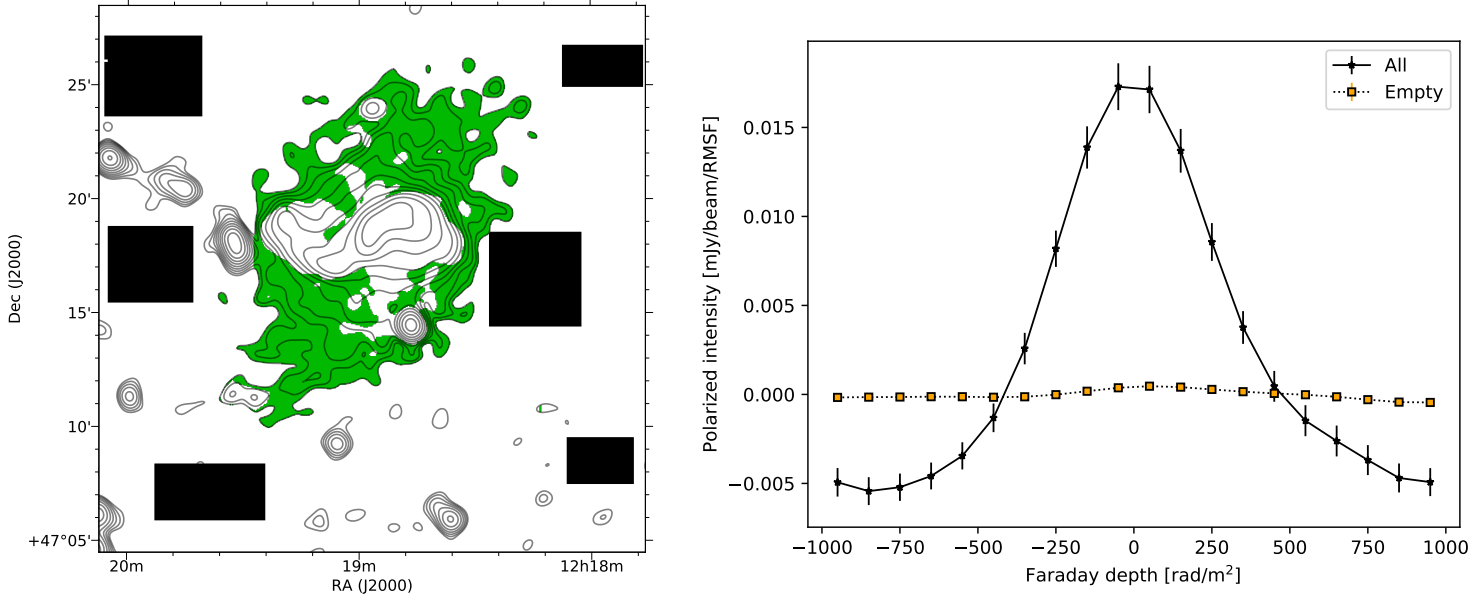


Figure 2.15 – Left: Image indicating the pixels that were used in the polarization stacking analysis. Pixels corresponding to the galactic disk that were stacked are shown in green and the regions shown in black correspond to the “empty” sky where we do not expect to detect any polarized emission. LOFAR contours lines are drawn at the same levels as in Fig 2.7. **Right:** Results from the stacking analysis showing the mean polarized intensity at 1.4 GHz as a function of Faraday depth for the two different regions indicated in the figure on the left. Note that the negative polarized intensity at large Faraday depths indicates an overestimation in the polarization bias correction.

For a list of polarized emission from nearby spiral galaxies, see Table 1 in [Heald \(2009\)](#). Since polarized emission from galactic disks trace the ordered (both anisotropic and regular) component of the mean magnetic field, the observed fractional polarization in the disk of NGC 4258 indicates that the presence of nuclear feedback (at least in the inner part of the galactic disk) has little influence on the ratio of the ordered-to-total magnetic field strength in galactic disks.

2.6 Where are the anomalous arms located?

As discussed in previous sections, NGC 4258 has been studied quite extensively across multiple wavelengths. For a previous summary of observations and how they fit the different models that have been proposed to explain the morphology of the anomalous arms in NGC 4258, see [van Albada & van der Hulst \(1982\)](#) and [Wilson et al. \(2001\)](#). Recall from the introduction that all models proposed to explain the morphology of NGC 4258 fall in two categories depending on where the anomalous arms are located with respect to the galactic disk (the *in-disk* and the *out-of-disk* models). Both models agree that the anomalous arms originate as nuclear jets but disagree on where the arms are located with respect to the galactic disk in NGC 4258. In light of the new sensitive radio continuum and neutral hydrogen observations, we reconsider, in the section below, the discussion presented in [van Albada & van der Hulst \(1982\)](#). Note that the papers mentioned above did not have any radio polarization information. As we will show below, radio polarization measurements, when used along with the multiwavelength data available in the literature, provide a strong constraint on the morphology of the anomalous arms in NGC 4258.

The H_I column density map of NGC 4258 discussed in section 2.4.6 show gaps in the distribution of H_I in two spiral arms where the western arm cuts through the galactic disk. Similar anticorrelations (presence of radio emission in the absence of other tracers) can also be seen between polarized emission (discussed in section 2.5.1) from the western arms and the spiral arms as traced by UV and H α . As shown in Fig. 2.16, the peak polarized intensity near the edge of the western arm occurs in a region devoid of UV, H_I or H α emission. This enhancement in polarized intensity is associated with a region where the H_I column density drops below $10 \times 10^{19} \text{ cm}^{-2}$ while its immediate surrounding appears to have twice as much H_I. These anti-correlations seen between the total and polarized emission and the distribution of UV, H_I, and H α emission from the western arm strongly suggest that the western arm interacts with the galactic disk.

In addition to the signatures due to interaction between the anomalous arms and the galactic disk, the linearly polarized emission and the Faraday depth values along the anomalous arms provide additional constraints to determine the location of the arms. The key difference between the *in-disk* and the *out-of-disk* models is that the synchrotron emission from the anomalous arms undergo different levels of Faraday rotation by the thermal electron (warm ionized medium) in the thick disk and the galactic halo. For example, if the anomalous arms are embedded in the disk, the linearly polarized synchrotron emission from

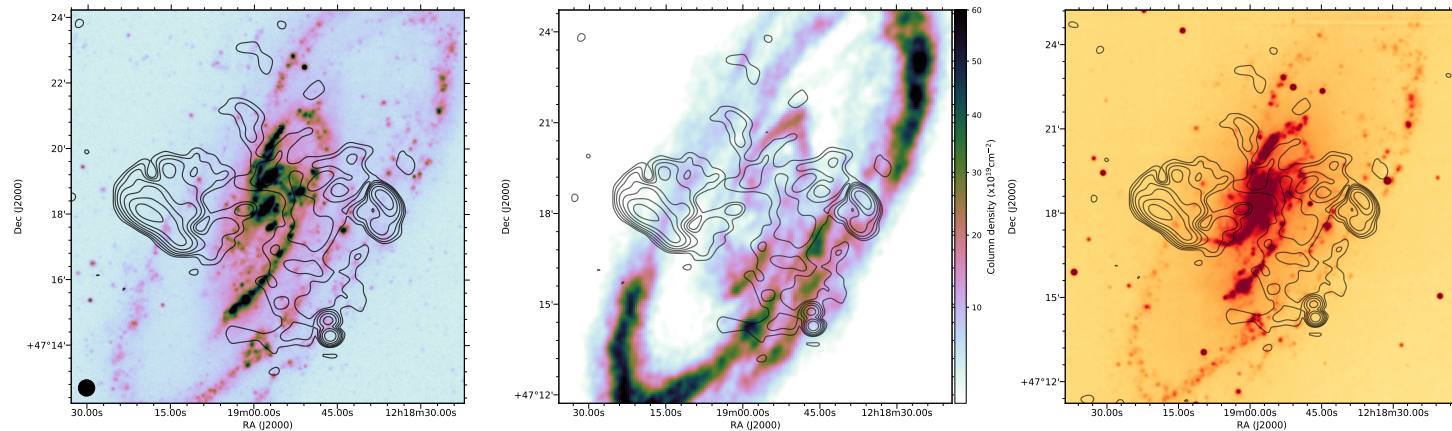


Figure 2.16 – Polarized emission at 1.4 GHz overlayed on GALEX UV, HALOGAS H I and H α maps indicating that the peak polarization in the outer parts of the western arm is coincident with a gap seen in UV, H I, and H α emission from the galactic disk.

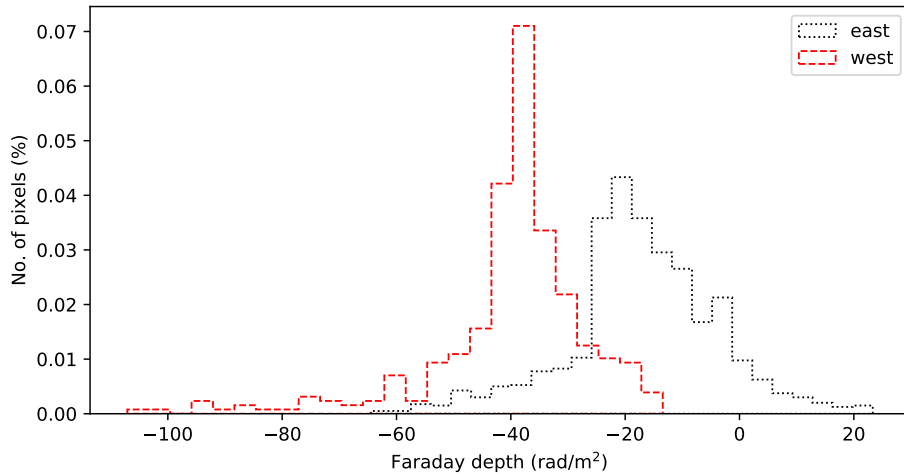


Figure 2.17 – Histogram distribution of Faraday depths seen in the outer parts of the eastern and the western anomalous arms. Note that the Faraday depth values have been corrected for Faraday rotation due to the Galactic foreground (11.8 rad/m^2).

the arms will undergo Faraday rotation due to magneto-ionic media in the galactic disk and in the halo. However, if an anomalous arm is outside the disk and is in front of the galactic disk (on the near side to the observer), the synchrotron emission from the arm will experience relatively small Faraday rotation in the galactic halo.

From the Faraday depth map presented in section 2.5.1, it is clear that the amount of Faraday rotation experienced by the eastern and the western arms is significantly different (also see Fig 2.17). Given the large Faraday rotation seen towards the outer parts of the anomalous arm and the gaps seen in UV, H_I, and H_α emission from the galactic disk, we conclude that the outer parts of the western arm are embedded in the galactic disk. We do not detect any polarized emission from the inner regions of both the eastern and the western arm. If the inner parts of both arms are embedded in the galactic disk, the lack of polarized emission can be attributed to wavelength-dependent depolarization due to differential Faraday rotation and internal Faraday dispersion (Burn 1966; Sokoloff et al. 1998) caused by the presence of regular and turbulent magnetic fields which are prevalent in the star-forming disk of spiral galaxies. The outer parts of the western arm are not affected by the depolarization effects of the turbulent ISM probably due to the gaps we see in H_I and other tracers. Towards the outer regions of the eastern arm, we do not find any evidence for interaction between the anomalous arm and the spiral arms in the galactic disk. This, taken with the fact that we see relatively small Faraday rotation suggests that outer parts of the eastern arm lie outside the galactic disk.

Thus, we conclude that the anomalous arms in NGC 4258 have an hybrid morphology where the western arm and the inner part of the eastern arm are embedded in the galactic disk while the outer part of the eastern arm is outside

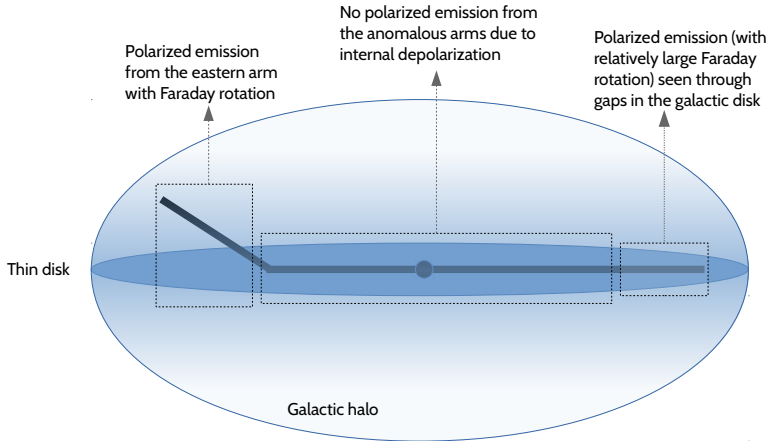


Figure 2.18 – A toy model illustrating the edge-on view of NGC 4258 depicting that the western arm is embedded in the galactic and the outer regions of the eastern arm is outside the disk. The observer is at the top of the figure.

the disk and is located on the near side to the observer. Note that the hybrid model proposed here deviates from the *in-disk* model only in the outer parts of the eastern arm. A toymodel depicting the hydrid morphology of the anomalous arms is shown in Fig 2.18.

Deflection of the jet due to density contrasts in the galactic plane is likely to have caused the outer parts of the eastern arm to leave the disk. From the high resolution LOFAR image (see the left panel of Fig 2.6), we find that the western arm undergoes a number of surface brightness enhancements just before it undergoes morphological change either in the form of arm bending or bifurcation. Bends seen along the western arm have been attributed to deflection of the nuclear outflow due to its interaction with the surrounding molecular gas (see for example [Cecil et al. 1992](#)). In the left panel of Fig 2.14, we find that the total intensity radio continuum emission along the eastern arm undergoes significant enhancement in surface brightness (near position 12:19:06 +47:16:56) coincident with the base of the polarized eastern arm. It is likely that the western arm is deflected near this position when it encounters a local density gradient. Once deflected, the most likely direction the jet can go is out of the galactic plane where the density of the ambient medium is low.

Alternately, a warped outer H_I disk on the eastern side of NGC 4258 in the direction away from the observer can also cause the eastern arm to appear in front of the disk. Warps in the outer parts of galactic disks can be produced by a number of factors including accretion and tidal interaction ([Binney 1992](#); [Sancisi et al. 2008](#)). In the H_I column density map shown in Fig 2.13, at low column density levels ($10 - 60 \times 10^{19} \text{ cm}^{-2}$), multiple filamentary structures are visible in the outer regions of the H_I disk. The most prominent H_I filamentary

structure is located to the east of the galactic disk and has a projected angular size of ~ 31 kpc. The data at hand do not offer any insight into the physical processes that could give rise to the low column density filamentary structure. These filamentary structures could be a sign of either accretion, or remnants of a past interaction. However, no clear evidence for the presence of a warped disk in NGC 4258 is seen in previous kinematic models ([van Albada 1977](#); [van Eymeren et al. 2011](#)). Constructing a new kinematic model for NGC 4258 with the sensitive HALOGAS H α data presented above using methods described in [Józsa et al. \(2007\)](#) and [Di Teodoro & Fraternali \(2015\)](#) could help resolve this issue.

2.7 Summary and conclusions

We have observed the nearby galaxy NGC 4258 in radio continuum using the LOFAR High Band Antenna (HBA) and the Westerbork radio telescope. The main findings presented in this paper are summarized below:

- We have, for the first time, traced the radio continuum emission from the galactic star-forming disk of NGC 4258 out to a distance of 20.73 kpc from its center.
- The integrated radio continuum spectrum of NGC 4258 does not show any spectral curvature between 0.142 and 10.55 GHz. We find that a single power law with an index of $\alpha = 0.63 \pm 0.03$ fits the integrated spectrum best between 0.142 and 10.55 GHz. Locally, flatter spectral indices ($\alpha \sim 0.3$) are seen towards H II regions.
- In addition to NGC 4258, we have also detected ten nearby galaxies within our LOFAR field of view. The integrated flux densities of these galaxies at 0.142 GHz are listed in Table 2.3. Using integrated flux estimates from the literature at 1.4 GHz, we find their spectral indices to lie generally between 0.5 – 0.9.
- Using an extinction-corrected H α image of the disk, we estimate the thermal contribution to the observed synchrotron emission to be less than 10% at both 1.4 GHz and at 141.8 MHz.
- In our high resolution non-thermal spectral index map between 0.142 and 1.4 GHz, we find that the two components of the western anomalous arms show different spectral index profiles. This is most probably due to the effects of spectral ageing. However, we do not see any radial trend in the spectral index distribution along the individual anomalous arms.
- Assuming energy equipartition between magnetic fields and cosmic ray electrons, we have estimated the strength of the total magnetic field in the disk of NGC 4258 to be $7.6\mu\text{G}$.

- The equipartition magnetic field strength varies from about $20\mu\text{G}$ in the inner galactic disk (in anomalous arms) and decreasing to $4\mu\text{G}$ about 20 kpc away from the nucleus.
- Stacking polarized emission from NGC 4258, we find a peak polarization fraction of 6.7% in the galactic disk between -4 rad m^{-2} and -100 rad m^{-2} .
- We do not detect any polarized emission from NGC 4258 at 141.8 MHz.
- The spiral arms in NGC 4258 show clear signs of gaps in regions coincident with the western anomalous arm. This interaction between the western arm and the underlying spiral disk and the large Faraday rotation seen towards the outer parts of the western arm suggests that this arm is embedded in the galactic disk, consistent with the *in-disk* model. Due to the small Faraday rotation seen towards the outer arm and the lack of visible interaction between the eastern arm and the galactic disk, we conclude that the outer part of the eastern arm is outside the galactic disk and located on the near side to the observer.

Chapter 3

Multifrequency radio continuum observations of the Pinwheel galaxy (M 101)

Sridhar, S. S., Heald, G., et al., To be submitted to
Astronomy & Astrophysics

3.1 Introduction

M 101 is a nearby (6.6 ± 0.5 Mpc; [Vinkó et al. 2012](#)) massive face-on spiral galaxy which is the most dominant member of the M 101 group of galaxies. Relevant parameters describing M 101 are listed in Table 3.1. Classified as an SAB(rs)cd galaxy ([de Vaucouleurs et al. 1976](#)), M 101 is known to host a large number of H II regions and H II complexes. More than 1000 H II regions have been identified in the disk of M 101 ([Hodge et al. 1990](#)); it also contains several giant H II complexes each containing a few times 10^6 M_\odot of ionised ([Israel et al. 1975](#)) and neutral ([Viallefond et al. 1981](#)) gas. All giant H II complexes are also known to be X-ray bright ([Kuntz & Snowden 2010](#)).

In addition to hosting massive H II complexes, the outer disk ($R \geq 3$ kpc) of M 101 is asymmetric and lopsided. Deep optical B band imaging with the Burrell Schmidt telescope revealed two prominent extensions in the outer disk: one to the east (called “E Spur”) and the other in the north-easterly direction pointing in the direction of NGC 5422 (referred to as the “NE Plume”) both extending to distances of ~ 38 and ~ 48 kpc respectively from the center of M 101 ([Mihos et al. 2013](#)). Figure 3.1 shows the optical B band image of M 101 along with the positions of the “E Spur” and the “NE Plume”. [Mihos et al. \(2013\)](#) also find that the optical B band morphology of features in the outer disk of M 101 matches well with features seen in neutral hydrogen. The asymmetric structure of the outer disk of M 101 has long been attributed to recent or past interactions with one or more of its companion galaxies (see for example [Waller et al. 1997](#)).

Evidence for past interaction stems from several independent observations including the lopsided gas distribution (for example, see [Baldwin et al. 1980](#)), non-circular gas motion in the outer disk ([Kamphuis 1993](#)), the presence of a massive ($\sim 10^8$ M_\odot) high-velocity gas complex ([Van der Hulst & Sancisi 1988](#)), and the presence of multiple linear arm segments visible in FUV ([Waller et al. 1997](#)) and H I in the outer disk. The outer asymmetric disk is optically blue ([Mihos et al. 2012](#)) with associated emission in UV ([Thilker et al. 2007](#)) which is probably due to star formation triggered by interaction. Furthermore, observations of M 101 across multiple wavelengths regimes including X-rays ([Kuntz et al. 2003; Warwick et al. 2007; Kuntz & Snowden 2010](#)), optical ([Mihos et al. 2013](#)), H I ([Kamphuis 1993](#)), CO ([Helper et al. 2003](#)), FUV ([Waller et al. 1997](#)), and mid-IR ([Jarrett et al. 2013](#)) all reveal the presence of short segments of spiral arms with abrupt changes in the pitch angle. The presence of such short linear spiral arm segments has also been attributed to galactic interaction in the past (see for example [Mihos et al. 2012](#)).

M 101 was first detected in radio continuum at 158 MHz using the 250 ft paraboloid at Jodrell Bank observatory ([Brown & Hazard 1961](#)). Since 1961, numerous papers have been published based on radio continuum observations of M 101. [Israel et al. \(1975\)](#) observed M 101 using the then newly built Westerbork Synthesis Radio Telescope (WSRT) and detected radio continuum emission from the giant H II regions. Using the Effelsberg radio telescope, [Graeve et al. \(1990\)](#) found that the radio spectrum of M 101 can be fit with a simple power-law with index $\alpha = 0.72 \pm 0.04$. This multifrequency study with the Effelsberg telescope

Table 3.1 – Physical properties of M 101.

Parameter	Value	Reference
Morphology	SAB(rs)cd	1
Distance	6.6 ± 0.5 Mpc	2
Position angle (PA)	40° ($R < 7'$)	3
	35° ($R > 7'$)	3
Inclination (i)	27° ($R < 7'$)	3
	25° ($R > 7'$ inSW)	
	40° ($R > 7'$ inNE)	
R_{25}	$8'$	4
M_B	-21.0	5
H I mass	$2.1 \times 10^{10} M_\odot$ at 7.2 Mpc	3

References. (1) [de Vaucouleurs et al. \(1976\)](#); (2) [Vinkó et al. \(2012\)](#); (3) [Kamphuis \(1993\)](#); (4) [Mihos et al. \(2013\)](#); (5) [de Vaucouleurs et al. \(1991\)](#)

also resulted in the first spectral index map of M 101. The first measurement of linearly polarized synchrotron emission towards M 101 was obtained at $\lambda 6.3$ cm using the Effelsberg radio telescope ([Graeve et al. 1990](#)). The orientation of the measured polarization vectors indicated the presence of a large-scale magnetic field aligned with the spiral arms. Further polarimetric observations of M 101 using the Effelsberg telescope by [Berkhuijsen et al. \(2016\)](#) revealed that the total magnetic field strength in M 101 is dominated by the random component of the magnetic field and that the random magnetic field strength is stronger than the ordered magnetic field by a factor of about 2.4.

While M 101 has been observed in radio continuum, previous studies in the literature have largely been based either on low resolution single dish observations or using interferometric observations that were not sensitive enough to study the diffuse radio continuum disk of M 101. In this first of a series of publications on this object, we present a detailed investigation of the synchrotron emitting disk of M 101 using radio continuum observations with the WSRT and the LOFAR radio telescopes that provide substantial improvements in sensitivity and in resolution as compared to previous radio continuum studies of M 101. In subsequent publications, we will present linear polarization measurements to map the orientation of the large-scale magnetic field in the galaxy and use the multi-frequency radio continuum images to model the propagation of cosmic ray electrons in M 101.

This chapter is organised as follows: In section 3.2 and 3.3, we present the observational setup and the data reduction procedure we followed to calibrate and image the WSRT and LOFAR datasets. In section 3.4, we present the radio continuum morphology of M 101 at four observed radio frequencies and discuss its relation to the H I disk of M 101. In section 3.7, we estimate the contribution of the free-free thermal emission to the observed radio continuum using H α and *Spitzer* images of M 101. After subtracting the estimated thermal contribution, in sections 3.8 and 3.9, we use the non-thermal radio continuum images to compute

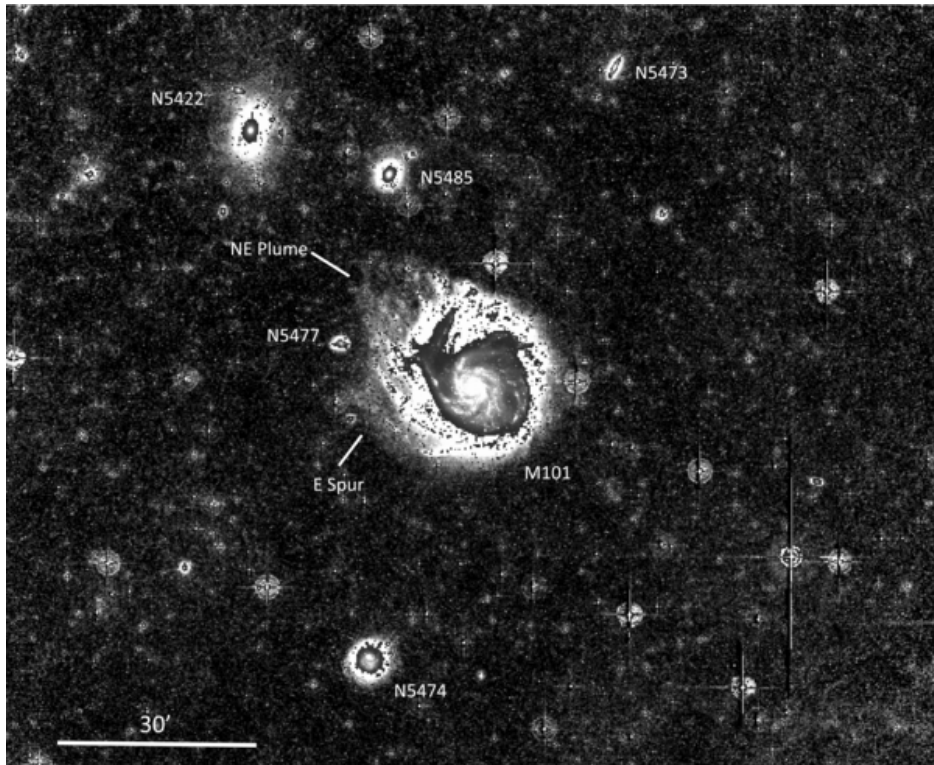


Figure 3.1 – Optical B band image of M 101 showing the locations of the two prominent extensions in the outer disk: “E Spur” and “NE Plume”. Image credit: [Mihos et al. \(2013\)](#)

the non-thermal spectral index images and equipartition magnetic field strength in M 101. Throughout this chapter, we follow the convention for spectral index α such that α is related to flux density S_ν as $S_\nu \propto \nu^{-\alpha}$.

3.2 WSRT observations and data reduction

We observed M 101 with the WSRT at 0.355, 1.4, and 2.27 GHz for multiple 12-hour tracks. Relevant observational parameters are listed in table 3.2. Each 12-hour track was bracketed with a 10-minute scan on a set of suitable polarized and unpolarized calibrator sources. The observations were carried with the array in the maxi-short configuration¹. Note that not all 14 Westerbork antennas were used during the 1.4 and 2.27 GHz observations due to the ongoing APERTIF² telescope upgrade (Oosterloo et al. 2009).

We used a common procedure to calibrate and image all three WSRT datasets. For most of the data reduction, we used the Common Astronomy Software Applications (**CASA**) package version 4.2.1 (McMullin et al. 2007) to calibrate the datasets. However, as **CASA** could not read the WSRT’s system temperature (T_{sys}) tables, we first imported the visibilities into **AIPS** (Greisen 1998) and applied T_{sys} corrections following the instructions provided in the WSRT data reduction cookbook³. After the system temperature correction, the datasets were exported to **UVFITS** format so that they could be read into **CASA**.

Each continuum dataset corresponding to a single 12-hour track was calibrated separately. Using **CASA**, we first derived bandpass solutions for each 12-hour track using the respective flux calibrators. The bandpass corrected visibilities of each calibrator were then flagged for radio frequency interference (RFI) using the semi-automated RFI excision tool **AOFagger** (Offringa et al. 2010, 2012). Bandpass solutions were applied prior to RFI flagging to ensure identification of RFI sources located close to the edge of each spectral window.

After RFI excision, we extracted the uncalibrated but RFI-flagged visibilities present in the **DATA** column of the measurement set to derive the gain solutions following the standard data reduction procedure. Amplitude calibration for the 92 cm dataset was carried out using the flux scale defined in Scaife & Heald (2012) while all other datasets were calibrated using the Perley & Butler (2013) flux scale. The calibrated target field visibilities were then imported into **miriad** (Sault et al. 1995) for self-calibration and imaging.

A few iterations of self-calibration were carried out to improve the applied phase solutions to the target field by progressively improving the model of the sky. With each iteration, we improved the CLEAN mask to include the diffuse emission from M 101. This was repeated until all detected radio emission was included in the model. During self-calibration, we noticed that the primary flux calibrator 3C 295 was present in the antenna sidelobes in the 92cm and the 20cm

¹<https://www.astron.nl/radio-observatory/astronomers/wsrt-guide-observations/3-telescope-parameters-and-array-configuration>

²www.apertif.nl

³<http://astron.nl/radio-observatory/astronomers/analysis-wsrt-data/analysis-wsrt-dzb-data-classic-aips/analysis-wsrt-d>

Table 3.2 – WSRT observational parameters.

Parameters	13 cm	20 cm	92 cm
RA (J2000)	14:03:12.51	14:03:12.00	14:03:12.60
Dec (J2000)	54:20:53.10	54:21:00.00	54:20:57.00
Integration time	4 × 12 hours	4 × 12 hours	4 × 12 hours
Correlations recorded	RR, RL, LR, LL	XX, XY, YX, YY	XX, XY, YX, YY
Flux calibrator	3C138	3C138	3C147
Secondary calibrator	3C147	3C147	PSR1937+21
WSRT Telescopes used	11/14	13/14	14/14
Bandwidth (MHz)	160.0	80.0	80.0
No. of channels	8 × 64 = 512	4 × 64 = 256	8 × 128 = 1024
Ch0 frequency (MHz)	2199.375	1440.625	320.078

datasets. For these two datasets, we subtracted 3C295 from the visibilities using the standard “peeling” technique ([Noordam 2004](#)).

Each self-calibrated uv dataset was imaged separately with Briggs weighting ([Briggs 1995](#)) using $\text{robust} = -0.25$. Clean masks from the self-calibration cycle were used to deconvolve each dirty image and the noise level in the respective stokes-V map was used to set the deconvolution threshold level. The deconvolved images were corrected for the primary beam of the WSRT which is given by the relation

$$A(r) = \cos^6(c\nu r) \quad (3.1)$$

where ν is the observational frequency, r is the distance from the pointing center in degrees and c is a constant that depends on the light crossing time across the effective diameter of the parabolic dish ([Brentjens 2008](#)).

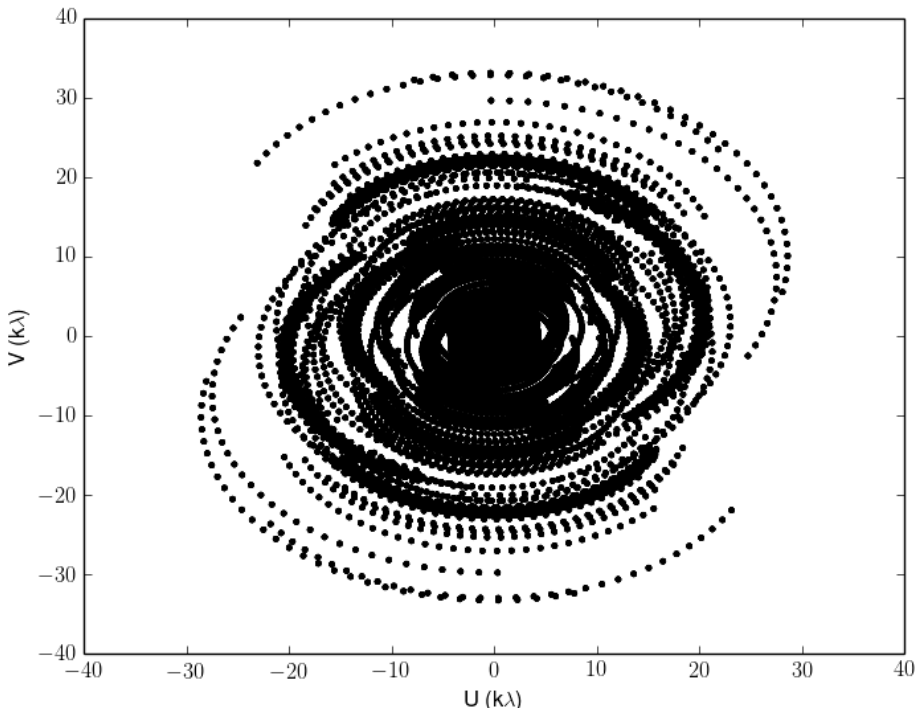
3.3 LOFAR observation and data reduction

The target galaxy M 101 and the calibrator source 3C 295 were observed with the LOFAR High Band Antenna (HBA) on 2013 June 26. Owing to the multi-beam capabilities of LOFAR and the proximity of 3C 295 to M 101, both the target field and the calibrator field were observed simultaneously for about eight hours covering a frequency range from 115 – 176 MHz with a 1s integration time. This 60.2 MHz bandwidth was split into 244 subbands (SBs), each in turn subdivided into 64 channels each with a channel width of 3 kHz. Such a high time and frequency resolution were used to identify and flag narrowband radio frequency interference (RFI). An overview of the observational parameters is presented in table 3.3.

The observations were carried out with the telescope in the ‘HBA_Dual_Inner’ configuration where each core station is split into two stations (HBA0 and HBA1) and only those tiles in the inner 31.3m were used for remote stations. This setup was chosen so as to achieve a common station beam size for both core and remote stations. The uv-coverage for this LOFAR observational setup is shown in fig 3.2.

Table 3.3 – LOFAR HBA Observational parameters

Parameter	Value
Measurement ID	L151878 (3C 295) L151879 (M 101)
Pointing centre	14h03m12.5441s +54d20m56.2200s
Integration time	1 s
Total on-source time	7.93 hr
Total bandwidth	60.2 MHz
Observation date	2013 June 26
Correlations	XX, XY, YX, YY
Frequency range	115 – 176 MHz
Subbands (SB)	244
Bandwidth per SB	195.3125 KHz
Channels per SB	64
LOFAR Array Mode	HBA Dual Inner
Stations	61 total 24 core (each split in two) 13 remote (Dutch)

**Figure 3.2** – *uv*-coverage for a single LOFAR sub band at 120 MHz. Note that each *uv* point represents 150 data points along the time axis.

During observations, a bug in the radio observatory’s software caused the measurement sets to contain wrong header information about broken tiles in each LOFAR station. Note that this does not affect the visibility data in the measurement set. The header information was corrected using a script⁴ provided by the radio observatory.

RFI excision was carried out on the raw visibilities with a 1 s time resolution and a frequency resolution of 64 channels per 195 kHz wide sub band using AOFlagger (Offringa et al. 2010, 2012). After RFI flagging, we averaged the visibilities down to a time resolution of 6 s and a frequency resolution of 8 channels per sub band using the New Default Pre-Processing Pipeline (NDPPP). In addition to RFI flagging, the core LOFAR stations CS013HBA0 and CS013HBA1 were also flagged due to the known problem of misaligned dipoles that existed at the time of observation.

The calibrator measurement sets were then used to derive antenna gain solutions with Black Board Selfcal (BBS) software (Pandey et al. 2009) on a timescale of 6s for each SB separately using a skymodel for 3C 295 containing two point-source components assuming the total flux scale defined in Scaife & Heald (2012). The derived gain solutions were then used to obtain the antenna gain amplitudes, a station-based offset between XX and YY phases and a correction term for clock offset between the core and remote stations. This correction for clock offset is important because though the core stations are all connected to a common clock, the remote stations all have their own clocks which are not synchronised with the core stations’ clock. The magnitude of the clock offset is expected to be of the order of 100ns which if not corrected can cause noticeable phase delays on core-remote and longer baselines. The antenna gain solutions were also used to derive median phase offsets between the X and Y parallel hands for each station. The derived median clock offset, X-Y phase offset and gain amplitudes were then applied to the target field visibilities using BBS. Note that this procedure corrects only for the clock offset and not for the clock drift that occurs within an observing run.

After correcting the target field visibilities using gain solutions derived from the calibrator scan, we performed “A-team clipping” to remove the contribution from bright, off-axis “A-team” sources (Cyg A, Cas A, Vir A, and Tau A). This was done by simulating model visibilities corresponding to each “A-team” source into the MODEL_DATA column of the target MSs and flagging the times and frequencies per baseline where the predicted flux from these sources exceeded 5 Jy. As the primary calibrator 3C 295 is $\sim 2.5^\circ$ away from M 101, deconvolution errors associated with this ~ 100 Jy source can affect all subsequent processing. To avoid this, we also subtracted 3C 295 from the visibilities using the standard “peeling” procedure.

Phase calibration was done with a skymodel extracted from the TIFR GMRT Sky Survey (TGSS ADR1; Intema et al. 2017) image of the field using the source finder pyBDSF⁵ (Mohan & Rafferty 2015). The extracted skymodel contains 1791

⁴<https://www.astron.nl/radio-observatory/observing-capabilities/depth-technical-information/system-notes/wrong-information->

⁵<http://www.astron.nl/citt/pybdsf/>

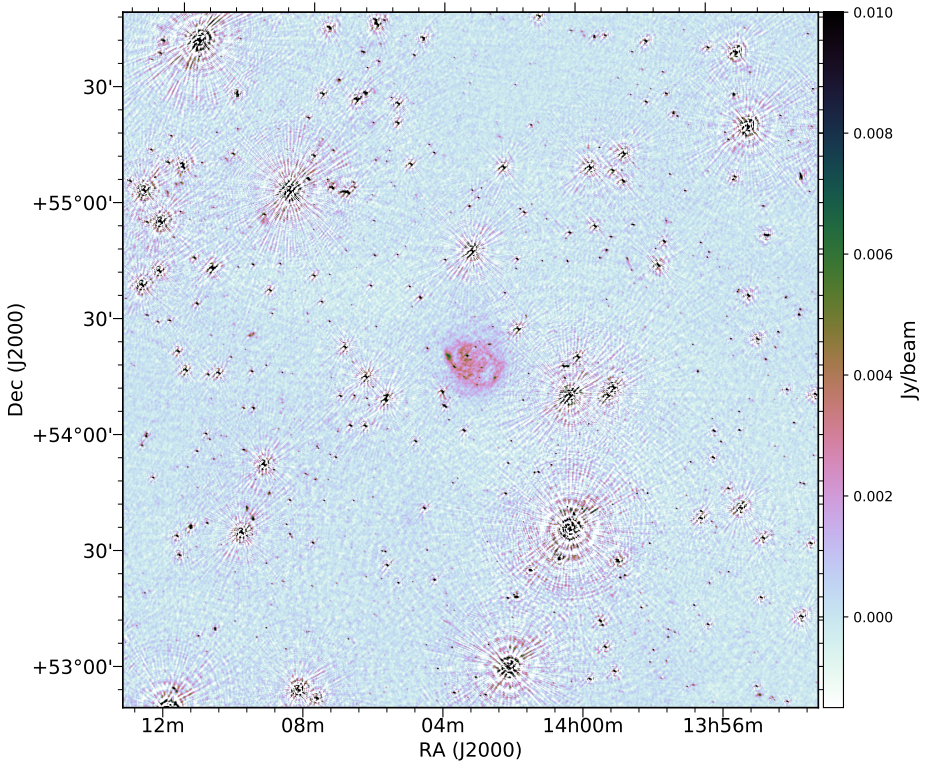


Figure 3.3 – A $17.8'' \times 13.5''$ resolution image with a $3^\circ \times 3^\circ$ field of view centered on M 101. Note that the LOFAR data was imaged after peeling 3C 295 from the visibilities. The artefacts seen around bright background point sources are due to residual direction-dependent errors that have not been corrected at this stage. The image has been corrected for LOFAR primary beam response and the rms noise near M 101 is $470\mu\text{Jy}/\text{beam}$.

components (378 point and 1413 gaussian). Since 3C 295 has been subtracted from the visibilities, the two corresponding gaussian components were manually identified and removed from the skymodel. A solution interval of 6 s was used and one solution was derived for each 2 MHz sub band block assuming no variation in the LOFAR station beam across the 2 MHz bandwidth.

The phase calibrated visibilities were then merged using NDPPP before imaging. Imaging and deconvolution were carried out using the AWIImager (Tasse et al. 2013) which was specifically written for LOFAR and corrects for both A-projection (Bhatnagar et al. 2008) and W-projection (Cornwell et al. 2008). A $17.8'' \times 13.5''$ resolution image imaged with a $13.3\text{ k}\lambda$ uv-cut and a robust value of -0.3 is shown in figure 3.3. While Figure 3.3 shows M 101 at the field center, the image is dominated by artefacts around background point sources due to residual direction-dependent effects that have not been corrected at this stage.

We next used the new LOFAR facet calibration algorithm (van Weeren et al. 2016; Williams et al. 2016) to correct for the direction-dependent artefacts seen

around bright point sources in Figure 3.3. We present a brief overview of the calibration procedure here. For a detailed discussion on the calibration algorithm, we refer the reader to van Weeren et al. (2016), Williams et al. (2016) and Appendix A. The facet calibration algorithm derives direction-dependent calibration solutions by dividing the LOFAR field of view into a number of facets such that each facet contains at least one point source that is brighter than 0.4 Jy. Splitting the field of view into multiple facets is achieved using Voronoi tessellation. For each facet, we derived local gain solutions by self-calibrating on the bright point source within that facet. We then applied the derived gain solutions to all the sources that lie within that facet. The facet containing M 101 was calibrated using direction-dependent gain solutions derived using the source *NVSS 140016+541139* which is about 0.45° from the center of M 101.

After applying direction-dependent corrections, we imaged the facet containing M 101 using the WSClean imager (Offringa et al. 2014). We inverted the visibilities using the Briggs weighting scheme (Briggs 1995) with `robust`=−0.7 and a Gaussian taper. Such a combination of uniform visibility weighting scheme and tapering was needed to minimise the PSF sidelobes while retaining the diffuse emission. The inverted images were deconvolved down to a 1σ threshold using a CLEAN mask and making use of the wideband deconvolution algorithm⁶ that is available in WSClean which accounts for spectral curvature within the bandpass.

We compared the integrated flux densities of a few point sources in the field with flux densities measured by the TGSS ADR1 and noticed that the LOFAR flux densities were systematically lower by a factor of 1.12. All LOFAR flux density estimates reported from here on have been corrected for this factor. We do not see any obvious astrometric position offsets compared to TGSS ADR1.

3.4 Radio continuum morphology of M 101

Smoothed total intensity contours of M 101 at 146, 355, 1400, and 2270 MHz overlayed on a *GALEX* NUV image are shown in Figure 3.4. While M 101 can be imaged at higher angular resolution (up to about 6'') using the LOFAR HBA dataset, due to the low surface brightness nature of the synchrotron emitting disk of M 101, high resolution images resolve out most of the diffuse radio continuum emission from the galactic disk and only a few bright, compact sources (like the H II regions) are visible clearly in the high resolution map. Since our primary interest is in the diffuse emission, we make use of the low-resolution imaging henceforth.

Radio continuum emission from the disk of M 101 comprises a superposition of diffuse, weak synchrotron emission from the disk and discrete localised emission from giant H II complexes. We find that the eastern and the north-eastern parts of the galactic disk dominate the total radio continuum emission at all four observed frequencies. In the south and the south-western part of the galaxy, we find weak diffuse emission from the prominent spiral arm hosting the giant H II region complex NGC 5447 (see Figure 3.4). The eastern spiral arm, which contains two

⁶<https://sourceforge.net/p/wsclean/wiki/WidebandDeconvolution/>

of the five large H_{II} complexes in M 101 (namely NGC 5461 and NGC 5462), shows a steep transverse intensity gradient in all our radio images along its entire length. At 1.4 GHz, the contours shown in Figure 3.4 drop in intensity by more than an order of magnitude within a synthesized beamwidth.

We see a large interarm region in the south-western part of M 101 near the H_{II} region NGC 5447. We find that the interarm region is devoid of detectable radio continuum emission in all our radio maps. At the highest frequency, the interarm region spans about 85° in azimuth and about 5.5 kpc at its widest point. Comparing our radio continuum images with the H_I column density distribution in M 101 (see section 3.5), we find that this interarm region is devoid of neutral gas. It is also interesting to note that the size of this interarm region decreases with decreasing frequency at fixed angular resolution indicating that at low radio frequencies, cosmic ray electrons from the surrounding spiral arms are perhaps diffusing into the interarm region. A similar signature of diffusion from material spiral arms in to the interarm regions has been seen in M51 by [Mulcahy et al. \(2014\)](#).

Beyond a distance of about 10 kpc from the nucleus, the total intensity radio continuum emission from the disk of M 101 shows an asymmetric distribution in all our radio continuum images. The radio emission is more extended towards the south-west than the north-east, mimicking the asymmetry in the distribution of star formation as traced by UV. The distribution of H_{II} regions shows similar lopsidedness as identified long ago by [Hodge et al. \(1990\)](#). Both the 146 and the 355 MHz radio images show extensions towards the south and the south-east. The diffuse extended emission seen towards the south-east coincides with the onset of the eastern spur identified in the deep optical image of M 101 (denoted as “E Spur” in [Mihos et al. 2013](#)). In the north-western part of the galaxy, we find that the radio emission at 355 MHz traces almost the entire length of the outermost spiral arm forming another interarm region. The 355 MHz image shows the most extended synchrotron emitting disk of M 101.

3.5 The H_I disk and the high-velocity gas complex

Figure 3.5 shows the neutral hydrogen column density map of M 101 overlayed with 355 MHz radio continuum contours shown in black. The neutral hydrogen observations of M 101 were performed as part of the 1.4 GHz WSRT observations mentioned in Table 4.3. The column density image of M 101 shown in Figure 3.5 has a resolution of 30''. A complete analysis of the H_I spectral line data including a new kinematic model of M 101 will be presented in a future paper (Oosterloo et al. in prep).

The column density distribution of H_I shown in Figure 3.5 reveals large concentrations of neutral gas associated with the spiral arms in the east and in the south. The largest concentrations of H_I in these spiral arms coincide with four of the five giant H_{II} regions found in M 101.

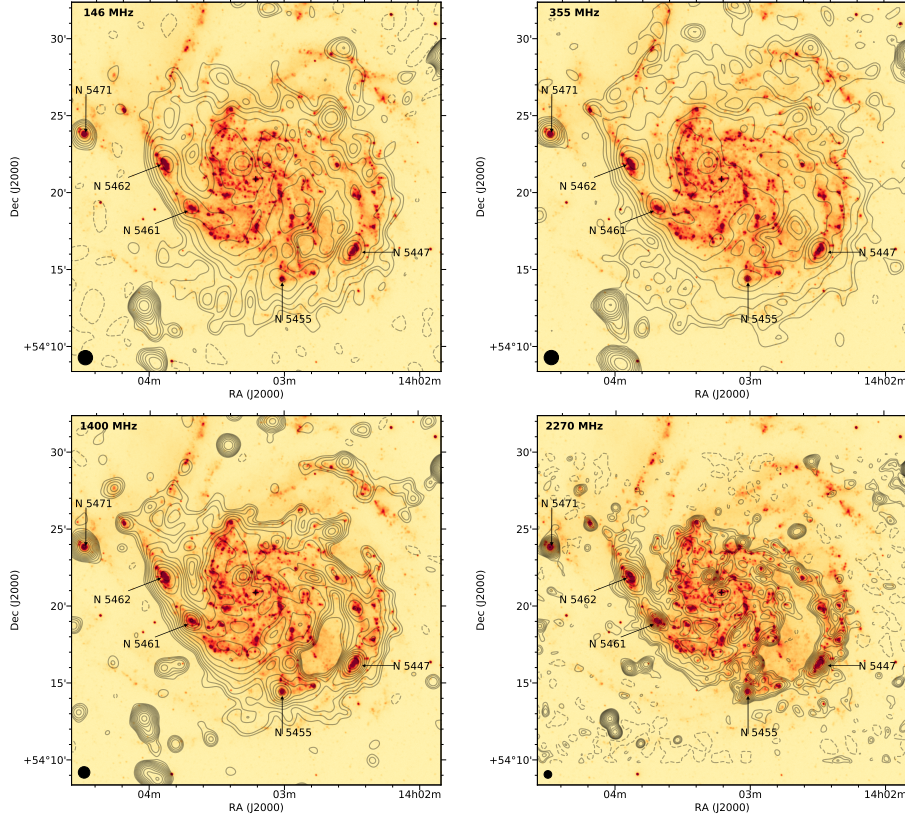


Figure 3.4 – Total intensity radio continuum contour lines of M 101 at 146, 355, 1400, and 2270 MHz overlaid on a *GALEX* NUV image of M 101. The size of the synthesized beam is indicated in the lower left corner of the each image. The five giant H II complexes labelled in the figure are discussed further in the text. The position of the nucleus is indicated using a ‘+’ symbol in all four images.

To the east of the eastern spiral arm containing the H II regions NGC 5461 and NGC 5462, the column density map shows a lack of H I along almost the entire length of the eastern spiral arm (indicated with a black arrow in Figure 3.5). This H I trough is about 26 kpc long and about 2.5 kpc wide. Comparing the radio continuum morphology along the eastern spiral arm with the H I column density, we find that this 26-kpc long H I trough coincides with the steep transverse intensity gradient seen along the eastern spiral arm in radio continuum.

The white contour lines overlayed on the column density map in Figure 3.5 show the structure of a large high-velocity complex in M 101. The column density map of the high-velocity gas complex was generated by summing all the H I in channel maps with velocities ranging from 351.82 km/s to 475.49 km/s. The high-velocity gas complex was discovered by [Van der Hulst & Sancisi \(1988\)](#) using neutral hydrogen observations of M 101 with the WSRT. It has a mass of a few times $10^8 M_\odot$ and deviates from local galactic rotation by 130 – 160 km/s. The origin of this and similar high-velocity gas seen in other nearby galaxies is still uncertain (for a review on high-velocity gas, see [Sancisi et al. 2008](#)). [Van der Hulst & Sancisi \(1988\)](#) rule out the possibility that the high-velocity complexes are gas expelled from the disk by supernova explosions or wind from OB associations because of the enormous kinetic energy ($\sim 10^{55}$ erg) that would be required to expel $\sim 10^8 M_\odot$ gas from the disk. Furthermore, there is no clear evidence for similar energetic events at other wavelength regimes (see for example [Stecher et al. 1982; Israel et al. 1975](#)). [Van der Hulst & Sancisi \(1988\)](#) favour a cloud-galaxy collision scenario where a $10^6 - 10^8 M_\odot$ gas cloud complex collides with the galactic disk to produce large H I structures like the ones seen in M 101.

[Combes \(1991\)](#) proposed an alternative scenario in which gravitational interaction between M 101 and its dwarf companion NGC 5477, with a mass ratio of 100:1, could have displaced the gas from the disk resulting in the observed high-velocity gas accompanied by a trough in the gas disk. In Combes' scenario, NGC 5477 passed through the outer disk and caused removal of gas from the disk, gas that we now observe as the high-velocity gas in M 101. The high-velocity gas will eventually fall back in to the disk, but it is unclear what stage of the interaction we are witnessing.

While the radio continuum emission cannot be used to discriminate between the two different scenarios, the morphology of the radio continuum emission and the presence of 26-kpc trough along the eastern spiral arm provides additional evidence for interaction between the high-velocity gas and the galactic disk. The radio continuum shows two sharp edges at the northern and the eastern side of the disk, lining up remarkably well with the morphology of the high-velocity gas (see right panel of Figure 3.5). Such steep edges have been seen in other galaxies like NGC 4501 ([Vollmer et al. 2008](#)) and NGC 2276 ([Hummel & Beck 1995](#)). In these cases, such sharp edges have been explained by compression by an external medium. Magnetohydrodynamical simulations show that compression and shear can cause a significant increase in radio continuum emission ([Otmianowska-Mazur & Vollmer 2003](#)). The enhancement of the continuum emission in their simulation is mainly the result of re-accretion of stripped material which happens about a Gyr after the stripping event.

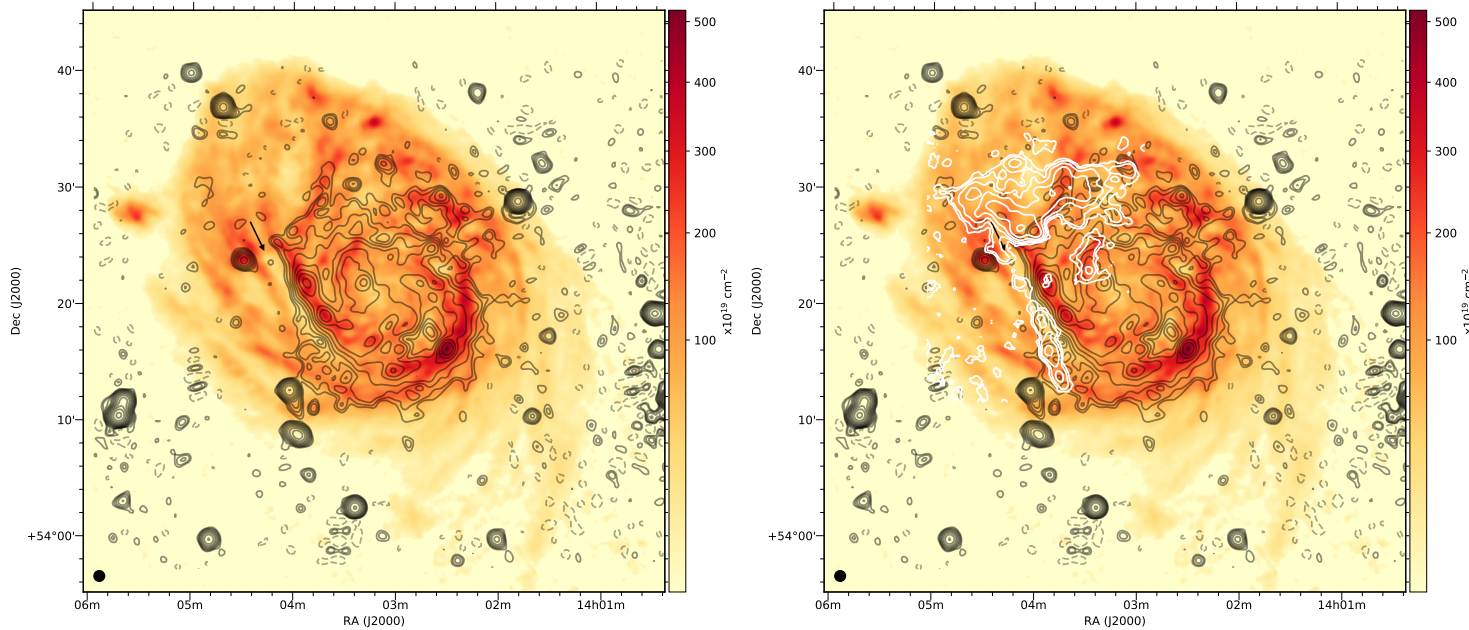


Figure 3.5 – Left: Total intensity 355 MHz radio continuum contours overlaid on a 30''H_I column density map. The black arrow indicates the position of the H_I ridge that runs along the steep transverse intensity gradient seen in radio continuum along the SE spiral arm. The image also shows extended diffuse radio continuum emission in the outer radio continuum disk of M 101. **Right:** Neutral hydrogen column density contours of a high-velocity gas complex overlayed on the image on the left. The white contour lines indicate H_I emission from the high-velocity gas between 351.82 – 475.49 km/s. The contour lines are drawn at levels $0.025 \times 2^n \text{ mJy/beam km/s}$ where $n = 0, 1, 2, \dots$. The high-velocity gas complex is about 130 – 160 km/s away from the local gas participating in the regular disk rotation.

3.6 Integrated flux densities and radio spectrum

While measuring the integrated flux density of M 101 from our radio images, we noticed that, due to its relatively large angular size, the diffuse radio emission, especially in the outer parts of M 101, is confused with a number of background radio sources. In total, we identified several distinct radio sources (including NVSS 140318+542159, NVSS 140238+542500, NVSS 140402+541237, NVSS 140357+540852, and NVSS 140147+542852) that could potentially be confused with diffuse radio continuum emission from M 101. To avoid over-estimating the integrated flux density of M 101, we first manually masked the confusing background point sources before integrating the pixel values.

The integrated flux density of M 101 at the four observed frequencies alongside a compilation of integrated flux densities reported in the literature is listed in Table 3.4. From Table 3.4, it is easy to notice that our reported integrated flux density at 1.4 GHz is lower than the literature values. This mismatch between our measurement and the values from the literature is due to the fact that the literature estimates are all based on low resolution images of M 101 and hence were over-estimated due to source confusion. For example, [Rogstad & Shostak \(1971\)](#) report an integrated flux density of 0.82 ± 0.10 Jy based on a $4'$ map of M 101. We convolved our 1.4 GHz WSRT radio continuum image to $4'$ resolution and estimated the integrated flux of M 101 to be 0.74 Jy if we do not mask the confusing background radio sources. Thus, we conclude that all low resolution estimates presented in the literature overestimate the integrated flux density of M 101.

For literature flux density estimates at 2.7 GHz and higher, single dish observations have sufficient resolution to distinguish the background radio sources from the diffuse continuum disk of M 101. [Graeve et al. \(1990\)](#) recognize that the source NVSS 140147+542852 could in fact be a background radio source. However, [Graeve et al. \(1990\)](#) report that they estimated the flux density of M 101 by integrating all radio continuum emission within a radius of $14'$ from the center of M 101 which includes all background sources mentioned above. Thus, we further assume that the integrated fluxes at 2.7, 4.75, and 10.7 GHz reported by [Graeve et al. \(1990\)](#) are affected by background source confusion.

Given that the literature values listed in Table 3.4 all over-estimate the integrated flux density of M 101, we compute the integrated radio spectrum of M 101 using only those flux densities estimated from our radio images. From the radio spectrum shown in the left panel of Fig 3.6, we see that a single power-law profile could not be used to fit all four flux density estimates. Only the WSRT flux density estimates could be fit using a power-law with a spectral index $\alpha = 1.03 \pm 0.08$. The flux density measured from our LOFAR HBA image is about 48% lower than the flux density predicted at 146 MHz using the power-law spectral index derived above.

This deviation from a power-law spectral index at low radio frequencies could be due to instrumental effects like flux scale error or due to an astrophysical effect like free-free absorption where the synchrotron emission is absorbed by the ionised gas. Based on the flux density comparison performed in section 3.3 between TGSS

Table 3.4 – Integrated flux densities of M 101. Note that the integrated flux density of M 101 reported in the literature all include confusing background point sources and hence are an over-estimate of the true integrated flux density.

Frequency (GHz)	Integrated flux density (Jy)	Reference
0.057	6.5 ± 2.5	1
0.146	2.14 ± 0.21	2
0.178	2.66 ± 0.55	7
0.355	1.87 ± 0.09	2
0.610	1.45 ± 0.10	8
0.750	1.21 ± 0.40	3
1.4	0.53 ± 0.03	2
1.4	0.75	4
1.4	0.808	5
1.4	0.820 ± 0.100	10
1.415	0.930 ± 0.130	11
2.270	0.333 ± 0.016	2
2.700	0.520 ± 0.060	12
4.750	0.335 ± 0.020	12
5.0	0.150 ± 0.025	6
10.7	0.207 ± 0.020	12

References. (1) Israel & van Driel (1990); (2) this work; (3) Heeschen & Wade (1964); (4) Condon et al. (2002); (5) White & Becker (1992); (6) Sulentic (1976); (7) Caswell & Wills (1967); (8) Israel et al. (1975); (10) Rogstad & Shostak (1971); (11) de La Beaujardière et al. (1968); (12) Graeve et al. (1990);

and our LOFAR image, it is highly unlikely that this is caused by a flux scale error. Furthermore, the radio spectrum of the source NVSS J140147+542852 (about 15' away from the center of M 101) shown in the right panel of Fig 3.6 shows no sign of flux scale error at low radio frequencies. The shortest projected baseline the LOFAR HBA observation is sensitive to is about 20λ which corresponds to an angular extent of about 172'. Since the angular size of M 101 in radio continuum is much smaller than the largest angular scale detectable by the interferometer, the observed low flux density at 146 MHz is likely not due to the missing short spacing problem. Thus, we conclude that the low integrated flux density seen at 146 MHz is due to free-free absorption occurring throughout the disk of M 101.

To estimate the emission measure of the absorbing medium, we fitted our four integrated flux densities with a function of the form

$$S = S_0 \left(\frac{\nu}{\nu_0} \right)^{-\alpha} e^{-\tau} \quad (3.2)$$

where α is the spectral index, τ is the optical depth, and S and S_0 are the flux densities measured at frequencies ν and ν_0 . The optical depth τ is related to the emission measure (EM) and the electron temperature of the warm medium (T_e) through the relation

$$\tau = \frac{8.2 \times 10^{-2} \nu^{2.1} EM}{T_e^{1.35}}. \quad (3.3)$$

As mentioned earlier, a significant fraction of the non-thermal synchrotron emitting disk is covered by H II regions (see for example Hodge et al. 1990), and we assume the electron temperature is of the order of 10^4 K (Mezger & Henderson 1967). The fitted spectral profile including free-free absorption is shown in Fig 3.6. The fit resulted in a spectral index of $\alpha = 1.13 \pm 0.08$ with emission measure $EM = 5.7 \pm 1.4 \times 10^4$ pc cm $^{-6}$. The fitted emission measure in M 101 is about an order of magnitude smaller than the values seen towards the nearby galaxies M 82 (Adebahr et al. 2013) and NGC 253 (Kapińska et al. 2017). If, however, the dominant absorbing media is due to the cool ($T_e \sim 10^3$ K) as suggested by Israel & Mahoney (1990), then the fit results in $EM = 2.5 \pm 0.6 \times 10^3$ pc cm $^{-6}$.

The emission measure is defined as

$$EM = \int_0^l n_e^2 ds \quad (3.4)$$

where n_e is the number density of the ionised medium and l is the path length through the ionised medium. Expressing the path length l in units of 1 kpc, $EM = 5.7 \pm 1.4 \times 10^4$ pc cm $^{-6}$ corresponds to $n_e = 7.5 \sqrt{l/1 \text{ kpc}} \text{ cm}^{-3}$.

3.7 Estimating the thermal contribution

The radio continuum emission observed from nearby galaxies at frequencies between 146 MHz and 2.27 GHz is a combination of both thermal (originating from free-free emission) and non-thermal radio emission (synchrotron radiation

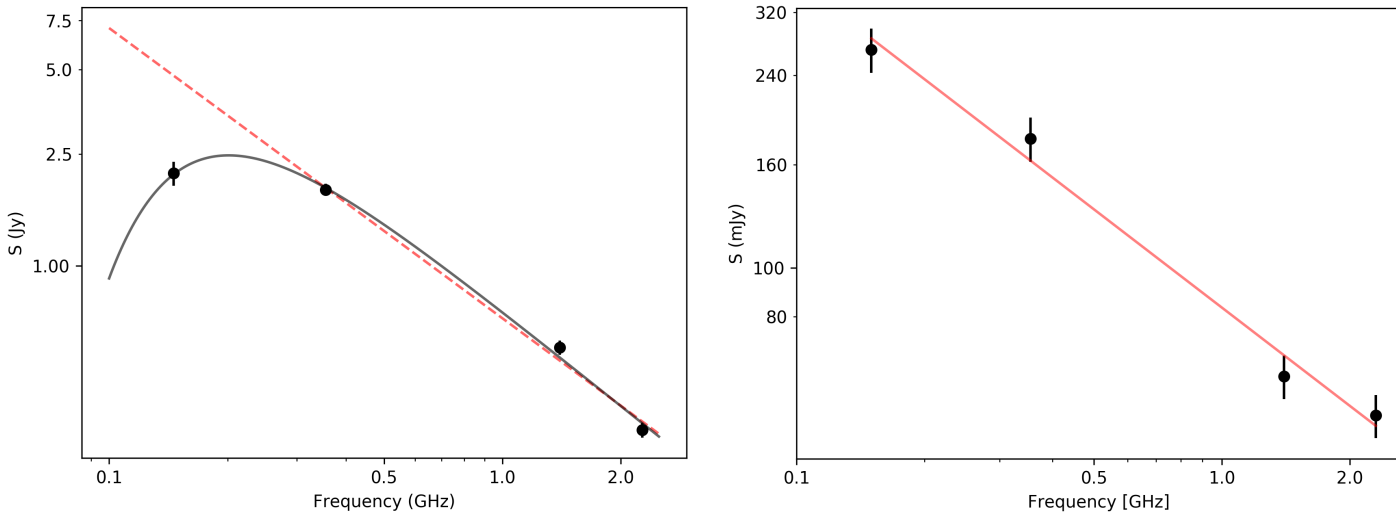


Figure 3.6 – Left: Radio spectrum of the integrated emission from M 101 using the flux densities estimated from our radio images. The four flux densities shown in the plot do not follow a power-law spectral index profile. The broken red line shows a power-law fit ($\alpha = 1.03 \pm 0.08$) to the three WSRT flux densities. The black line shows a spectral index fit including a term for free-free absorption (see equation 3.2). **Right:** Radio spectrum of the source NVSS J140147+542852. All four flux densities can be fit using a power-law with spectral index $\alpha = -0.64 \pm 0.05$. The power-law fit to the flux densities demonstrates that our LOFAR image does not suffer from a systematic flux scale error.

emitted by relativistic electrons accelerating across interstellar magnetic field lines). Thus, to be able to model the magnetic field distribution and propagation of cosmic ray electrons in the interstellar medium of galaxies as traced by the non-thermal synchrotron emission, an estimate of the thermal free-free emission has to be subtracted from the observed radio continuum emission.

We estimated the thermal contribution to the total radio continuum emission at 146, 355, 1400, and 2270 MHz using a foreground-corrected KPNO H α map of M 101 (Van Zee, private communication). Following [Hunt et al. \(2004\)](#), the radio flux at a given frequency due to thermal contribution can be estimated using the relation

$$\left(\frac{F_\nu}{\text{mJy}} \right) = 1.16 \left(1 + \frac{n(\text{He}^+))}{n(\text{H}^+)} \right) \left(\frac{T}{10^4 \text{ K}} \right)^{0.617} \times \left(\frac{\nu}{\text{GHz}} \right)^{-0.1} \left(\frac{F_{\text{H}\alpha, \text{corr}}}{10^{-12} \text{ erg cm}^{-2} \text{ s}^{-1}} \right). \quad (3.5)$$

In the above equation, F_ν is the estimated radio flux at frequency ν , and $F_{\text{H}\alpha, \text{corr}}$ is the extinction-corrected H α flux. T is the temperature within the emitting region assumed to be 10^4 K. We have also assumed that the ratio of the number density of ionised helium to that of ionised hydrogen $n(\text{He}^+)/n(\text{H}^+)$ to be 0.087 ([Martin & Kennicutt 1997](#)).

In addition to the Milky Way foreground extinction, H α emission also undergoes interstellar extinction in the host galaxy. Before estimating the thermal contribution using equation 3.5, we corrected our H α map for extinction in the host galaxy using the publicly available 24 μm map of M 101 from the Spitzer Local Volume Legacy survey ([Dale et al. 2009](#)) using the relation ([Kennicutt et al. 2009](#))

$$F_{\text{H}\alpha, \text{corr}} = F_{\text{H}\alpha} 10^{A_{\text{H}\alpha}/2.5} + 0.02F_{24\mu\text{m}} \quad (3.6)$$

where $F_{\text{H}\alpha, \text{corr}}$ is the extinction-corrected H α emission, $F_{\text{H}\alpha}$ is the uncorrected H α emission, $A_{\text{H}\alpha}$ is the foreground dust extinction provided by [Schlegel et al. \(1998\)](#), and $F_{24\mu\text{m}}$ is the observed 24 μm flux.

Figure 3.7 shows the estimated thermal fraction in the disk of M 101 at four different frequencies overlayed with 1.4 GHz radio continuum contours. A histogram showing the distribution of thermal fraction across the disk of M 101 at different observed frequencies is shown in Figure 3.8. Figures 3.7 and 3.8 show that at both 146 MHz and 355 MHz, the thermal contribution to the total radio continuum emission is negligible. At both frequencies, the mean thermal fraction is less than a per cent throughout the disk including the giant H II complexes. The peak thermal fraction of about 1 – 1.4 % is seen towards the H II complex NGC 5471. At 1.4 GHz, the mean thermal fraction throughout the disk is about 3% with thermal fractions of about 10 – 20 % seen towards the H II regions. At 2.27 GHz, larger thermal fractions of up to 40% are seen towards the giant H II complexes and the mean thermal fraction throughout the disk is about 18%. At both 1.4 GHz and 2.27 GHz, we find that the thermal fraction in the western spiral arm to be systematically larger than the eastern part of the galactic disk

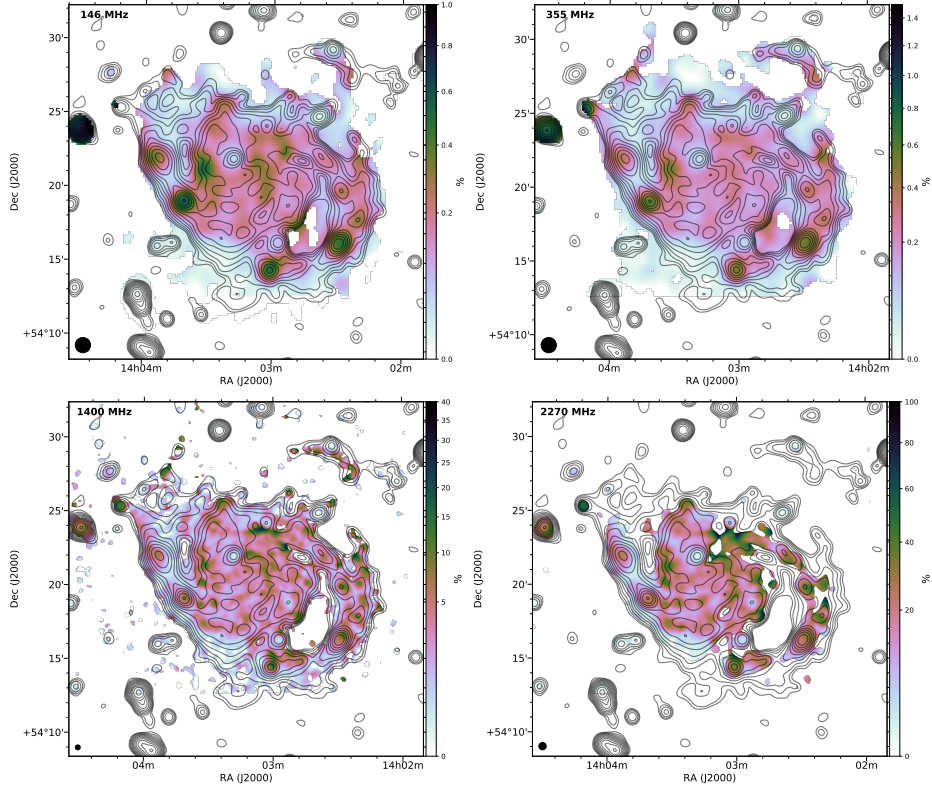


Figure 3.7 – Thermal fraction at 146, 355, 1400, and 2270 MHz estimated using H α and Spitzer 24 μ m maps. The resolution of the thermal fraction images is shown in the lower left corner of each frame. The overlayed 20cm total intensity contour lines are drawn at the same level as in Figure 3.4.

which dominates the total radio continuum emission from M 101. The observed low thermal fraction throughout the disk of M 101 is consistent with the thermal fraction seen in other nearby normal star-forming galaxies like NGC 5055 and NGC 6946 (see for example Basu et al. 2012).

3.8 Non-thermal spectral index

To estimate the non-thermal spectral index (α_{nth}) between 146 – 355 MHz and 355 – 1400 MHz, we first subtracted the thermal contribution based on the thermal estimation described in section 3.7. We then computed the non-thermal spectral index on a pixel-by-pixel basis using the thermal-emission-subtracted images. Uncertainty on the computed spectral index values was determined based on the relation

$$\alpha_{\text{err}} = \frac{1}{\log(\nu_1/\nu_2)} \sqrt{\left(\frac{S_{1,\text{err}}}{S_1} \right)^2 + \left(\frac{S_{2,\text{err}}}{S_2} \right)^2} \quad (3.7)$$

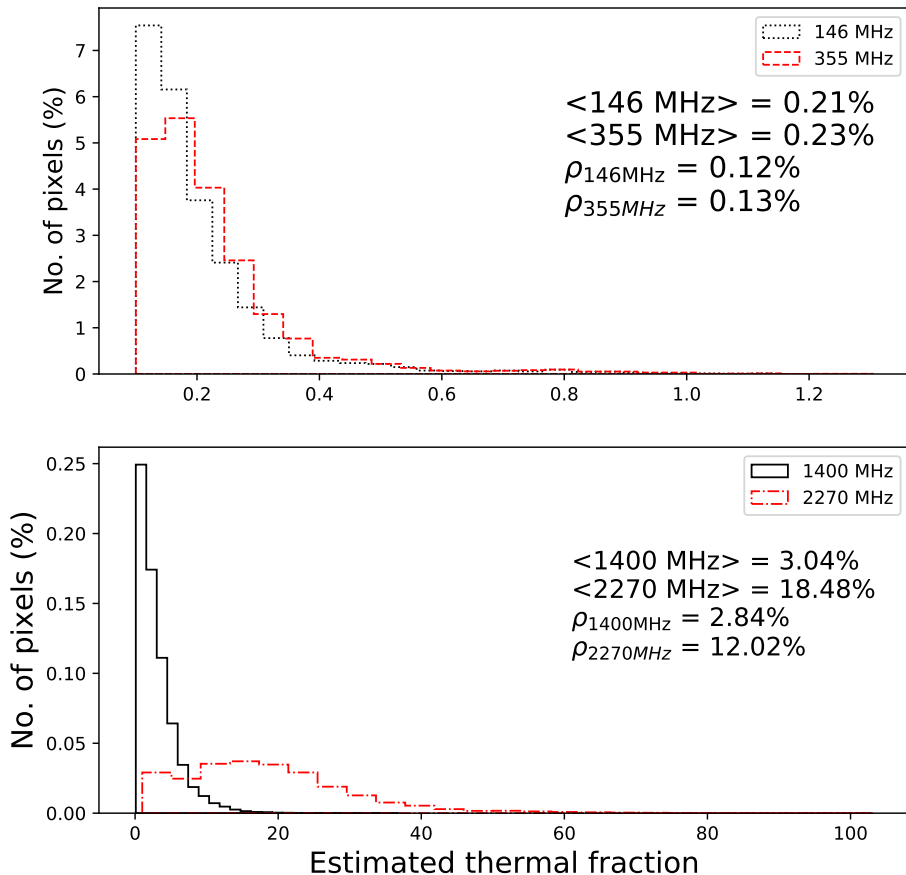


Figure 3.8 – Histogram of the estimated thermal fraction throughout the disk of M 101 at 146, 355, 1400, and 2270 MHz.

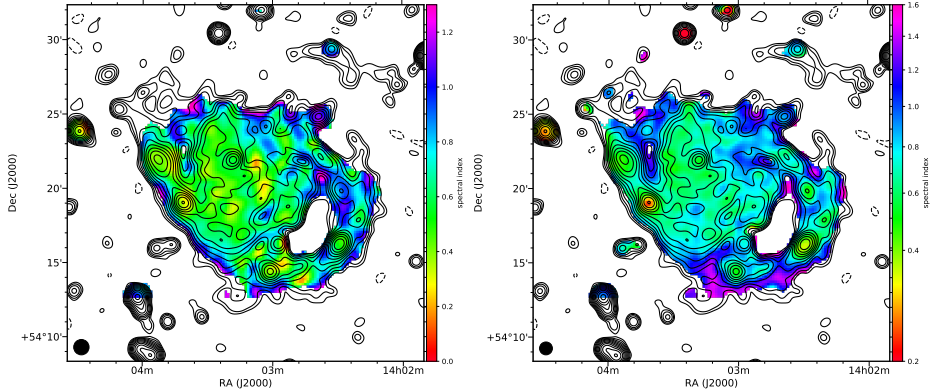


Figure 3.9 – Non-thermal spectral index map of M 101 between 146–355 MHz (*left*) and 355–1400 MHz (*right*). The resolutions of the spectral index maps are shown in the lower left corner of each image. Black contour lines represent the 1.4 GHz brightness distribution and are drawn at the same level as in the top left panel of Figure 3.4.

where S_1 and S_2 are the pixel values in the radio continuum maps at frequencies ν_1 and ν_2 and $S_{1,\text{err}}$ and $S_{2,\text{err}}$ are the corresponding uncertainties on the pixel values. All pixels in the computed spectral index maps with corresponding spectral index error greater than 0.15 in the $\alpha_{\text{nth},355-1400}$ and greater than 0.3 in $\alpha_{\text{nth},146-355}$ have been blanked.

Figure 3.9 shows the non-thermal spectral index maps between 146 – 355 MHz and between 355 – 1400 MHz. We see that, except for the flattening towards the H II regions NGC 5461 and NGC 5462, the non-thermal spectral index shows little variation in the inner 2 – 3 kpc. It is clear from Figure 3.9 that flatter spectral indices ($\alpha_{\text{nth}} \sim 0.2$) are predominantly seen towards the giant H II regions, most notably NGC 5461 and NGC 5471. In both spectral index maps, we also see that there is a steepening of spectral index with increasing galactocentric radius.

We obtained the radial distribution of the non-thermal spectral index by estimating the mean spectral indices inside concentric rings with a width given by the synthesized beam. This was carried out using the task `ellint` which is part of the `miriad` software package. The radial profile of the non-thermal spectral index is shown in Fig 3.10. The radial non-thermal spectral index profiles show two interesting features. First, we see that the azimuthally averaged non-thermal spectral index increases radially outwards. The radial steepening of non-thermal spectral index can be explained by the increasing energy loss that the cosmic ray electrons experience due to diffusion (see for example [Mulcahy et al. 2014](#)) as they travel away from their sites of (re)acceleration ([Segalovitz 1977](#)). This radial increase in azimuthally averaged spectral index in M 101 is consistent with the radial spectral index profiles seen in other nearby spiral galaxies (see for example [Tabatabaei et al. 2007; Basu et al. 2012](#)). Secondly, we see from Fig 3.10 that the mean spectral index within each ring is systematically flatter at longer wavelengths. This systematic flattening at longer wavelengths is also evident from the histogram representation of the distribution of non-thermal spectral

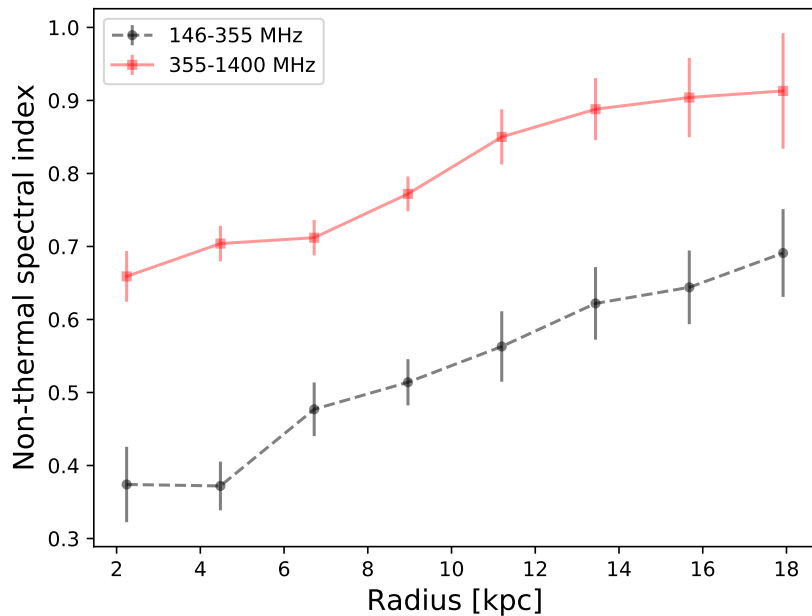


Figure 3.10 – Azimuthally-averaged non-thermal spectral index profile of M 101.

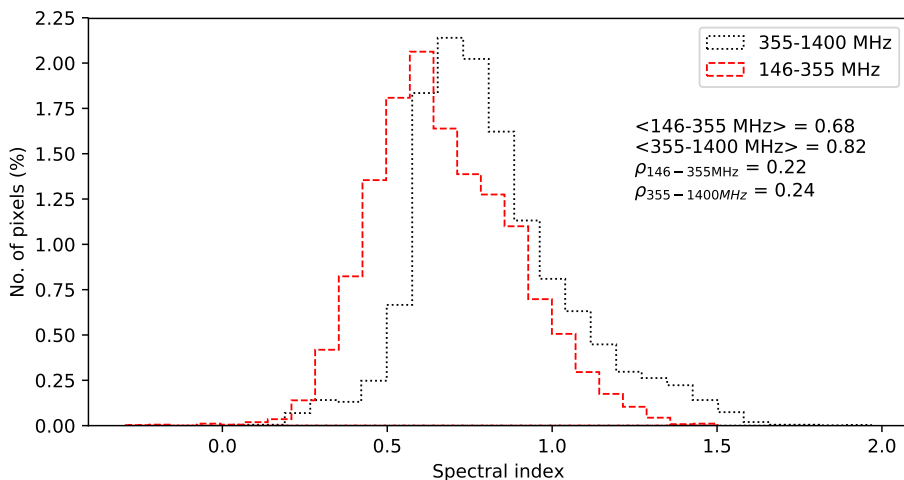


Figure 3.11 – Histogram of the non-thermal spectral index estimated using 146, 355, and 1400 MHz radio continuum images of M 101.

indices shown in Fig 3.11. This is contrary to what is observed in M 101 as one would expect the non-thermal spectral index to be steeper at long wavelengths due to synchrotron loss. The observed flattening of non-thermal spectral index throughout the galactic disk could be the same as for the observed flattening of the integrated radio spectrum discussed in section 3.6: the presence of a galaxy-wide free-free absorption of non-thermal synchrotron emission by an ionised medium.

3.8.1 Radial scale length

Examining the average radial brightness distribution at the various observing frequencies provides insight in to the average reservoir of relativistic electrons and is an easy way to search for radial changes in spectral index, indicative for radial diffusion of the relativistic plasma. Figure 3.12 shows the radial profile of the continuum brightness at the four observed frequencies. The radial profiles were generated by computing the mean of the pixel values inside concentric ellipses using the position angle and inclination from Table 3.1. Each annulus is one synthesized beam wide. Only pixels above 1σ were taken into account and all background radio sources were masked before estimating the radial profiles.

Note that the radial profiles derived from all four radio images show a change in slope after a radius of about 11.5 kpc. A similar change in radial scale length has also been seen in M 101 by [Berkhuijsen et al. \(2016\)](#) using a 4.85 GHz Effelsberg image of M 101. A similar change in the radial scale length is also seen in M 101 in the optical data of [Miros et al. \(2013\)](#) although the change in scale length occurs in the radial range $R = 7' - 9'$ which corresponds to a galactocentric radius of 14 – 18 kpc.

To determine the scale lengths in the inner and the outer disk, we fit the radial profiles with two exponential functions of the form

$$I(R) = \begin{cases} I_0 \exp(-R/l_{R<10 \text{ kpc}}) & \text{for } R < 10 \text{ kpc} \\ I_{12.5} \exp(-R/l_{R>12.5 \text{ kpc}}) & \text{for } R > 12.5 \text{ kpc.} \end{cases} \quad (3.8)$$

We ignored the data points that lie within the 10–12.5 kpc range. The radial profiles at higher frequencies show structure in this range and hence we were unable to fit a single exponential profile when we included those data points during the fitting procedure. The resulting inner and outer exponential scale lengths obtained for all four of our radio images are listed in Table 3.5.

From the exponential scale lengths quoted in Table 3.5, we see that the scale lengths determined using the three low frequency radio images are larger in the inner disk implying that the radio surface brightness decreases more slowly with radius in the inner disk than in the outer disk. The exponential fits in the outer disk shows that the scale length increases by almost 65% between 1400 and 146 MHz.

Differences in radial scale lengths of the inner and the outer disks have been reported in other nearby spiral galaxies like M 33 ([Tabatabaei et al. 2007](#)) and M 51 ([Mulcahy et al. 2014](#)). In both M 33 and M 51, the scale length in the outer disk is a factor of two smaller than that of the inner disk. Similar to our observations in M 101, [Mulcahy et al. \(2014\)](#) find that the scale length in the outer

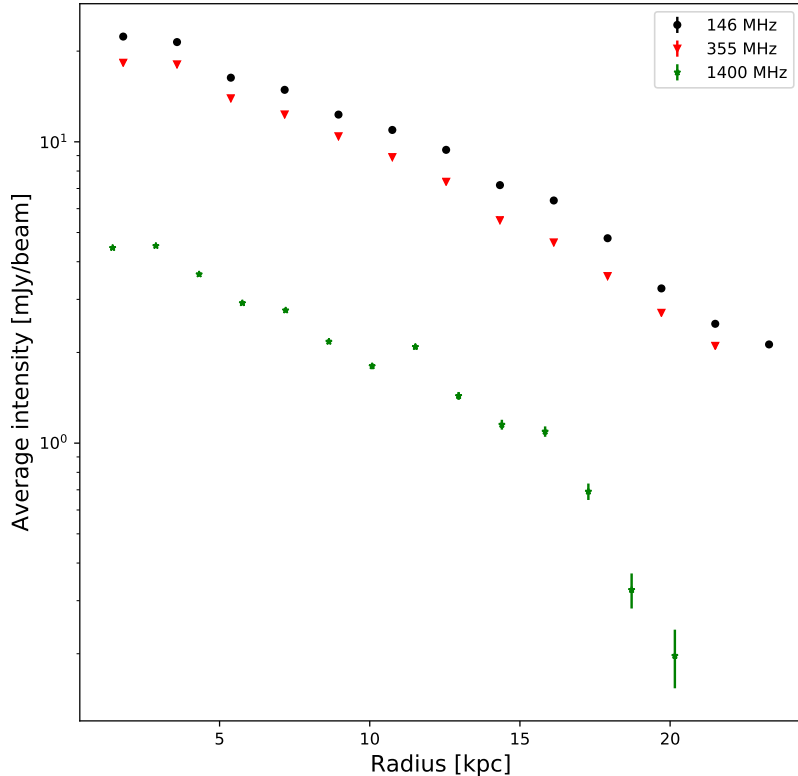


Figure 3.12 – Azimuthally-averaged intensity profile of M 101 estimated using the radio continuum images.

Table 3.5 – Exponential scale lengths of the inner and the outer disk of M 101.

Frequency (MHz)	$l_{R<10 \text{ kpc}}$ (kpc)	$l_{R>12.5 \text{ kpc}}$ (kpc)
146	18.1 ± 2.2	16.4 ± 0.5
355	18.1 ± 2.7	17.9 ± 0.7
1400	13.1 ± 0.8	10.6 ± 0.3
2270	12.4 ± 1.1	13.4 ± 0.1

disk of M 51 increases at lower frequencies. This observed change in slope of the radial profile with wavelength is consistent with the idea that low energy cosmic ray electrons have longer lifetime and hence can propagate to larger galactic radii causing a steepening of scale lengths at low frequencies.

3.9 Equipartition magnetic field strength

Non-thermal radio continuum emission, in combination with the non-thermal spectral index, can be used to estimate the distribution of total magnetic field strength assuming energy equipartition between the energy densities of cosmic ray electrons and magnetic field in the interstellar medium. Assuming energy equipartition, the total magnetic field strength in the plane of the sky ($B_{\text{tot},\perp}$) is proportional to the synchrotron intensity (I_{sync}) as

$$B_{\text{tot},\perp} \propto I_{\text{sync}}^{1/(3+\alpha)}. \quad (3.9)$$

For a full derivation of the equipartition relation, we refer the reader to [Beck & Krause \(2005\)](#) and for the full equation relating $B_{\text{tot},\perp}$ to I_{sync} , see equation 3 in [Beck & Krause \(2005\)](#). In addition to the radio continuum and spectral index maps, further assumptions like the path length through the synchrotron emitting media and the ratio of proton-to-electron number density are needed to compute the equipartition magnetic field strength using equation 3.9.

Assuming that the ratio of proton-to-electron number densities is 100 ([Bell 1978](#)) and path length through the synchrotron emitting media is about 1 kpc, we computed the equipartition magnetic field strength using the thermal emission subtracted 355 MHz radio continuum and the 355 – 1400 MHz non-thermal spectral index map presented in sections 3.7 and 3.8 on a pixel-by-pixel basis. Since the equipartition relation from [Beck & Krause \(2005\)](#) diverges for spectral indices shallower than 0.54, we have masked out all the pixels with $\alpha_{\text{nth}} \leq 0.54$. We have also masked out the background radio source that is located to the NE of the nucleus of M 101. Varying the spectral index values by about 10% results in less than 5% change in the estimated value of the total equipartition magnetic field strength. Similarly, we also notice that a factor of two variation in the value of the proton-to-electron ratio and the pathlength results in less than 20% change in B_{tot} .

Figure 3.13 shows the distribution of equipartition magnetic field strength in the disk of M 101 and the azimuthally-averaged $B_{\text{tot},\perp}$ as a function of radius. From Figure 3.13, we find that a peak magnetic field strength of about 15 μG is seen in the inner kpc and this decreases to about 8 – 9 μG in the periphery of the disk. We find that the mean magnetic field strength throughout the disk is about 10.5 μG and the interarm regions show relatively weak fields of about 7 – 9 μG . We also see that the eastern half of the galaxy has stronger magnetic field strength than the western half.

The distribution of equipartition magnetic field strength in M 101 shows a remarkable asymmetry between the south-eastern and the north-western halves of the galactic disk. A histogram representation of the observed asymmetric

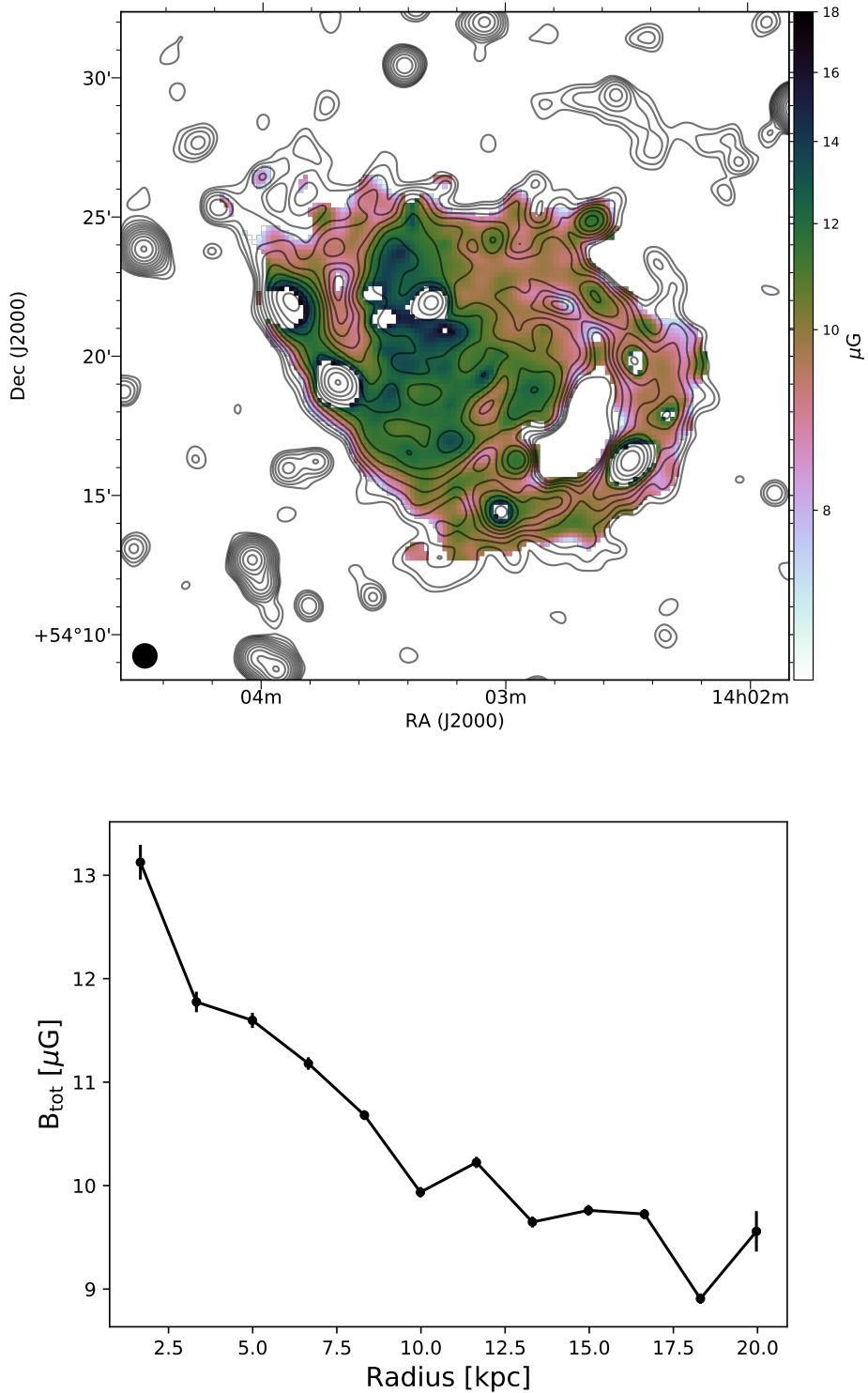


Figure 3.13 – Top: Equipartition magnetic field distribution in M 101 overlaid with 20cm total intensity radio continuum contours. The contours are drawn at the same level as in Figure 3.4. **Bottom:** Radial profile of equipartition magnetic field strength in M 101.

distribution of the equipartition magnetic field strengths in the north-eastern and the south-western parts of M 101 is shown in Fig 3.14. Similar asymmetry is also visible in the total intensity continuum images (Fig 3.4) and in the non-thermal spectral index distribution (especially in the right panel of Fig 3.9), although the asymmetry is most pronounced in the distribution of the magnetic field strengths. While the neutral hydrogen in the disk of M 101 does not exhibit an asymmetric distribution, the presence of the H I HVC (see section 3.5) is certainly dominant on the eastern side.

As mentioned earlier in section 3.5, the high-velocity gas complex is either gas that is being accreted onto the disk of M 101 (Van der Hulst & Sancisi 1988) or it is a byproduct of a past interaction (Combes 1991). Irrespective of its origin, the interaction between the HVC and the underlying spiral arm can compress both gas and the magnetic field lines in the disk resulting in the observed asymmetric distribution. Further evidence for compression can be seen along the eastern spiral arm in the form of a steep edge along the entire length of that arm (see Fig 3.4). Enhancement in mean magnetic field strength due to compression by a number of factors like spiral density waves and ram pressure have been observed in a number of nearby spiral galaxies (see for example Vollmer et al. 2007; Weżgowiec et al. 2007; Fletcher et al. 2011; Weżgowiec et al. 2012; Vollmer et al. 2013). Furthermore, star formation can be enhanced in the ISM that is compressed by environmental effects like interaction and ram pressure stripping (Moore et al. 1996). Using optical spectroscopy, Hu et al. (2018) showed that the mean age of the stellar population along the eastern arm in M 101 is about 1 – 2 Myr (also see Lin et al. 2013) which is also consistent with the expected interaction timescale.

A natural consequence of compression of magnetic field lines is that the regions influenced by compression will have a higher degree of polarization (or fractional polarization) compared to the rest of the disk (see for example Laing 1980). We recently procured broadband radio polarimetry data in the L- and S-band using the Very Large Array (VLA) which will be the subject of a future work. A map of the degree of polarization in M 101 using this new dataset will allow us to confirm if the observed asymmetry in field strengths in the south-eastern part of M 101 is indeed due to compression by the HVC.

An additional factor that could be contributing to the asymmetric distribution of the magnetic field strength is the rotational velocity of M 101. The rotational velocity of M 101 is known to be asymmetric about its major axis in H I. The H I rotation curve derived by Kamphuis (1993) show that the rotational velocity in the approaching side (eastern side) of the galaxy is higher by about 80 km/s compared to the receding side (western side). According to the theory of galactic dynamos, the mean magnetic field in late-type galaxies are amplified and maintained through the combined action of helical turbulence and differential rotation by a process known as the $\alpha - \Omega$ dynamo (see Widrow 2002, and references therein). Observationally, Tabatabaei et al. (2016) find a correlation between the equipartition magnetic field strength and the rotational velocity in a sample of nearby non-interacting, non-cluster galaxies. This correlation implies that galaxies with higher rotational velocities posses stronger field strengths. It

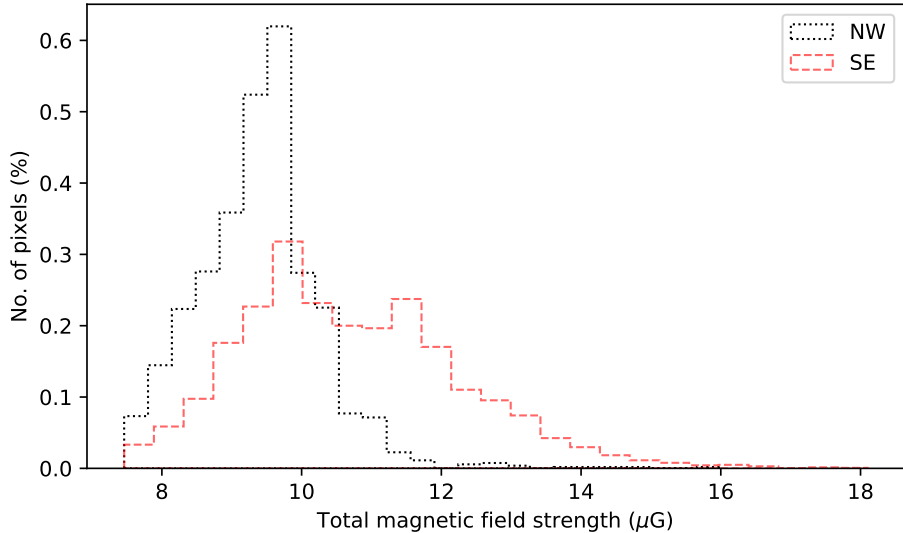


Figure 3.14 – Histogram representation of the equipartition magnetic field strengths in the north-western (NW) and the south-eastern (SE) parts of M 101.

is likely that the magnetic field lines in the eastern and the western parts of the galaxy experience difference factors of amplification. However, asymmetric rotation profiles in spiral galaxies are short-lived and galaxy rotation tends to stabilise within few rotations (~ 1 Gyr) in the absence of external factors. It is unclear if the dynamo mechanism in the eastern half of M 101 is strong enough to produce significant amplification within such a short period of time.

3.10 Summary and conclusions

In this chapter, we have carried out resolved, sensitive radio continuum observations of the nearby spiral galaxy M 101 using the WSRT and LOFAR radio telescopes. The high resolution and sensitivity of our radio images allowed us to study the synchrotron emitting disk of M 101 in the frequency range spanning from 146 MHz to 2270 MHz. The radio continuum morphology of M 101 is similar to the *GALEX* NUV morphology of M 101 implying that radio continuum is a good tracer of star formation. Using our high resolution radio continuum images, we demonstrate that the integrated flux densities of M 101 reported in the literature are all biased by confusion due to background radio sources. After careful removal of the background radio sources from our new maps, we show that the integrated radio spectrum of M 101 shows spectral flattening towards low radio frequencies which we attribute to free-free absorption.

We see a steep gradient along the eastern arm of M 101 in all four radio images. Comparing our radio images with new H I neutral hydrogen column density map, we find that the steep gradient seen in radio is coincident with a 10^8 M_\odot high-

velocity gas complex. The steep gradient in radio continuum is consistent with the picture suggested in the literature where the high-velocity complex is either being accreted on to the disk or produced by a recent interaction between M 101 and its companion NGC 5477.

We find that the slope of the radial brightness distribution changes at a radius of about 11 kpc and most strongly so at the two low frequencies. The outer slope at the low frequencies is steeper than at the high frequencies, including a dominance of old electrons in the outer parts.

Using H α and *Spitzer* 24 μ m data, we estimated the thermal contribution to the observed radio continuum emission from M 101. At 146 and 355 MHz, we find that the estimated thermal fraction is less than 1%. At 1.4 and 2.27 GHz, we find thermal fractions of up to 40% towards giant H II complexes. The overall thermal fraction in M 101 is consistent with thermal fractions observed in other nearby spiral galaxies like NGC 5055.

The radial profile of the azimuthally averaged non-thermal spectral index distribution in M 101 shows spectral steepening with increasing radii between 146 – 355 MHz and between 355 – 1400 MHz. This radial steepening of non-thermal spectral index implies that the relativistic cosmic ray electrons lose energy as they propagate away from their sites of acceleration. We also notice that the radial profile for the spectral index distribution between 146 MHz and 355 MHz is systematically flatter than the radial profile for the spectral index between 355 MHz and 1400 MHz. This is most probably caused by free-free absorption of synchrotron radiation by the cool ionised gas and the optically thick H II regions distributed throughout the disk of M 101.

Assuming energy equipartition, we find that the galaxy-wide mean magnetic field strength is $10.3 \pm 1.5 \mu\text{G}$. We also find that the magnetic field strength decreases by about 40 – 50% between the inner kpc and the periphery of the disk. A similar contrast is also seen between the spiral arms and the inter-arm regions. The distribution of equipartition magnetic field strength in M 101 is asymmetric such that the south-eastern side of the galactic disk exhibits enhanced field strengths compared to the north-western side. The observed asymmetry could be caused by compression of magnetic field lines in the eastern part of the galaxy due to an infalling high-velocity gas complex. Wideband polarimetric observations combined with a better kinematic model for M 101 is required to gain a better picture of how star formation and magnetic field are affected by the high-velocity gas complex.

Chapter 4

Resolved low-frequency radio images of nearby dwarf galaxies

Sridhar, S. S., Heesen, V., et al., To be submitted to
Astronomy & Astrophysics

4.1 Introduction

Within the hierarchical structure formation scenario, present-day starburst dwarf galaxies are thought to be the closest analogues to the first galaxies that were bubbling with star formation (Kanekar et al. 2009, 2014; Buitrago et al. 2013; Alavi et al. 2016). For example, the rest frame UV spectrum of the nearby dwarf galaxy NGC 4214 strongly resembles starforming galaxies at redshift $z \geq 3$ (Steidel et al. 1996). Dwarf galaxies are also considered to be the progenitors of the normal spiral galaxies we see in the local universe (see White & Frenk 1991; Baugh 2006). Therefore, understanding the physical processes that take place in the interstellar media of nearby dwarf galaxies is crucial for formulating a consistent picture of the evolution of galaxies within the cosmological context.

Compared to normal spiral galaxies, dwarf galaxies differ in key global properties such as morphology, metallicity, dust content and star formation rate. In contrast to normal spiral galaxies, star formation in dwarf galaxies is episodic/stochastic (Lequeux et al. 1979; Gerola et al. 1980; Stinson et al. 2007) and occurs without the influence of spiral density waves (Hunter et al. 1998). Due to their low star formation rates, dwarf galaxies tend to be fainter in radio continuum than normal spiral galaxies.

Unlike normal spiral galaxies, dwarf galaxies have relatively low rotational velocities (Begum et al. 2008; Oh et al. 2008; Ott et al. 2012; McNichols et al. 2016) implying that the classical $\alpha - \Omega$ dynamo mechanism might not be strong enough to amplify the magnetic fields in them. However strong magnetic field strengths have been detected in nearby dwarf galaxies (Chyžý et al. 2000; Kepley et al. 2010). For example, Chyžý et al. (2000) detected a $14\mu\text{G}$ total field strength in the nearby dwarf galaxy NGC 4449 which is similar to total field strengths observed in normal spiral galaxies. Detection of magnetic field strengths that are equal in strength compared to normal spiral galaxies indicates that turbulent gas motion, driven by mechanical feedback from supernova explosions, could result in an efficient fluctuating dynamo mechanism. Thus, radio continuum studies of nearby dwarf galaxies can provide a wealth of information about the magnetised interstellar media in these objects and help understanding the physical conditions of the interstellar medium in these cosmological building blocks.

Most of the studies of dwarf galaxies published in the literature have been based on integrated radio continuum properties which can at times be severely affected by background source confusion (see for example Klein 1986). However, resolved radio continuum observations of dwarf galaxies have been few and far between. Only a handful of studies (in the literature) have been based on resolved radio continuum and spectral index observations of dwarf galaxies (for example see Lisenfeld et al. 2004; Kepley et al. 2011; Chyžý et al. 2011; Heesen et al. 2011; Basu et al. 2017). Roychowdhury & Chengalur (2012) performed a stacking analysis of NVSS images of 57 dwarf galaxies to study the typical magnetic fields in faint dwarf galaxies. To date, there has not been a systematic resolved study of dwarf galaxies in radio continuum. An attempt was made by Chyžý et al. (2011) to map the total and polarized radio continuum emission in dwarf galaxies in the local group using the Effelsberg telescope at 2.64 GHz but they were able

to detect only three of the 12 targeted galaxies. Furthermore resolved studies of dwarf galaxies have never been carried out at frequencies below 300 MHz.

This picture is about to change with the advent of new low-frequency radio telescopes like LOFAR and MWA which have significantly improved survey speeds compared to traditional radio telescopes due to their large fields of view. For example, the LOFAR Two-metre Sky Survey (LoTSS; [Shimwell et al. 2017](#)) is an ongoing 120–168 MHz survey that aims to image the entire northern sky with a sensitivity of $100 \mu\text{Jy}/\text{beam}$ at an angular resolution of $5''$. The LoTSS survey aims to make calibrated, science-ready images public with the first data release scheduled to be released in 2018. To prepare for science-ready images from the LoTSS survey, we have carried out a pilot radio continuum observing campaign of four nearby dwarf irregular galaxies (NGC 1569, NGC 4214, NGC 2366, and DDO 50) at 120–168 MHz using the LOFAR High Band Antenna (HBA). These four galaxies were chosen because of their radio brightness at higher radio frequencies using data from the Local Irregulars That Trace Luminosity Extremes - The H α Nearby Galaxy Survey (LITTLE-THINGS; [Hunter et al. 2012](#)) and availability of complementary data at other wavelengths. The physical parameters of the four dwarf galaxies studied in this work are listed in Table 4.1.

This chapter is structured as follows: We present our LOFAR HBA observations and the data reduction procedure in Section 4.2. In Section 4.3, we present our total intensity radio continuum maps and we discuss the observed morphology of the galaxies in detail in comparison with other higher frequency observations. In Sections 4.4 through 4.6, we estimate the thermal contribution to the observed total continuum emission and use the non-thermal maps to estimate the equipartition magnetic field strengths. In section 4.7, we present details of our search for polarized emission from the dwarf galaxies and from other extragalactic radio sources within our field of view. Finally, we summarize our conclusions in Section 4.9. Throughout this work, we define spectral index through $S_\nu \propto \nu^{-\alpha}$, where S_ν is the flux density at frequency ν , and α is the spectral index.

4.2 LOFAR observations and data reduction

4.2.1 Observational setup and preprocessing

We observed the targets listed in Table 4.1 for eight hours each with the International LOFAR Telescope (ILT, [van Haarlem et al. 2013](#)) using its HBA. All four galaxies were observed with identical instrumental setup and imaged following the same calibration scheme. All Dutch and international LOFAR stations were used during observation, and the stations were operated under the HBA_Dual_Inner mode. In the HBA_Dual_Inner mode, all core LOFAR stations are split in two and data from only the 24 inner tiles are used. This operating mode was chosen to ensure that all LOFAR stations have the same field of view.

Each eight-hour continuous scan on the target was bracketed with a ten-minute scan on the nearest flux density calibrator (either 3C 295 or 3C 196). All four polarisation products in the linear basis (XX, XY, YX, YY) were recorded. The target and the calibrators were observed with identical time and frequency

Table 4.1 – Physical parameters of the observed dwarf galaxies.

Galaxy (1)	Distance [Mpc] (2)	M_V (mag) (3)	Inclination [°] (4)	PA [°] (5)	$\log_{10} \Sigma_{\text{SFR}}(\text{FUV})$ $M_\odot \text{ yr}^{-1} \text{ kpc}^{-2}$ (6)	R_H (arcmin) (7)	M_{HI} $(10^8 M_\odot)$ (8)	W_{50} (km s^{-1}) (9)
NGC 1569	3.36 [G08]	-18.2	69 [O15]	123 [O15]	-0.01 ± 0.01	–	0.75	100.8
NGC 2366	3.44 [T95]	-16.8	65	40 [O08]	-1.66 ± 0.01	4.72	6.49	101.2
NGC 4214	2.9 [D09]	-17.6	38	65	-1.08 ± 0.01	4.67	4.08	69.8
DDO 50	3.4 [D09]	-16.6	31	177 [P92]	-1.55 ± 0.01	3.97	5.95	57.4

Notes. Comments on columns: (1) galaxy name; (2) distances in Mpc; (3) V -band magnitude from Hunter & Elmegreen (2006); (4) inclination angle from de Blok et al. (2008); (5) position angle; (6) star formation rate density estimated using *GALEX* FUV flux (Hunter et al. 2010) over the area πR_D^2 where R_D is the disk scale length (Hunter & Elmegreen 2004); (7) Holmberg radius from Hunter & Elmegreen (2006); (8) H I mass taken from Walter et al. (2008); (9) H I profile width at 50% of the peak intensity from Walter et al. (2008);

References. G08: Grocholski et al. (2008); O15: Oh et al. (2015); O08: Oh et al. (2008); P92: Puche et al. (1992); T95: Tolstoy et al. (1995); D09: Dalcanton et al. (2009);

setup. We used 243 non-contiguous sub-bands (SBs) to span the frequency range from 120 MHz to 182 MHz with a total bandwidth of 47.4 MHz. Each SB is 195.3125 kHz wide and is further sub-divided into 64 channels. The visibilities were correlated using a 1s integration time. Relevant observational parameters are listed in Tables 4.2 and 4.3.

After correlation, the recorded visibility data were flagged for Radio Frequency Interference (RFI) using the `AOFagger` (Offringa et al. 2010, 2012) software package. The flagged data were then averaged down to four channels per SB and 4s time resolution. Only the averaged visibility data were stored on the LOFAR Long Term Archive (LTA)¹ and the raw data were deleted.

4.2.2 Calibration

We followed the new direction dependent facet calibration procedure (van Weeren et al. 2016; Williams et al. 2016) to calibrate and image our LOFAR HBA data. Here, only the Dutch baselines (including core and remote stations) were used for calibration and imaging. Analysis of the sub-arcsec resolution maps of the compact H_{II} regions in the dwarf galaxies using international LOFAR baselines will be presented in a future study. The calibration procedure was carried out in two stages: a direction-independent step where we first applied flux calibration and a correction for station clock offsets followed by a direction-dependent step where we corrected for direction-dependent effects due to the ionosphere and due to our insufficient knowledge of the LOFAR beam.

In the direction-independent step, we first derived calibration solutions for the diagonal gain terms (G_{xx} and G_{yy}) using either 3C 295 or 3C 196. For 3C 295, we assumed a two-point source model using the flux scale defined in Scaife & Heald (2012) while we used a four-component model 3C 196 characterised using a second order spectral curvature (Pandey, private communication). The modelled total flux density of 3C 196 differs from the Scaife & Heald (2012) flux scale by a factor of 1.074 ± 0.024 (Williams et al. 2016). We return to this in section 4.2.3. In addition to the gain terms, we also solved for a rotation angle term that accounts for differential Faraday rotation. We derived gain solutions for each subband separately with a 4s solution interval. Using these gain solutions, we estimated the station clock offsets and the phase offset between the X and the Y dipoles of each station using the “clock-TEC” separation method described in van Weeren et al. (2016). The correction for clock offset is required because the core and the remote LOFAR stations are not connected to the same clock, and hence synchronisation errors can lead to clock offsets of the order of 100ns. We transferred the derived gain amplitude, clock offset and phase offset solutions to the target data using the NDPPP software.

At low radio frequencies, the ionospheric Faraday rotation has to be calibrated out to prevent depolarisation due to the ionosphere. We determined the corrections using the publicly available `RMExtract`² software package. `RMExtract` uses the model of the Earth’s magnetic field (Finlay et al. 2010) and the Total

¹<http://lofar.target.rug.nl/>

²<https://github.com/maaijke/RMextract/>

Table 4.2 – LOFAR HBA telescope setup

Parameter	Value
Integration time	1 s
Total on-source time	8.0 hr
Correlations	XX, XY, YX, YY
Frequency range	120 – 182 MHz
Total bandwidth	47.4 MHz
Subbands (SBs)	243
Bandwidth per SB	195.3125 KHz
Channels per SB	64
LOFAR Array Mode	HBA Dual Inner
Stations	72 ^a total 23 core (each split in two) 14 remote 12 international

Notes. (a) Some LOFAR HBA stations were flagged either during observation or during calibration. Stations CS004HBA0 and CS031HBA0 were flagged in the NGC 4214 dataset. Station RS409HBA was flagged in the DDO 50 dataset. Station RS210HBA was flagged while observing NGC 1569 due to hardware issues related to oscillating dipoles.

Electron Content maps from the Center for Orbit Determination in Europe (CODE) to estimate the required ionospheric Rotation Measure (RM) correction. The applied ionospheric RM corrections ranged from 0.09 rad m^{-2} to 0.79 rad m^{-2} .

After transferring the calibrator solutions to the target and correcting for ionospheric Faraday rotation, we merged the target measurement sets into blocks of 10 SBs such that each block has a bandwidth of 2 MHz. Phase calibration was applied to the SB blocks using a $6^\circ \times 6^\circ$ model of the sky extracted from the 150 MHz Giant Metrewave Radio Telescope (GMRT) Sky Survey Alternate Data Release (Intema et al. 2017, TGSS ADR). Phase solutions were derived for and applied to each SB block separately with an 8s solution interval.

The aim of the direction-dependent calibration step is to allow the recovery of weak, diffuse radio continuum emission by minimising calibration artefacts around bright point sources within the LOFAR field of view. To achieve this, we divided the region within the primary beam into facets using Voronoi tessellation such that each facet has at least one point source, or facet calibrator, brighter than 0.4 Jy/beam. We processed the facets individually in decreasing order of the total flux in each facet. For each facet, we performed self-calibration to improve the skymodel and to derive good gain solutions for that facet. After deriving direction-dependent solutions, we corrected the visibility dataset corresponding to each target using solutions derived from the nearest facet calibrator. The list of facet calibrators used and their distances from the corresponding target galaxies is shown in Table 4.3.

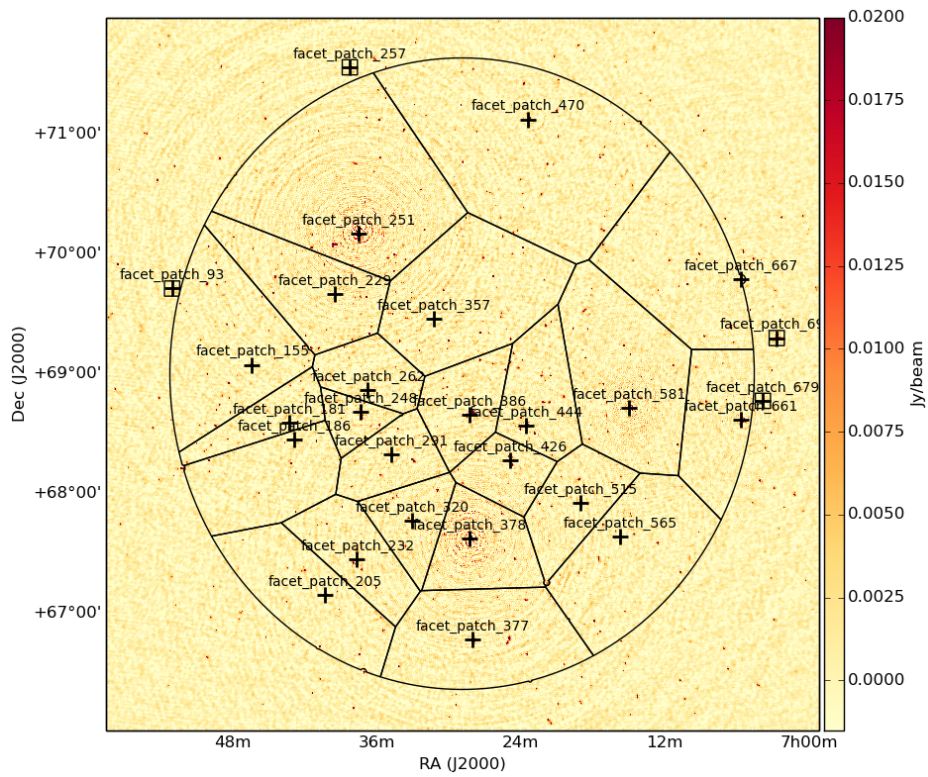


Figure 4.1 – Facet layout for NGC 2366

Table 4.3 – LOFAR HBA observational and imaging parameters.

Parameter	NGC 1569	NGC 2366	DDO 50	NGC 4214
Pointing center	04h30m49.2s +64d50m52.5s	07h28m54.6s +69d12m57s	08h19m05.0s +70d43m12s	12h15m39.2s +36d19m37s
Flux density calibrators	3C 196	3C 196	3C 196	3C 295
Observation ID	557200	560195	570739	582785
Observation date	Nov 03, 2016	Nov 30, 2016	March 02, 2017	April 05, 2017
Direction-dependent facet calibrator	J042932+645627	J072753+685256	J082216+705308	J121420.7+361426
Distance from facet calibrator	9'.87	20'.75	18'.60	16'.63
High resolution:				
Robust parameter	-0.7	-0.7	-0.7	-0.7
Gaussian taper ('')	10	10	10	10
Beam ('')	14.8×11.4	15.1×11.5	15.6×11.9	16.2×11.1
Noise ($\mu\text{Jy beam}^{-1}$)	138	216	198	185
Low resolution:				
Robust parameter	-0.7	-0.7	-0.7	-0.7
Gaussian taper ('')	30	20	20	30
Beam ('')	33.7×30.1	24.6×21.5	24.8×21.8	34.7×32.0
Noise ($\mu\text{Jy beam}^{-1}$)	315	561	495	356
Integrated flux density at 143 MHz (mJy)	899.0 ± 92.0	32.5 ± 3.3	124.0 ± 12.4	275.7 ± 27.6
Thermal contribution at 143 MHz (mJy)	114.3	15.0	6.2	26.5

4.2.3 Final imaging

After correcting the visibilities with the direction-dependent gain solutions, we imaged the facets containing the target galaxies using the WSClean³ imager (Offringa et al. 2014) making use of its Wideband Deconvolution algorithm⁴ which accounts for spectral curvature within the bandpass. We weighted the visibilities using the Briggs weighting scheme (Briggs 1995) with `robust=-0.7` and a Gaussian taper. We deconvolved the dirty maps down to 1σ threshold using a CLEAN mask to minimize CLEAN bias (Becker et al. 1995; Cohen et al. 2007).

During imaging, a combination of a more uniform visibility weighting and a Gaussian taper was needed to suppress PSF sidelobes in our final total intensity maps while enhancing the diffuse emission by down-weighting the long baselines. Figures 4.2 and 4.3 show the shape of the PSF for three different visibility weighting schemes. As can be seen from Figures 4.2 and 4.3, the first sidelobe of the PSFs are as high as 40 and 20% when imaging the LOFAR HBA data with Briggs weighting using `robust` parameters 0.0 and 0.5.

We followed the procedure explained above to image the calibrated visibilities at two different resolutions to highlight the diffuse and high-resolution morphological features in the galaxies. Different resolutions were achieved using different Gaussian tapering values while keeping all other imaging parameters the same. The relevant imaging parameters used to make the high and low resolution total intensity maps are listed in Table 4.3.

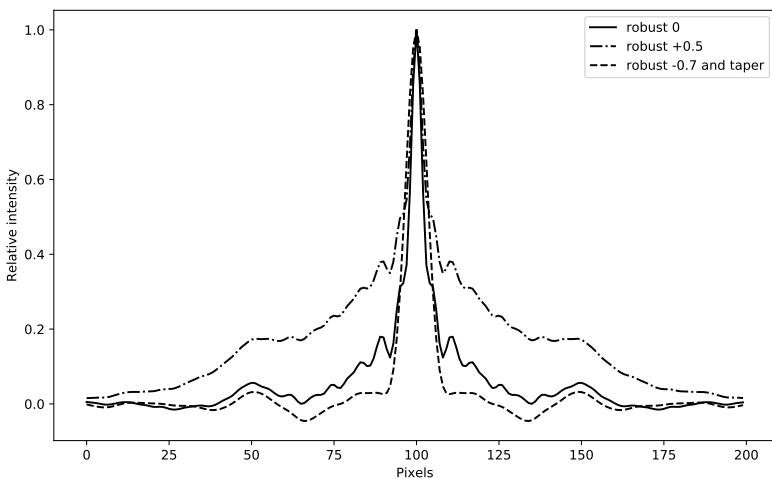


Figure 4.2 – A slice through the different point spread functions shown in Figure 4.3.

³<https://sourceforge.net/p/wsclean/wiki/Home/>

⁴<https://sourceforge.net/p/wsclean/wiki/WidebandDeconvolution/>

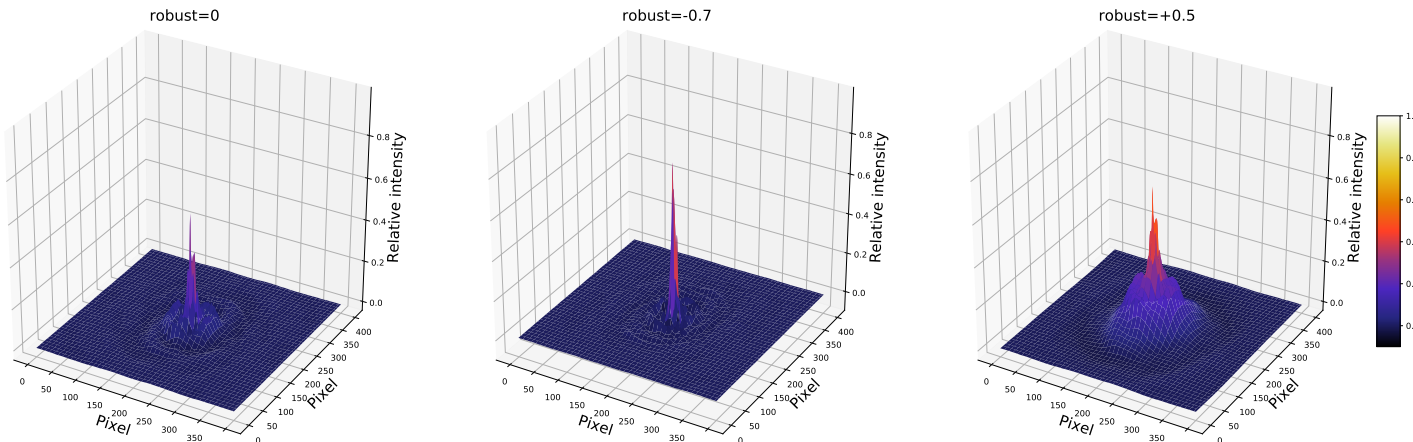


Figure 4.3 – Point Spread Functions for a typical LOFAR HBA observation including all Dutch baselines and imaged using different visibility weighting schemes. Two dimensional slices along the minor axis of all three PSFs are shown in Figure 4.2.

Primary beam correction was not applied to the final images as all the diffuse emission from the dwarf galaxies is within the 99.5% level of the primary beam. While the point source models used to calibrate the visibility data have $\leq 4\%$ intrinsic flux uncertainty within our observational bandwidth (see Figure 3 in [Scaife & Heald 2012](#)), we assume a conservative 10% uncertainty on the measured flux densities for all our subsequent analysis.

Note that the total flux included in the model for 3C 196 used to calibrate the LOFAR dataset deviates from the [Scaife & Heald \(2012\)](#) flux scale by a factor of 1.074 ± 0.024 . Final total intensity images that were calibrated using 3C 196 were scaled by this factor so that the maps are consistent with the [Scaife & Heald \(2012\)](#) flux scale.

4.3 Total intensity maps

We detect radio continuum emission at 143 MHz from all four dwarf galaxies. Figures [4.4](#) and [4.5](#) show the high and low resolution LOFAR HBA total intensity contour lines overlayed on the corresponding H α ([Hunter & Elmegreen 2004](#)) and Digitized Sky Survey (DSS) maps. In the following sub-sections, we provide comments on the individual galaxies.

4.3.1 NGC 1569

The LOFAR total intensity radio continuum contours of NGC 1569 overlayed on an H α and optical DSS image are shown in Figures [4.4](#) and [4.5](#). The overall radio morphology of the diffuse radio continuum emission in NGC 1569 seen at 143 MHz is consistent with the 20 cm radio continuum morphology presented in the literature (see for example [Kepley et al. 2010](#)).

Contour lines drawn in Figure [4.4](#) reveal that the isocontour shape of the galaxy changes from being oval in the inner regions of the galaxy to a boxy-shape in the outer parts. Comparing the morphology of the galaxy at 3, 6, 13 and 20 cm, [Kepley et al. \(2010\)](#) also noticed that the morphology changes from oval-shaped to box-shaped as one moves towards low radio frequencies. We see a continuation of the same morphological effect with our new LOFAR data.

Figures [4.4](#), [4.5](#), [4.6](#), and [4.7](#) show the LOFAR radio contour lines overlayed on H α , optical DSS, *GALEX* NUV, and neutral hydrogen column density images of NGC 1569. Comparing the radio continuum morphology of NGC 1569 with images from higher frequency observations, we find interesting correspondences between radio emission and features seen at other frequencies.

Comparing the *GALEX* NUV image and the LOFAR radio image of NGC 1569 (see Figure [4.6](#)), we see that the peak radio emission is coincident with the site of intense star formation in the western part of the galactic disk. It is also interesting to note that while most intense star formation is occurring in the north-eastern part of the disk, it is the south-western part of the radio halo that shows the most extended vertical structure in our maps. Comparing our 143 MHz radio image with those presented in ([Kepley et al. 2010](#), see their Figure 1), it is interesting to note that the south-western part of the radio halo

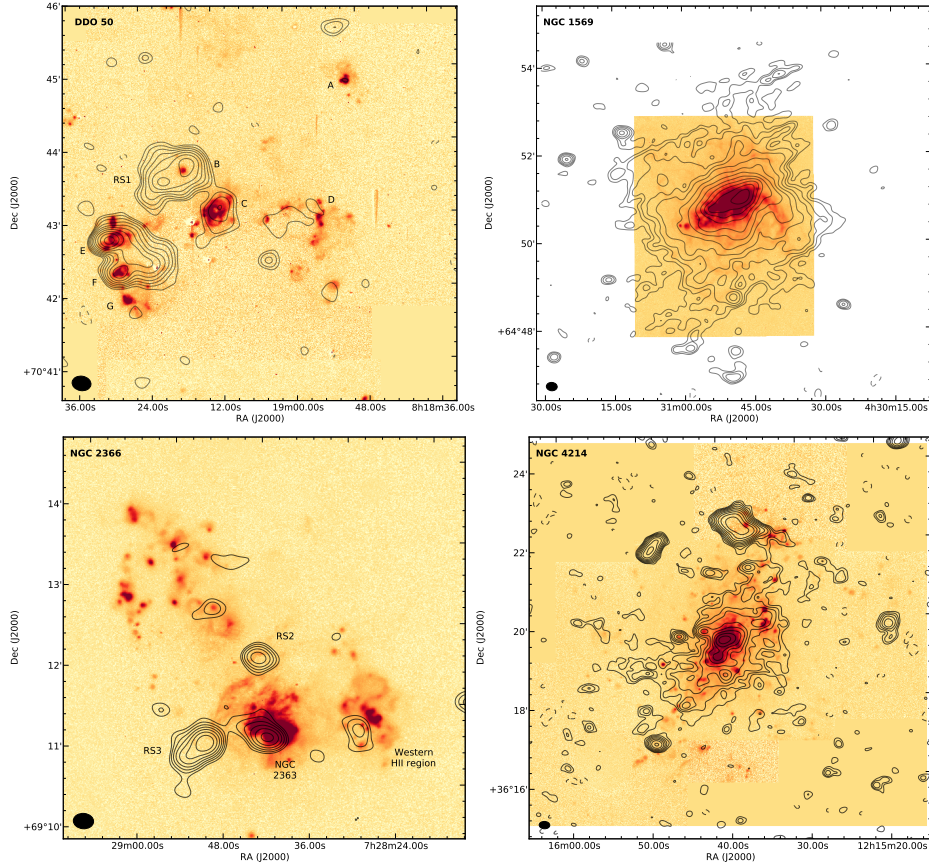


Figure 4.4 – LOFAR high resolution total intensity contours overlaid on H α maps (Hunter & Elmegreen 2004). Contour levels are drawn at $2 \times \sigma_I \times 1.5^n$ where $n = 0, 1, 2, 3, \dots$. Broken contour lines in the maps are drawn at -2σ level. The LOFAR maps were generated using a 10'' Gaussian taper and the resolutions of the LOFAR maps are listed in Table 4.3. The size of the LOFAR beam is shown in the lower left corner of each image.

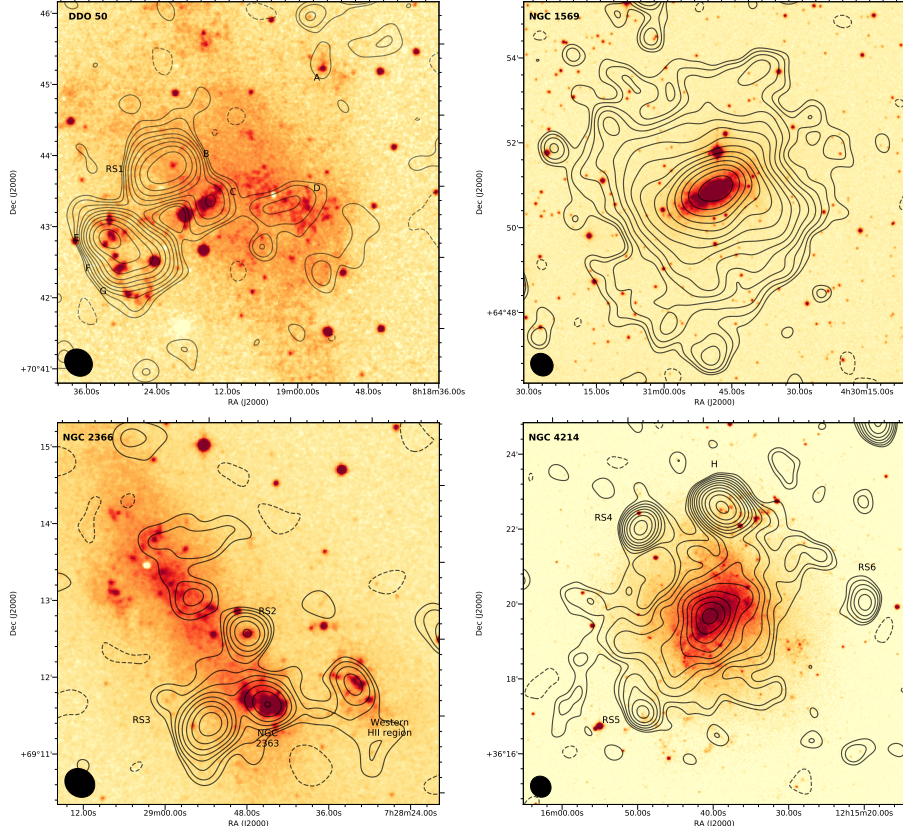


Figure 4.5 – LOFAR low resolution total intensity contours overlaid on optical DSS maps. Contour levels are drawn at $2 \times \sigma_I \times 1.5^n$ where $n = 0, 1, 2, 3, \dots$. Broken contour lines in the maps are drawn at -2σ level. The LOFAR maps were generated using a $30''$ Gaussian taper and the resolutions of the LOFAR maps are listed in Table 4.3. The size of the LOFAR beam is shown in the lower left corner of each image.

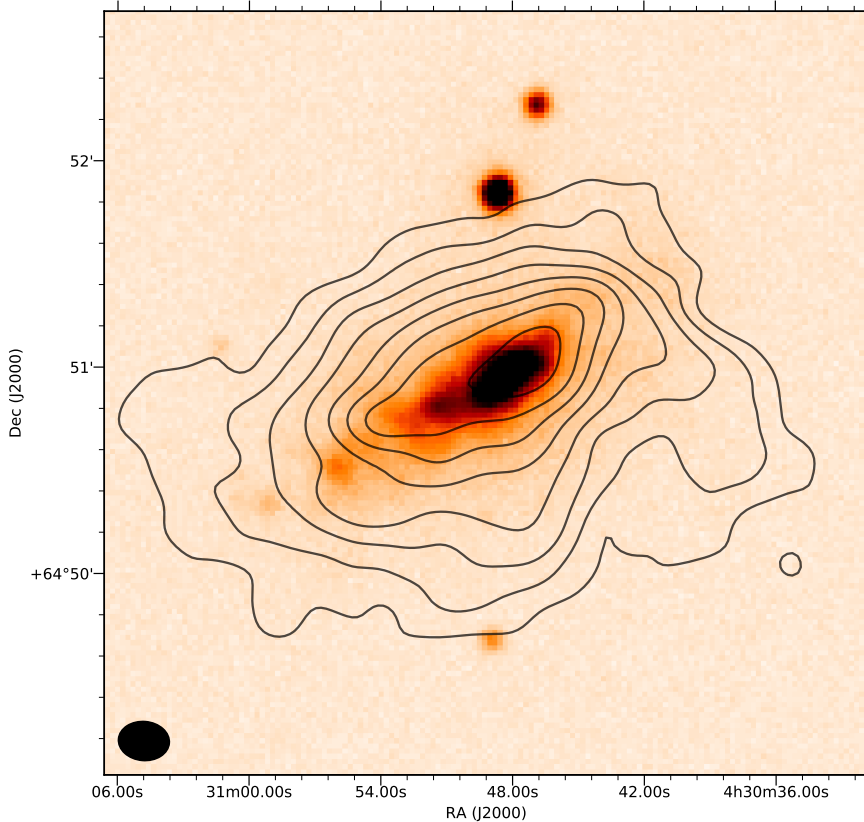


Figure 4.6 – LOFAR total intensity radio continuum contours overlaid on *GALEX* NUV image of NGC 1569. The contour lines are drawn at $10 \times \sigma \times 1.5^n$ where $n = 1, 2, 3, \dots$ and $\sigma = 210$ mJy/b. The image shows that the peak radio continuum emission in NGC 1569 coincides with a site of intense star formation in the western part of the disk.

increases in size only at frequencies below 2.27 GHz. In fact, the north-eastern halo appears to be more extended at 3, 6, and 13 cm. Only in radio maps with wavelengths longer than 20 cm do we see more extended emission in the south-east.

Notice that the H α image in figure 4.4 shows the presence of an arm-like structure protruding from the western end of the galactic disk. While this extended H α filament is usually referred to as the “western arm” (see Klein & Graeve 1986, and references therein), the H α emission from the filament originates from the limb of a bubble. The radio continuum contours shown in Figures 4.4 trace the “western arm” quite clearly in the south-western part of the galaxy.

The low resolution LOFAR contours overlaid on a neutral hydrogen column density map of NGC 1569 in Figure 4.7 shows that the peak radio continuum emission, which is coincident with the site of intense star formation, is coincident with a region that shows a lack of H I emission compared to its surroundings.

In comparison with the sensitive 20cm total intensity map from Kepley et al. (2011), we find that the radio continuum emission at 143 MHz appears extended perpendicular to the inner disk while no noticeable extended emission is seen along the major axis. In our low-resolution LOFAR map, we can trace the diffuse radio continuum emission out to a distance of $4'.18$ from the kinematic center ($4:30:48.600, +64:50:57.89$). Assuming a distance of 2.96 ± 0.22 Mpc, this corresponds to a projected linear size of 3.60 ± 0.27 kpc. Similar vertical extensions have also been seen at low radio frequencies in NGC 253 (Kapińska et al. 2017) and in NGC 5775 (Heald et al. in prep). Given that NGC 1569 is a post-starburst galaxy, this extension perpendicular to the disk probably indicates the presence of a galactic wind. H α kinematics of the outer parts of the halo indicate the presence of a large-scale outflow of ionised gas (Tomita et al. 1994; Heckman et al. 1995; Martin 1998; Westmoquette et al. 2007a,b, 2008). Modelling the propagation of cosmic ray electrons with tools like SPINNAKER⁵ (Heesen et al. 2016) using our LOFAR HBA data and future observations with LOFAR low band antenna (LBA) will allow us to study the nature of cosmic-ray transport from the galactic disk to the halo (advection- or diffusion-dominated) and measure the outflow wind speed.

We measure the integrated flux density from NGC 1569, after masking out a few background point sources, to be 0.965 ± 0.096 Jy. As discussed in section 4.2.2, the model for the flux density calibrator that was used to calibrate the NGC 1569 LOFAR data deviates from the Scaife & Heald (2012) flux scale by a factor of 1.074 ± 0.024 . Thus, the integrated flux density from NGC 1569 needs to be rescaled resulting in an integrated flux of 0.899 ± 0.092 Jy in the Scaife & Heald (2012) flux scale. The integrated LOFAR flux density is consistent with flux density estimates from the 6C survey (Hales et al. 1993). Fitting a power-law (see fig 4.8), we find that the integrated spectral index for NGC 1569 is 0.46 ± 0.02 .

4.3.2 NGC 4214

The radio morphology of NGC 4214 shown in Figures 4.4 and 4.5 is composed of two bright radio emission components in the inner regions of the galaxy superimposed on a weaker diffuse component. In addition to these two components, the radio images also show several point-like sources (labelled as ‘RS4’, ‘RS5’, ‘RS6’, and ‘H’). The nature of these sources is discussed below.

Comparing the distribution of radio emission and H α emission from ionised gas in NGC 4214, we see that the peak in radio and H α emission coincide quite well. The two bright radio-emitting regions (with associated bright H α emitting regions) correspond to the H II regions: NGC 4214-I and NGC 4214-II. The radio continuum morphology of NGC 4214 at 143 MHz is consistent with the 1.4 GHz WSRT radio image of NGC 4214 published by Kepley et al. (2011) but shows more extended emission.

Figure 4.9 shows the comparison between the radio continuum morphology of NGC 4214 and the distribution of neutral hydrogen in the galaxy. Unlike NGC 1569, the neutral hydrogen distribution in NGC 4214 is more extended

⁵ <https://github.com/vheesen/Spinnaker>

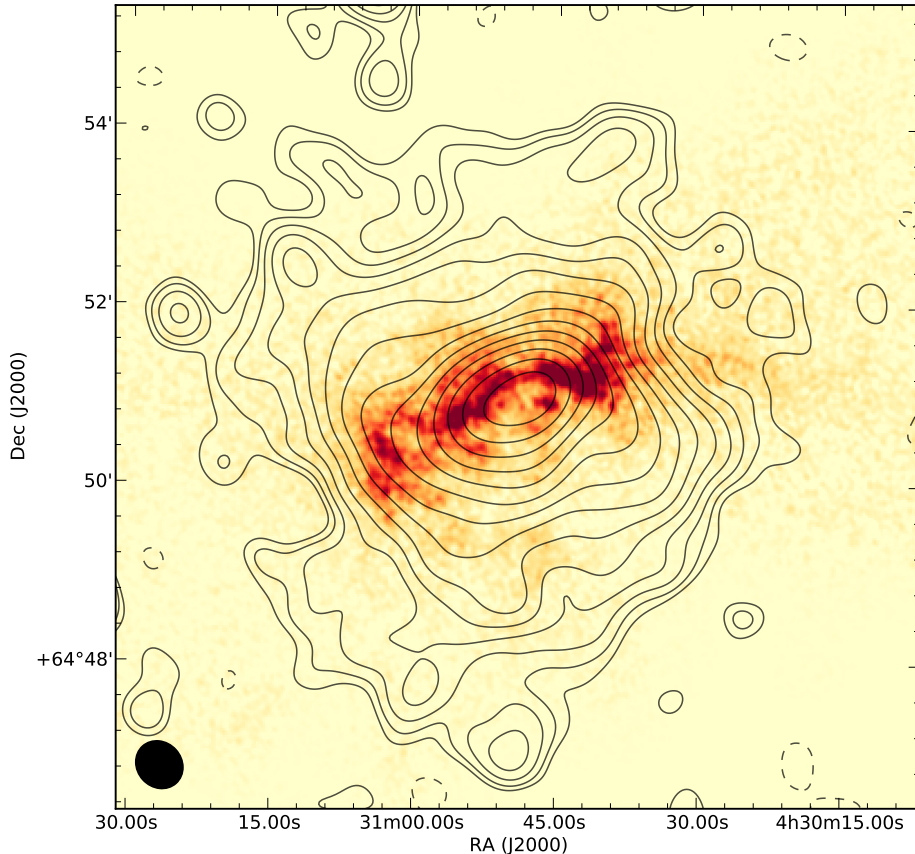


Figure 4.7 – Low resolution LOFAR contours on the THINGS H I column density map (Walter et al. 2008) of NGC 1569. The column density sensitivity of the THINGS map is $4 \times 10^{19} \text{ cm}^{-2}$. The contour lines are drawn at the same level as in Figure 4.5. The $33''.7 \times 30''.1$ resolution of the LOFAR map is indicated as a filled circle in the lower left corner.

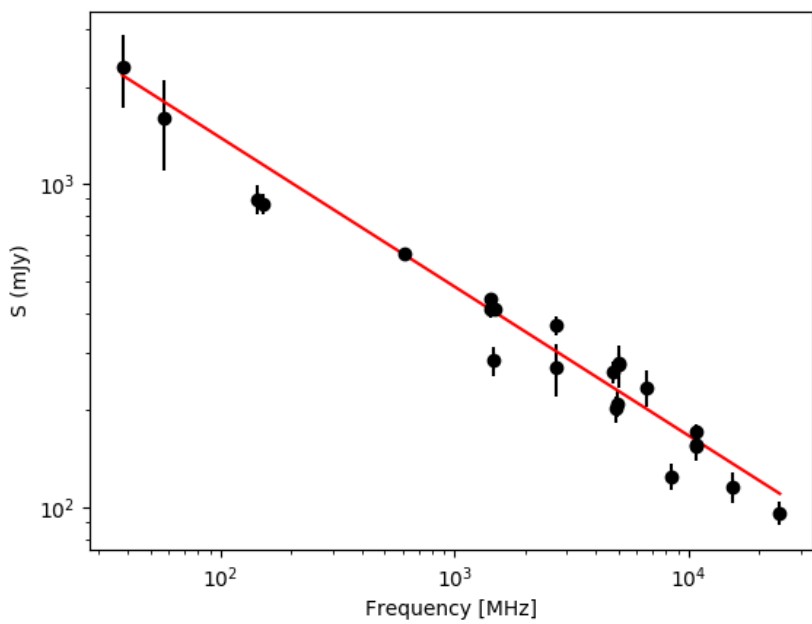


Figure 4.8 – Integrated spectral index for NGC 1569.

than the low frequency radio continuum emission as is often seen in normal spiral galaxies. The radio continuum emission at 143 MHz traces two arm-like features (containing the background radio sources ‘RS4’ and ‘RS6’) seen in H_i. These arm-like features also trace two inter-arm regions one to the south of ‘RS4’ and the other to the south-east of ‘RS6’.

Before estimating the integrated flux density of NGC 4214, it is imperative to understand the nature of the point sources seen towards NGC 4214. The point-like radio sources marked H and RS4 in both Figures 4.4 and 4.5 are detected in the 1.4 GHz radio continuum maps published in Kepley et al. (2011). In the high resolution LOFAR image ($7''.3 \times 4''.8$) shown in Figure 4.10, the source RS4 gets resolved into a double-lobed radio source. This is consistent with the conclusions of Kepley et al. (2011) who also classify the source RS4 to be background AGN based on its resolved structure in the FIRST maps, hard X-ray emission detected by Hartwell et al. (2004), and steep spectral index between 6 and 3cm. Comparing the radio continuum map with the optical and H _{α} maps, Kepley et al. (2011) argue that the source marked H is part of NGC 4214. While the source ‘H’ looks like a point source in the 1.4 GHz WSRT radio image of Kepley et al. (2011), the high resolution image shown in Figure 4.10 resolves source ‘H’ into a bright core surrounded by diffuse radio emission. The morphology of this source at high resolution looks similar to the radio morphology of sources like Fornax A (for example, see Fomalont et al. 1989) or the remnant radio galaxy discovered by Brienza et al. (2016). Source ‘H’ also appears to have a steep spectral index (see Figure 4.13) For these reasons, we consider the source marked ‘H’ to be a background radio galaxy. The nature of sources marked ‘RS5’ and ‘RS6’ is uncertain due to the lack of emission at other wavelengths and we assume them to be background radio sources.

After masking out RS4, RS5, and RS6, we estimated the integrated flux density from NGC 4214 to be 275.7 ± 27.6 at 143 MHz. The total spectral index is $\alpha = 0.65 \pm 0.06$.

4.3.3 NGC 2366

The low frequency radio continuum morphology of NGC 2366 is consistent with previous L-band and higher frequency observations (for example, see Thuan et al. 2004; Kitchener 2016). The radio continuum emission from NGC 2366 is dominated by two prominent H_{II} regions in the southern part of the galaxy: the Giant Extragalactic H_{II} Region (GEHR) NGC 2363 (= Mrk 71) and the Western H_{II} region (labelled NGC 2366-III in Drissen et al. 2000). In both H_{II} regions, the peak of the radio continuum emission is offset from the peak of the H _{α} emission. A similar positional offset is also seen between the H _{α} emission and the H_i intensity map (van Eymeren et al. 2009). Positional offsets are also seen between H _{α} and H_i intensity maps in other dwarf galaxies such as Sextans A (Hodge et al. 1994) and IC 10(Hodge et al. 1990), and can be explained as the consequence of sequential star formation (Elmegreen & Lada 1977).

Optical and H _{α} maps resolve the GEHR NGC 2363 (= Mrk 71) into two superstar clusters: NGC 2366-I and NGC 2366-II. NGC 2366-I dominates the

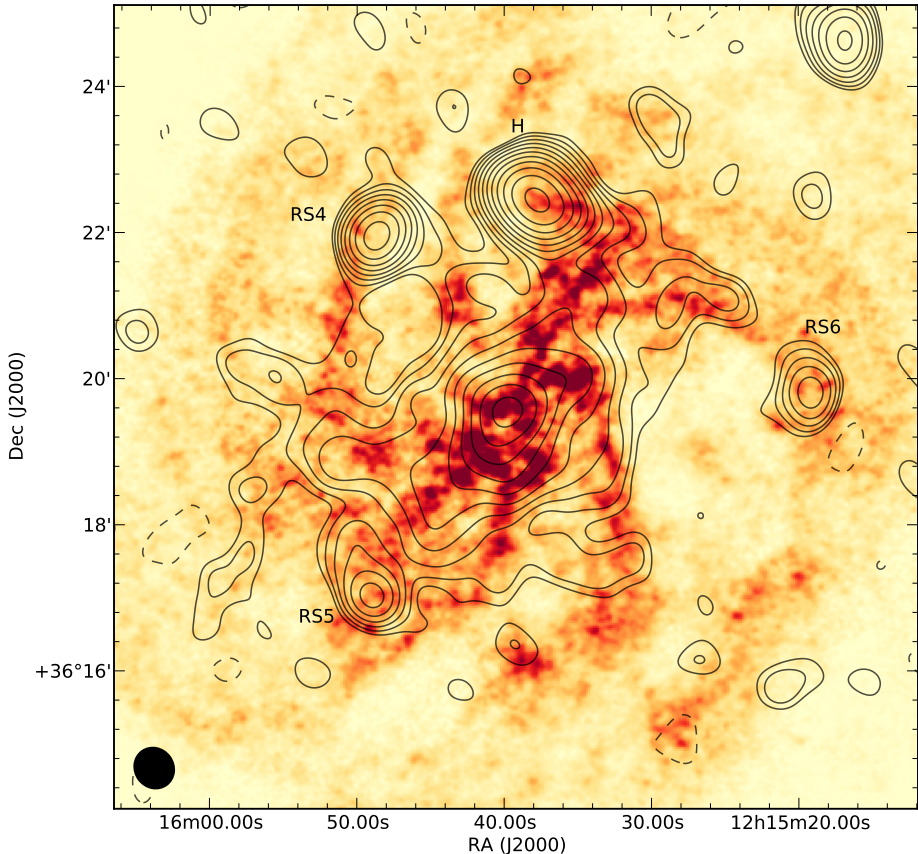


Figure 4.9 – Low resolution total intensity LOFAR contours of NGC 4214 overlaid on the integrated intensity H₁ map from THINGS (Walter et al. 2008). The column density sensitivity of the THINGS map is 4×10^{19} cm⁻². The 34''.7 × 32''.0 LOFAR beam is indicated in the lower left corner of the image. The contour lines are drawn at the same level as in Figure 4.5.

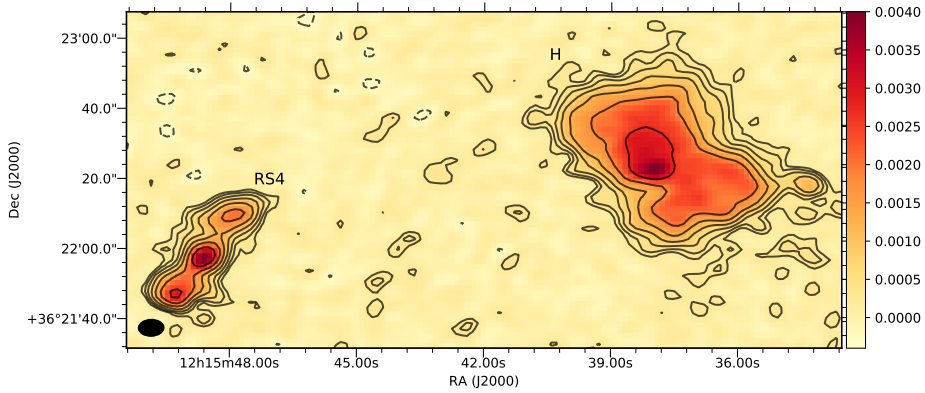


Figure 4.10 – A high resolution blow-up of the northern part of NGC 4214 showing the sources ‘RS4’ and ‘H’ marked in Figure 4.5. The rms noise in this map is $112\mu\text{Jy}/\text{beam}$ and the contour levels are drawn at $2 \times \sigma \times 1.5^n$ where $n = 0, 1, 2, \dots$. The $7''.3 \times 4''.8$ beam is shown in the lower left corner of the map.

Table 4.4 – Integrated radio continuum flux density for NGC 4214

Frequency (GHz)	Flux density (mJy)	Reference
0.14	275.7 ± 27.6	7
1.40	51.5 ± 10.3	6
1.40	38.3 ± 7.7	5
2.38	36.0 ± 3.0	4
4.86	34.0 ± 6.8	6
4.85	30.0 ± 4.5	2
4.85	30.0 ± 7.0	3
8.46	20.5 ± 0.5	1
8.46	24.2 ± 4.8	6

References. (1) Schmitt et al. (2006); (2) Becker et al. (1991); (3) Gregory & Condon (1991); (4) Dressel & Condon (1978); (5) Condon et al. (2002); (6) Kepley et al. (2011); (7) this work.

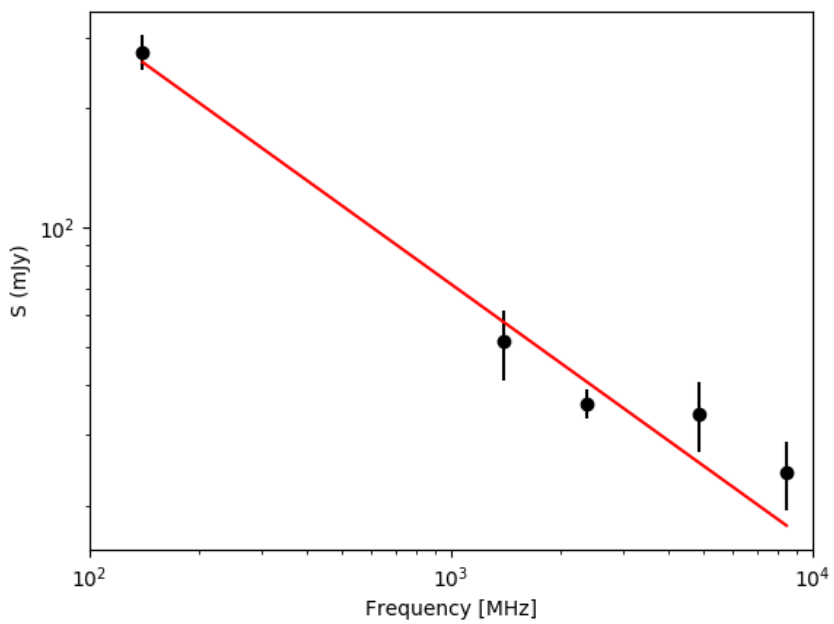


Figure 4.11 – Integrated spectral index for NGC 4214.

Table 4.5 – Integrated radio continuum flux density for NGC 2366.

Frequency (GHz)	Flux density (mJy)	Reference
0.143	32.5 ± 3.3	1
1.400	11.7	2
1.400	19.9	3
4.750	10.0 ± 1.0	4

References. (1) this work; (2) Thuan et al. (2004); (3) Condon et al. (2002); (4) Klein & Graeve (1986)

radio continuum emission from this region. While we see an extension towards NGC 2366-II, we do not see a second continuum peak associated with this superstar cluster. We estimate the combined radio continuum flux density from the superstar clusters NGC 2366-I and -II to be 8.75 ± 0.90 mJy/beam at 143 MHz. Comparing the estimated integrated flux density from Mrk 71 at 143 MHz with higher frequency measurements from Thuan et al. (2004) and Klein et al. (1984), it appears that Mrk 71 shows a spectral turnover ($\alpha < 0$).

The source marked RS3 is resolved into a double-lobed structure in the 3'' resolution C-band radio continuum map of Kitchener (2016). Thuan et al. (2004) misidentify this source as radio emission from an H_{II} region in the galaxy. Also, due to low resolution of the single dish Effelsberg map, the 4.75 GHz integrated flux density reported by Klein & Graeve (1986) is an overestimate as it confuses the double-lobed structure with NGC 2366. This is likely to be the cause for the mismatch between the 1.4 GHz flux densities reported by Condon et al. (2002) and Thuan et al. (2004). While there is H α emission coincident with the source marked RS2, it is not clear if it is part of the galaxy or if it is a background radio source.

Apart from these, low-level diffuse radio continuum emission is seen in the northern part of the galaxy and to the south-west of the Western H_{II} region. Assuming that the source ‘RS2’ and ‘RS3’ are not related to NGC 2366, we estimate the total radio continuum flux density at 143 MHz to be 32.2 ± 3.3 mJy. The power-law spectral index between 0.143 GHz and 4.750 GHz is 0.34 ± 0.10 .

4.3.4 DDO 50

The low frequency radio continuum emission from DDO 50 shown in Figure 4.4 appears to be very clumpy. We also find that the radio continuum morphology is strongly correlated with the distribution of H α emission in the galaxy. DDO 50 was also observed at 20 cm using the Westerbork Synthesis Radio Telescope as part of the WSRT-SINGS survey (Braun et al. 2007). Braun et al. (2007) found that most of the radio continuum emission is confined to the prominent H_{II} regions in DDO 50. The radio continuum morphology of DDO 50 in our LOFAR HBA image shown in Figure 4.5 is consistent with the 20cm map from Braun et al. (2007).

Table 4.6 – Integrated Radio continuum flux density for DDO 50.

Frequency (GHz)	Flux density (mJy)	Reference
0.143	124.0 ± 12.4	1
0.335	52.0 ± 5.0	2
1.365	27.0 ± 1.0	3
1.465	18.9 ± 0.2	2
4.860	11.7 ± 0.1	2

References. (1) this work; (2) [Tongue & Westpfahl \(1995\)](#); (3) [Heesen et al. \(2014\)](#)

In Figures 4.4 and 4.5, we have marked a few regions of interest (A – G and RS1) following the same naming scheme used by [Tongue & Westpfahl \(1995\)](#). In our high resolution image shown in Figure 4.4, we detect radio continuum emission from all discrete radio sources identified by [Tongue & Westpfahl \(1995\)](#) except source ‘A’. Based on the spectral indices of source ‘E’, ‘F’, and ‘G’, [Tongue & Westpfahl \(1995\)](#) suggest that these sources could be supernova remnants near or associated with the underlying star-forming regions visible in H α . Radio emission labelled ‘RS1’ (or radio source one) has no counterpart in the optical or H α and is considered to be a background point source.

In addition to clumpy radio emission associated with the above-mentioned sources, the low resolution image in Figure 4.5 shows low-level diffuse emission surrounding regions with relatively high radio surface brightness. [Tongue & Westpfahl \(1995\)](#) argue that the low-level radio continuum emission seen around the prominent H α regions could be due to local enhancement of cosmic ray electron population injected by supernovae associated with the H α regions and/or due to local enhancements of magnetic field strength as a result of compression.

We estimate the integrated flux density from DDO 50 to be 124.0 ± 12.4 mJy/beam after masking out the point source RS1. Table 4.6 shows a list of integrated flux densities from DDO 50 reported in the literature. A power-law fit to the integrated flux densities result in a spectral index of $\alpha = 0.62 \pm 0.11$.

4.4 Estimating thermal fraction

Thermal contribution to total intensity radio continuum emission can be estimated using the following equation from [Hunt et al. \(2004\)](#):

$$\left(\frac{F_\nu}{\text{mJy}} \right) = 1.16 \left(1 + \frac{n(\text{He}^+))}{n(\text{H}^+)} \right) \left(\frac{T}{10^4 \text{ K}} \right)^{0.617} \times \left(\frac{\nu}{\text{GHz}} \right)^{-0.1} \left(\frac{F_{H\alpha, \text{corr}}}{10^{-12} \text{ erg cm}^{-2} \text{ s}^{-1}} \right). \quad (4.1)$$

In the above relation, F_ν is the estimated radio flux due to thermal emission at frequency ν and $F_{H\alpha, \text{corr}}$ is the extinction-corrected H α flux. T is the electron

temperature within the emitting region and is assumed to be 10^4 K. We have also assumed that the ratio of the number density of ionised helium to that of ionised hydrogen $n(\text{He}^+)/n(\text{H}^+)$ is 0.087 (Martin & Kennicutt 1997).

We estimated the thermal emission at 143 MHz for all four of our galaxies using the publicly available flux-calibrated and continuum-subtracted H α maps⁶ published by Hunter & Elmegreen (2004). All H α maps were observed using the Perkins 1.8-m telescope at the Lowell observatory and have a resolution of $2''.2 \times 2''.2$.

While H α is a good tracer of the thermal component, the measured H α flux is always lower than the true H α flux due to interstellar extinction by the Milky Way foreground and in the host galaxy. We correct for interstellar extinction in the host galaxy using the relation (Kennicutt et al. 2009)

$$F_{\text{H}\alpha,\text{corr}} = F_{\text{H}\alpha} 10^{A_{\text{H}\alpha}/2.5} + 0.02 F_{24\mu\text{m}} \quad (4.2)$$

where $F_{\text{H}\alpha,\text{corr}}$ is the extinction-corrected H α flux, $F_{\text{H}\alpha}$ is the observed H α flux, and $F_{24\mu\text{m}}$ is the observed $24\mu\text{m}$ flux. Since NGC 1569 is at a relatively low galactic latitude ($b \sim 11$ deg), we first corrected for the foreground dust extinction using a value of $A_{\text{H}\alpha} = 1.26$ (Relaño et al. 2006) instead of using the value from Schlegel et al. (1998). For the remaining galaxies, the Galactic foreground extinction was determined using the standard dust extinction maps from Schlegel et al. (1998).

To correct for intrinsic extinction, we used the publicly available $24\mu\text{m}$ maps observed with the *MIPS* instrument onboard the *Spitzer* space telescope. DDO 50 was observed as part of the SINGS survey Kennicutt et al. (2003) while the remaining three galaxies were published by Bendo et al. (2012). The pixels in all the $24\mu\text{m}$ maps have units ‘MJy/sr’ and we scaled the pixel values by 958.772 to have units of $\mu\text{Jy}/\text{beam}$ assuming a resolution of $6'' \times 6''$. The H α , $24\mu\text{m}$ and the radio continuum maps were first convolved to a $16''.5$ resolution and regridded to a common coordinate grid. After correcting for extinction due to the Galactic foreground and intrinsic dust extinction using equation 4.2, we estimated the thermal contribution on a pixel by pixel basis using equation 4.1.

The integrated thermal flux density at 143 MHz estimated for each galaxy is shown in Table 4.3. The galaxy-wide integrated thermal fraction at 143 MHz is less than 15% for all galaxies except NGC 2366. In the case of NGC 2366, the overall thermal fraction is about 50%. Such a high value even at low radio frequencies is not surprising given that the radio continuum morphology of NGC 2366 is dominated by two large H II regions. The thermal fraction⁷ maps for all four galaxies are shown in Figure 4.12.

In NGC 1569, the peak in thermal fraction ($\sim 30\%$) is at the north-western part of the optical disk which is a site of intense star formation. Within the rest of the optical disk, the thermal fraction is on average about 15%. Immediately above and below the optical disk, the thermal fraction drops below 10% except in the extraplanar H α filaments like the “western H α arm” where the thermal

⁶<http://www2.lowell.edu/users/dah/littlethings/>

⁷Thermal fraction (f_{th}) is defined as $f_{\text{th}} = F_{\text{th}}/F_{\text{tot}}$ where F_{th} is the estimated thermal emission and F_{nth} is the observed radio continuum emission.

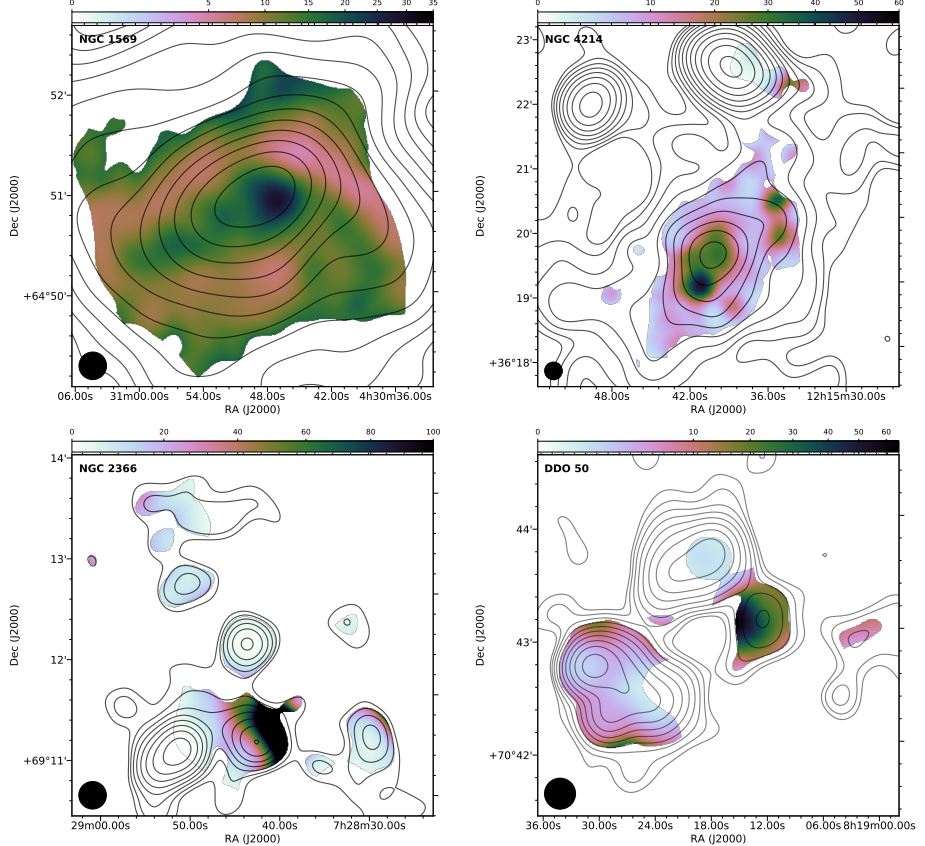


Figure 4.12 – Thermal fraction map estimated at 143 MHz for all four dwarf galaxies. The $16''.5$ beam is shown in the lower left corner of each image. LOFAR total intensity contours overlaid on the thermal fraction estimates are drawn at the same level as in Figure 4.5. The colour bar at the top of each panel gives the thermal fraction scale.

fraction is similar to that of the optical disk. In NGC 4214, the two H_{II} regions - NGC 4214-I and NGC 4214-II - show the highest thermal fraction of about 30 and 50 per cent respectively. Beyond the inner region of NGC 4214, the rest of the radio continuum disk shows low ($S_{\text{th}} < 10\%$) thermal fraction including the region ‘H’. In the case of NGC 2366, the Giant H_{II} region NGC 2363 (Mrk 71) appears to be entirely thermal which is consistent with the spectral turnover inferred in Section 4.3.3. Apart from this giant H_{II} region, the thermal fraction in the other parts of NGC 2366 is about 10% on average. In DDO 50, the peak thermal fraction of about 20 – 60 % is seen around the H_{II} marked ‘C’ in the total intensity maps. For the rest of the galaxy including the regions around the supernova remnants E, F, and G, the thermal fraction is lower than 10%.

4.5 Non-thermal spectral index maps

Figure 4.13 shows the non-thermal spectral index maps of NGC 1569 and NGC 4214 computed using our 143 MHz LOFAR HBA and archival 1.4 GHz radio images from Kepley et al. (2010) and Kepley et al. (2011) respectively. Before computing the spectral index, we first subtracted the estimated thermal contribution at 143 MHz and 1.4 GHz from the total intensity radio images. Non-thermal spectral index was computed on a pixel-by-pixel basis using the thermal emission subtracted images. Uncertainty on the computed spectral index values was determined based on the relation

$$\alpha_{\text{err}} = \frac{1}{\log(\nu_1/\nu_2)} \sqrt{\left(\frac{S_{1,\text{err}}}{S_1} \right)^2 + \left(\frac{S_{2,\text{err}}}{S_2} \right)^2} \quad (4.3)$$

where S_1 and S_2 are the pixel values in the radio continuum maps at frequencies ν_1 and ν_2 and $S_{1,\text{err}}$ and $S_{2,\text{err}}$ are the corresponding uncertainties on the pixel values. All pixels in the spectral index maps corresponding to a spectral index error greater than 0.2 were blanked. Histograms of the spectral index distribution in NGC 1569 and NGC 4214 are shown in Figure 4.14.

Spectral index values in NGC 4214 vary between about -0.2 to 1.2. A steeper spectral index of about 1.7 is seen towards the source marked as ‘H’ in Figure 4.5. The H_{II} region NGC 4214-II shows a flat spectrum with spectral index $\alpha \sim 0$. In NGC 1569, we see spectral index variations between $\alpha \sim 0.2 – 1.3$ with flatter spectral index seen in the north-western part of the galactic disk which is also the site of intense star formation.

4.6 Equipartition magnetic field strength

The strength of the total magnetic field can be estimated from the total intensity radio continuum image assuming energy equipartition between cosmic rays and magnetic fields (Beck & Krause 2005). The observed synchrotron intensity I_{syn} is related to the strength of the total magnetic field perpendicular to the line of sight ($B_{\text{tot},\perp}$) as

$$B_{\text{tot},\perp} \propto I_{\text{sync}}^{1/(3+\alpha)} \quad (4.4)$$

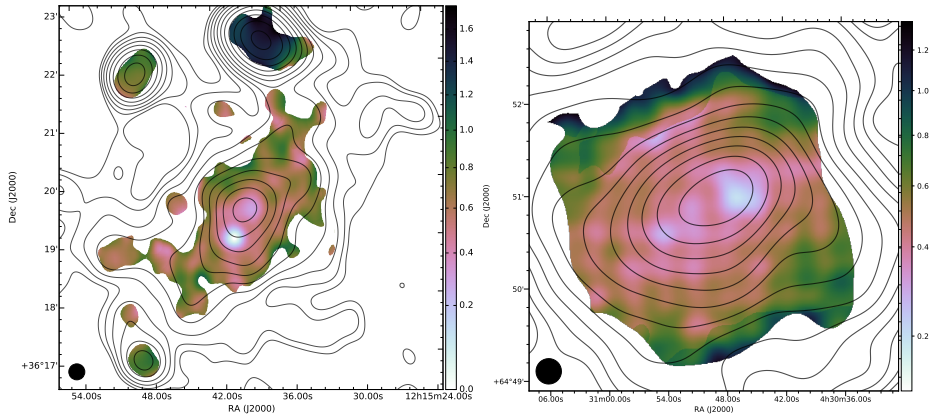


Figure 4.13 – Non-thermal spectral index maps of NGC 4214 and NGC 1569 estimated between 0.143 and 1400 MHz. The 16''.5 beam is shown in the lower left corner of both maps and the contour levels are drawn at the same levels as in Figure 4.5. The colour bar to the right of each panel gives the spectral index scale.

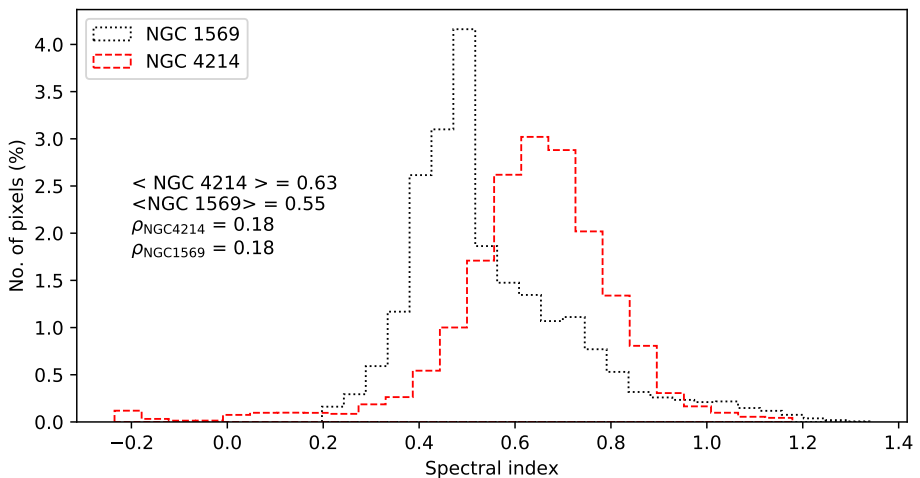


Figure 4.14 – Histograms of non-thermal spectral index distribution in NGC 1569 and NGC 4214. Background radio sources RS4, RS5, RS6, and H were masked before generating the histograms. The mean and the standard deviations of the spectral indices are also indicated.

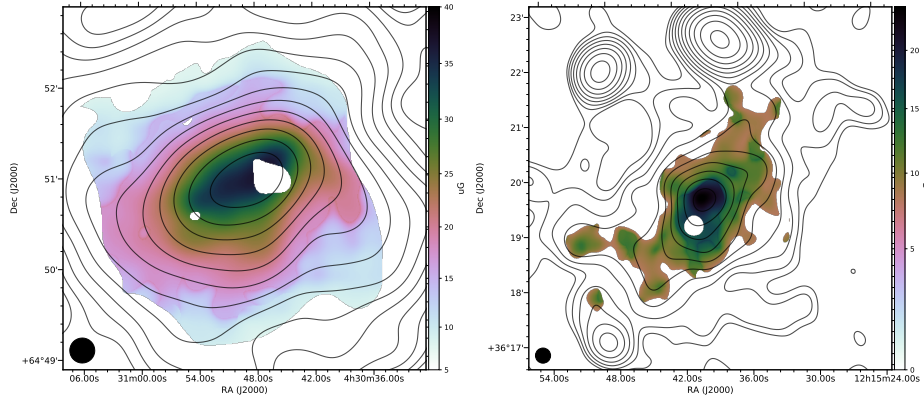


Figure 4.15 – Total magnetic field strength of NGC 1569 and NGC 4214 estimated assuming energy equipartition. Pixels with high thermal fraction have been masked. Pixels corresponding to background radio sources have also been masked. The $16''.5$ resolution of the non-thermal radio map used to compute the magnetic field strength is indicated in the lower left corner of each image. The LOFAR total intensity contour lines are drawn at the same level as in Figure 4.5.

where α is the non-thermal spectral index. Further assumptions, like path length through the synchrotron emitting media and the ratio of proton-to-electron number density, are needed to compute the equipartition magnetic field strength from the total intensity map.

The equipartition magnetic field strength maps of NGC 1569 and NGC 4214 shown in Figure 4.15 were computed using maps of non-thermal emission that were estimated in section 4.5. We did not compute the equipartition magnetic field maps for DDO 50 and NGC 2366 since they do not show significant diffuse radio emission as seen in NGC 1569 and in NGC 4214. While computing the magnetic field strengths, we assumed that the synchrotron path length is 1 kpc and that the ratio of the proton-to-electron number density is 100 (Bell 1978). Note that these assumptions do not affect the resulting magnetic field strengths significantly. Varying the path length and proton-to-electron number density by a factor of two results in less than a 20% change in the value of B_{tot} .

The mean equipartition magnetic field strength in the optical disk of NGC 1569 is about $32 \mu\text{G}$. The mean magnetic field strength drops to about $16 \mu\text{G}$ in the halo. In the case of NGC 4214, the mean magnetic field strength is about $11.5 \mu\text{G}$. Our estimates of equipartition magnetic field strength in NGC 1569 and in NGC 4214 confirm the values estimated by Kepley et al. (2010) and Kepley et al. (2011).

4.7 Search for polarized emission

We used the rotation measure (RM) synthesis technique (Brentjens & de Bruyn 2005) to search for polarized emission in our LOFAR data (see chapter 5 for more information on RM synthesis). For our observational setup, we have

Table 4.7 – Polarization imaging parameters

Parameter	Low resolution	High resolution
Resolution	250"	26"
Channel width	48.8 kHz	48.8 kHz
# of channels	850	849
λ_{\min}	1.805 m ($\nu = 166.087$ MHz)	
λ_{\max}	2.493 m ($\nu = 120.238$ MHz)	
UV limit	10 – 800 λ	80 – 10000 λ
robust value	1.0	-0.3

$\lambda_{\min} = 1.805$ m and $\lambda_{\max} = 2.493$ m resulting in a resolution of $\text{FWHM} = 1.172 \text{ rad m}^{-2}$ and the largest detectable scale $\phi_{\max} = 0.964 \text{ rad m}^{-2}$. Any magnetised structure wider than 0.964 rad m^{-2} will be depolarized. Also note that RM synthesis rotates all instrumentally polarized emission to Faraday depth $\phi \approx 0 \text{ rad m}^{-2}$. However, the ionospheric RM corrections applied in Section 4.2 smear the instrumentally polarized emission in Faraday depth space. The ionospheric RM corrections that we applied during calibration varies from 0.12 rad m^{-2} to 0.25 rad m^{-2} . This implies polarized emission that appears between Faraday depths $-1.052 \text{ rad m}^{-2}$ and 1.422 rad m^{-2} is dominated by instrumental polarization.

Before making the Stokes Q and U channel maps, we flagged all ear-to-ear baselines in the LOFAR core to avoid cross-talk which is known to occur within the station cabinet electronics. We imaged our calibrated visibilities at two different resolutions: 30" and 250". The low resolution channel maps were used to detect weak, diffuse polarized emission from the Galactic foreground while the higher resolution maps were used to search for polarized emission from NGC 1569. The channel maps were made using the **AWImager** (Tasse et al. 2013) and the imaging parameters used to make channel maps at the two different resolutions are listed in Table 4.7. **AWImager** estimates the time- and frequency-dependent LOFAR beam and applies the corrections during the visibility gridding and degridding steps. Due to low signal-to-noise in the individual channel maps, we did not perform deconvolution and used the “dirty” channel maps for RM synthesis. Since we did not deconvolve our channel maps, the data products produced by RM synthesis will not be affected by artefacts described in Pratley & Johnston-Hollitt (2016).

Inspecting the polarization cubes, we do not find any polarized emission towards any of the four dwarf galaxies in our sample. However, we do detect linearly polarized emission from the Galactic foreground and from a few extragalactic radio sources. While a detailed analysis of polarized emission at low radio frequencies from the Galaxy and from background radio sources is beyond the scope of this thesis, we present some preliminary results to demonstrate the quality of the polarization data.

4.7.1 Polarized Galactic foreground

Figure 4.16 shows diffuse polarized emission from the Galactic foreground at four different Faraday depths. Polarized intensity in the maps are displayed in brightness temperature units using the conversion factor of $1 \text{ Jy}/\text{beam} = 949.84 \text{ K}$ estimated close to the center of the band at 143.5 MHz using equation 9-25 from [Wrobel & Walker \(1999\)](#).

The maps shown in Figure 4.16 are at Faraday depth 4.6, 5.6, 6.9, and 7.9 rad m⁻² and correspond to the LOFAR field of view centered on NGC 1569. The images show a filamentary structure extending from the bottom left corner of the field to the top right corner as one advances in Faraday depth. An interesting aspect of the linear feature seen in Figure 4.16 is that it can be traced in the LOFAR polarized intensity maps towards the nearby spiral galaxy IC 342 published by [Van Eck et al. \(2017\)](#)⁸. Note that IC 342 is about $5^{\circ}.4$ away from NGC 1569. The orientation and morphology of the filamentary structure visible in our Faraday depth cube is similar to that seen by [Van Eck et al. \(2017\)](#) (see their figures 5 and 7) suggesting that the polarized emission from the Galactic foreground is caused by a single magnetised structure which spans a few degrees in angular extent.

Similar linear features in polarized intensity have been using a variety of radio telescopes ([Wieringa et al. 1993](#); [Duncan et al. 1999](#); [Jelić et al. 2014, 2015](#); [Lenc et al. 2016](#)) and some have also noticed striking similarities between H I filaments and the polarized structures (see [Clark et al. 2014](#), and references therein). While the origin of such filamentary structures in the ISM is still unclear, polarized intensity images like the ones shown in Figure 4.16 indicate that the physical mechanism giving rise to them span a large angular distances in the sky consistent with MWA results over large sky area ([Lenc et al. 2016](#)).

4.7.2 Polarized emission from a giant radio galaxy

The inverse relationship between the field of view of a radio telescope and the observing frequency implies that observations at low radio frequencies will have larger fields of view compared to their high frequency counterparts. Furthermore, modern radio telescopes like LOFAR are constructed using fixed dipoles (instead of steerable dishes) whose sensitivity pattern on the sky results in large fields of view. Consequently, low frequency observations tend to contain other interesting radio sources in addition to the primary science target and the LOFAR datasets discussed in this chapter are no exception.

While hunting for interesting radio sources other than the primary science target, we identified an extended (about $7'.7$ in angular extent) double-lobed source in the DDO 50 dataset about 1.5 degrees away from the pointing center. The total intensity image of the radio source is shown in the left panel of Figure 4.17. Cross-matching the source with the NASA/IPAC Extragalactic Database, the extended radio source turned out to be the known giant radio galaxy 8C 0821+695 ([Lacy et al. 1993](#)). Located at a redshift of $z = 0.538$, an

⁸The top right corner of the field of view shown in Fig 4.16 coincides with the bottom-left corner of the field of view published in Fig 5 of [Van Eck et al. \(2017\)](#).

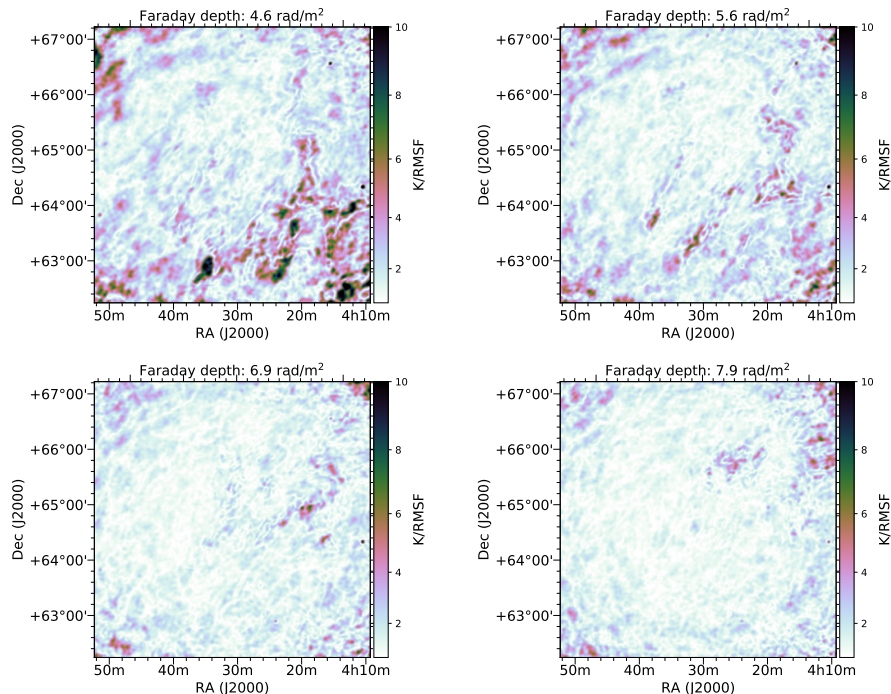


Figure 4.16 – Diffuse polarized emission from the Galactic foreground at four different Faraday depths.

angular extent of $7'.7$ corresponds to a projected linear size of about 2.65 Mpc. Also, notice that the northern lobe shows a tail-like structure near its base which is a canonical sign of gas backflow interacting with a density gradient in the surrounding medium ([Leahy & Williams 1984](#)).

VLA observations at 1.4 GHz reveal linearly polarized emission from both the northern and the southern lobes with a mean polarization fraction of 23 and 26% respectively ([Lara et al. 2000](#)). Inspecting the Faraday depth cube for any polarization feature towards the giant radio galaxy, we identified polarized emission from the northern lobe corresponding to a Faraday depth of -22 rad m^{-2} . The Faraday depth spectrum towards the northern lobe of the giant radio galaxy is shown in the right panel of Figure [4.17](#). We do not detect any polarized emission from the southern lobe.

In addition to the giant radio galaxy, visual inspection of the Faraday depth cubes revealed the presence of several other polarized extragalactic sources within the field of view of all four LOFAR HBA datasets discussed in this chapter. However, catalogues obtained through visual inspection of large datasets like these tend not to be complete and are prone to selection biases. Recently, a number of automated polarization source detection and characterisation pipelines have been developed ([Farnes et al. 2017](#); [Van Eck et al. 2018](#), and Neld et al., submitted) within the LOFAR Magnetism Key Science Project ([Beck et al. 2013](#)). We aim to re-process the polarization data products using these automated pipelines and publish a catalogue of polarized extragalactic sources elsewhere.

4.8 Discussion

In this chapter, we present sensitive low-frequency radio continuum images of four nearby dwarf galaxies. Comparing the total integrated flux density measured at 143 MHz with flux density values measured at higher frequencies reported in the literature, we find that the integrated flux densities of all four galaxies can be best fitted using a single power-law implying none of the observed dwarf galaxies show any sign of spectral flattening at low radio frequencies. However, we observe non-thermal spectral index consistent with $\alpha \sim 0$ towards multiple star-forming regions. Relativistic cosmic ray electrons that produce synchrotron emission are thought to be injected into the interstellar medium by supernova remnants. When a population of relativistic cosmic ray electron with an energy spectrum $Q(E) \propto E^p$ is accelerated in a magnetic field, they emit synchrotron emission. The spectral index of the energy spectrum p is related to the spectral index of the emitted synchrotron α through the relation $\alpha = (1 - p)/2$. Observations of supernova remnants in the Galaxy ([Kothes et al. 2006](#); [Green 2009](#)) and models of shock acceleration in supernova remnants [Bell \(1978\)](#) indicate that $p \sim -2$ implying that the injection spectral index of cosmic ray electrons in galaxies is $\alpha \sim 0.5$. The observed non-thermal spectral index flatter than the injection index in sites of intense star formation in NGC 1569 and in NGC 4214 suggest that synchrotron emission from these regions undergo free-free absorption.

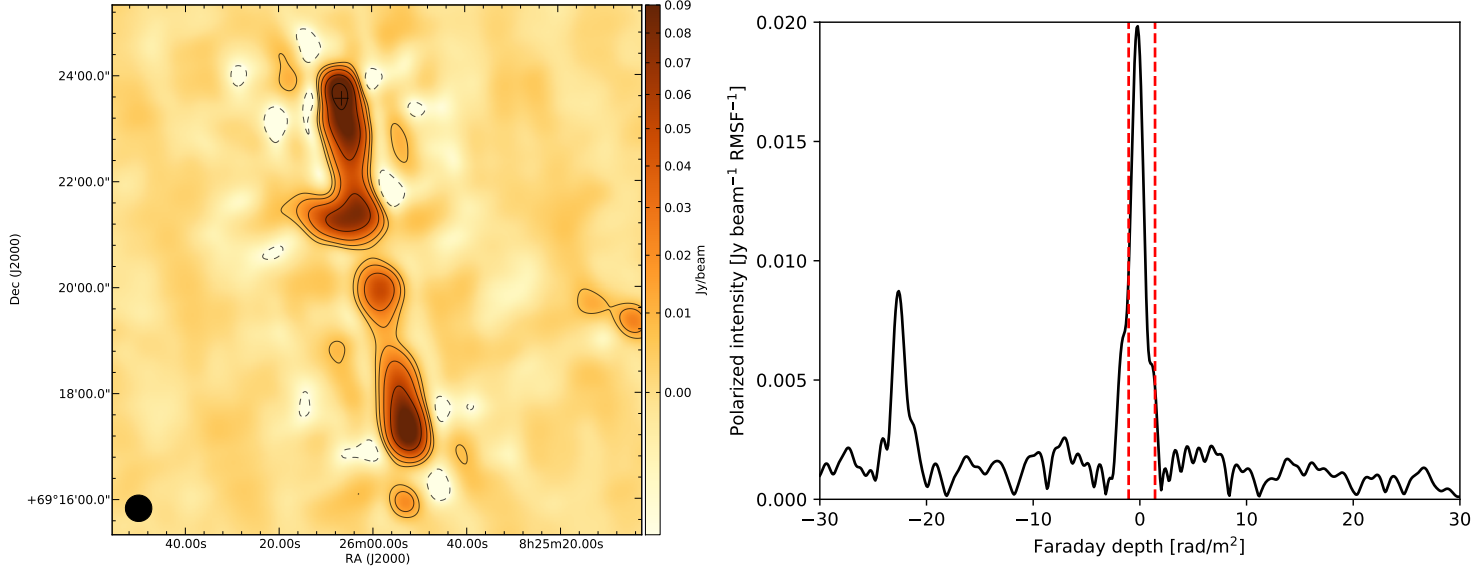


Figure 4.17 – Left: LOFAR HBA total intensity image of the giant radio galaxy 8C 0821+695 located at redshift $z = 0.53$. The LOFAR contour lines are drawn at 7×2^n mJy/beam where $n = 1, 2, 3, \dots$. The location where the polarization emission is detected is indicated using a ‘+’ symbol. Right: Faraday depth spectrum for the region indicated with a ‘+’ symbol on the image on the left. The Faraday depth spectrum show two peaks near Faraday depth -22 rad/m² and 0 rad/m². The feature near Faraday depth 0 rad/m² (enclosed by the two vertical lines) is due to instrumental polarization while the peak near Faraday depth -22 rad/m² corresponds to polarized emission from the giant radio galaxy.

Of the four dwarf galaxies studied in this chapter, NGC 1569 shows the most extended radio continuum emission. Our LOFAR radio images reveal the presence of radio continuum emission in the halo of NGC 1569 up to a distance of ~ 4 kpc from the galactic disk. The extended low frequency radio halo seen around NGC 1569 is morphologically similar to the radio continuum halos detected around normal late-type galaxies like NGC 891 and NGC 5775 where kpc-scale extensions are seen perpendicular to the galactic disk (see for example [Ekers & Sancisi 1977](#); [Soida et al. 2011](#); [Mulcahy et al. 2018](#)). In normal edge-on galaxies, the extended radio halo is typically seen only above the star-forming disk (see for example [Dahlem et al. 2006](#)) and this vertical extension seen only above the star-forming disk appears to hold in the case of NGC 1569 as well (see Figure 4.7). Furthermore, based on H α and radio continuum observations of late-type spiral galaxies, [Dahlem et al. \(2006\)](#) reported a direct, linear relationship between the radial extent of radio continuum halos and the sizes of star-forming regions in the disks of the host galaxies (also see [Dahlem et al. 1995](#); [Tüllmann et al. 2006a,b](#)). [Dahlem et al. \(1995\)](#) argued that there exists a threshold in energy input to the ISM (through supernova feedback) above which it is possible to launch outflows driving gas and cosmic ray electrons into the halo. They also observed that relatively compact regions of star formation are more likely to produce an extended halo than galaxies with widely spread star formation. This implies that regions with intense star formation are more likely to give rise to the “break out condition” necessary for matter to escape the galactic disk in the form of galactic chimneys ([Norman & Ikeuchi 1989](#)). Given the presence of filamentary structure seen in H α in the halo of NGC 1569, regions with intense star-formation in the galactic disk, and the radial steepening of non-thermal spectral index in the extended radio halo, it is very likely possible that a galaxy-wide wind similar to the disk-halo interaction first defined in [Norman & Ikeuchi \(1989\)](#) is at play in NGC 1569.

The presence of a large-scale wind in dwarf galaxies can be of vital importance to the various models that attempt to explain the magnetization of the intergalactic medium using primaeval galaxies. [Kronberg et al. \(1999\)](#) proposed that burst-like star formation in the shallow potential wells of the first galaxies can give rise to magnetised outflows which can pollute the immediate vicinity of the first galaxies with seed magnetic fields. [Kronberg et al. \(1999\)](#) showed that acausal diffusion ([Hogan 1983](#)) of the seed magnetic field combined with cosmological expansion of the universe can propagate the fields to large-scales within a Hubble time. Hydrodynamic simulations and radio polarimetry observations of superbubbles in nearby spiral galaxies indicate that starburst-driven galactic outflows can transport the ordered magnetic field lines from the inner regions of galaxies to the outer halo (see for example [Brandenburg et al. 1995](#); [Chyží et al. 2011](#); [Heald 2012](#)). Furthermore, numerical simulations such as the one carried out by [Bertone et al. \(2006\)](#) do show that a significant fraction of the cosmological volume can be magnetised through seed magnetic fields in the range of $10^{-12} < B < 10^{-8}$ G setup by outflows from the first galaxies (see also [Dubois & Teyssier 2010](#)). However, direct observations of the first galaxies to test this scenario are impossible even with the sensitivity of the next generation radio

telescopes like the Square Kilometre Array (SKA). However, nearby star-burst dwarf galaxies like NGC 1569 are considered to be the closest analogues to the first galaxies (see for example [Steidel et al. 1996](#)). Thus, a detailed model for the propagation of cosmic rays in the halos of dwarf galaxies and the various physical processes that give rise to outflows is key to figuring out whether the first galaxies could be responsible for magnetizing the early universe.

Finally, as mentioned briefly in the introduction, one of the objectives behind our pilot LOFAR observations of dwarf galaxies discussed in this chapter was to prepare for the upcoming LoTSS data release by getting a sense for the sort of science that can be carried out using sensitive radio continuum images of nearby dwarf galaxies at ~ 150 MHz. Observations for our pilot study were carried out using the same observational setup that is employed by the LoTSS survey. The results from our study clearly demonstrate that radio images from the LoTSS survey (with a sensitivity of about $100 \mu\text{Jy}/\text{beam}$ ⁹ at $5''$ resolution) might not be sensitive enough to detect weak, diffuse emission from the radio halos around all nearby dwarf galaxies. From the radio continuum images shown in this chapter, we can see quite clearly that while extended radio emission is detected around the brightest nearby dwarf galaxies like NGC 1569, we do not detect any diffuse emission from even moderately bright galaxies like NGC 2366 and DDO 50. Thus, to be able to detect the diffuse component of the radio continuum emission from nearby dwarf galaxies and to study the propagation of cosmic ray electrons in their halos, deeper observations with both LOFAR LBA and HBA are needed. A brief motivation to pursue this line of research further is provided in chapter [6](#).

4.9 Summary and conclusions

In this chapter, we have presented a pilot study with the LOFAR High Band Antenna to produce deep, resolved radio continuum images of four nearby dwarf galaxies. The key findings are summarised as follows:

- The low frequency total intensity radio continuum map of NGC 1569 and NGC 4214 show diffuse extended emission as compared to previous sensitive observations at 20cm. In NGC 1569, the diffuse emission is more extended by $\sim 1'$ especially in the northern part of the radio halo.
- The integrated radio continuum spectra of all four dwarf galaxies can be fitted with a single power-law spectral index showing no indications of spectral flattening at low frequencies. However, on small scales, non-thermal spectral indices flatter than the injection spectral index (~ 0.5) are seen towards several star-forming regions in all four dwarf galaxies hinting at the presence of free-free absorption in H II regions. Further observations in the $30 - 70$ MHz frequency range using the LOFAR LBA array are required to determine if these regions exhibit spectral turnover.

⁹Note that the “true” sensitivity limit in each LoTSS image can deviate from this advertised $100 \mu\text{Jy}/\text{beam}$ limit due to several reasons like changing RFI conditions around the telescope, the presence of bright off-axis sources, and bad ionospheric conditions.

- Less than 15% of the radio continuum emission observed at 143 MHz appears to be thermal for all galaxies except NGC 2366. About 50% of the radio continuum emission from NGC 2366 at 143 MHz appears to be thermal. This is not surprising given that the two giant H_{II} regions dominate the radio continuum morphology of the galaxy.
- Assuming energy equipartition, we estimated the total magnetic field strength in NGC 4214 and NGC 1569. The mean magnetic field strength in NGC 4214 is about 11.5 μG . In the case of NGC 1569, the mean magnetic field in the inner galaxy is about 32 μG and falls down to 16 μG in the halo.
- No linear polarization was detected towards any of the four dwarf galaxies studied in this chapter. However, the Faraday depth cubes reveal linearly polarized emission from the Galactic foreground and several polarized extragalactic radio sources (including one lobe of a giant radio galaxy at a redshift of 0.538).
- Faraday depth images of the Galactic foreground generated using the linearly polarized emission from the NGC 1569 field show filamentary structure spanning several degrees in angular size.
- Imaging products released by the LOFAR Tier-1 Sky Survey (LoTSS) will not be sensitive enough to detect diffuse radio halos around all nearby dwarf galaxies.

Chapter 5

cuFFS: A GPU-accelerated Rotation Measure Synthesis Code

Sridhar, S. S., Heald, G., & van de Hulst, J. M.
Under review with Astronomy & Computing

5.1 Introduction

A processor is the logic circuit that responds to and processes the basic instructions (fetch, decode, execute, writeback) that drive a computer. Owing to improvements in semiconductor technology, processor manufacturers have been able to pack more transistors onto a single chip while also increasing the processor clock rate¹ thereby achieving higher processing speeds. For example, Intel's 4004 processor released in 1971 had a clock rate of 108 kHz while the Intel Core i7 which is currently available in the market has a clock rate of about 4.2 GHz. Until the early 2000s, improvements in the executions speeds of scientific programs were largely due to the increase in CPU clock rates. This however changed in last decade when chip manufacturers realised that it was hard to keep increasing the clock rate as it led to overheating of the chips due to thermal losses ([Markoff 2004](#)).

Processor manufacturers work around the “thermal wall” by implementing multiple processing units (or cores) on a single chip leading to the design of multicore processors. While each core on the chip is not faster than its predecessor, multicore processors achieve higher compute throughput using parallelisation. Processor vendors typically ship commercially available chips with upto 32 cores. GPUs extend this strategy of implementing multiple cores on a single chip to an extreme limit. In comparison to multicore CPUs, GPUs achieve high compute throughput by maximising the number of processing units (or cores) on a chip. For example, NVIDIA's Tesla P100 card has 56 streaming microprocessors each with 64 processing units resulting in a total of 3584 single precision (or 1792 double precision) floating point compute cores on a single chip. An added advantage of using GPUs over CPU compute clusters is that GPUs consume less energy measured in Watts per FLOP² ([Trancoso & Charalambous 2005; Michalakes & Vachharajani 2008](#)).

While GPUs were originally designed to be used as graphics coprocessors³ to handle higher resolution and display rates demanded by the gaming industry, the massive compute capability of GPUs has been exploited leading to the creation of a new field called GPGPU (General Purpose GPU) computing ([Owens et al. 2007](#)). While the initial scientific programs that were run on GPUs had to be ported to the GPU native programming languages, software solutions made available in the last decade have made it far easier to develop GPU codes ([Nvidia 2017](#)). A review of GPU use in scientific computing can be found in [Owens et al. \(2007\)](#) and [Owens et al. \(2008\)](#).

Graphical processing units have been used quite extensively in astronomy in areas of research ranging from real-time applications like adaptive optics (for example, see [Bouchez et al. 2012](#)) and correlators for radio interferometry ([Schaaf & Overeem 2004](#)), easily parallelisable algorithms like N-body simulations ([Portegies Zwart et al. 2007; Elsen et al. 2007](#)), to more complex algorithms in

¹The clock rate of a processor is proportional to the number of instructions that a processor can execute per unit time.

²Floating point operations

³Coprocessors are secondary processors mounted on a device that complements the compute capabilities of the primary processor.

general relativistic magnetohydrodynamics (Zink 2011). For a detailed discussion on the use of GPUs in astronomy, see Fluke et al. (2011) and Fluke (2012).

Within the field of radio astronomy, GPUs have largely been restricted to implementing fast real-time signal processing applications like correlators and real-time calibration pipelines (for example, see Schaaf & Overeem 2004; Harris et al. 2008; Ord et al. 2009; Chennamangalam et al. 2014; Price et al. 2016), and pulsar de-dispersion pipelines (Magro et al. 2011). Recently, the Dynamic Radio Astronomy of Galactic Neutron stars and Extragalactic Transients (DRAGNET; Bassa et al. 2017)⁴ project with the LOFAR radio telescope has started using GPUs to search for fast radio transients in real-time. GPUs have also been used to accelerate solving the Radio Interferometer Measurement Equation (Hamaker et al. 1996) to calibrate radio interferometry data (Perkins et al. 2015). Within the context of medical imaging, it has been demonstrated that the gridding procedure that needs to be carried out before applying two-dimensional inverse Fourier transform to the data can be accelerated using GPUs (Schomberg & Timmer 1995; Schiwietz et al. 2006). Furthermore, a GPU implementation of the fast Fourier transform library cuFFT is available as part of the official CUDA toolkit.

In this chapter, we present a GPU-accelerated program – CUDA-accelerated Fast Faraday Synthesis (cuFFS) – to perform a commonly used technique in radio polarimetry called Faraday rotation measure (RM) synthesis. This chapter is organised as follows: The theoretical background and computational complexity of the rotation measure synthesis method are presented in §5.2.1 and 5.2.2. Our GPU implementation of the RM Synthesis code is explained in §5.3 and science verification and benchmark tests are presented in section §5.3.2. Finally, we present our conclusion and future prospects for improvements to the software package in §5.4.

5.2 Background

5.2.1 RM synthesis: Theory

Linearly polarized synchrotron emission is an important observational probe to study astrophysical magnetic fields. Synchrotron emission is produced by cosmic ray electrons accelerating across magnetic field lines. The polarization angle of the synchrotron radiation depends on the orientation of the magnetic field in the plane of the sky. Thus resolved polarimetric observations allow us to probe and study the structure of astrophysical magnetic field⁵. However, in practice, this is complicated owing to the fact that the observed polarization angle and polarization fraction⁶ is different from the intrinsic properties at the source due to propagation effects caused by Faraday rotation.

⁴www.astron.nl/dragnet/

⁵To be precise, polarized synchrotron emission probes only the ordered component of the magnetic field. Distinction between different components of astrophysical magnetic fields and the observational probes used to study them is beyond the scope of this chapter. For a recent review on this topic, see Fletcher & Klein (2015) and Beck (2016).

⁶polarized intensity divided by total intensity of the synchrotron radiation

Faraday rotation is a phenomenon by which the plane of polarization of a linearly polarized electromagnetic vector gets rotated due to circular birefringence as it propagates through a magneto-ionic medium like the interstellar medium or the ionosphere. The observed polarization angle (χ) is related to the intrinsic polarization angle (χ_0) through a quantity called Faraday depth (ϕ) as

$$\chi(\lambda^2) = \chi_0 + \phi\lambda^2 \quad (5.1)$$

where ϕ is related to the strength of the magnetic field projected along the line of sight ($B_{||} = \vec{B} \cdot d\vec{l}$) as

$$\phi = 0.81 \int_{source}^{observer} n_e \vec{B} \cdot d\vec{l}. \quad (5.2)$$

In the above equation, n_e is the number density of electrons measured in units of cm^{-2} , l is the pathlength in parsec, B is in μG , and ϕ is in rad m^{-2} .

The observed complex polarization vector $P(\lambda^2) = Q(\lambda^2) + iU(\lambda^2)$ is related to the observed polarization angle $\chi(\lambda^2)$, fractional polarization p , and total intensity I as

$$P(\lambda^2) = pIe^{2i\chi(\lambda^2)}. \quad (5.3)$$

Note that equations 5.1 and 5.3 allows us to relate the observed polarization vector with the intrinsic polarization angle and the Faraday rotation measure. Replacing the Faraday rotation measure with a generalized Faraday depth ϕ , and since emission from multiple ϕ can contribute to the observed polarization vector $P(\lambda^2)$, we can write

$$P(\lambda^2) = \int_{-\infty}^{+\infty} pIe^{2i[\chi_0 + \phi\lambda^2]} d\phi = \int_{-\infty}^{+\infty} F(\phi)e^{2i\phi\lambda^2} d\phi. \quad (5.4)$$

where $F(\phi)$ is defined as the Faraday Dispersion Function $F(\phi) := pIe^{2i\chi_0}$. Inverting this Fourier transform-like equation,

$$F(\phi) = \int_{-\infty}^{+\infty} P(\lambda^2)e^{-2i\phi\lambda^2} d\lambda^2 \quad (5.5)$$

we can see that the Faraday Dispersion Function (FDF) represents the emitted polarized flux as a function of Faraday depth. From equations 5.4 and 5.5, it is easy to see that $P(\lambda^2)$ and $F(\phi)$ form a Fourier-like transform pair.

Recovering $F(\phi)$ from the observed $P(\lambda^2)$ is however not straight-forward as we cannot measure $P(\lambda^2)$ for $\lambda < 0$. Furthermore, $P(\lambda^2)$ is also not measured for all possible values of $\lambda > 0$. Rotation measure synthesis is a technique that was formulated by [Brentjens & de Bruyn \(2005\)](#) which tries to recover $F(\phi)$ using a discrete sampling of $P(\lambda^2)$. In addition to reconstructing $F(\phi)$, the procedure also improves the sensitivity of the polarization measurement by adding up derotated polarization signal across the entire observed bandwidth. In the following section, we provide a brief overview of the procedure. For a detailed account on RM synthesis, we refer the reader to [Brentjens & de Bruyn \(2005\)](#) and [Heald \(2009\)](#).

The rotation measure synthesis technique works around this problem by introducing a window function $W(\lambda^2)$ which is non-zero only for λ^2 values at which complex polarization $P(\lambda^2)$ has been measured. Thus, equation 5.4 can be modified as

$$\tilde{P}(\lambda^2) = W(\lambda^2)P(\lambda^2) = W(\lambda^2) \int_{-\infty}^{+\infty} P(\lambda^2)e^{-2i\phi\lambda^2} d\lambda^2 \quad (5.6)$$

Combining the above equation with equation 5.5 and applying the convolution theorem, the reconstructed Faraday dispersion function $\tilde{F}(\phi)$ is related to the “true” Faraday dispersion function as

$$\tilde{F}(\phi) = F(\phi) * R(\phi) = K \int_{-\infty}^{+\infty} \tilde{P}(\lambda^2)e^{-2i\phi\lambda^2} d\lambda^2 \quad (5.7)$$

From the above equation, it is easy to see that the recovered Faraday dispersion function is a convolution of the “true” Faraday dispersion function with smoothing kernel called the Rotation Measure Spread Function (RMSF). Conceptually, this is analogous to synthesis imaging where $\tilde{F}(\phi)$ is equivalent to the dirty image and $R(\phi)$ is equivalent to the dirty beam. The RMSF is related to the weight function $W(\lambda^2)$ as

$$R(\phi) = K \int_{-\infty}^{+\infty} W(\lambda^2)e^{-2i\phi\lambda^2} d\lambda^2 \quad (5.8)$$

where

$$K = \left(\int_{-\infty}^{+\infty} W(\lambda^2)d\lambda^2 \right)^{-1}. \quad (5.9)$$

5.2.2 RM synthesis: In practice

As discussed in the previous section, the complex polarization vector is not measured for all values of λ^2 . Modern radio telescopes measure $P(\lambda^2)$ in narrow frequency channels spread across a wide bandwidth each with equal bandwidth. In such a scenario, the integrals in equations 5.7, 5.8 and 5.9 can be replaced by sums over each frequency channel provided $\phi\delta\lambda^2 \ll 1$:

$$\tilde{F}(\phi) \approx K \sum_{i=1}^N \tilde{P}_i e^{-2i\phi(\lambda_i^2 - \lambda_0^2)} \quad (5.10)$$

$$R(\phi) \approx K \sum_{i=1}^N w_i e^{-2i\phi(\lambda_i^2 - \lambda_0^2)} \quad (5.11)$$

$$K = \left(\sum_{i=1}^N w_i \right)^{-1} \quad (5.12)$$

In the above equations, \tilde{P}_i is the complex polarization vector measured at λ_i and $w_i = W(\lambda_i)$. Figure 5.1 shows a RMSF calculated using equation 5.11 for

a mock L-band dataset consisting of 1000 frequency channels covering the 1 – 2 GHz frequency range. Notice in equations 5.10 and 5.11, we have introduced an additional term λ_0^2 in the exponent which is set to the mean of λ_i^2 . Introducing this additional λ_0^2 term is useful as it prevents rapid rotation of $\tilde{Q}(\phi)$ and $\tilde{U}(\phi)$ as can be seen in Figure 5.1. Scaling these two quantities allows one to make an accurate estimate of Q_{peak} and U_{peak} and thus make an accurate estimate of the polarization angle $\chi = 0.5 \tan^{-1}(U/Q)$.

The aim of the RM synthesis software package is to compute equations 5.10 and 5.12. Equation 5.11 is needed only if one wishes to deconvolve $R(\phi)$ from the reconstructed Faraday dispersion function using a procedure called RM-CLEAN⁷ (Heald 2009).

Since $\tilde{F}(\phi)$ and $\tilde{P}(\phi)$ in equation 5.10 are complex vectors, the equation can be written in terms of its Stokes Q and Stokes U components as

$$\tilde{Q}(\phi) = K \sum_{i=1}^N Q_{\lambda i} \cos 2\phi (\lambda_i^2 - \lambda_0^2) + U_{\lambda i} \sin 2\phi (\lambda_i^2 - \lambda_0^2) \quad (5.13)$$

$$\tilde{U}(\phi) = K \sum_{i=1}^N U_{\lambda i} \cos 2\phi (\lambda_i^2 - \lambda_0^2) - Q_{\lambda i} \sin 2\phi (\lambda_i^2 - \lambda_0^2). \quad (5.14)$$

$$\tilde{P}(\phi) = \sqrt{\tilde{Q}^2(\phi) + \tilde{U}^2(\phi)} \quad (5.15)$$

The above two equations compute the recovered Faraday dispersion function for a given value of ϕ . In practice, the above equations need to be computed for a wide range of values of ϕ to get a sense for the variation of the intrinsic polarization vector as a function of Faraday depth. Thus the above equations become

$$\tilde{Q}(\phi_j) = K \sum_{i=1}^N Q_{\lambda i} \cos 2\phi_j (\lambda_i^2 - \lambda_0^2) + U_{\lambda i} \sin 2\phi_j (\lambda_i^2 - \lambda_0^2); \forall \phi_j \in [\phi_{\min}, \phi_{\max}] \quad (5.16)$$

$$\tilde{U}(\phi_j) = K \sum_{i=1}^N U_{\lambda i} \cos 2\phi_j (\lambda_i^2 - \lambda_0^2) - Q_{\lambda i} \sin 2\phi_j (\lambda_i^2 - \lambda_0^2); \forall \phi_j \in [\phi_{\min}, \phi_{\max}]. \quad (5.17)$$

These two equations need to be computed for each line of sight in a radio image to construct a 3D RM-cube contains the Faraday dispersion function for all lines of sight.

5.2.3 RM synthesis: Computational costs

From equations 5.13 and 5.14, it is easy to see that K , 2ϕ , and $\lambda_i^2 - \lambda_0^2$ need to be computed only once for the entire dataset and have negligible compute cost.

⁷RM-CLEAN is not supported in the current version of cuFFS. However, we intend to implement this in the next code release.

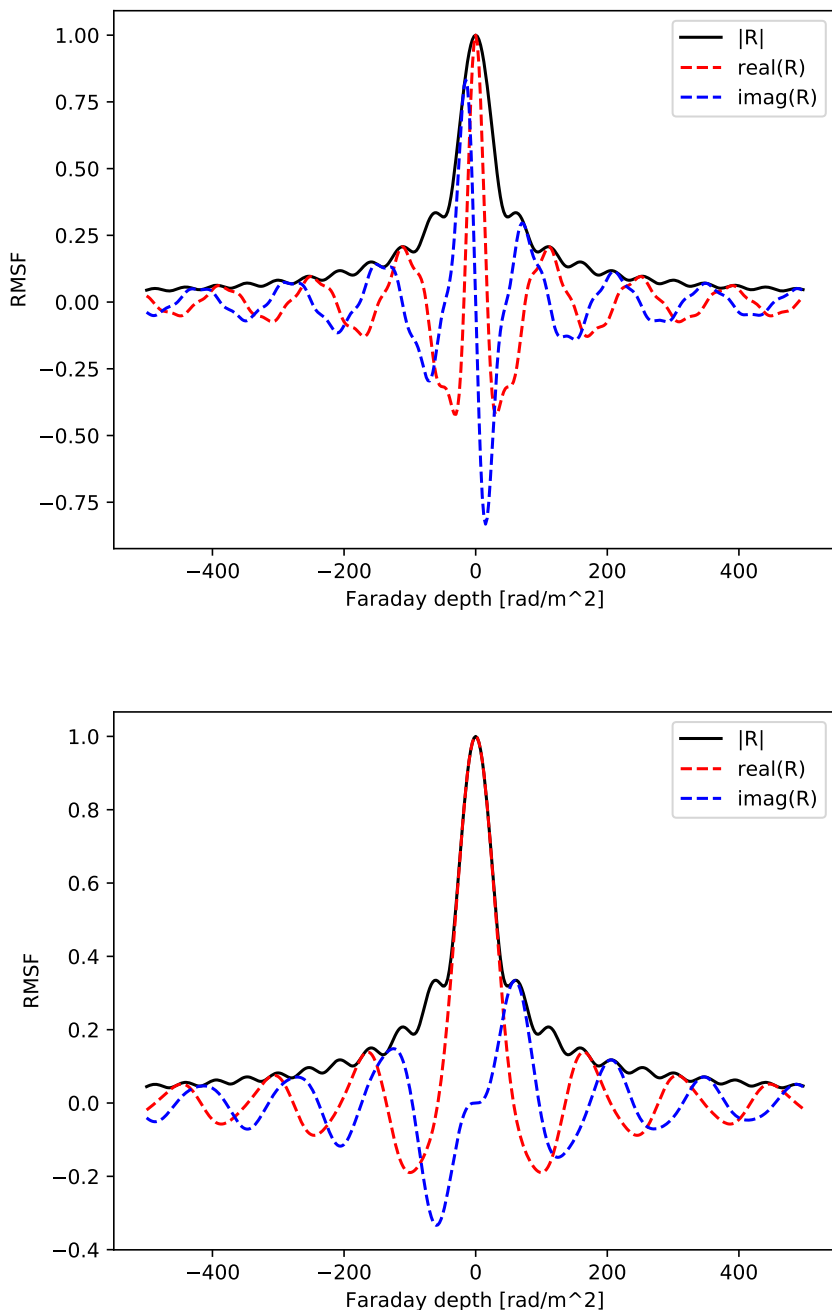


Figure 5.1 – Rotation Measure Spread Function (RMSF) for a mock L-band dataset consisting of 1000 frequency channels covering the 1 – 2 GHz frequency range with $\lambda_0^2 = 0$ (*top*) and $\lambda_0^2 \neq 0$ (*bottom*).

The compute cost to calculate $\tilde{Q}(\phi)$, $\tilde{U}(\phi)$, and $\tilde{P}(\phi)$ for one ϕ and one λ^2 is 13 FLOP (7 multiplications, 2 trigonometric functions, 2 additions, 1 subtraction and 1 square root operation).

Thus to calculate $\tilde{Q}(\phi)$, $\tilde{U}(\phi)$, and $\tilde{P}(\phi)$ for one Faraday depth value using N_{chan} frequency channels is

- $15 * N_{\text{chan}}$ FLOP to compute equations 5.13 – 5.15 for a given ϕ using all λ_i^2 .
- $2(N_{\text{chan}} - 1)$ additions for summations over all i .
- 2 multiplications to scale the values by K .

The above operations need to be repeated N_ϕ times to create RM-cubes of $\tilde{Q}(\phi)$, $\tilde{U}(\phi)$, and $\tilde{P}(\phi)$ with N_ϕ Faraday depth planes using N_{chan} input frequency channels. This amounts to a total computation cost of $15N_{\text{chan}}N_\phi$ FLOP for a single line of sight. Since each line of sight in the input datacubes can be treated independently, we can scale the computation cost further by the number of spatial pixels in the input datacubes making the final computational cost to be $\sim 15N_{\text{chan}}N_\phi N_{\text{los}}$.

For a typical polarimetry data set from the Westerbork Synthesis Radio Telescope, for example from the Westerbork Spitzer Nearby Galaxy Survey (SINGS) survey (Braun et al. 2007; Heald et al. 2009), which has 512^2 spatial pixels, 803 frequency channels and 401 Faraday depth planes, the computational cost required to carry out RM synthesis is about 1.27 TFLOP⁸.

To make this estimate, we assumed that each arithmetic and trigonometric functions amount to a single floating point operation. In practice, this is however not true. For example, standard libraries evaluate trigonometric functions as Taylor series expansions and the number of Taylor terms used in the expansion can be implementation-dependent. Furthermore, the exact number of instructions needed for different mathematical operations available in the standard C libraries can vary depending on the implementation, system hardware and compiler optimisation options. Thus the above compute cost should be treated only as a lower limit and not as a precise value.

5.3 GPU implementation of RM Synthesis

cuFFS is written in C, and GPU acceleration is achieved using the CUDA Application Programming Interface (API). User input is provided to the program using a configuration file which is parsed using the structured configuration file parser libconfig⁹. Sample input parset file and output produced by the program are shown in Figures 5.2 and 5.3.

Input and output data cubes can either be in FITS (Pence 1999) or in HDFITS (Price et al. 2015) formats. FITS files are read in and written out using the

⁸1 TFLOP = 1 trillion floating-point operations.

⁹<http://www.hyperrealm.com/libconfig/>

```

// How many GPUs to use?
// In version 1.0, this is always 1.
nGPU = 1;

// What is the input format?
// Can be "FITS" or "HDF5" (not case-sensitive).
fileFormat = "FITS";

// Define how fits files are stored on disk
qCubeName = "cube-Q.rot.fits";
uCubeName = "cube-U.rot.fits";
freqFileName = "frequencies-Q.txt";

// Define the faraday depth axis. All units in rad/m/m
plotRMSF = False;
phiMin = -500.;
nPhi = 401; // integer
dPhi = 2.5;

// Prefix for output filenames
outPrefix = "trial1_";

```

Figure 5.2 – Sample input parset to cuFFS.

CFITSIO¹⁰ library while the HDFITS is accessed using the HDF5 library¹¹. Justification for supporting data formats in addition to the standard FITS format is provided in section 5.3.1.

A fast CPU implementation of RM synthesis, like Brentjens (2007), computes the RM cubes by evaluating all Faraday depth values for each input channel. The main advantage of using such a strategy is that it minimises disk I/O as each input channel is read only once and the output cubes are written to disk only once as long as the output cubes fit in the memory. If all output Faraday depth planes do not fit in memory, the CPU program computes a subset of Faraday depth planes that fits in memory, writes the output planes to disk, and then proceeds to compute the next subset of Faraday depth planes.

Note that adopting a similar scheme is not very efficient on a GPU as this CPU implementation would involve numerous data transfers between the *host* and the *device*. To speed up RM synthesis using a GPU, a new programming model that reduces the data transfer between the host and the GPU is needed. Since each line of sight in the data cube can be processed independent of each other, each core on the processor can be assigned to process a particular line of sight and hence RM synthesis can be efficiently implemented on multi-core architectures like GPUs.

¹⁰<https://heasarc.gsfc.nasa.gov/fitsio/>

¹¹<https://support.hdfgroup.org/HDF5/>

```
RM Synthesis v0.2
Written by Sarrvesh S. Sridhar
INFO: Parsing input file /home/see041/RMSynth_GPU/parsetFile
INFO: Checking input files
INFO: Detected 1 CUDA-supported GPU(s)
INFO: Selected device 0

#####
Q Cube: /data/see041/lofar_lowres/fits/cube-U.rot.fits
U Cube: /data/see041/lofar_lowres/fits/cube-U.rot.fits
phi min: -350.00
# of phi planes: 7000
delta phi: 0.10

Input dimension: 540 x 540 x 850
Output dimension: 540 x 540 x 7000
#####
INFO: Computing RMSF
INFO: Writing RMSF to trial1rmsf.txt
INFO: Starting RM Synthesis
INFO: Launching 540x219 blocks each with 32 threads
INFO: Timing Information
    Input read time: 0.647 s
    Compute time: 0.386 s
    Output write time: 12.966 s
    D2H Transfer time: 0.219 s
INFO: Total execution time: 0:0:17
```

Figure 5.3 – Sample output produced by cuFFS.

Figure 5.4 shows a flow chart representation of the program execution cycle. Transferring data between the host (CPU) and the device (GPU) can be expensive and time-consuming. To maximise the compute-to-transfer time ratio, our implementation ensures that the same data is transferred between the host and the device only once. The program carries out the following steps for each line of sight:

1. Transfer $\tilde{Q}(\lambda^2)$ and $\tilde{U}(\lambda^2)$ to the GPU memory.
2. Each thread on the GPU computes $\tilde{Q}(\phi)$, $\tilde{U}(\phi)$, and $\tilde{P}(\phi)$ for a given Faraday depth value.
3. Transfer the computed $\tilde{Q}(\phi)$, $\tilde{U}(\phi)$, and $\tilde{P}(\phi)$ to the host memory.

By repeating these steps for each line of sight in the input datacubes, the program constructs the final RM cubes.

Modern GPUs come with substantial amount of DRAM which implies that multiple lines of sight can be processed at the same time. Additionally, transferring a larger chunk of data between host memory and device memory is more efficient than issuing multiple data transfers. As a result, in practice, cuFFS processes multiple lines of sight at once. The GPU kernel is implemented such that each spawned thread on the GPU computes $\tilde{Q}_i(\phi_j)$, $\tilde{U}_i(\phi_j)$ and $\tilde{P}_i(\phi_j)$ for a given line of sight (i) for a fixed Faraday depth (ϕ_j). Thus, the total number of independent threads that are executed on the GPU is $(N_\phi \times N_{\text{los}})$ where N_{los} is the total number of independent sight lines processed at a time and N_ϕ is the number of output Faraday depth values that need to be computed.

Our code is publically available through Github¹².

5.3.1 FITS, HDF5, and HDFITS

As discussed in the previous section, our code achieves parallelism by exploiting the fact that each line-of-sight and each Faraday depth output for a given line of sight in RM synthesis can be treated independently of each of other. However, during the initial development and testing phase, we quickly realised that reading and writing the FITS data cubes along the third data axis (or each line-of-sight) was the major bottleneck in our code. Even for small datacubes like the ones corresponding to WSRT observations, reading and writing datacubes along the third data axis was significantly longer than the amount of time required to carry out the actual RM synthesis computation. In addition to the bottleneck caused by the FITS I/O, it is becoming clear that the FITS data format is not best suited for large multi-dimensional datasets. An excellent review of the limitations of the FITS data format in the era of big data (radio) astronomy is presented in [Thomas et al. \(2015\)](#).

The slow read/write speed associated with the FITS format can be alleviated by rotating (for example using the `reorder` task in miriad ([Sault et al. 1995](#))) the input datacubes such that the frequency axis is the fastest-varying dimension.

¹²https://github.com/sarrvesh/RMSynth_GPU

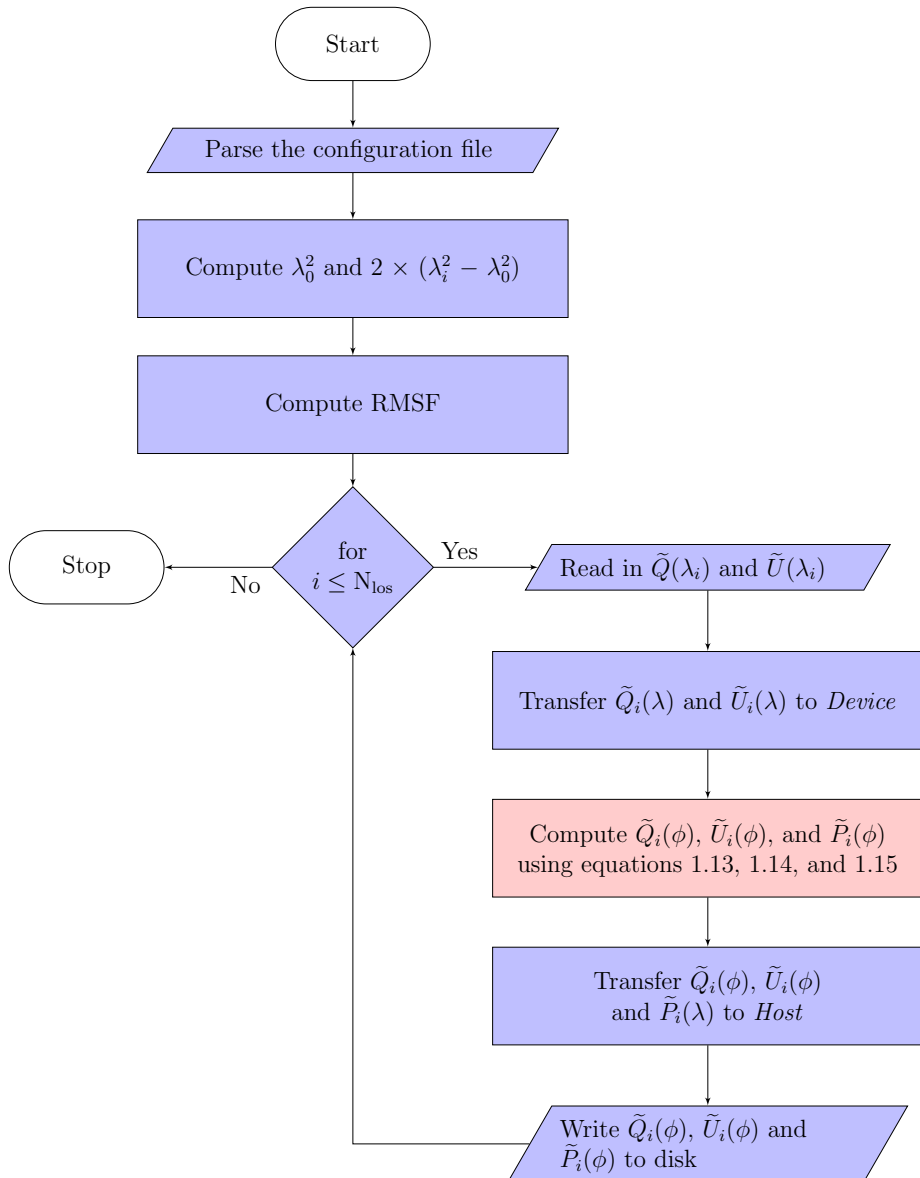


Figure 5.4 – A flowchart depicting the execution cycle of cuFFS. All nodes shown in blue represent operations carried out on the CPU nodes shown in red indicate operations performed on the GPU.

After running cuFFS, the output datacubes, which contain the Faraday depth axis as the fastest-varying dimension, can be derotated back to the original order. This rotation can be easily implemented in python-based imaging pipelines using NumPy’s `numpy.memmap` and `numpy.swapaxis` functions. For the LOFAR_HR dataset described in the next section, this rotation has an incremental overhead cost of a few seconds.

Another approach to reduce the read/write time would be to adopt data formats other than the standard FITS file format. File formats like the Hierarchical Data Format version 5 (HDF5) are well suited for storing large datacubes and have a significantly lower read/write time compared to the FITS format¹³ especially while reading along the slowest-varying axis. Recently, Price et al. (2015) proposed a new format called HDFITS which merges the FITS data model with the HDF5 file format. Note that data model defines how a dataset is structured and file format specifies how the bits are stored on disk. A similar strategy has also been adopted by fields like climatology and oceanography where the NetCDF data format is built on top of the HDF5 file format. In the remainder of this section, we provide a brief overview of the HDF5 file format and explain how HDFITS ports the FITS data model to the HDF5 file format.

HDF5 (Hierarchical Data Format version 5) can be thought of as a container that is capable of storing heterogeneous datasets. The basic components of an HDF5 file are groups and datasets and hierarchy within a dataset is achieved using a binary tree-like arrangement. Figure 5.5 shows the structure of a HDF5 file. In addition to groups and datasets, each HDF5 object can have one or more *attributes* that provide additional information about the corresponding object. This hierarchical nature of HDF5 supported by a variety of metadata makes it easy to handle complex data objects. A detailed documentation on HDF5 can be found in The HDF Group (2011).

A Single Image FITS (SIF) file consists of primary header and data unit (HDU; [FITS Working Group 2008](#)). The structure of a sample HDFITS image is shown in Listing 5.1. The HDFITS file has two groups: ROOT (indicated as “/”) and PRIMARY. The PRIMARY group, which is the child of the ROOT group, contains the image data (defined as the dataset DATA) which in this example has dimension $1 \times 1 \times 2048 \times 2048$. In addition to the dataset DATA, notice that the group PRIMARY also has attributes named CDELT1 and BMAJ. In the HDFITS format, the FITS keywords are all stored as attributes of the PRIMARY group. The main advantage of using HDFITS in our program is that the structure of the dataset stored in the HDF5 file is similar to the standard FITS format with the added advantage of higher read/write speed.

Listing 5.1 – Output of the `h5dump` tool showing the hierarchical layout of an HDFITS image using the Data Definition Language (DDL) syntax. For the sake of brevity, only two FITS keywords (CDELT1 and BMAJ) are shown here.

```
1 HDF5 "NGC1569-final.h5" {
2 GROUP "/" {
3     ATTRIBUTE "CLASS" {
```

¹³Shortridge (2015) has an excellent overview of new data formats that have recently been proposed.

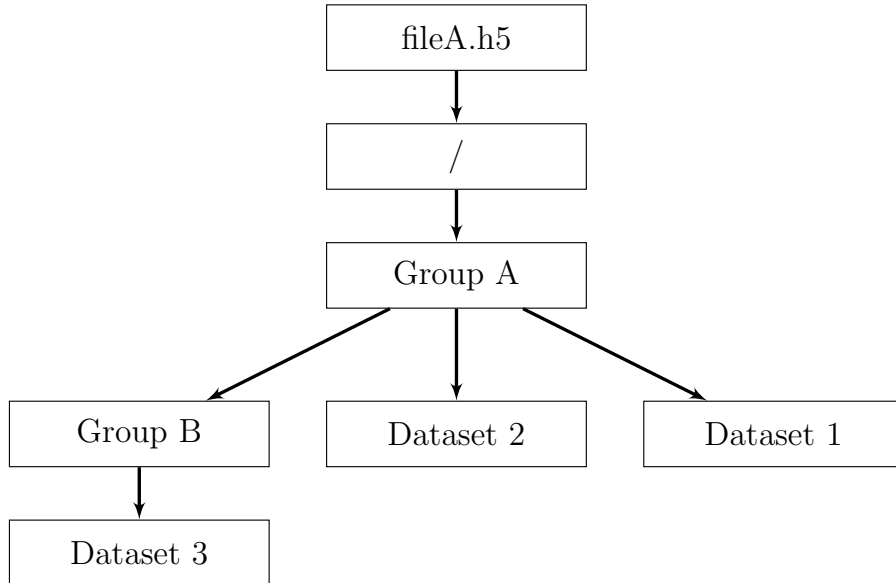


Figure 5.5 – Structure of a HDF5 containing the group and dataset objects arranged as a binary tree. Image adapted from [The HDF Group \(2011\)](#).

```

4      DATATYPE H5T_STRING {
5          STRSIZE 10;
6          STRPAD H5T_STR_NULLPAD;
7          CSET H5T_CSET_ASCII;
8          CTYPE H5T_C_S1;
9      }
10     DATASPACE SCALAR
11 }
12 GROUP "PRIMARY" {
13     ATTRIBUTE "CDELT1" {
14         DATATYPE H5T_IEEE_F64LE
15         DATASPACE SIMPLE { ( 1 ) / ( 1 ) }
16     }
17     ATTRIBUTE "BMAJ" {
18         DATATYPE H5T_IEEE_F64LE
19         DATASPACE SIMPLE { ( 1 ) / ( 1 ) }
20     }
21     DATASET "DATA" {
22         DATATYPE H5T_IEEE_F32BE
23         DATASPACE SIMPLE { ( 1, 1, 2048, 2048 ) / ( 1, 1, 2048, 2048 ) }
24         ATTRIBUTE "CLASS" {
25             DATATYPE H5T_STRING {
26                 STRSIZE 9;
27                 STRPAD H5T_STR_NULLPAD;
28                 CSET H5T_CSET_ASCII;
29                 CTYPE H5T_C_S1;
  
```

```

30         }
31         DATASPACE SCALAR
32     }
33     ATTRIBUTE "IMAGE_VERSION" {
34         DATATYPE H5T_STRING {
35             STRSIZE 7;
36             STRPAD H5T_STR_NULLPAD;
37             CSET H5T_CSET_ASCII;
38             CTYPE H5T_C_S1;
39         }
40         DATASPACE SCALAR
41     }
42 }
43 }
44 }
45 }
```

To achieve higher read/write throughput and to be consistent with existing data format, the current version of cuFFS supports input and output datacubes in both **FITS** and **HDFITS** formats. While operating in the **FITS** mode, cuFFS assumes that the user has rotated the input cubes such that the frequency axis is the fast-varying dimension. Since **HDF5/HDFITS** is efficient in reading along the frequency axis, no such prior rotation is required while using cuFFS in **HDF5** mode.

As discussed above, numerous data formats have been proposed in the recent years for archiving large datasets. If desired, additional data formats like N-dimensional Data Format (NDF; [Jenness et al. 2015](#)), Starlink Hierarchical Data System (HDS; [Jenness 2015](#)) and Advanced Scientific Data Format (ASDF; [Greenfield et al. 2015](#)) can be supported easily with minimal change to the existing code.

5.3.2 Science verification and benchmarks

To verify the output produced by cuFFS, we compared the output ($\tilde{P}(\phi)$) produced by cuFFS with a CPU implementation of RM synthesis from [Brentjens \(2007\)](#). The CPU and the GPU codes were used to process a data cube from the Westerbork Synthesis Radio Telescope Spitzer Infrared Nearby Galaxies Survey (WSRT-SINGS; [Heald et al. 2009](#)). We compared the output data cubes ($\tilde{P}(\phi)$) on a pixel-by-pixel basis and found that the mean of the ratio between the outputs produced by the GPU and the CPU to be 1.0 with a standard deviation of 1.5×10^{-6} implying that the output produced by cuFFS matches the output produced by the CPU code very well.

Figure 5.6 shows the ratio of the pixels values produced by the GPU and the CPU code ($\tilde{P}_{\text{GPU}}(\phi)/\tilde{P}_{\text{CPU}}(\phi)$) plotted as a function of the output pixel values in $\tilde{P}_{\text{GPU}}(\phi)$. As can be seen from Figure 5.6, the pixel values in the two output cubes match very well.

To judge the performance of cuFFS, we compared the execution time of our GPU code with a CPU implementation of RM Synthesis from [Brentjens \(2007\)](#)

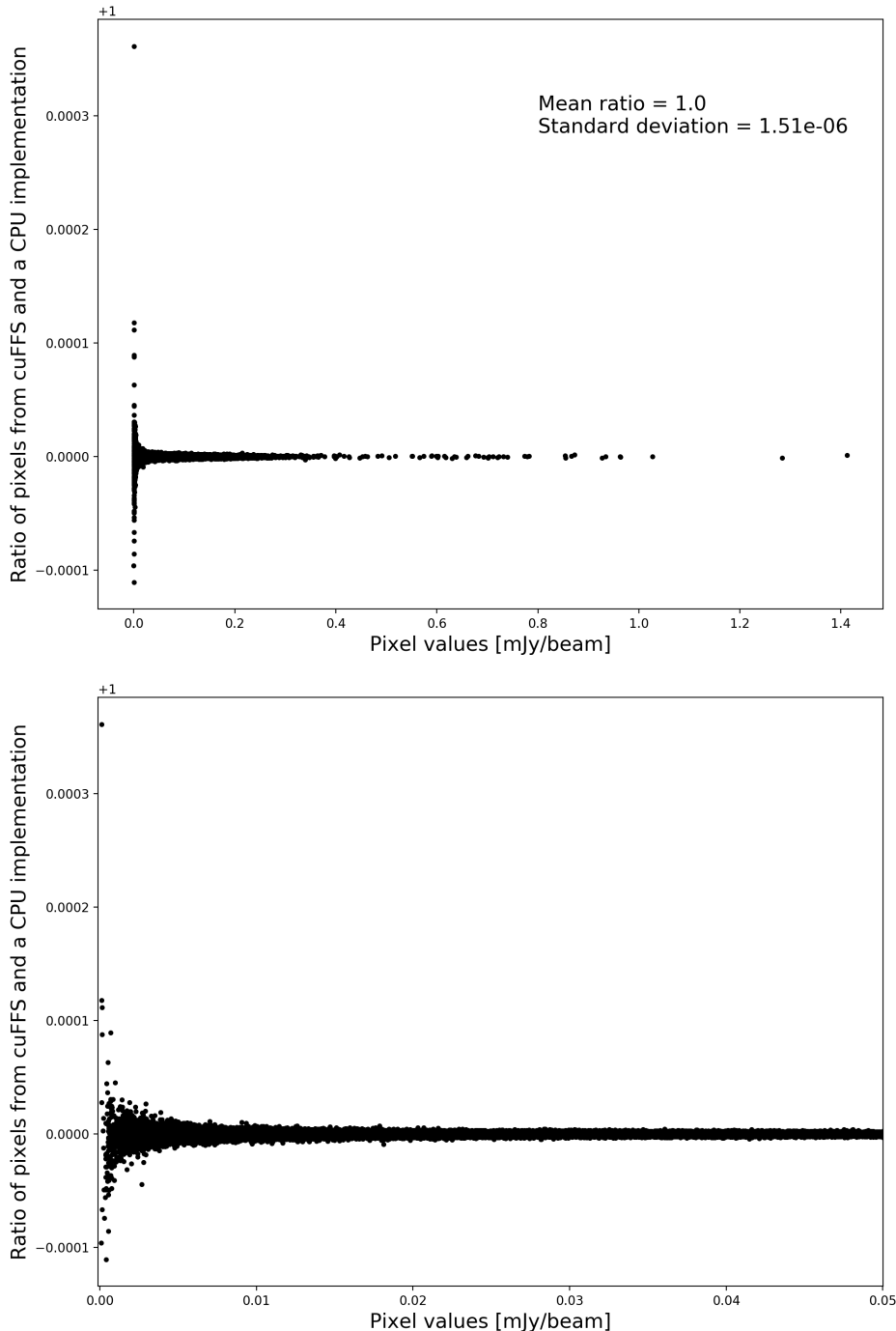


Figure 5.6 – Top: Comparison between the output pixel values produced by cuFFS and a CPU implementation by Brentjens (2007). **Bottom:** Zoomed-in version of the figure shown in the left panel to better display the scatter in pixel values computed by the GPU and the CPU codes. The scatter seen for the low output pixel values is probably due to numerical error.

using a combination of both real and mock datasets from current and upcoming telescope facilities. A brief description of each test dataset is presented below:

- **WSRT**: As a typical Westerbork polarimetry dataset, we used one of the datacubes produced as part of the Westerbork SINGS survey (WSRT-SINGS; [Heald et al. 2009](#)). After removing frequency channels corrupted by RFI, the final datacube consists of 803 frequency channels. The frequency setup used in the WSRT-SINGS survey results in a Faraday depth resolution of 144 rad m^{-2} . Based on these values, the input and the output datasets have dimensions $512 \times 512 \times 803$ and $512 \times 512 \times 401$ respectively.
- **LOFAR_LR**: Diffuse polarized emission from the Galactic foreground can be detected at 150 MHz in low resolution LOFAR maps with a resolution of a few arcmins ([Jelić et al. 2015](#); [Van Eck et al. 2017](#)). The LOFAR low resolution dataset used for this test corresponds to a field around the nearby dwarf galaxy NGC 1569. The input datacubes are at a resolution of $250''$. Calibration and imaging procedure used to obtain the datacubes are discussed elsewhere in this thesis. After visual inspection and rejecting channel maps corrupted by RFI, the final datacube contains 856 frequency channels. With 48.8 kHz-wide channel maps covering the bandwidth ranging from 120.238 – 166.087 MHz, the output Faraday cubes will have a Faraday depth resolution of 1.17 rad m^{-2} and sensitive to a maximum Faraday depth value of about 350 rad m^{-2} . Thus the dimensions of the input and the output datacubes are $540 \times 540 \times 856$ and $540 \times 540 \times 7000$.
- **LOFAR_HR**: The LOFAR high resolution dataset was produced from the same visibility data that was used to create the **LOFAR_LR** datacubes. The only difference between the **LOFAR_HR** and **LOFAR_LR** datacubes is that **LOFAR_HR** are at a higher angular resolution of $26''$. The dimensions of the input and the output datacubes are $4000 \times 4000 \times 856$ and $4000 \times 4000 \times 7000$.

All CPU and GPU benchmarks were carried out on CSIRO’s Bracewell computer cluster. Each node on the cluster is powered by 28 Intel(R) Xeon(R) CPU E5-2690 v4 2.60GHz processors with 256 GB RAM and is equipped with four Nvidia Tesla P100-SXM2-16GB GPUs. The CPU code was permitted to use up to 245 GB of RAM. The execution times for different datacubes using the CPU and the GPU implementation is listed in Table 5.1. Note that the execution times for the CPU code will increase linearly with decreasing RAM size.

From the execution times reported in Table 5.1, it can be seen quite clearly that our GPU implementation in both FITS and HDF5 mode is substantially faster than the execution times achieved using the CPU implementation. Execution times reported in Table 5.1 while using cuFFS in FITS mode indicate that rotating and derotating the input and output datacubes still dominates the total execution time. If, however, the data rotation is done as part of the imaging pipeline that produces the Stokes Q and U cubes, then the GPU implementation is about two orders of magnitude faster than the CPU implementation for large datasets.

Table 5.1 – Comparison of CPU and GPU execution times for different input and output data cubes.

Dataset	Number of			Execution time [hh:mm:ss]		
	Spatial pixels	Channels	ϕ planes	CPU ^(a)	GPU ^(a)	GPU ^(b)
WSRT	512 × 512	803	401	00:02:02	00:00:50 ^(c) + 00:00:08 ^(d)	00:00:25
LOFAR_LR	540 × 540	856	7000	00:39:30	00:04:37 ^(c) + 00:00:17 ^(d)	00:04:36
LOFAR_HR	4000 × 4000	856	7000	58:01:32	12:53:39 ^(c) + 00:13:47 ^(d)	02:28:02

Notes. CPU tests (single threaded, vectorized) were carried out on a single node with Intel(R) Xeon(R) CPU E5-2690 processor at 2.6 GHz clock with 256 GB RAM. The CPU code was permitted to use a maximum of 200 GB RAM. GPU tests was carried out using an NVIDIA Tesla P100-SXM2-16GB device. (a) FITS file format; (b) HDF5 file format; (c) Time spent reordering the input datacube to have the frequency axis as the first axis and reordering the output datacubes so that the Faraday depth axis is the third axis; (d) Compute time.

5.4 Conclusion and future outlook

In this chapter, we have presented a GPU-accelerated CUDA program to perform a widely used radio astronomy algorithm called rotation measure synthesis. The software package is made publically available through Github. The software package is capable of handling input and output datacubes in either the FITS or the HDFITS format. If needed, additional data formats can also be supported with very little change to the existing code base. In addition to rotation measure synthesis, we plan to implement advanced polarization processing tools like RM-CLEAN (Heald 2009) in the future version of our software package.

Comparing our GPU implementation on NVidia Tesla P100-SXM2-16GB GPU with single-threaded, vectorized CPU implementation, depending on the input and output format, we observe gains in execution times by at least a factor of 15 for smaller dataset from telescopes like WSRT and by at least by two orders of magnitude for larger datasets from telescopes like LOFAR and SKA1. Further speedup can be achieved by using Fast Fourier Transforms (FFT) instead of Discrete Fourier Transforms (DFT) in equations 5.13 and 5.14. CUDA accelerated Fast Fourier Transform can be accelerated using standard libraries like cuFFT¹⁴. We aim to implement these advanced features in future versions of cuFFS.

Finally, as discussed in section 5.3.2 and Table 5.1, the main bottleneck in our implementation of RM synthesis is the FITS file access using CFITSIO. Even for a small WSRT dataset, rotating the cubes to speedup I/O can be an order of magnitude longer than the actual compute time. In light of the large data cubes that will be produced by the current and upcoming radio telescopes, this I/O overload is certainly a cause for concern. To minimise the amount of time spent rearranging data, we make the following two recommendations to teams carrying out large polarization surveys:

1. Adopt data formats like HDFITS which benefit from combining the FITS data model with the HDF5 file format. Accessing an array stored in HDFITS format along the slowest-varying dimension can be two orders of magnitude faster than FITS format.
2. If surveys prefer to use the standard FITS format to store their data products, they should at least consider archiving the data products not intended for visualisation (like Q and U cubes) with the frequency axis as the first/fastest-varying axis.

¹⁴<https://developer.nvidia.com/cufft>

Chapter 6

Conclusions

6.1 Summary of key results

In this PhD thesis, we have investigated the low-frequency radio continuum properties of a sample of nearby dwarf and normal late-type spiral galaxies. For this work, we observed two normal late-type spiral galaxies (NGC 4258 and NGC 5457) and four starburst dwarf galaxies (NGC 1569, NGC 4214, NGC 2366, and DDO 50) using the Low Frequency ARray (LOFAR) with complementary 1.4 GHz observations with the Westerbork Synthesis Radio Telescope (WSRT). We summarise our main results below:

In [chapter 2](#), we studied the radio continuum properties of the star-forming disk and the anomalous arms in the nearby spiral galaxy NGC 4258 using new radio continuum observations with LOFAR and the WSRT radio telescopes. Using the new sensitive radio images of NGC 4258 at 150 MHz and 1400 MHz, we were able to trace weak radio continuum emission from the star-forming disk up to a distance of 20.73 kpc from its center. Using the new radio images, we have also determined for the first time the equipartition magnetic field strength in the disk of NGC 4258 which peaks at about $20 \mu\text{G}$ in the inner disk and decreases to $4 \mu\text{G}$ about 20 kpc away from the nucleus.

The 3-dimensional orientation of the anomalous arms in NGC 4258 with respect to its star-forming disk has been a mystery since the discovery of the anomalous arms in 1961. In [chapter 2](#), we have shown that radio polarimetry data can be used to help resolve this long-standing question. Our 1.4 GHz radio polarimetry data, complemented by H α and H α images of NGC 4258, suggest that the anomalous arms have a hybrid morphology where the inner parts of the arms are embedded in the disk while the outer parts of one of the arm (the eastern arm) is located out of the plane, on the near side to the observer.

In [chapter 3](#), we presented a multi-frequency radio continuum study of the nearby spiral galaxy M 101 using data from the LOFAR and the WSRT radio telescopes. In this chapter, we have demonstrated that diffuse radio continuum emission on arcmin-scales can be recovered at 150 MHz after applying an advanced facet-based direction-dependent calibration and imaging techniques.

From the LOFAR and WSRT radio images of M 101 in the frequency range spanning from 146 MHz to 2270 MHz, we see that the angular extent of the radio continuum disk increases with decreasing frequency. The observed steepening in the slope of the radial brightness distribution and the steepening of the azimuthally averaged non-thermal spectral index profile suggest that the radio emission arising from the outer parts of the galactic disk, which are most prominent at low radio frequencies, are dominated by an old population of cosmic rays.

The high angular resolution radio images of M 101 presented in this thesis allowed us to demonstrate that the integrated flux density values of M 101 reported in the literature are all biased by confusing background radio sources. The integrated radio spectral energy distribution – corrected for confusing radio sources – shows spectral flattening towards low radio frequencies which we attribute to free-free absorption.

In [chapter 4](#), we studied a sample of four bright, nearby dwarf galaxies (NGC 1569, NGC 4214, NGC 2366, and DDO 50) which were selected based on their particularly high radio brightness. Of the four dwarf galaxies studied, extended diffuse emission was detected in only two of these galaxies (NGC 1569 and NGC 4214) with NGC 1569 showing a low-frequency extension of more than an arcmin beyond that detected in an archival 1.4 GHz radio image from WSRT. In the remaining two dwarf galaxies (NGC 2366 and DDO 50), the radio continuum emission appears clumpy with emission from H II regions dominating the integrated flux density. Assuming energy equipartition, we estimated the total magnetic field strength in NGC 4214 and NGC 1569. The mean magnetic field strength in NGC 4214 is about $11.5 \mu\text{G}$. In the case of NGC 1569, the mean magnetic field in the inner galaxy is about $32 \mu\text{G}$ and falls down to $16 \mu\text{G}$ in the halo. The estimated field strengths are significantly stronger than the typical field strengths observed towards normal spiral galaxies. Since the sample of four galaxies studied here was selected based on their radio brightness, we argued in [chapter 4](#) that the upcoming LOFAR Two-metre Sky Survey (LoTSS; [Shimwell et al. 2017](#)) will not be sensitive enough to map the diffuse radio halos in a large number of nearby dwarf galaxies.

While the individual galaxies studied in chapters 2, 3, and 4 are all unique in their own way, four galaxies (NGC 4258, M 101, NGC 1569, and NGC 4214) show an interesting common feature: the angular extent of these four galaxies increases with decreasing frequency. We also find that the spectral index distribution in the outer parts of all four galaxies is steeper than their inner regions which suggests a dominance of old electrons in the outer parts of galaxies. In the outer parts of all four galaxies detected in our LOFAR images, we find weak magnetic fields with equipartition field strengths of the order of a few microGauss. The results presented in this thesis, along with recent low-frequency observations of other nearby spiral galaxies like M 51 ([Mulcahy et al. 2014](#)) and IC 10 ([Heesen et al. 2018](#)), paint a consistent picture that low-energy cosmic ray electrons (with long synchrotron lifetime) can propagate to large radii resulting in a systematic increase in the angular sizes of galaxies towards low radio frequencies. Thus, we can conclude that sensitive, low-frequency observations of nearby galaxies are an

excellent tracer to study magnetic fields in the outer parts of galactic disks and halos of nearby galaxies.

Finally, in the era of data-intensive radio astronomy, a number of image processing algorithms can be sped up using new computational tools like General Purpose Graphical Processing Units (GPGPUs) to cope with the increasing data rates. In [chapter 5](#), we have demonstrated a clear example of this by implementing a commonly used algorithm in radio polarimetry called Faraday Rotation Measure (RM) synthesis to work with GPGPUs thereby achieving a high compute throughput compared to existing CPU implementations of the same algorithm. Additionally, we have also demonstrated that the format in which the astronomical data is stored can have a significant impact on the performance of the algorithm. In the case of RM synthesis, we noticed that adopting the Hierarchical Data Format (HDF5) instead of the standard FITS format results in a significant decrease in the code execution time.

6.2 Avenues for future research

6.2.1 Broadband polarimetry as a probe of anomalous arms in NGC 4258

Recall from [chapter 2](#) that since the discovery of the anomalous arms in NGC 4258, numerous models have been proposed to explain the orientation of the arms with respect to the galactic disk. All the proposed models for the arms can be classified in two categories: *in-disk* and *out-of-disk* models. Both model categories are based on the assumption that the anomalous arms are produced by the interaction of matter ejected from the nucleus with either the gas in the disk (*in-disk* model) or with coronal gas in the halo (*out-of-disk* model). The 1.4 GHz radio polarimetry data presented in [chapter 2](#), complemented by H α and H β data suggests that the anomalous arms have a hybrid morphology where the outer parts of the eastern arm are located in front the galactic disk (on the near side to the observer) while the rest is embedded in the galactic disk.

While the polarization results presented in [chapter 2](#) favour a hybrid model for the anomalous arms, the results derived from our WSRT polarimetry data are only qualitative and the limited bandwidth of the WSRT data prevents us from performing any quantitative analysis such as comparing the observed Faraday depth along the anomalous arms with predicted Faraday depth distributions for different *in-disk* and *out-of-disk* models. Furthermore, we suggested that mapping the Faraday depth distribution along the anomalous arms could pinpoint the exact location where the eastern arm exits the disk. In order to carry out a quantitative analysis of the morphology of the anomalous arms using broadband polarimetry data, we have proposed to observe NGC 4258 in the L- and S-band covering the frequency range 1 – 4 GHz using the Karl G. Jansky Very Large Array.

6.2.2 Mapping the halos of nearby dwarf galaxies

Winds and outflows from galaxies play a vital role in shaping the evolutionary histories of galaxies. The energy and momentum from star formation that drives the outflows can enhance turbulence in the ISM which provides pressure balance to the gas in the ISM. The additional pressure generated in the ISM can balance gravity and hence impede further star formation. Additionally, outflows can remove gas and metals from the ISM and drive them out into the halo or into the circum-galactic medium if the outflow velocity is greater than the escape velocity of the galaxy. For a review of winds and outflows in galaxies, see [Veilleux et al. \(2005\)](#). On the other hand, if the outflow velocity is lower than the escape velocity of the galaxy, the hot gas driven by the outflow can provide a seeding mechanism to cool the hot coronal gas present in the halos of galaxies. The cool gas produced in this process can then rain down on the disk providing fuel for subsequent star formation in the galaxy through a mechanism called galactic fountains ([Sancisi et al. 2008; Marinacci et al. 2010](#)).

Dwarf galaxies are subject to strong outflows having only weak gravitational potentials and bursty star formation histories. Cosmic rays have long been suspected to play a vital role in driving these outflows. Hydrodynamic simulations of cosmic ray driven galactic winds by [Uhlig et al. \(2012\)](#) predict that dwarf galaxies with such an outflow should possess a large-scale spherically symmetric radio halo produced by cosmic ray electrons accelerating in the galactic magnetic field.

In addition to driving outflows in galaxies, cosmic rays also play a vital role in regulating the evolution of large-scale ordered magnetic fields in galaxies. Both simulations and radio polarimetric observations of superbubbles in nearby spiral galaxies indicate that starburst-driven galactic outflows can transport the ordered magnetic field lines from the inner regions of galaxies to the outer halo (see for example [Brandenburg et al. 1995; Chyží et al. 2011; Heald 2012](#)). Thus, studying outflows in dwarf galaxies can provide vital information not only about the winds and outflows but also about the evolution of large-scale magnetic fields in such systems. However, strong observational evidence for such a cosmic ray-driven outflow has been hard to come by due to (i) lack of sensitive radio observations to detect weak radio emission from the halos of dwarf galaxies, and (ii) lack of tools necessary to model different types of cosmic ray propagation.

Until recently, sensitive radio continuum searches for diffuse radio halos around nearby dwarf galaxies at GHz frequencies had failed to detect any synchrotron emission. However, our recent LOFAR HBA observations of the nearby dwarf galaxy NGC 1569 presented in [chapter 4](#) and our unpublished HBA observations of the dwarf galaxy NGC 4449 show that LOFAR is sensitive enough to map the weak, diffuse radio continuum emission from the halos that had evaded detection in previous higher frequency radio continuum observations. Furthermore, recent developments in software modelling of the 1D cosmic ray transport process in the radio halos of galaxies (see for example [Heesen et al. 2016](#)) allow us to differentiate between advective and diffusive winds in the halos of galaxies, as well as measure their wind speed. Thus, combining the power of LOFAR in detecting diffuse radio emission from the halos of a large sample of

nearby dwarfs along with modelling the advective/diffuse outflows in the halos of these galaxies will provide important insights into the role of cosmic rays in driving outflows in dwarf galaxies.

Appendices

Appendix A

Calibrating LOFAR HBA Data

Based on van Weeren et al.
ApJS, 223, 2 (2016)

A.1 Need for direction-dependent calibration

In order to better motivate the need for advanced direction-dependent calibration procedure for data from telescopes like LOFAR that have wide fields of view, it is useful to first consider the mathematical model behind the traditional standard calibration procedure called the Radio Interferometry Measurement Equation or RIME.

In a cartesian coordinate system with z pointing from the antenna to the assumed source, the signal from the source at a given point in space and in time can be represented as a column vector composed of two complex numbers as

$$\mathbf{e} = \begin{pmatrix} e_x \\ e_y \end{pmatrix}. \quad (\text{A.1})$$

Before modelling the calibration procedure, it is useful to make an important assumption, called linearity, about the signal path involved in an interferometric measurement. Assuming linearity, all transformations that the signal undergoes between the source and the telescope (like atmospheric absorption and propagation delays) can be represented as a 2×2 matrix \mathbf{J} called the Jones matrix (Jones 1941) such that

$$\mathbf{v} = \mathbf{J}\mathbf{e}. \quad (\text{A.2})$$

In the above equation, \mathbf{J} is the Jones matrix representing the transformation that the signal \mathbf{e} from the source undergoes before being measured as a voltage \mathbf{v} at the telescope. With these two definitions in mind, we can now proceed to model the radio interferometer.

Consider a simple setup containing two antennas forming a single baseline. In radio interferometry, voltages measured at each antenna are cross-correlated to form the visibility matrix. Cross-correlation is an operation where the voltages measured at one antenna is multiplied with the Hermitian transpose of the voltage measured at the second antenna. Recall that radio telescopes measure voltages induced by two components of the electric field vector (X and Y or R and L depending on the feed mounted on the telescope) forming a two component vector of the form

$$\mathbf{v} = \begin{pmatrix} v_x \\ v_y \end{pmatrix} = \begin{pmatrix} v_r \\ v_l \end{pmatrix}. \quad (\text{A.3})$$

For the sake of simplicity, we assume linear (X and Y) feeds from here on. If ‘a’ and ‘b’ are the two antennas forming the baseline, then the voltages ‘ \mathbf{v}_a ’ and ‘ \mathbf{v}_b ’ measured at the two antennas result in a 2×2 visibility matrix \mathbf{V}_{ab} of the form

$$\mathbf{V}_{ab} = \langle \mathbf{v}_a \mathbf{v}_b^H \rangle = \begin{pmatrix} \langle v_{ax} v_{bx}^* \rangle & \langle v_{ax} v_{by}^* \rangle \\ \langle v_{ay} v_{bx}^* \rangle & \langle v_{ay} v_{by}^* \rangle \end{pmatrix} = \begin{pmatrix} V_{xx} & V_{xy} \\ V_{yx} & V_{yy} \end{pmatrix}. \quad (\text{A.4})$$

The angled brackets in the above equation denote summation over a finite correlation time interval. Notice from equation A.1, A.2 and A.4 that in the above equation, the visibility V_{xx} formed using the voltage measured by the ‘X’ feeds of antennas ‘a’ and ‘b’ is related to the electric field component e_x . Thus, if we assume that the linear transformation \mathbf{J} is constant within the correlation

time interval over which the summation is carried out, we can rewrite the visibility matrix as

$$\mathbf{V}_{ab} = \mathbf{J}_a \begin{pmatrix} \langle e_x e_x^* \rangle & \langle e_x e_y^* \rangle \\ \langle e_y e_x^* \rangle & \langle e_y e_y^* \rangle \end{pmatrix} \mathbf{J}_b^H. \quad (\text{A.5})$$

Stokes parameters (I, Q, U, V), a set of four parameters used to represent the polarization state of an electromagnetic vector, are related to the matrix in the above equation as (Born & Wolf 1964; Thompson et al. 2001; Hamaker et al. 1996)

$$\begin{pmatrix} \langle e_x e_x^* \rangle & \langle e_x e_y^* \rangle \\ \langle e_y e_x^* \rangle & \langle e_y e_y^* \rangle \end{pmatrix} = \begin{pmatrix} I+Q & U+iV \\ U-iV & I-Q \end{pmatrix} = \mathbf{B} \quad (\text{A.6})$$

where \mathbf{B} is called the brightness matrix which is related to the brightness distribution of the source in the sky. Thus equation A.5 can be written in a condensed form as

$$\mathbf{V}_{ab} = \mathbf{J}_a \mathbf{B} \mathbf{J}_b^H. \quad (\text{A.7})$$

In addition to the single linear transformation represented by \mathbf{J} in the above equation, the principle of linearity assumed at the beginning of this section allows us to include any number of linear transformations that appear along the signal path between the astronomical source and the radio telescope. Thus, we can replace the Jones matrix (\mathbf{J}) in the above equation with a *Jones chain* (?) as

$$\mathbf{V}_{ab} = \mathbf{J}_{an} \dots \mathbf{J}_{a2} \mathbf{J}_{a1} \mathbf{B} \mathbf{J}_{b1}^H \mathbf{J}_{b2}^H \dots \mathbf{J}_{bm}^H. \quad (\text{A.8})$$

Note that the number of Jones matrices for telescope ‘a’ and telescope ‘b’ is not the same in the above equation. This is because the signal path between the astrophysical sources and the telescopes ‘a’ and ‘b’ can be different and hence are indicated using different Jones matrices.

Now consider that the sky has a complex brightness distribution and can be decomposed into a set of point sources. The visibility matrix measured for a given baseline is a linear sum of the brightness matrices corresponding to each point source. However, as the signal from each point source travels to the telescope, each signal path can be different and hence the Jones matrix that applies to the brightness matrix of one point source does not necessarily apply to another point source. In such a case, the visibility matrix becomes

$$\mathbf{V}_{ab} = \sum_s \mathbf{J}_{sa} \mathbf{B}_s \mathbf{J}_{sb}^H \quad (\text{A.9})$$

where \mathbf{J}_{sa} is the Jones matrix corresponding to telescope ‘a’ for a point source in direction ‘s’. Recall from equation A.8 that the brightness matrix for each point source can be accompanied by more than one Jones matrix. Some Jones matrices that appear in this extended Jones chain like those corresponding to hardware imperfection will be identical for all brightness matrices and hence can be taken out of the summation. So, we can rewrite the relation between the observed visibility matrix and the brightness distribution of the sky as

$$\mathbf{V}_{ab} = \mathbf{J}'_a \left(\sum_s \mathbf{J}_{sa} \mathbf{B}_s \mathbf{J}_{sb}^H \right) \mathbf{J}'_b^H \quad (\text{A.10})$$

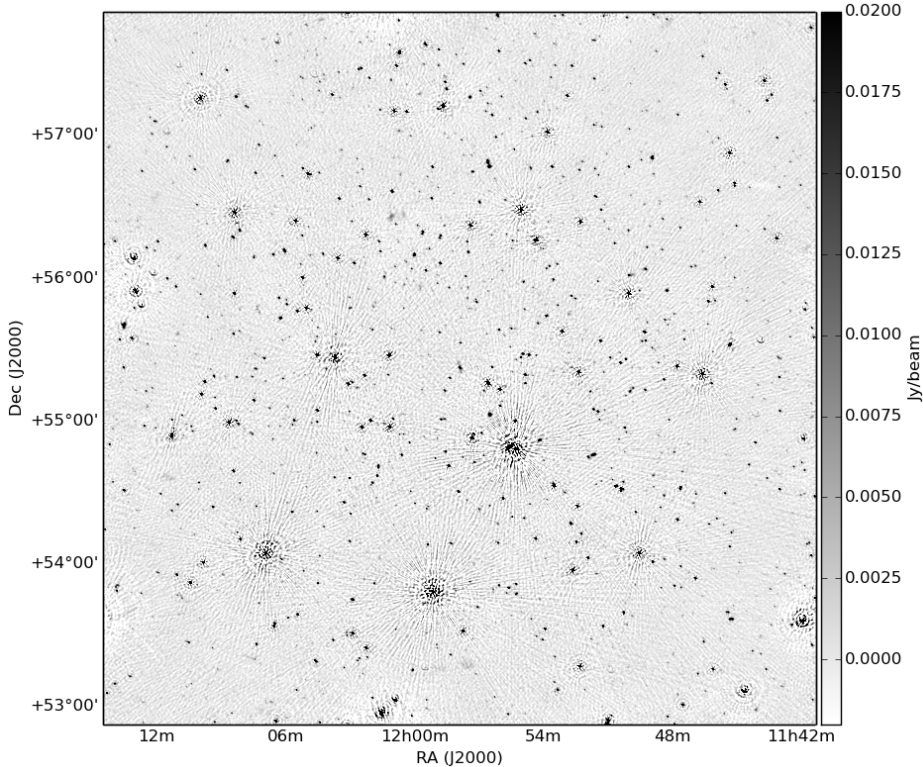


Figure A.1 – A typical LOFAR HBA field before direction-dependent calibration showing the LOFAR field around the nearby early-type galaxy NGC 3998 (Sridhar et al in prep).

In the above equation, the Jones matrices that lie outside the summation describe direction-independent effects while the Jones matrices that lie inside the summation correspond to direction dependent effect. For traditional radio telescope arrays like WSRT and the JVLA, the field of view is small enough that a single set of Jones matrices were sufficient to represent the signal path between the source and the telescopes¹. However, for new telescopes like LOFAR, the large field of view implies that direction-dependent effects can no longer be ignored and have to be explicitly corrected.

Failing to correct for direction-dependent effects can lead to calibration artefacts in the image especially around bright sources as shown in Figure ???. Figure ?? shows a typical LOFAR HBA image containing strong calibration artefacts around bright point sources due to direction-dependent calibration errors.

As we step into the era of wide-field radio astronomy, a number of new direction-dependent calibration and imaging algorithms including AW-projection

¹This is not strictly true. Low frequency observations (at and below the P frequency band) with these telescopes have large enough field of view that direction-dependent effects become important.

(Cornwell et al. 2008; Bhatnagar et al. 2008), field-based calibration (FBC; Cotton et al. 2004), source peeling and atmospheric modelling (SPAM; Intema et al. 2009) and Sagecal (Yatawatta et al. 2008; Kazemi et al. 2011) have been proposed to tackle this issue. In this chapter, I present a brief overview of a relatively new facet calibration procedure (van Weeren et al. 2016) that is used to calibrate and image LOFAR HBA data.

A.2 LOFAR Facet Calibration

As discussed in section A.1, calibrating LOFAR data involves correcting for effects that are both direction-dependent and direction-independent. To overcome these calibration challenges, a new calibration framework called “facet calibration” (van Weeren et al. 2016; Williams et al. 2016) has been developed to calibrate and image LOFAR HBA datasets. A schematic overview of both the direction-independent and the direction-dependent parts of facet calibration is shown in figure A.2. A detailed account of each of these steps is provided in the following sections.

The pipeline used to carry out both the direction-independent² and the direction-dependent³ calibration are publicaly available on GitHub.

A.2.1 Direction-independent steps

Pre-processing

A typical LOFAR HBA imaging observation⁴ is carried out such that the visibilities are recorded with a 1s correlator integration time and with a frequency resolution of 64 channels per sub band where a sub band is 195.3125 kHz wide. The raw correlated data are averaged down to 16 channels per sub band by the Radio Observatory at ASTRON and only the averaged data is made available to the community through the LOFAR Long Term Archive (LTA)⁵.

The first step in calibrating LOFAR HBA data involves filtering data that are corrupted by radio frequency interference (RFI), by instrumental effects due to malfunctioning station hardware, and by bright off-axis sources. RFI flagging is carried out using the automated flagging software `AOFagger` (Offringa et al. 2010, 2012).

Emission from bright off-axis sources – like Cas A, Cyg A, Tau A, and Vir A – can contribute to the measured flux . Visibility data affected by contribution from bright off-axis sources are flagged using a technique called “A-team clipping”. In A-team clipping, model visibilities corresponding to bright off-axis sources are predicted taking the LOFAR station beam into account and the simulated visibilities are written to the MODEL_DATA column of each measurement set. The effect of the off-axis sources are removed by flagging the time slots for which

²<https://github.com/lofar-astron/prefactor>

³<https://github.com/lofar-astron/factor>

⁴See section XX in chapter YY for specific information about the LOFAR HBA observing strategy.

⁵<http://lofar.target.rug.nl/>

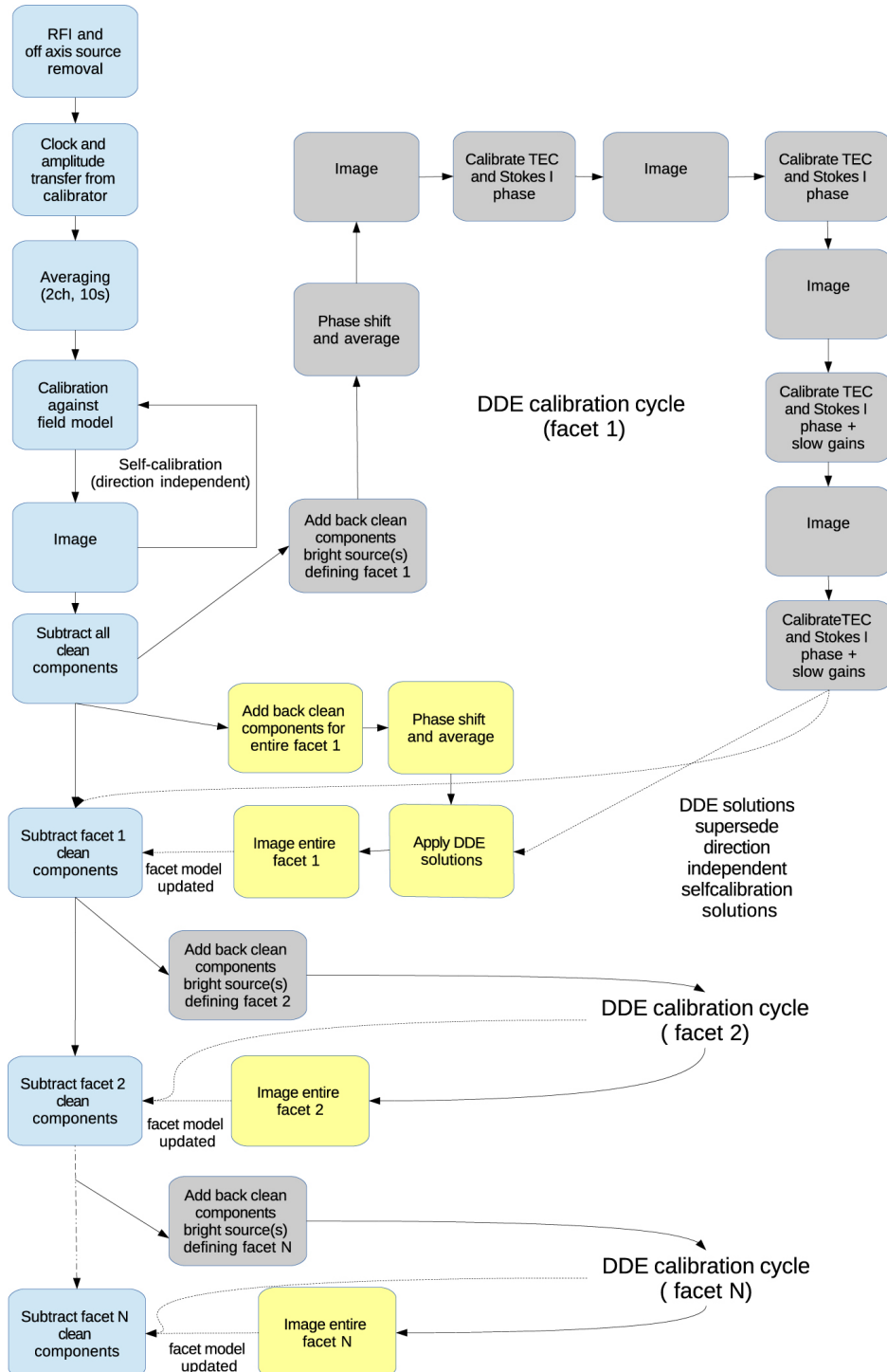


Figure A.2 – A schematic overview of the facet calibration procedure. Image adapted from van Weeren et al. (2016).

the MODEL_DATA contains visibility amplitudes larger than 5.0 Jy. For a typical 8-hour observing run with LOFAR HBA, $\sim 10\%$ of the visibility data are flagged after carrying out RFI excision and A-team clipping.

After flagging the measurement sets for bad data, the visibility data are further averaged down to 4s and 4 channels per sub band. Both RFI flagging and averaging are carried out using the New Default Pre-Processing Pipeline (NDPPP) that is part of the LOFAR software suite⁶.

Amplitude calibration

The preprocessed calibrator measurement sets were used to solve for the diagonal elements of the gain matrix (G_{xx} and G_{yy}) using the BlackBoard Selfcal (BBS) software package assuming the fluxscale defined in Scaife & Heald (2012). In addition to the gain matrix, we also solved for a rotation angle (β) to account for the effects caused by differential Faraday Rotation. The Jones matrix representation of differential Faraday Rotation (\mathbf{F}) is

$$\mathbf{F} = \begin{pmatrix} \cos \beta & -\sin \beta \\ \sin \beta & \cos \beta \end{pmatrix}. \quad (\text{A.11})$$

Correction for clock delay and phase offsets

While all core LOFAR stations are connected to a common clock, all remote stations have their own clocks that are synchronised with the core station clock using a GPS signal. Due to synchronisation errors, the remote station clocks can drift from the core station clock by up to 200 ns and the clock offset result in strong phase delays (phase $\propto \nu$) across the observing frequency band on the core-remote and remote-remote baselines.

Since clock offsets are direction-independent and affect all subsequent calibration steps, they have to be corrected while setting the flux scale. Applying a correction for the clock delay is analogous to applying a time- and frequency-dependent phase correction for each station. However, determining corrections for clock offsets is complicated at low radio frequencies due to additional phase corruption caused by the ionosphere. Within the LOFAR HBA bandpass, phase distortions due to the ionosphere scale as phase $\propto \nu^{-1}$ and are related to the ionospheric column density of electrons , also known as the total electron content (TEC), along a given line of sight. For a given baseline, the observed phase difference ($\Delta\phi$) is then related to the clock difference (p_0) and TEC difference (p_1) as

$$\Delta\phi(\nu, t) = 2\pi p_0(t)\nu - \frac{8.448 \times 10^9 p_1(t)}{\nu} \quad (\text{A.12})$$

For each time slot (4 s), the clock and TEC differences for each station can be determined by carrying out a least square fitting to the phase solutions determined using a scan on a bright flux calibrator. The fitting procedure is

⁶http://www.lofar.org/wiki/doku.php?id=public:user_software:start

carried out for XX and YY phases separately using the `scipy.optimize.leastsq` routine available in `python`.

In addition to the clock and TEC differences, XX and YY phases for a few stations exhibit a small but a non-negligible constant phase offset. The phase offset for each station is determined by finding the median offset between the XX and the YY phases. The origin of this phase offset is unknown. The fitted clock and TEC differences along with the XX-YY offset derived from an 8-hour scan on the flux calibrator 3C 295 are shown in figures A.3 and A.4. As expected, all core stations display very small clock and TEC differences as compared to remote stations. Also note that the clock differences are not constant and vary with the observing epoch. The remaining residual clock differences are taken out in the direction-dependent step.

Solution transfer to target field data

The fitted clock and XX-YY phase offsets are then transferred to the target field along with the gain amplitudes using the ‘applycal’ step in NDPPP. After transferring these solutions, the target field visibilities are in units of Jansky and are free from clock and XX-YY phase offsets. The TEC differences are not transferred to the target field data as they are direction-dependent and the TEC values determined from the calibrator solutions might not be valid for the target field pointing.

Phase calibration and source subtraction

The clock and amplitude calibrated target field sub bands are concatenated in to groups of 10 sub bands such that each concatenated group is 2 MHz wide. After concatenation, an additional RFI excision step is carried out on the concatenated sub band groups. The wide bandwidth of the sub band groups provide better statistics for RFI detection and hence any residual RFI present in the data will be removed in this stage.

Phase calibration is applied to each group of sub bands separately using a model of the sky extracted from the 150 MHz Giant Metrewave Radio Telescope (GMRT) Sky Survey Alternate Data Release ([Intema et al. 2017](#), TGSS ADR). Phase solutions are determined using an 8s solution interval and one solution across the 2 MHz bandwidth.

The last step in the direction-independent processing involves generating a catalogue of all the sources in the field and making an “empty” dataset with all the detected sources subtracted from the visibility data. To generate a database of sources for each sub band group, the phase calibrated sub band groups are imaged separately using the `WSClean` imager ([Offringa et al. 2014](#)) and source finding is performed using the automated source finder `pyBDSM`⁷ ([Mohan & Rafferty 2015](#)). Since a single automated source detection strategy does not work for both point and diffuse sources in the field, source peeling is done at two different resolutions.

⁷<http://www.astron.nl/citt/pybdsdm/>

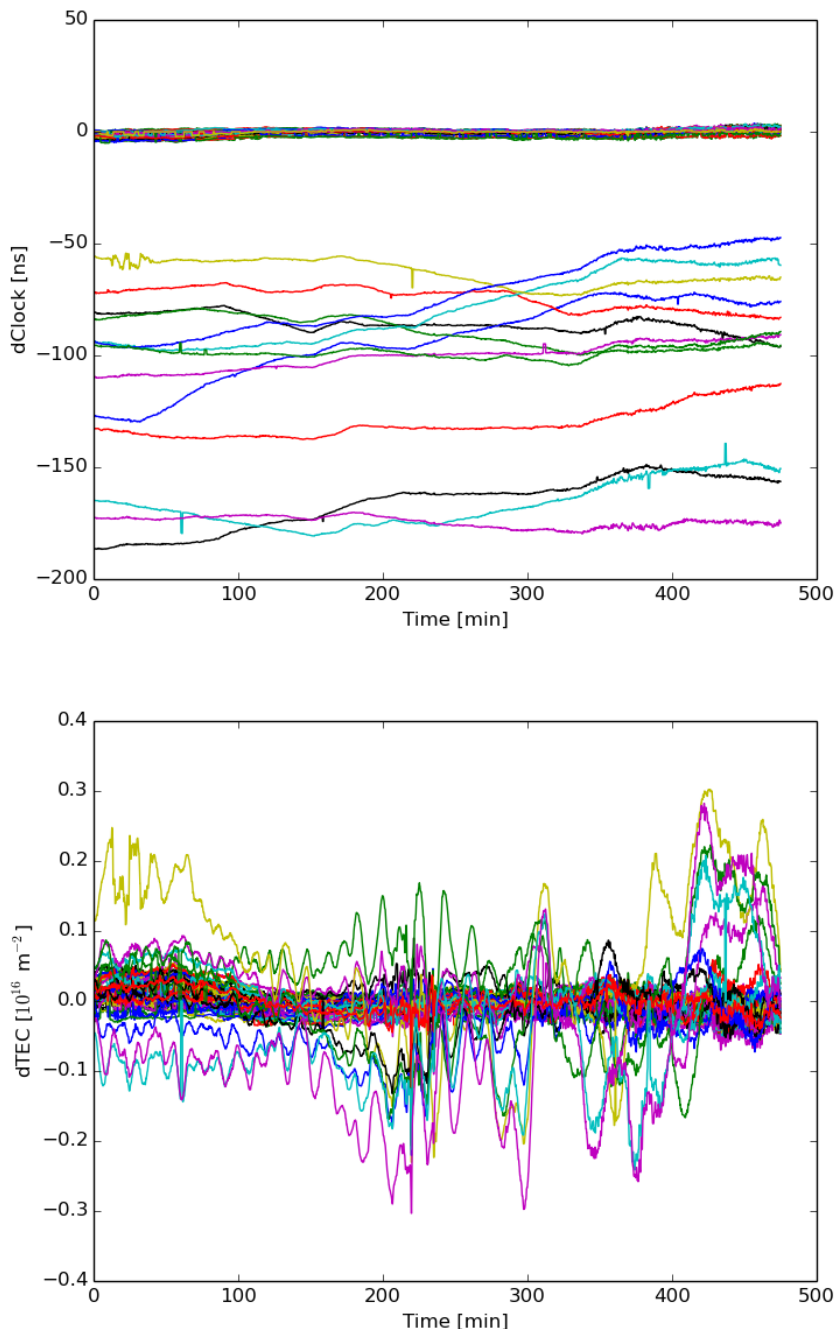


Figure A.3 – Per-station clock offsets and Total Electron Content (TEC) variations as a function of time derived using the clock-TEC fitting procedure.



Figure A.4 – Offset between the XX and YY phases.

First, a “high” resolution image of the field is made imposing a $7k\lambda$ outer uv-cut. The images are deconvolved using a mask generated with the source finder pyBDSM and the clean component model from each sub band group image is subtracted from the visibility data. Next, a “low” resolution image of the field is made using the subtracted visibility data with a $2k\lambda$ outer uv-cut. The low-resolution clean component model of any diffuse emission is again subtracted from the visibility data resulting in an “empty” dataset for each sub band group.

At the end of the direction-independent step, we are left with three sets of data products for each sub band group: (i) clean-component sky models, (ii) measurement sets containing the “empty”, residual sky, and (iii) direction-independent phase solutions. These three set of data products are fed as input to the pipeline that carries out the direction-dependent processing.

A.2.2 Direction-dependent steps

Tessellating the field of view

The first step in the direction-dependent calibration procedure is to determine a suitable set of calibrator sources within the field of view that can be used to derive direction dependent gain solutions. To obtain good direction-dependent solutions, point sources brighter than ~ 0.4 Jy are needed for each direction. In the absence of enough bright point sources in the field, closely-situated faint point sources can also be used as calibrators provided the sum of their fluxes is greater

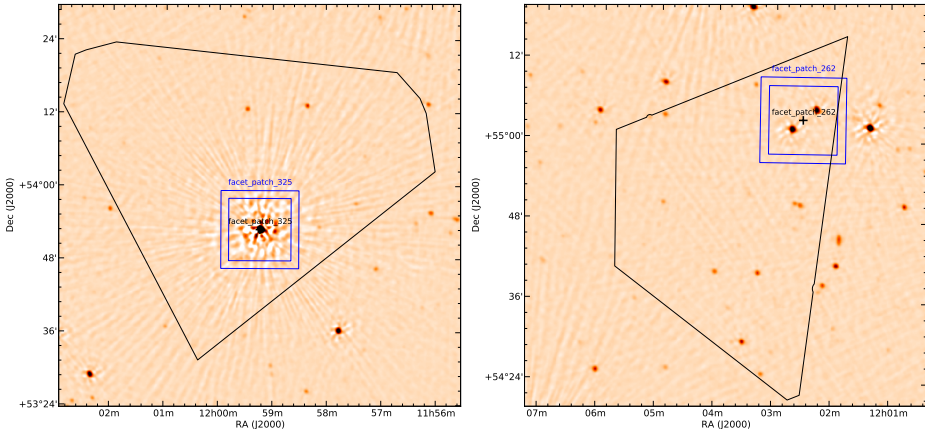


Figure A.5 – Either a single bright point source or a group of point sources can be used as facet calibrators. All source(s) inside the blue squares are used to derive direction-dependent gains which are then used to correct all sources inside the corresponding facet bound by the black polygon. The image on the left has a facet calibrator whose peak brightness is 4.85 Jy. The two point sources in the image on the right have a peak brightness of 0.44 Jy and 0.26 Jy.

than ~ 0.4 Jy. Two examples of suitable calibrators along with their facets are shown in figure A.5.

Once a set of suitable calibrators are chosen, the LOFAR field of view can be divided into a set of facets using a Voronoi tessellation scheme. Such a tessellation scheme matches each point on the sky to the nearest available facet calibrator. An example facet layout for a LOFAR HBA pointing is shown in figure A.6.

Once the facets are defined from tessellating the field of view, each facet is processed independently in decreasing order of the brightness of the corresponding facet calibrator. In this order, each facet undergoes three processing steps: (i) facet self-calibration where the direction dependent solutions are derived, (ii) facet subtraction step where an improved model of all the sources in a facet is subtracted from the visibility data, and (iii) the final facet imaging step which generates images of facets which are mosaicked together to make an image of the full field of view.

Facet self-calibration

For each facet, good direction dependent gain solution is derived by performing self-calibration on the chosen facet calibrator. During each self-calibration cycle, imaging is done using the `WSClean` imager making use of its new wideband deconvolution⁸ algorithm that accounts for spectral curvature. The dirty images are deconvolved using clean masks that are generated using the automated source finder `pyBDSM`. Note that only a small field of view around the calibrator (indicated by the blue square in figure A.5) is imaged during the self-calibration cycles.

⁸<https://sourceforge.net/p/wsclean/wiki/WidebandDeconvolution/>

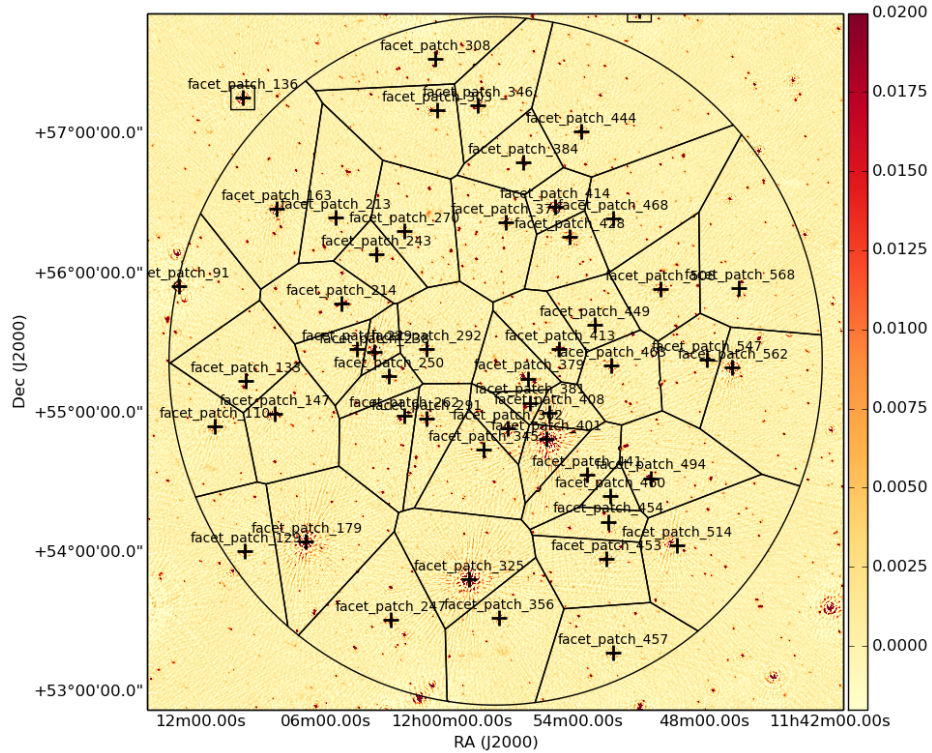


Figure A.6 – Tessellating the LOFAR field of view into multiple facets. The facet calibrators for each facet is indicated using the ‘+’ sign.

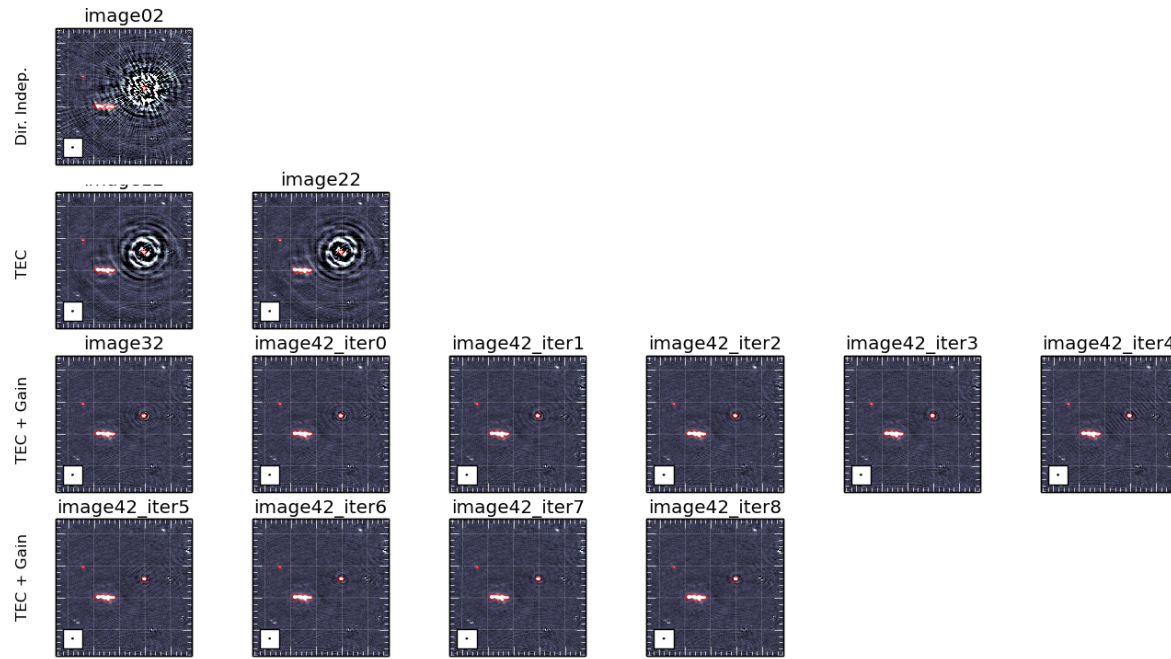


Figure A.7 – Images of the facet calibrator after each facet self-calibration step (see text). Each row corresponds to a unique facet self-calibration step while each column corresponds to the different iteration carried out in that self-calibration step. Notice that the rms noise and the representation of the calibrator in the shown images improves as one moves from the top-left to the bottom-right.

For the first two self-calibration cycles, only the stokes I phase and TEC solutions are solved on 8 – 16s time scales. For the subsequent self-calibration cycles, the (slow) amplitude and (fast) phase solutions are derived on 5 – 10 minute and 8 – 16s time scales respectively. The slow amplitude gain calibration corrects for the slowly varying LOFAR station beam while the fast phase calibration corrects for ionospheric effects that changes on much shorter timescales. The amplitude and phase self-calibration cycles are carried out until there is no noticeable improvement in the noise level in the self-calibrated image.

The improved DD gain solutions derived in the last self-calibration cycle are then used to correct all the other sources within that facet. After adding all the sources in the facet to the visibility data, the full facet (the black polygon in figure A.5) is imaged using `WSClean` to get an improved image of the facet.

Facet subtraction

The facet image made at the end of the facet self-calibration step contains an improved high-resolution model of all the sources in that facet. Source finding is run on this new improved image and the detected sources are subtracted from the visibilities. This is similar to the “source subtraction” step carried out at the end of the direction-independent step but with a better model of the sources in the field.

Since each facet is processed sequentially in decreasing order of the brightness of the facet calibrator (and thus facets with stronger calibration artefacts), the facet self-calibration and facet subtraction steps progressively improve the model of the sky and reduce the residuals present in the “empty” dataset that is provided as input to the direction-dependent step. This correction is necessary because it ensures that residual un-subtracted emission in nearby facets do not influence the gain solutions derived for facets containing fainter calibrators.

Facet imaging

While all images generated during facet self-calibration and facet subtraction have the highest possible resolution with an image pixel size of 1''.5, the final facet images can be generated for any specific set of imaging parameters.

At the end of the direction-dependent processing, for each facet, the above described calibration strategy derives good DD gain solutions and an improved high resolution model of all the sources in that facet. Each facet is imaged separately (for a set of user specified imaging parameters) by adding the sources back to the “empty” dataset using the corresponding DD gain solutions and imaging the visibilities with `WSClean`. This imaging procedure is repeated for each facet everytime starting with the same “empty” dataset. An image of the full LOFAR field of view can then be obtained by making a mosaic of all the facet images. Correction for the primary beam attenuation is applied to the mosaic image with an average primary beam produced by the `AWImager` ([Tasse et al. 2013](#)).

Figures A.1 and A.8 show a $5^\circ \times 5^\circ$ LOFAR HBA field before and after applying facet calibration. Comparing the two images, it can be seen quite clearly

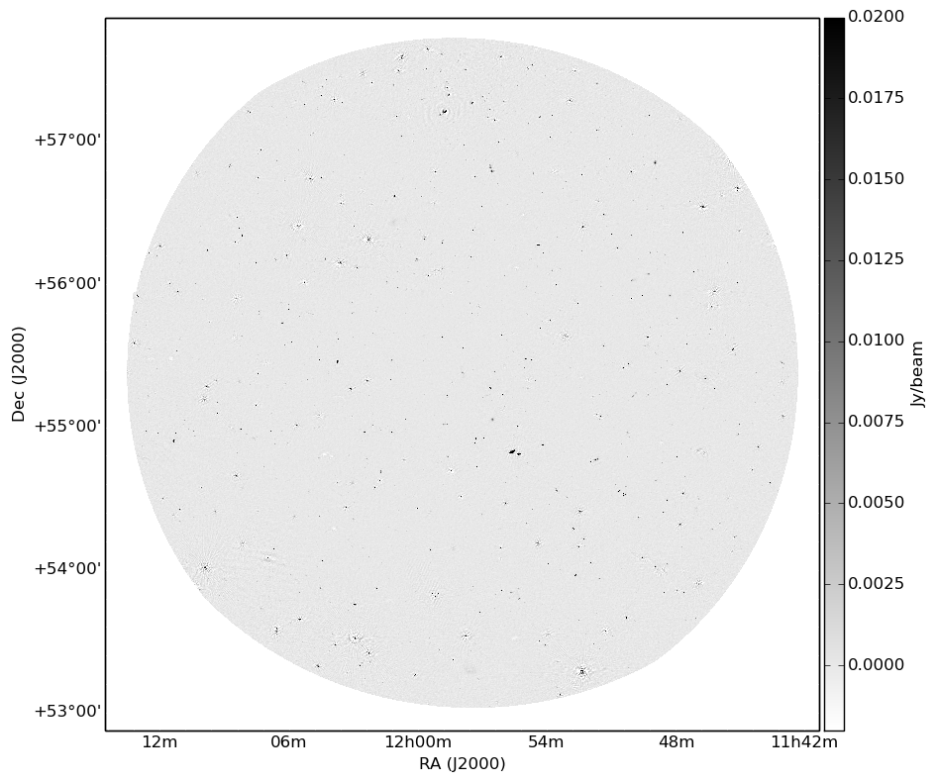


Figure A.8 – Same field shown in figure A.1 after applying direction-dependent calibration.

that facet calibration suppresses the artefacts around bright point sources in the field thereby bringing down the rms noise in the image.

Note however that for some bright point sources, calibration artefacts can still be seen albeit at a low level compared to the direction-independent case. This is probably due to residual effects like imperfect source subtraction at the end of the direction-independent step or due to calibration errors on short timescales. Additional self-calibration iterations or careful manual masking might be required to alleviate such artefacts.

Samenvatting

Breedbandemissie van sterrenstelsels op radiogolfengtes wordt gedomineerd door straling als gevolg van twee fysische processen: niet-thermische synchrotronemissie van relativistische elektronen die versnellen in galactische magnetische velden en thermische, vrij-vrij emissie van plaatsen van stervorming ([Condon 1992](#)). Hoewel de fysieke mechanismen die aanleiding geven tot de thermische en de niet-thermische radiostraling verschillend zijn, zijn ze beide gerelateerd aan de onderliggende populatie van massieve sterren in melkwegstelsels.

De synchrotronemissie bij lage radiofrequenties is afkomstig van oude, energieuze kosmische stralingselektronen die zich ver van hun oorsprongslocaties / heracceleratie hebben voortgeplant vanwege hun langere halfwaardetijd. Daarom zijn gevoelige lage radiofrequentieobservaties van sterrenstelsels een uitstekende manier om de zwakke magnetische velden die zich op grote galactische radii bevinden te bestuderen.

Eerdere pogingen om de opgeloste laagfrequente radiocontinuumemissie van een groot aantal nabij de melkwegstelsels in kaart te brengen, zijn echter grotendeels beperkt door een lage gevoeligheid en lage hoekresolutie die wordt bereikt door telescopen die traditioneel in dit frequentieregime worden gebruikt. [Israel & Mahoney \(1990\)](#) observeerde bijvoorbeeld een selectie van nabij gelegen sterrenstelsels op 57,5 MHz met behulp van de Clarke Lake telescoop, maar ze hebben nauwelijks een van de waargenomen 133 sterrenstelsels opgelost. Dit beeld wordt verder gecompliceerd door technische uitdagingen in verband met het uitvoeren van waarnemingen bij lage radiofrequenties. Tot op heden zijn M 51 ([Mulcahy et al. 2014](#)), IC 10 ([Heesen et al. 2018](#)) en NGC 253 ([Kapińska et al. 2017](#)) de enige nabij de melkwegstelsels waarvoor radiocontinuumkaarten in de literatuur voorkomen bij frequenties onder ongeveer 300 MHz.

Dit gaat veranderen met de komst van nieuwe laagfrequente radiotelescopen zoals LOFAR die een verbeterde gevoeligheid en een sub-boogseconde hoekresolutie bieden. De LOFAR Two-meter Sky Survey (LoTSS; [Shimwell et al. 2017](#)) heeft als doel om de hele noordelijke hemel af te beelden op 120 – 168 MHz met een gevoeligheid van 0,1 mJy/bundel bij een hoekresolutie van ongeveer 6''. Om me voor te bereiden op grote datasets van laagfrequente radio-onderzoeken zoals LoTSS, heb ik in dit proefschrift een steekproef van nabijgelegen sterrenstelsels bestudeerd, inclusief spiraalstelsels en (post) starburst dwergstelsels, op zoek naar de kenmerkende diffuse radiocontinuumemissie uit de buitenregio's van sterrenstelsels.

Radiotelescopen gebruikt in dit proefschrift

De hoofdstukken 2, 3 en 4 die in dit proefschrift worden gepresenteerd, zijn voornamelijk gebaseerd op observaties van het radio-continuüm van nabije sterrenstelsels op 150 MHz en 1,4 GHz, die werden uitgevoerd met respectievelijk de LOw Frequency Array (LOFAR) en de Westerbork Synthesis Radio Telescope (WSRT). In de volgende subparagrafen presenteert ik een kort overzicht van deze twee radiotelescopen.

De Westerbork Synthesis Radio Telescope (WSRT) is een radio interferometrische array in het noordoosten van Nederland. De huidige WSRT werd voltooid in 1970 (met verdere hardware-upgrades in de jaren 80 en 90) en bestaat uit 14 parabolschotels die langs de oost-westrichting zijn gerangschikt. Tien van de 14 telescopen staan op een vast pad met een afstand van 144 m tussen aangrenzende antennes. De overige vier telescopen bevinden zich op rails en kunnen worden verplaatst om verschillende basislijnconfiguraties te bereiken, afhankelijk van de wetenschappelijke behoeftes. De WSRT biedt een minimale niet-geprojecteerde basislijnlengte van 36 meter tussen antennes ‘9’ en ‘A’ en een maximale basislijnlengte van 2,7 km tussen antennes ‘0’ en ‘D’.

LOFAR, de LOw-Frequency ARray, is een radio-interferometrische array die werkt in het frequentiebereik van 10 – 240 MHz. De 51 individuele telescopen (vanaf januari 2018) - of stations - die de telescooparray vormen, zijn verdeeld over zeven landen in Europa en worden aangestuurd door ASTRON in Nederland. Van de 51 LOFAR-stations bevinden zich 24 stations op dezelfde locatie binnen een straal van 2 km die de LOFAR corestations (CS) vormen en uitstekende *uv*-dekking bieden op korte basislijnen. De overige 14 stations in Nederland worden binnen een straal van 90 km van de LOFAR-kern gedistribueerd en worden meestal de remote stations (RS) genoemd. De overige 13 internationale stations bevinden zich in Duitsland, Zweden, Frankrijk, Polen, Ierland, en het Verenigd Koninkrijk.

Elk LOFAR-station heeft twee soorten antennes: de Low Band Antenna (LBA) die werkt van 10 – 90 MHz en de High Band Antenna (HBA) die werkt in het 110 – 240 MHz frequentiebereik. Zowel de LBA als de HBA gebruiken een omgekeerde V-antenne om de binnenvkomende elektromagnetische straling te detecteren. De basisfunctie van een LOFAR-station is verwant aan de conventionele radiotelescoop, waarbij beide opstellingen het verzamelgebied verschaffen voor het meten van de inkomende elektromagnetische golf, samen met noodzakelijke richt- en volgmechanismen. In tegenstelling tot de meeste traditionele radiotelescopen hebben LOFAR-stations echter geen bewegende componenten. In plaats daarvan gebruikt LOFAR een vaste reeks dipolen per station waarvan de signalen elektronisch worden gecombineerd om het richten en volgen van een traditionele bestuurbare schotel na te bootsen.

Hoewel het werken met gegevens van de Westerbork-telescoop eenvoudig is, kunnen interferometrische waarnemingen bij lage radiofrequenties een uitdaging zijn vanwege een aantal fysieke effecten die het ruisniveau verhogen en artefacten in het beeld creëren. Om deze problemen te verlichten, moesten nieuwe kalibratie- en beeldvormingsalgoritmen worden ontwikkeld en de LOFAR-gegevens in dit

proefschrift werden verwerkt met behulp van een dergelijke techniek genaamd “facetkalibratie” ([van Weeren et al. 2016](#)).

Dit proefschrift

In dit proefschrift hebben we de laagfrequente radiocontinuumeigenschappen onderzocht van een steekproef van nabije spiraalvormige melkstelsels van de dwerg en de late soort. Voor dit werk hebben we twee late-type spiraalstelsels (NGC 4258 en NGC 5457) en vier starburst dwergstelsels (NGC 1569, NGC 4214, NGC 2366 en DDO 50) waargenomen met behulp van de LOw Frequency ARray (LOFAR) met aanvullende 1,4 GHz-waarnemingen met de Westerbork Synthesis Radio Telescope (WSRT). We vatten onze belangrijkste resultaten hieronder samen:

In **hoofdstuk 2** bestudeerden we de radiocontinuumeigenschappen van de stervormende schijf en de afwijkende armen in het nabijgelegen spiraalstelsel NGC 4258 met behulp van nieuwe radiocontinuumwaarnemingen met LOFAR en de WSRT radiotelescopen. Met behulp van de nieuwe gevoelige radiobeelden van NGC 4258 op 150 MHz en 1400 MHz konden we de zwakke radiocontinuumemissie van de stervormende schijf traceren tot een afstand vanuit het midden van 20,73 kpc. Met behulp van de nieuwe radiobeelden hebben we ook voor het eerst de equipartitie magnetische veldsterkte bepaald in de schijf van NGC 4258 die piekt op ongeveer $20 \mu\text{G}$ in de binnenste schijf en daalt tot $4 \mu\text{G}$ ongeveer 20 kpc verwijderd van het galactische centrum.

De driedimensionale oriëntatie van de afwijkende armen in NGC 4258 ten opzichte van de stervormende schijf is een mysterie sinds de ontdekking van de afwijkende armen in 1961. In **hoofdstuk 2** hebben we aangetoond dat gegevens uit de radiopolimetrie kunnen worden gebruikt om te helpen deze lang bestaande vraag op te lossen. Onze 1.4 GHz-polarimetriegegevens, aangevuld met H α - en H α -afbeeldingen van NGC 4258, suggereren dat de afwijkende armen een hybride morfologie hebben waarbij de binnenste delen van de armen zijn ingebed in de schijf terwijl de buitenste delen van een van de armen (de oostelijke arm) zich buiten het vlak bevindt, aan de nabije zijde van de waarnemer.

In **hoofdstuk 3** presenteerden we een multi-frequentie radio-continuumstudie van het nabijgelegen spiraalstelsel M 101 met behulp van gegevens van de LOFAR en de WSRT radiotelescopen. In dit hoofdstuk hebben we aangetoond dat diffuse radiocontinuumemissie op voogminuut-schalen kan worden hersteld op 150 MHz na toepassing van geavanceerde facet-gebaseerde richtingsafhankelijke kalibratie-en beeldvormingstechnieken. Uit de LOFAR en WSRT radiobeelden van M 101 in het frequentiebereik van 146 MHz tot 2270 MHz, zien we dat de hoekomvang van de radio-continuumschijf toeneemt met afnemende frequentie. De waargenomen steiler wordende helling van zowel de radiale helderheidsverdeling als van het azimultaal gemiddelde niet-thermische spectrale indexprofiel suggereren dat de radiostraling die ontstaat uit de buitenste delen van de galactische schijf, die het meest prominent zijn bij lage radiofrequenties, wordt gedomineerd door een oude populatie kosmische stralingselektronen.

De radiofoto's met hoge hoekresolutie van M 101, gepresenteerd in dit proefschrift, stelden ons in staat aan te tonen dat de geïntegreerde fluxdichtheidswaarden van M 101 die in de literatuur worden gerapporteerd allemaal vertekend zijn door verwarringende achtergrondradiobronnen. De geïntegreerde radiospectrale energiedistributie – gecorrigeerd voor verwarringende radiobronnen – toont spectrale vervlakking naar lage radiofrequenties die we toeschrijven aan vrij-vrij absorptie.

In **hoofdstuk 4** bestudeerden we een groep van vier heldere, nabijgelegen dwergstelsels (NGC 1569, NGC 4214, NGC 2366 en DDO 50) die werden geselecteerd op basis van hun bijzonder hoge radiohelderheid. Van de vier dwergstelsels die werden bestudeerd, werd uitgebreide diffuse emissie gedetecteerd in slechts twee van deze sterrenstelsels (NGC 1569 en NGC 4214), waarbij NGC 1569 een laagfrequente uitbreiding van meer dan een boogminuut weergaf boven die gedetecteerd in een 1,4 GHz radiobeeld van WSRT. In de resterende twee dwergsterrenstelsels (NGC 2366 en DDO 50) lijkt de radio-continuümmissie klonterig met emissie uit H II-gebieden die de geïntegreerde fluxdichtheid domineren. Omdat het selectie van vier sterrenstelsels dat hier werd bestudeerd, werd geselecteerd op basis van hun helderheid van de radio, hebben we in hoofdstuk 4 betoogd dat de aankomende LOFAR twee meter hemelonderzoek (LoTSS; Shimwell et al. 2017) niet gevoelig genoeg zal zijn om de diffuse radiohalo's in kaart te brengen in een groot aantal nabijgelegen dwergstelsels.

Hoewel de afzonderlijke sterrenstelsels die in hoofdstuk 2, 3 en 4 zijn bestudeerd allemaal op hun eigen manier uniek zijn, vertonen vier sterrenstelsels (NGC 4258, M 101, NGC 1569 en NGC 4214) een interessant gemeenschappelijk kenmerk: de hoekomvang van deze vier sterrenstelsels neemt toe met afnemende frequentie. We vinden ook dat de verdeling van de spectrale index in de buitenste delen van alle vier sterrenstelsels steiler is dan hun binnenste regionen, wat duidt op een dominantie van oude elektronen in de buitenste delen van sterrenstelsels. In de buitenste delen van alle vier sterrenstelsels die worden gedetecteerd in onze LOFAR-beelden, vinden we zwakke magnetische velden met equipartitieveldsterkten in de orde van enkele microGauss. De resultaten die gepresenteerd worden in dit proefschrift, samen met de recente laagfrequente waarnemingen van andere nabijgelegen spiraalstelsels zoals M 51 (Mulcahy et al. 2014) en IC 10 (Heesen et al. 2018), geven een consistent beeld dat laag-energetische kosmische straling elektronen (met een lange synchrotron-levensduur) zich tot grote radii kunnen voortplanten, wat resulteert in een systematische toename van de hoekgroottes van sterrenstelsels naar lage radiofrequenties. We kunnen dus concluderen dat gevoelige, laagfrequente observaties van nabije sterrenstelsels een uitstekende tracer zijn om magnetische velden te bestuderen in de buitenste delen van galactische schijven en halo's van nabije sterrenstelsels.

Ten slotte, in het tijdperk van data-intensieve radioastronomie, kan een aantal algoritmen voor beeldverwerking worden versneld met behulp van nieuwe computationele hulpmiddelen zoals GPGPU's (General Purpose Graphical Processing Units) om de toenemende datasnelheden aan te kunnen. In **hoofdstuk 5** hebben we een duidelijk voorbeeld hiervan gedemonstreerd door een algemeen gebruikt algoritme in radio-polarimetrie genaamd Faraday Rotation Measure (RM) - synthese te implementeren om met GPGPU's te werken, waardoor een hoge

rekendoorvoer wordt bereikt in vergelijking met bestaande CPU-implementaties van hetzelfde algoritme. Daarnaast hebben we ook aangetoond dat het formaat waarin de astronomische gegevens worden opgeslagen een aanzienlijke invloed kan hebben op de prestaties van het algoritme. In het geval van RM-synthese zagen we dat de goedkeuring van het hiërarchisch gegevensformaat (HDF5) in plaats van het standaard FITS-formaat resulteert in een aanzienlijke afname van de uitvoeringstijd van de code.

Ten slotte heb ik de afgelopen vier jaar plezier gehad met het werken met gegevens van verschillende radio-interferometers. Ik hoop dat u als lezer ook mijn vreugde deelt over deze datasets. Ik zou dit proefschrift uiteindelijk willen afsluiten met de volgende opmerking. In 1944 schreef de toenmalige directeur van de Leidse Sterrewacht Hoogleraar Jan Oort in een brief aan zijn toenmalige student Henk Van de Hulst dat “...by the way, radio astronomy can really become very important if there were at least one line in the radio spectrum.” ([van de Hulst 1957](#)). Hoewel deze verklaring de frustratie toont van een astronoom in het omzetten van vroege radiowaarnemingen in tastbare wetenschappelijke vragen, hebben observaties van het radio-continuum een lange weg afgelegd sinds de jaren 1950 en hebben we de manier waarop we ons universum begrijpen enorm veranderd. Kijkend naar het veld in 2017, ziet de toekomst er rooskleuriger uit dan ooit tevoren met nieuwe en geplande radiotelescopen op zes van de zeven continenten.

Acknowledgements

I moved to Groningen in November 2013 to start working on this PhD thesis and, over the years, this thesis would not have come to fruition without the help and support of many colleagues and friends.

First and foremost, this thesis would not have materialised without the constant support and encouragement from my advisors George Heald and Thijs van der Hulst. I came to the Netherlands with minimal experience in observational astronomy, and I've learnt everything I know about radio interferometry from you. While I could knock on your door whenever I had problems, I also enjoyed independence to pursue my interests. Thanks to you both for putting up with my constant change of plans with the research projects that occasionally lead to dead ends. I honestly could not have asked for a better set of supervisors.

Thanks to Judith, Peter, and Anna for agreeing to be on the reading committee and for taking your time to read the thesis.

I am also indebted to my colleagues from Kapteyn Institute and ASTRON for creating such a stimulating work environment. Thanks to Hannah, Hans, and Nadine for the excellent time we had in office 183. A special thanks to the joint H_I group – especially Erwin, Mark, Tom, Anastasia, Davide, and Filippo – for making me feel at home and putting up with my occasional radio continuum and polarization discussions. Thanks to Ajinkya and Dorota (thanks for agreeing to be a paranymp) for numerous after-work talks ranging from astronomy to working for the private sector. Christa, Lucia, and Martine, thanks a lot for your incredible support; Kapteyn wouldn't be the same without you.

Thanks to Raffaela Morganti for providing me access to the FLITS computer cluster at ASTRON where most of the LOFAR data presented in this thesis were calibrated and imaged. Also to Mike Sipior, Nicolas Vilchez, and Yan Grange for keeping the cluster up and running. I am also thankful to Betsey Adams and Charlotte Sobey for a stimulating conversation over racks of spare ribs and few pints that eventually led to chapter 4. And for the record Charlotte, Pershwari naan does not go well with chicken Madras. To Kelley and Evandro for being great partners in our search for better “hop-flavoured beverage” :-). Gemma and Cees, thanks for organising the spare-ribs dinners in Dwingeloo and the yearly trips to Efteling that have now become a tradition. We should keep this up for years to come. Thanks also to Roberto and the all of SOS for welcoming me into the group. Thanks Matthijs and Sander for your help with the samenvatting.

Most of the work presented in this thesis was carried out under close collaboration with the LOFAR Magnetism Key Science Project (MKSP) and the Surveys KSP. Thanks especially to Rainer, Uli, Volker, Arpad, Kati, Björn, Andrew, Krzysztof, Ralf-Juergen, and David for productive discussions at various conferences across Europe. I should also acknowledge and thank Tim, Reinout, Wendy, Martin, David, Tammo and Andreas for conversations during my second and the third year when the facet calibration scripts were developed and tested. Thanks also to Alex, Therese, Marisa, and Georgi for occasionally sharing my pain related to LOFAR data.

I spent a significant portion of my final year in Perth, Australia working at CSIRO Astronomy and Space Sciences (CASS). Marilyn, you are irreplaceable; It is sad to see you go and it is hard to imagine CASS without you. Cormac, Hayley, Chris, Gulay, Craig, Kevin, J. C., and Tony: You all make CASS a fantastic place to visit and to work. I hope I can find another excuse to visit Perth sometime soon. Thanks to Christopher Hales at the Pawsey Supercomputing Center for various discussions regarding CUDA programming. Narelle, thanks for letting me stay at your apartment in East Vic park for the six months I was there.

Many people helped me in shaping up my career scientific career. My thanks go to my MSc advisors Cathy Horellou and Sebastien Muller. Cathy, we should one day revisit PKS 1830-211. Thanks also to Kirsten, Susanne, Magnus, Carina, Alessandro, Gabriele, John B. and John C. for great lectures and discussions at Chalmers and at Onsala. Thanks also to Marek Abramowicz and Michał Bejger at the Nicolaus Copernicus Astronomical Center for hosting me in Warsaw and introducing me to the beautiful world of collisional Penrose process. Thanks to Maria and Rico for providing much-needed moral support during some tough times in Gothenburg and for welcoming me to your place almost every other week.

Outside of work, several people played a crucial role in making me feel right at home here in Groningen. I am also indebted to two groups of people who made Groningen home away from home. Thanks to Joseph, Raveen, Aarthi, Prachi, Kavya, Nivedhya, Kumar, and Bindhu for creating a mini-India here in Groningen. Thanks also to Joe (thanks for agreeing to be my paronymph, mate), Jack, Hannah, Kelley, Leon, Vanessa, and Glenn for your friendship. Agnes, Dipayan, Sytze, and Simone, it is impossible to image Dierenriemstraat without you.

The last eight years of my life would have looked very different if not for the constant encouragement from members of the Tamil Nadu Astronomers Association (TANASTRO). In particular, I am indebted to Ramesh Kumar, Natrajan, Chidam, Vinodh Kumar, Shan, Vino, Balaji, and soon-to-be-Drs Kav, and Anusha. I will always cherish our conversations under the starry skies at the Birla Planetarium in Chennai.

Thanks Marine for welcoming me into a beautiful French family. And, to my parents, for putting up with my terribly short visits to India over the last seven years.

Finally, over the last four years, I have enjoyed working with data from a variety of radio interferometers. I hope that as a reader, you too share my joy

concerning these datasets. I would finally like to end this thesis with the following note. In 1944, the late director of the Leiden Observatory Professor Jan Oort wrote in a letter to his then student Henk Van de Hulst that “...by the way, radio astronomy can really become very important if there were at least one line in the radio spectrum.”⁹ ([van de Hulst 1957](#)). While this statement shows the frustration of an astronomer in converting early radio observations into tangible scientific questions, radio continuum observations have come a long way since the 1950s and have tremendously changed the way we understand our universe. Looking at the field in 2018, the future looks brighter than ever with new planned radio telescopes on five of the seven continents.

*Sarrvesh S. Sridhar
Groningen, November 5, 2018.*

⁹I should acknowledge [Elbers \(2017\)](#) for bringing this letter by Professor Oort to my attention. For interested readers, [Elbers \(2017\)](#) contains an excellent review of the history of radio astronomy in the Netherlands between 1940 and 1970 including the series of events that eventually led to the construction of the interferometer at Westerbork.

Bibliography

- Adebahr, B., Krause, M., Klein, U., et al. 2013, A&A, 555, A23
Alavi, A., Siana, B., Richard, J., et al. 2016, ApJ, 832, 56
Baars, J. W. M. & Hooghoudt, B. G. 1974, A&A, 31, 323
Baldwin, J. E., Lynden-Bell, D., & Sancisi, R. 1980, MNRAS, 193, 313
Bassa, C. G., Pleunis, Z., & Hessels, J. W. T. 2017, Astronomy and Computing, 18, 40
Basu, A., Mitra, D., Wadadekar, Y., & Ishwara-Chandra, C. H. 2012, MNRAS, 419, 1136
Basu, A., Roychowdhury, S., Heesen, V., et al. 2017, ArXiv e-prints
Baugh, C. M. 2006, Reports on Progress in Physics, 69, 3101
Beck, R. 2016, A&A Rev., 24, 4
Beck, R., Anderson, J., Heald, G., et al. 2013, Astronomische Nachrichten, 334, 548
Beck, R. & Krause, M. 2005, Astronomische Nachrichten, 326, 414
Becker, R. H., White, R. L., & Edwards, A. L. 1991, ApJS, 75, 1
Becker, R. H., White, R. L., & Helfand, D. J. 1995, ApJ, 450, 559
Begum, A., Chengalur, J. N., Karachentsev, I. D., Sharina, M. E., & Kaisin, S. S. 2008, MNRAS, 386, 1667
Bell, A. R. 1978, MNRAS, 182, 147
Bendo, G. J., Galliano, F., & Madden, S. C. 2012, MNRAS, 423, 197
Berge, G. L. & Seielstad, G. A. 1967, ApJ, 148, 367
Berkhuijsen, E. M., Urbanik, M., Beck, R., & Han, J. L. 2016, A&A, 588, A114
Bertone, S., Vogt, C., & Enßlin, T. 2006, MNRAS, 370, 319
Bhatnagar, S., Cornwell, T. J., Golap, K., & Uson, J. M. 2008, A&A, 487, 419
Binney, J. 1992, ARAA, 30, 51
Born, M. & Wolf, E. 1964, Principles of Optics Electromagnetic Theory of Propagation, Interference and Diffraction of Light 2nd edition
Bouchez, A. H., Actonb, D. S., Biasic, R., et al. 2012, in Proc. of SPIE Vol, Vol. 9148, 91480W-1
Brandenburg, A., Moss, D., & Shukurov, A. 1995, MNRAS, 276, 651
Braun, R., Heald, G., & Beck, R. 2010, A&A, 514, A42
Braun, R., Oosterloo, T. A., Morganti, R., Klein, U., & Beck, R. 2007, A&A, 461, 455
Brentjens, M. A. 2007, PhD thesis, University of Groningen
Brentjens, M. A. 2008, A&A, 489, 69

- Brentjens, M. A. & de Bruyn, A. G. 2005, A&A, 441, 1217
- Brienza, M., Godfrey, L., Morganti, R., et al. 2016, A&A, 585, A29
- Briggs, D. 1995, PhD thesis, PhD Thesis, New Mexico Institute of Mining and Technology
- Brown, R. H. & Hazard, C. 1961, MNRAS, 122, 479
- Buitrago, F., Trujillo, I., Conselice, C. J., & Häußler, B. 2013, MNRAS, 428, 1460
- Burbidge, E. M., Burbidge, G. R., & Prendergast, K. H. 1963, ApJ, 138, 375
- Burn, B. J. 1966, MNRAS, 133, 67
- Casse, J. L. & Muller, C. A. 1974, A&A, 31, 333
- Caswell, J. L. & Wills, D. 1967, MNRAS, 135, 231
- Cecil, G., Wilson, A. S., & Tully, R. B. 1992, ApJ, 390, 365
- Chennamangalam, J., Scott, S., Jones, G., et al. 2014, PASA, 31, e048
- Chincarini, G. & Walker, M. F. 1967, ApJ, 149, 487
- Chyžý, K. T., Beck, R., Kohle, S., Klein, U., & Urbanik, M. 2000, A&A, 355, 128
- Chyžý, K. T., Weżgowiec, M., Beck, R., & Bomans, D. J. 2011, A&A, 529, A94
- Clark, S. E., Peek, J. E. G., & Putman, M. E. 2014, ApJ, 789, 82
- Cohen, A. S., Lane, W. M., Cotton, W. D., et al. 2007, AJ, 134, 1245
- Combes, F. 1991, A&A, 243, 109
- Condon, J. J. 1992, ARAA, 30, 575
- Condon, J. J., Cotton, W. D., & Broderick, J. J. 2002, AJ, 124, 675
- Condon, J. J., Cotton, W. D., Greisen, E. W., et al. 1998, AJ, 115, 1693
- Cornwell, T. J. 1983, A&A, 121, 281
- Cornwell, T. J., Golap, K., & Bhatnagar, S. 2008, IEEE Journal of Selected Topics in Signal Processing, 2, 647
- Cotton, W. D., Condon, J. J., Perley, R. A., et al. 2004, in Proc. SPIE, Vol. 5489, Ground-based Telescopes, ed. J. M. Oschmann, Jr., 180–189
- Courtes, G. & Cruvellier, P. 1961, Publications of the Observatoire Haute-Provence, 5
- Dahlem, M., Lisenfeld, U., & Golla, G. 1995, ApJ, 444, 119
- Dahlem, M., Lisenfeld, U., & Rossa, J. 2006, A&A, 457, 121
- Dalcanton, J. J., Williams, B. F., Seth, A. C., et al. 2009, ApJS, 183, 67
- Dale, D. A., Cohen, S. A., Johnson, L. C., et al. 2009, ApJ, 703, 517
- Davis, Jr., L. & Greenstein, J. L. 1951, ApJ, 114, 206
- de Blok, W. J. G., Walter, F., Brinks, E., et al. 2008, AJ, 136, 2648
- de Bruyn, A. G. 1977, A&A, 58, 221
- de Jong, M. L. 1965, ApJ, 142, 1333
- de La Beaujardière, O., Kazés, I., Le Squeren, A. M., & Nguyen-Quang-Rieu. 1968, Annales d'Astrophysique, 31, 387
- de Vaucouleurs, G., de Vaucouleurs, A., Corwin, Jr., H. G., et al. 1991, Third Reference Catalogue of Bright Galaxies. Volume I: Explanations and references. Volume II: Data for galaxies between 0^h and 12^h . Volume III: Data for galaxies between 12^h and 24^h .
- de Vaucouleurs, G., de Vaucouleurs, A., & Corwin, J. R. 1976, in Second reference catalogue of bright galaxies, Vol. 1976, p. Austin: University of Texas Press.,

- Vol. 1976
- Di Teodoro, E. M. & Fraternali, F. 2015, MNRAS, 451, 3021
- Dressel, L. L. & Condon, J. J. 1978, ApJS, 36, 53
- Driessen, L., Roy, J.-R., Robert, C., Devost, D., & Doyon, R. 2000, AJ, 119, 688
- Dubois, Y. & Teyssier, R. 2010, A&A, 523, A72
- Duncan, A. R., Reich, P., Reich, W., & Fürst, E. 1999, A&A, 350, 447
- Ekers, R. D. & Sancisi, R. 1977, A&A, 54, 973
- Elbers, A. 2017, The rise of radio astronomy in the Netherlands (Springer International Publishing)
- Elmegreen, B. G. & Lada, C. J. 1977, ApJ, 214, 725
- Elsen, E., Vishal, V., Houston, M., et al. 2007, ArXiv e-prints
- Farnes, J. S., Green, D. A., & Kantharia, N. G. 2013, ArXiv e-prints
- Farnes, J. S., Heald, G., Junkleweitz, H., et al. 2017, ArXiv e-prints
- Fermi, E. 1949, Physical Review, 75, 1169
- Ferrière, K. & Terral, P. 2014, A&A, 561, A100
- Finlay, C. C., Maus, S., Beggan, C. D., et al. 2010, Geophysical Journal International, 183, 1216
- Fletcher, A., Beck, R., Shukurov, A., Berkhuijsen, E. M., & Horellou, C. 2011, MNRAS, 412, 2396
- Fletcher, A. & Klein, U. 2015, Galactic and Intergalactic Magnetic Fields (Heidelberg: Springer)
- Fluke, C. J. 2012, in Astronomical Society of the Pacific Conference Series, Vol. 461, Astronomical Data Analysis Software and Systems XXI, ed. P. Ballester, D. Egret, & N. P. F. Lorente, 3
- Fluke, C. J., Barnes, D. G., Barsdell, B. R., & Hassan, A. H. 2011, PASA, 28, 15
- Fomalont, E. B., Ebneter, K. A., van Breugel, W. J. M., & Ekers, R. D. 1989, ApJL, 346, L17
- Gardner, F. F. & Whiteoak, J. B. 1966, ARAA, 4, 245
- Gerola, H., Seiden, P. E., & Schulman, L. S. 1980, ApJ, 242, 517
- Gil de Paz, A., Boissier, S., Madore, B. F., et al. 2007, ApJS, 173, 185
- Gioia, I. M. & Gregorini, L. 1980, A&AS, 41, 329
- Graeve, R., Klein, U., & Wielebinski, R. 1990, A&A, 238, 39
- Green, D. A. 2009, Bulletin of the Astronomical Society of India, 37, 45
- Green, D. A. 2011, Bulletin of the Astronomical Society of India, 39, 289
- Greenfield, P., Droettboom, M., & Bray, E. 2015, Astronomy and Computing, 12, 240
- Gregory, P. C. & Condon, J. J. 1991, ApJS, 75, 1011
- Greisen, E. W. 1998, in Astronomical Society of the Pacific Conference Series, Vol. 145, Astronomical Data Analysis Software and Systems VII, ed. R. Albrecht, R. N. Hook, & H. A. Bushouse, 204
- Grocholski, A. J., Aloisi, A., van der Marel, R. P., et al. 2008, ApJL, 686, L79
- Hale, G. E. 1908a, ApJ, 28, 315
- Hale, G. E. 1908b, ApJ, 28, 315
- Hales, S. E. G., Masson, C. R., Warner, P. J., Baldwin, J. E., & Green, D. A. 1993, MNRAS, 262, 1057
- Hamaker, J. P., Bregman, J. D., & Sault, R. J. 1996, A&AS, 117, 137

- Harris, C., Haines, K., & Staveley-Smith, L. 2008, Experimental Astronomy, 22, 129
- Hartwell, J. M., Stevens, I. R., Strickland, D. K., Heckman, T. M., & Summers, L. K. 2004, MNRAS, 348, 406
- Heald, G. 2009, in IAU Symposium, Vol. 259, IAU Symposium, ed. K. G. Strassmeier, A. G. Kosovichev, & J. E. Beckman, 591–602
- Heald, G., Bell, M. R., Horneffer, A., et al. 2011, Journal of Astrophysics and Astronomy, 32, 589
- Heald, G., Braun, R., & Edmonds, R. 2009, A&A, 503, 409
- Heald, G., McKean, J., Pizzo, R., et al. 2010, ArXiv e-prints
- Heald, G. H. 2012, ApJL, 754, L35
- Heckman, T. M., Dahlem, M., Lehnert, M. D., et al. 1995, ApJ, 448, 98
- Heeschen, D. S. & Wade, C. M. 1964, AJ, 69, 277
- Heesen, V., Brinks, E., Leroy, A. K., et al. 2014, AJ, 147, 103
- Heesen, V., Dettmar, R.-J., Krause, M., Beck, R., & Stein, Y. 2016, MNRAS, 458, 332
- Heesen, V., Rafferty, D. A., Horneffer, A., et al. 2018, ArXiv e-prints
- Heesen, V., Rau, U., Rupen, M. P., Brinks, E., & Hunter, D. A. 2011, ApJL, 739, L23
- Helfer, T. T., Thornley, M. D., Regan, M. W., et al. 2003, ApJS, 145, 259
- Hey, J. S., Phillips, J. W., & Parsons, S. J. 1946, Nature, 157, 296
- Hiltner, W. A. 1949, Science, 109, 165
- Hodge, P., Kennicutt, R. C., & Strobel, N. 1994, PASP, 106, 765
- Hodge, P. W., Gurwell, M., Goldader, J. D., & Kennicutt, Jr., R. C. 1990, ApJS, 73, 661
- Hogan, C. J. 1983, Physical Review Letters, 51, 1488
- Högbom, J. A. & Brouw, W. N. 1974, A&A, 33, 289
- Hu, N., Wang, E., Lin, Z., et al. 2018, ApJ, 854, 68
- Hummel, E. & Beck, R. 1995, A&A, 303, 691
- Hummel, E., Krause, M., & Lesch, H. 1989, A&A, 211, 266
- Humphreys, E. M. L., Reid, M. J., Moran, J. M., Greenhill, L. J., & Argon, A. L. 2013, ApJ, 775, 13
- Hunt, L. K., Dyer, K. K., Thuan, T. X., & Ulvestad, J. S. 2004, ApJ, 606, 853
- Hunter, D. A. & Elmegreen, B. G. 2004, AJ, 128, 2170
- Hunter, D. A. & Elmegreen, B. G. 2006, ApJS, 162, 49
- Hunter, D. A., Elmegreen, B. G., & Baker, A. L. 1998, ApJ, 493, 595
- Hunter, D. A., Elmegreen, B. G., & Ludka, B. C. 2010, AJ, 139, 447
- Hunter, D. A., Ficut-Vicas, D., Ashley, T., et al. 2012, AJ, 144, 134
- Hyman, S. D., Calle, D., Weiler, K. W., et al. 2001, ApJ, 551, 702
- Icke, V. 1979, A&A, 74, 42
- Intema, H. T., Jagannathan, P., Mooley, K. P., & Frail, D. A. 2017, A&A, 598, A78
- Intema, H. T., van der Tol, S., Cotton, W. D., et al. 2009, A&A, 501, 1185
- Israel, F. P., Goss, W. M., & Allen, R. J. 1975, A&A, 40, 421
- Israel, F. P. & Mahoney, M. J. 1990, ApJ, 352, 30
- Israel, F. P. & van Driel, W. 1990, A&A, 236, 323

- Jansky, K. G. 1933, *Nature*, 132, 66
- Jarrett, T. H., Masci, F., Tsai, C. W., et al. 2013, *AJ*, 145, 6
- Jelić, V., de Bruyn, A. G., Mevius, M., et al. 2014, *A&A*, 568, A101
- Jelić, V., de Bruyn, A. G., Pandey, V. N., et al. 2015, *A&A*, 583, A137
- Jenness, T. 2015, *Astronomy and Computing*, 12, 221
- Jenness, T., Berry, D. S., Currie, M. J., et al. 2015, *Astronomy and Computing*, 12, 146
- Jones, R. C. 1941, *Journal of the Optical Society of America (1917-1983)*, 31, 488
- Józsa, G. I. G., Kenn, F., Klein, U., & Oosterloo, T. A. 2007, *A&A*, 468, 731
- Kamphuis, J. 1993, PhD thesis, PhD Thesis, University of Groningen
- Kanekar, N., Prochaska, J. X., Smette, A., et al. 2014, *MNRAS*, 438, 2131
- Kanekar, N., Smette, A., Briggs, F. H., & Chengalur, J. N. 2009, *ApJL*, 705, L40
- Kapińska, A. D., Staveley-Smith, L., Crocker, R., et al. 2017, *ApJ*, 838, 68
- Kazemi, S., Yatawatta, S., Zaroubi, S., et al. 2011, *MNRAS*, 414, 1656
- Kazès, I., Le Squeren, A. M., & Nguyen-Quang-Rieu. 1970, *Astrophys. Lett.*, 6, 193
- Kennicutt, Jr., R. C., Armus, L., Bendo, G., et al. 2003, *PASP*, 115, 928
- Kennicutt, Jr., R. C., Hao, C.-N., Calzetti, D., et al. 2009, *ApJ*, 703, 1672
- Kennicutt, Jr., R. C., Lee, J. C., Funes, J. G., et al. 2008, *ApJS*, 178, 247
- Kepley, A. A., Mühle, S., Everett, J., et al. 2010, *ApJ*, 712, 536
- Kepley, A. A., Zweibel, E. G., Wilcots, E. M., Johnson, K. E., & Robishaw, T. 2011, *ApJ*, 736, 139
- Kiepenheuer, K. O. 1950, *Physical Review*, 79, 738
- Kitchener, G. 2016, PhD thesis, PhD Thesis, University of Hertfordshire, The United Kingdom, (2016)
- Klein, U. 1986, *A&A*, 168, 65
- Klein, U. & Graeve, R. 1986, *A&A*, 161, 155
- Klein, U., Wielebinski, R., & Thuan, T. X. 1984, *A&A*, 141, 241
- Kothes, R., Fedotov, K., Foster, T. J., & Uyaniker, B. 2006, *A&A*, 457, 1081
- Krause, M., Fendt, C., & Neininger, N. 2007, *A&A*, 467, 1037
- Krause, M., Klein, U., & Beck, R. 1984, *A&A*, 138, 385
- Krause, M. & Löhr, A. 2004, *A&A*, 420, 115
- Kronberg, P. P., Lesch, H., & Hopp, U. 1999, *ApJ*, 511, 56
- Kuntz, K. D. & Snowden, S. L. 2010, *ApJS*, 188, 46
- Kuntz, K. D., Snowden, S. L., Pence, W. D., & Mukai, K. 2003, *ApJ*, 588, 264
- Lacy, M., Rawlings, S., Saunders, R., & Warner, P. J. 1993, *MNRAS*, 264, 721
- Laing, R. A. 1980, *MNRAS*, 193, 439
- Lara, L., Mack, K.-H., Lacy, M., et al. 2000, *A&A*, 356, 63
- Leahy, J. P. & Williams, A. G. 1984, *MNRAS*, 210, 929
- Lenc, E., Gaensler, B. M., Sun, X. H., et al. 2016, *ApJ*, 830, 38
- Lequeux, J., Peimbert, M., Rayo, J. F., Serrano, A., & Torres-Peimbert, S. 1979, *A&A*, 80, 155
- Lin, L., Zou, H., Kong, X., et al. 2013, *ApJ*, 769, 127
- Lisenfeld, U., Wilding, T. W., Pooley, G. G., & Alexander, P. 2004, *MNRAS*, 349, 1335
- Longair, M. S. 2010, *High Energy Astrophysics* (Cambridge University Press)

- Magro, A., Karastergiou, A., Salvini, S., et al. 2011, MNRAS, 417, 2642
- Manchester, R. N. 1972, ApJ, 172, 43
- Manchester, R. N. 1974, ApJ, 188, 637
- Marinacci, F., Binney, J., Fraternali, F., et al. 2010, MNRAS, 404, 1464
- Markoff, J. 2004, Intels big shift after hitting technical wall, The New York Times
- Martin, C. L. 1998, ApJ, 506, 222
- Martin, C. L. & Kennicutt, Jr., R. C. 1997, ApJ, 483, 698
- Martin, P., Roy, J.-R., Noreau, L., & Lo, K. Y. 1989, ApJ, 345, 707
- Mathewson, D. S., van der Kruit, P. C., & Brouw, W. N. 1972, A&A, 17, 468
- McMullin, J. P., Waters, B., Schiebel, D., Young, W., & Golap, K. 2007, in Astronomical Society of the Pacific Conference Series, Vol. 376, Astronomical Data Analysis Software and Systems XVI, ed. R. A. Shaw, F. Hill, & D. J. Bell, 127
- McNichols, A. T., Teich, Y. G., Nims, E., et al. 2016, ApJ, 832, 89
- Mezger, P. G. & Henderson, A. P. 1967, ApJ, 147, 471
- Michalakes, J. & Vachharajani, M. 2008, Parallel Processing Letters, 18, 531
- Mihos, J. C., Harding, P., Spengler, C. E., Rudick, C. S., & Feldmeier, J. J. 2013, ApJ, 762, 82
- Mihos, J. C., Keating, K. M., Holley-Bockelmann, K., Pisano, D. J., & Kassim, N. E. 2012, ApJ, 761, 186
- Mohan, N. & Rafferty, D. 2015, PyBDSM: Python Blob Detection and Source Measurement, Astrophysics Source Code Library
- Moore, B., Katz, N., Lake, G., Dressler, A., & Oemler, A. 1996, Nature, 379, 613
- Morris, D. & Berge, G. L. 1964, AJ, 69, 641
- Mulcahy, D. D., Horneffer, A., Beck, R., et al. 2014, A&A, 568, A74
- Mulcahy, D. D., Horneffer, A., Beck, R., et al. 2018, ArXiv e-prints
- Nelles, A., Hörandel, J. R., Karskens, T., et al. 2015, Journal of Instrumentation, 10, P11005
- Nixon, C. J., Hands, T. O., King, A. R., & Pringle, J. E. 2018, MNRAS
- Noordam, J. E. 2004, in Proc. SPIE, Vol. 5489, Ground-based Telescopes, ed. J. M. Oschmann, Jr., 817–825
- Norman, C. A. & Ikeuchi, S. 1989, ApJ, 345, 372
- Nvidia. 2017, CUDA Programming Guide 8.0
- Offringa, A. R., de Bruyn, A. G., Biehl, M., et al. 2010, MNRAS, 405, 155
- Offringa, A. R., McKinley, B., Hurley-Walker, N., et al. 2014, MNRAS, 444, 606
- Offringa, A. R., van de Gronde, J. J., & Roerdink, J. B. T. M. 2012, A&A, 539, A95
- Ogle, P. M., Lanz, L., & Appleton, P. N. 2014, ApJL, 788, L33
- Oh, S.-H., de Blok, W. J. G., Walter, F., Brinks, E., & Kennicutt, Jr., R. C. 2008, AJ, 136, 2761
- Oh, S.-H., Hunter, D. A., Brinks, E., et al. 2015, AJ, 149, 180
- Oosterloo, T., Verheijen, M. A. W., van Cappellen, W., et al. 2009, in Wide Field Astronomy & Technology for the Square Kilometre Array, 70
- Ord, S., Greenhill, L., Wayth, R., et al. 2009, in Astronomical Society of the Pacific Conference Series, Vol. 411, Astronomical Data Analysis Software and Systems XVIII, ed. D. A. Bohlender, D. Durand, & P. Dowler, 127

- Otmianowska-Mazur, K. & Vollmer, B. 2003, A&A, 402, 879
- Ott, J., Stilp, A. M., Warren, S. R., et al. 2012, AJ, 144, 123
- Owens, J. D., Houston, M., Luebke, D., et al. 2008, Proceedings of the IEEE, 96, 879
- Owens, J. D., Luebke, D., Govindaraju, N., et al. 2007, Computer Graphics Forum, 26, 80
- Pacholczyk, A. G. 1970, Radio astrophysics. Nonthermal processes in galactic and extragalactic sources
- Pandey, V. N., van Zwieten, J. E., de Bruyn, A. G., & Nijboer, R. 2009, in Astronomical Society of the Pacific Conference Series, Vol. 407, The Low-Frequency Radio Universe, ed. D. J. Saikia, D. A. Green, Y. Gupta, & T. Venturi, 384
- Pence, W. 1999, in Astronomical Society of the Pacific Conference Series, Vol. 172, Astronomical Data Analysis Software and Systems VIII, ed. D. M. Mehringer, R. L. Plante, & D. A. Roberts, 487
- Perkins, S. J., Marais, P. C., Zwart, J. T. L., et al. 2015, Astronomy and Computing, 12, 73
- Perley, R. A. & Butler, B. J. 2013, ApJS, 204, 19
- Portegies Zwart, S. F., Bellemans, R. G., & Geldof, P. M. 2007, New A, 12, 641
- Pratley, L. & Johnston-Hollitt, M. 2016, MNRAS, 462, 3483
- Price, D. C., Barsdell, B. R., & Greenhill, L. J. 2015, Astronomy and Computing, 12, 212
- Price, D. C., Staveley-Smith, L., Bailes, M., et al. 2016, Journal of Astronomical Instrumentation, 5, 1641007
- Puche, D., Westpfahl, D., Brinks, E., & Roy, J.-R. 1992, AJ, 103, 1841
- Reber, G. 1940, ApJ, 91, 621
- Relaño, M., Lisenfeld, U., Vilchez, J. M., & Battaner, E. 2006, A&A, 452, 413
- Rengelink, R. B., Tang, Y., de Bruyn, A. G., et al. 1997, A&AS, 124, 259
- Riley, J. M. W., Waldram, E. M., & Riley, J. M. 1999, MNRAS, 306, 31
- Rogstad, D. H. & Shostak, G. S. 1971, A&A, 13, 99
- Roychowdhury, S. & Chengalur, J. N. 2012, MNRAS, 423, L127
- Sancisi, R., Fraternali, F., Oosterloo, T., & van der Hulst, T. 2008, A&A Rev., 15, 189
- Sanders, R. H. 1982, in IAU Symposium, Vol. 97, Extragalactic Radio Sources, ed. D. S. Heeschen & C. M. Wade, 145–147
- Sault, R. J., Teuben, P. J., & Wright, M. C. H. 1995, in Astronomical Society of the Pacific Conference Series, Vol. 77, Astronomical Data Analysis Software and Systems IV, ed. R. A. Shaw, H. E. Payne, & J. J. E. Hayes, 433
- Scaife, A. M. M. & Heald, G. H. 2012, MNRAS, 423, L30
- Schaaf, K. & Overeem, R. 2004, Experimental Astronomy, 17, 287
- Schiwietz, T., Chang, T.-c., Speier, P., & Westermann, R. 2006in , 61423T
- Schlegel, D. J., Finkbeiner, D. P., & Davis, M. 1998, ApJ, 500, 525
- Schmitt, H. R., Calzetti, D., Armus, L., et al. 2006, ApJS, 164, 52
- Schomberg, H. & Timmer, J. 1995, IEEE transactions on medical imaging, 14, 596
- Segalovitz, A. 1977, A&A, 54, 703

- Shimwell, T. W., Röttgering, H. J. A., Best, P. N., et al. 2017, *A&A*, 598, A104
- Shklovskii, I. S. 1960, Cosmic radio waves
- Shortridge, K. 2015, in Astronomical Society of the Pacific Conference Series, Vol. 495, Astronomical Data Analysis Software and Systems XXIV (ADASS XXIV), ed. A. R. Taylor & E. Rosolowsky, 527
- Sofue, Y. 1980, *PASJ*, 32, 79
- Soida, M., Krause, M., Dettmar, R.-J., & Urbanik, M. 2011, *A&A*, 531, A127
- Sokoloff, D. D., Bykov, A. A., Shukurov, A., et al. 1998, *MNRAS*, 299, 189
- Spencer, M., Loebman, S., & Yoachim, P. 2014, *ApJ*, 788, 146
- Stecher, T. P., Bohlin, R. C., Hill, J. K., & Jura, M. A. 1982, *ApJL*, 255, L99
- Steidel, C. C., Giavalisco, M., Pettini, M., Dickinson, M., & Adelberger, K. L. 1996, *ApJL*, 462, L17
- Stinson, G. S., Dalcanton, J. J., Quinn, T., Kaufmann, T., & Wadsley, J. 2007, *ApJ*, 667, 170
- Sulentic, J. W. 1976, *ApJS*, 32, 171
- Tabatabaei, F. S., Krause, M., & Beck, R. 2007, *A&A*, 472, 785
- Tabatabaei, F. S., Martinsson, T. P. K., Knapen, J. H., et al. 2016, *ApJL*, 818, L10
- Tasse, C., van der Tol, S., van Zwieten, J., van Diepen, G., & Bhatnagar, S. 2013, *A&A*, 553, A105
- Taylor, A. R., Stil, J. M., & Sunstrum, C. 2009, *ApJ*, 702, 1230
- FITS* Working Group. 2008, Definition of the Flexible Image Transport System (*FITS*)
- The HDF Group. 2011, *HDF5 User's Guide* release 1.8.8
- Thilker, D. A., Bianchi, L., Meurer, G., et al. 2007, *ApJS*, 173, 538
- Thomas, B., Jenness, T., Economou, F., et al. 2015, *Astronomy and Computing*, 12, 133
- Thompson, A. R., Moran, J. M., & Swenson, Jr., G. W. 2001, *Interferometry and Synthesis in Radio Astronomy*, 2nd Edition
- Thuan, T. X., Hibbard, J. E., & Lévrier, F. 2004, *AJ*, 128, 617
- Tolstoy, E., Saha, A., Hoessel, J. G., & McQuade, K. 1995, *AJ*, 110, 1640
- Tomita, A., Ohta, K., & Saito, M. 1994, *PASJ*, 46, 335
- Tongue, T. D. & Westpfahl, D. J. 1995, *AJ*, 109, 2462
- Trancoso, P. & Charalambous, M. 2005, in *Digital System Design*, 2005. Proceedings. 8th Euromicro Conference on, IEEE, 306–313
- Tüllmann, R., Breitschwerdt, D., Rossa, J., Pietsch, W., & Dettmar, R.-J. 2006a, *A&A*, 457, 779
- Tüllmann, R., Dettmar, R.-J., Soida, M., Urbanik, M., & Rossa, J. 2000, *A&A*, 364, L36
- Tüllmann, R., Pietsch, W., Rossa, J., Breitschwerdt, D., & Dettmar, R.-J. 2006b, *A&A*, 448, 43
- Tully, R. B. & Fisher, J. R. 1988, Catalog of Nearby Galaxies
- Uhlig, M., Pfrommer, C., Sharma, M., et al. 2012, *MNRAS*, 423, 2374
- van Albada, G. D. 1977, *A&A*, 61, 297
- van Albada, G. D. 1978, PhD thesis, Ph. D. thesis, University of Leiden (1978)
- van Albada, G. D. 1980, *A&A*, 90, 123

- van Albada, G. D. & Shane, W. W. 1975, A&A, 42, 433
- van Albada, G. D. & van der Hulst, J. M. 1982, A&A, 115, 263
- van de Hulst, H. C. 1957, in IAU Symposium, Vol. 4, Radio astronomy, ed. H. C. van de Hulst, 3
- Van der Hulst, T. & Sancisi, R. 1988, AJ, 95, 1354
- van der Kruit, P. C. 1974, ApJ, 192, 1
- van der Kruit, P. C., Oort, J. H., & Mathewson, D. S. 1972, A&A, 21, 169
- van der Tol, S., Jeffs, B. D., & van der Veen, A.-J. . 2007, IEEE Transactions on Signal Processing, 55, 4497
- Van Eck, C. L., Havercorn, M., Alves, M. I. R., et al. 2018, ArXiv e-prints
- Van Eck, C. L., Havercorn, M., Alves, M. I. R., et al. 2017, A&A, 597, A98
- van Eymeren, J., Jütte, E., Jog, C. J., Stein, Y., & Dettmar, R.-J. 2011, A&A, 530, A29
- van Eymeren, J., Marcelin, M., Koribalski, B., et al. 2009, A&A, 493, 511
- van Haarlem, M. P., Wise, M. W., Gunst, A. W., et al. 2013, A&A, 556, A2
- van Weeren, R. J., Röttgering, H. J. A., Brüggen, M., & Hoeft, M. 2010, Science, 330, 347
- van Weeren, R. J., Röttgering, H. J. A., Intema, H. T., et al. 2012, A&A, 546, A124
- van Weeren, R. J., Williams, W. L., Hardcastle, M. J., et al. 2016, ApJS, 223, 2
- Veilleux, S., Cecil, G., & Bland-Hawthorn, J. 2005, ARAA, 43, 769
- Viallefond, F., Allen, R. J., & Goss, W. M. 1981, A&A, 104, 127
- Vinkó, J., Sárneczky, K., Takáts, K., et al. 2012, A&A, 546, A12
- Vollmer, B., Soida, M., Beck, R., et al. 2013, A&A, 553, A116
- Vollmer, B., Soida, M., Beck, R., et al. 2007, A&A, 464, L37
- Vollmer, B., Soida, M., Chung, A., et al. 2008, A&A, 483, 89
- Waller, W. H., Bohlin, R. C., Cornett, R. H., et al. 1997, ApJ, 481, 169
- Walter, F., Brinks, E., de Blok, W. J. G., et al. 2008, AJ, 136, 2563
- Warwick, R. S., Jenkins, L. P., Read, A. M., Roberts, T. P., & Owen, R. A. 2007, MNRAS, 376, 1611
- Westerhout, G., Brouw, W. N., Muller, C. A., & Tinbergen, J. 1962, AJ, 67, 590
- Westmoquette, M. S., Exter, K. M., Smith, L. J., & Gallagher, J. S. 2007a, MNRAS, 381, 894
- Westmoquette, M. S., Smith, L. J., & Gallagher, J. S. 2008, MNRAS, 383, 864
- Westmoquette, M. S., Smith, L. J., Gallagher, J. S., & Exter, K. M. 2007b, MNRAS, 381, 913
- Weżgowiec, M., Urbanik, M., Beck, R., Chyzy, K. T., & Soida, M. 2012, A&A, 545, A69
- Weżgowiec, M., Urbanik, M., Vollmer, B., et al. 2007, A&A, 471, 93
- White, R. L. & Becker, R. H. 1992, ApJS, 79, 331
- White, S. D. M. & Frenk, C. S. 1991, ApJ, 379, 52
- Widrow, L. M. 2002, Reviews of Modern Physics, 74, 775
- Wielebinski, R. 2012, Journal of Astronomical History and Heritage, 15, 76
- Wielebinski, R. & Shakeshaft, J. R. 1962, Nature, 195, 982
- Wieringa, M. H., de Bruyn, A. G., Jansen, D., Brouw, W. N., & Katgert, P. 1993, A&A, 268, 215

- Wijnholds, S. J. & van der Veen, A.-J. 2009, IEEE Transactions on Signal Processing, 57, 3512
- Wijnholds, S. J. & van der Veen, A.-J. 2010, ArXiv e-prints
- Williams, W. L., van Weeren, R. J., Röttgering, H. J. A., et al. 2016, MNRAS
- Wilson, A. S., Yang, Y., & Cecil, G. 2001, ApJ, 560, 689
- Wrobel, J. M. & Walker, R. C. 1999, in Astronomical Society of the Pacific Conference Series, Vol. 180, Synthesis Imaging in Radio Astronomy II, ed. G. B. Taylor, C. L. Carilli, & R. A. Perley, 171
- Yatawatta, S., Zaroubi, S., de Bruyn, G., Koopmans, L., & Noordam, J. 2008, ArXiv e-prints
- Zink, B. 2011, ArXiv e-prints